ADVERTIMENT. La consulta d'aquesta tesi queda condicionada a l'acceptació de les següents condicions d'ús: La difusió d'aquesta tesi per mitjà del servei TDX (www.tesisenxarxa.net) ha estat autoritzada pels titulars dels drets de propietat intel·lectual únicament per a usos privats emmarcats en activitats d'investigació i docència. No s'autoritza la seva reproducció amb finalitats de lucre ni la seva difusió i posada a disposició des d'un lloc aliè al servei TDX. No s'autoritza la presentació del seu contingut en una finestra o marc aliè a TDX (framing). Aquesta reserva de drets afecta tant al resum de presentació de la tesi com als seus continguts. En la utilització o cita de parts de la tesi és obligat indicar el nom de la persona autora.

ADVERTENCIA. La consulta de esta tesis queda condicionada a la aceptación de las siguientes condiciones de uso: La difusión de esta tesis por medio del servicio TDR (www.tesisenred.net) ha sido autorizada por los titulares de los derechos de propiedad intelectual únicamente para usos privados enmarcados en actividades de investigación y docencia. No se autoriza su reproducción con finalidades de lucro ni su difusión y puesta a disposición desde un sitio ajeno al servicio TDR. No se autoriza la presentación de su contenido en una ventana o marco ajeno a TDR (framing). Esta reserva de derechos afecta tanto al resumen de presentación de la tesis como a sus contenidos. En la utilización o cita de partes de la tesis es obligado indicar el nombre de la persona autora.

WARNING. On having consulted this thesis you're accepting the following use conditions: Spreading this thesis by the TDX (www.tesisenxarxa.net) service has been authorized by the titular of the intellectual property rights only for private uses placed in investigation and teaching activities. Reproduction with lucrative aims is not authorized neither its spreading and availability from a site foreign to the TDX service. Introducing its content in a window or frame foreign to the TDX service is not authorized (framing). This rights affect to the presentation summary of the thesis as well as to its contents. In the using or citation of parts of the thesis it's obliged to indicate the name of the author

Alessandro Acampora, PhD Candidate
Centre Tecnologic de Telecomunicacions de Catalunya (CTTC)

Nonlinear Simulation and Design of Microwave, Multi-Device Distributed Autonomous Circuits

Barcelona, March 22, 2013.

Nonlinear Simulation and Design of Microwave Distributed Multi-Device Autonomous Circuits

PhD Candidate: Alessandro Acampora, M.Sc
Centre Tecnologic de Telecomunicacions de Catalunya (CTTC)
Universitat Politecnica de Catalunya (UPC)
Dept. of. Signal Theory and Communications (TSC)

A DISSERTATION SUBMITTED IN PARTIAL FULFILLMENT OF THE REQUIREMENTS FOR THE DEGREE DOCTOR OF PHILOSOPHY IN TELECOMMUNICATION ENGINEERING

Barcelona, March 22, 2013

Thesis Director: Dr. Apostolos Georgiadis, Ph.D
Centre Tecnologic de Telecomunicacions de Catalunya (CTTC)

Thesis Supervisor (University): Prof. Jordi Mateu, Ph.D
Centre Tecnologic de Telecomunicacions de Catalunya (CTTC)
Universitat Politecnica de Catalunya (UPC)

This Page Intentionally Left Blank

Acta de qualificació de tesi doctoral

Curs acadèmic:2012/13

Nom i cognoms Alessandro Acampora

Programa de doctorat Teoria del Senyal i Comunicacions

Unitat estructural responsable del programa Centre Tecnologic de Telecomunicacions de Catalunya (CTTC)

Resolució del Tribunal

Reunit el Tribunal designat a l'efecte, el doctorand / la doctoranda exposa el tema de la seva tesi doctoral titulada _____Nonlinear Simulation and Design of Microwave Multi Device, Distributed Autonomous Circuits _____ _____.

Acabada la lectura i després de donar resposta a les qüestions formulades pels membres titulars del tribunal, aquest atorga la qualificació:

☐ APTA/E ☐ NO APTA/E

(Nom, cognoms i signatura)		(Nom, cognoms i signatura)
President/a		Secretari/ària
(Nom, cognoms i signatura)	(Nom, cognoms i signatura)	(Nom, cognoms i signatura)
Vocal	Vocal	Vocal

_____, _____ d'/de _____ de _____

El resultat de l'escrutini dels vots emesos pels membres titulars del tribunal, efectuat per l'Escola de Doctorat, a instància de la Comissió de Doctorat de la UPC, atorga la MENCIÓ CUM LAUDE:

☐ SÍ ☐ NO

(Nom, cognoms i signatura)	(Nom, cognoms i signatura)
Presidenta de la Comissió de Doctorat	Secretària de la Comissió de Doctorat

Barcelona, _____ d'/de _____ de _____

This Page Intentionally Left Blank

"Der Mensch kann tun was er will; er kann aber nicht wollen was er will." (Arthur Schopenauer)

© ALESSANDRO ACAMPORA, 2013. All rights reserved.

THESIS ABSTRACT

It is widely believed that many drawbacks in today's wireless communication paradigm might be relieved by enabling high carrier frequency transmission, and endowing both the network and the user equipment with some degree of reconfigurability. The urgency of a new framework in wireless digital transmission which should allow for higher bit rate, lower latency and tighter delay constraints, led us to investigate the fundamental building blocks which, at the circuital/device level, will foster a change towards more efficient communication schemes, delivering a more satisfactory end user experience.

Specifically, this work deals with the inherently analog devices, found at the core of each transceiver module and capable of providing the carrier signal; these are the oscillators. In particular, two distinct classes of oscillators are regarded central to our contribution. One class is constituted by N-push oscillators, which thanks to coupling effect of N identical core oscillators allow *N-fold* harmonic generation (and thus high frequency transmission). The second class is constituted by wideband tunable oscillators, whose topology derives from a feedback distributed amplifier and therefore called distributed oscillators; by adequately altering the bias level at each section Distributed Voltage Controlled Oscillators can be implemented (which can scan a wide frequency range). The introductory part of this work, deals with their operation principles in great detail.

As microwave oscillators are nonlinear devices, a full nonlinear analysis, synthesis, and optimization is considered for their implementation. Consequently, nonlinear numerical techniques have been reviewed in the second part of the thesis. Particularly, the role of Harmonic Balance simulations and the auxiliary generator/probe method for obtaining the oscillator solutions has been emphasized; the overall research goal of this dissertation is to show that the former techniques are very effective in obtaining detailed information about the periodic steady state behavior for the two class of circuits being investigated.

A triple-push oscillator topology has been initially considered. Provided a certain phase distribution is maintained among the oscillating elements, the output power of the third harmonic increases while the lower order harmonics cancel out, which represents the default operating mode. Due to circuit symmetry, to the presence of delay in the coupling network and to unavoidable mismatches, unwanted oscillating modes might coexist with the intended one. A design strategy relying on the Harmonic Balance parametric analysis of the oscillating voltage at a selected node in the coupling network with respect to coupling phase and coupling strength is presented, to the aim of quenching undesired oscillation modes.

Moreover the design of a four stage reverse mode distributed voltage controlled oscillator (DVCO) has been described. All the design steps have been reported, from a very idealized, purely behavioral design to a very concrete one, involving details derived from electromagnetic simulations. Harmonic Balance techniques were used to evaluate its tuning function, output power and DC current consumption, which have been completely characterized across the tuning bandwidth. Finally, a method for an optimized design with reduced variations in the output

power has been presented. An alternative implementation, targeting wider tuning ranges/ higher oscillation frequencies was introduced. The measurements performed on the fabricated prototypes revealed good agreement with the simulation results, confirming the validity of the approach.

RESUMEN DE LA TESIS

Muchos inconvenientes en el paradigma actual de comunicación inalámbrica podrían ser aliviados al permitir la transmisión de alta frecuencia de la portadora, y dotando a la red y el equipo de usuario con un cierto grado de reconfigurabilidad. La urgencia de un nuevo marco en la transmisión digital inalámbrica que debe tener en cuenta bit-rates elevados, menor latencia y restricciones en el retardo máximo, nos llevó a investigar los principales elementos constitutivos para fomentar un cambio, a nivel circuital y de dispositivo, hacia esquemas de comunicación más eficientes.

Específicamente, este trabajo se ocupa de los subsistemas inherentemente analógicos, que se encuentran en el núcleo de cada módulo transceptor y proporcionan la señal portadora, los osciladores. En particular, nuestra contribución se enfoca en el análisis y el diseño de dos tipologías distintas de osciladores. La primera, está constituida por osciladores N-push, que gracias a un efecto de acoplamiento de N osciladores elementales, permite subir el nivel de potencia de la componente armónica de orden N y por lo tanto, alcanzar la transmisión de alta frecuencia. La segunda clase está constituida por osciladores sintonizables de banda ancha, cuya topología se deriva de un amplificador distribuido (con bucle de realimentación) llamados osciladores distribuidos; modificando el nivel de polarización en cada sección, se obtienen osciladores distribuidos controlados por tensión (DVCO) que pueden escanear una amplia gama de frecuencias.

En la sección introductora, se abordan los fundamentos de ambas clases de osciladores. Como los osciladores de microondas funcionan a través de mecanismos no lineales, se consideran técnicas de análisis, síntesis y optimización no lineal para evaluar sus prestaciones. Consecuentemente, se han revisado técnicas numéricas no lineales en la segunda parte de la tesis. En particular, se ha destacado el papel de las simulaciones utilizando el método del Balance Armónico (Harmonic Balance, HB), aprovechando de la técnica del Generador Auxiliar para obtener las soluciones oscilantes. Estas técnicas se han aplicado con éxito a dos clases de osciladores.

Inicialmente, ha sido considerado el análisis y el diseño de un oscilador triple-push. A condición de que una distribución de fase determinada se quede constante entre los elementos oscilantes, en un oscilador triple-push se observa un incremento de la potencia de salida del tercero armónico, mientras que los armónicos de orden inferior resultan suprimidos; esto es su funcionamiento designado. Sin embargo, debido a la simetría del circuito, a la presencia de retardo en la red de acoplamiento y a otros desajustes, otros modos de oscilación no deseados pueden aparecer, coexistiendo con aquello previsto por defecto. Se ha presentado una estrategia de diseño basada en simulaciones paramétricas con el método del Balance Armónico. Siguiendo la evolución del primer armónico de la tensión oscilante (en un nodo seleccionado en la red de acoplamiento) en función de dos parámetros del circuito (relacionados con la fase de acoplamiento y la fuerza de acoplamiento) se proporcionó una análisis no lineal completa obteniendo la posibilidad de evitar los modos de oscilación no deseados.

Además, se ha descrito el diseño de un oscilador distribuido controlado por tensión en modalidad de ganancia inversa (reverse mode DVCO) compuesto por cuatro secciones activas. Conjuntamente, se ha presentado un método para lograr un diseño optimizado que presentase variaciones reducidas de la potencia de salida. En conclusión, se introdujo una implementación alternativa, dirigida hacia más amplias gamas de sintonía / mayores frecuencias de oscilación. Las medidas realizadas sobre los prototipos fabricados mostraron buena coincidencia con los resultados de la simulación, confirmando la validez de la aproximación.

RESUM DE LA TESIS

Molts inconvenients en el paradigma actual de comunicació sense fils podrien ser alleujats en permetre la transmissió d'alta freqüència de la portadora, i dotant a la xarxa i l'equip d'usuari amb un cert grau de reconfigurabilitat. La urgència d'un nou marc en la transmissió digital sense fils que ha de tenir en compte bit-rates elevats, menor latència i restriccions al retard màxim, ens va portar a investigar els principals elements constitutius per fomentar un canvi, a nivell circuital i de dispositiu, cap a esquemes de comunicació més eficients.

Específicament, aquest treball s'ocupa dels subsistemes inherentment analògics, que es troben en el nucli de cada mòdul transceptor i proporcionen el senyal portadora, els oscil · ladors. En particular, la nostra contribució s'enfoca en l'anàlisi i el disseny de dues tipologies diferents d'oscil · ladors. La primera, està constituïda per oscil · ladors N-push, que gràcies a un efecte d'acoblament de N oscil · ladors elementals, permet pujar el nivell de potència de la component harmònica d'ordre N i per tant, aconseguir la transmissió d'alta freqüència. La segona classe està constituïda per oscil · ladors sintonitzables de banda ampla, la topologia es deriva d'un amplificador distribuït (amb bucle de realimentació) anomenats oscil · ladors distribuïts; modificant el nivell de polarització a cada secció, es obtienenen oscil · ladors distribuïts controlats per tensió (DVCO) que puguin escanejar una àmplia gamma de freqüències.

A la secció introductora, s'aborden els fonaments de les dues classes d'oscil · ladors. Com els oscil · ladors de microones funcionen a través de mecanismes no lineals, es consideren tècniques d'anàlisi, síntesi i optimització no lineal per avaluar les seves prestacions. Conseqüentment, s'han revisat tècniques numèriques no lineals en la segona part de la tesi. En particular, s'ha destacat el paper de les simulacions utilitzant el mètode del Balanç Harmònic (Harmonic Balanç, HB), aprofitant de la tècnica del Generador Auxiliar per obtenir les solucions oscil · lants. Aquestes tècniques s'han aplicat amb èxit a dues classes d'oscil · ladors. Inicialment, ha estat considerat l'anàlisi i el disseny d'un oscil · lador triple-push. A condició que una distribució de fase determinada es quedi constant entre els elements oscil · lants, en un oscil · lador triple-push s'observa un increment de la potència de sortida del tercer harmònic, mentre que els harmònics d'ordre inferior resulten suprimits, és a dir el seu funcionament designat. No obstant això, a causa de la simetria del circuit, a la presència de retard en la xarxa d'acoblament i altres desajustos, altres maneres d'oscil · lació no desitjats poden aparèixer, coexistint amb allò previst per defecte. S'ha presentat una estratègia de disseny basada en simulacions paramètriques amb el mètode del Balanç Harmònic. Seguint l'evolució del primer harmònic de la tensió oscil · lant (en un node seleccionat a la xarxa d'acoblament) en funció de dos paràmetres del circuit (relacionats amb la fase d'acoblament i la força d'acoblament) es va proporcionar una anàlisi no lineal completa obtenint la possibilitat d'evitar les maneres d'oscil · lació no desitjats.

A més, s'ha descrit el disseny d'un oscil · lador distribuït controlat per tensió en modalitat de guany inversa (reverse mode DVCO) compost per quatre seccions actives. Conjuntament, s'ha presentat un mètode per aconseguir un disseny optimitzat que presentés variacions reduïdes de la potència de sortida. En conclusió, es va introduir una implementació alternativa, dirigida cap més àmplies gammes de sintonia / majors freqüències d'oscil · lació. Les mesures realitzades sobre els

prototips fabricats mostrar bona coincidència amb els resultats de la simulació, confirmant la validesa de l'aproximació.

ACKNOWLEDGMENTS

It seems like yesterday when I started the journey towards my PhD thesis completion; matter of fact more than four years have passed! I surely remember very well my early days in Barcelona, when I moved my first steps in the institution I've had the pleasure to carry out my research, the CTTC. It was an amazing experience, to be in a place where I had the opportunity to meet extraordinary people with whom I shared my working days, and most of all, my life twist and turns. For that reason, I sincerely express my deepest gratitude to my "Room 1.09" colleagues (some aren't there anymore!). I'd like especially to thank Angelos, Musbah, for not missing any opportunity to talk with me, giving always valuable suggestions when I needed them most; Jaime for having shown his support when my path towards my doctoral dissertation was uphill; Pol for always being interested in my progress, and Giuseppe for discussions about specific technical issues (regarding guitar-playing‼). A big hug to Jessica, Laia, Ana-Maria and Maria,*(las chicas del despacho!),* for providing their hints when interesting debates were opened (while waiting long simulation runs to be completed‼).

I have to acknowledge the role of my adviser, Dr. Apostolos Georgiadis, during the course of my PhD studies. He gave me the opportunity to introduce me to the Nonlinear Analysis for describing Microwave circuits Dynamics, a really fascinating subject. He taught me how to strive for reaching my goals, pushing me to the limits, in order to surmount the obstacles I inevitably came across. I'm also greatly indebted with Dr. Ana Collado, for her early continuous support with various aspects of nonlinear simulation techniques, and for her patience she showed in explaining all the art of lab tweaking in circuit prototypes. This thesis wouldn't be finalized without my UPC thesis supervisor, Prof. Jordi Mateu endorsement and assistance. Jordi, I really thank you for demonstrating to be more than an institutional support when disputes had to be settled.

It would be impossible to list all the people that here in BCN apart from my working environment helped in a way or another; I take the opportunity to thank those who I don't explicitly mention. Many people were sympathetic and always encouraging; Giorgio and Mauro specifically suggested me never to give up, and helped me in finding a balance between my stressful duties and the joy of life (Piergiuseppe *docet*). From that point of view, I'm also grateful to Luisa, Silvia, Maria, Kasia & Magda, for being always supportive, and to Alessandro and Giampaolo for enjoying routes through Barcelona! I would like to thank my friends-since-ever Agostino & Giancarlo for their involvement in all the PhD process; which have been always asking how it was, despite they were back home; to Michele, Salvo, Giuseppe Botter, and Luca for the same reason.

My family demonstrated always to be close to me, providing me guidance. I thank my father, Vincenzo, my mother Elena, my brother Massimiliano and my sister Rosalba, for giving me relief when I felt overwhelmed. Rosalba, I'll never forget how you helped me when I had hard times. Finally, my last thought goes to Valeria, the person with whom I've been sharing my feelings more than anyone else. I'll never regret a single moment spent with you: thank you!

PERSONAL CONTRIBUTIONS

Conference Proceedings

[i] S.Via, A. Collado, A. Georgiadis, and A. Acampora, "Mode control in triple-push oscillator architectures," *Proceedings of the 2008 Workshop on Integrated Nonlinear Microwave and Millimetre-wave Circuits (INMMIC 2008),* pp.61-64, 24-25, Nov. 2008.

The author has contributed in setting up Auxiliary Generators driven Harmonic Balance simulations which have been used to investigate the co-existence of simultaneously stable oscillation modes, for triple-push oscillators, verifying previously obtained results. Specifically, initializing the auxiliary generators with the amplitude–phase relationships corresponding to various modes, parametric swept harmonic balance solution curves were traced for the magnitude of the first harmonic voltage at a convenient circuit node with respect to the coupling line length.

[ii] A. Acampora, A. Collado, and A. Georgiadis, "Nonlinear analysis and optimization of a Distributed Voltage Controlled Oscillator for Cognitive Radio," *Proceedings of the 2010 IEEE International Microwave Workshop Series) on RF Front-ends for Software Defined and Cognitive Radio Solutions (IMWS 2010)*, pp.1-4, Feb. 2010.

The author has contributed in the design and implementation of a reverse-gain Distributed Voltage Controlled Oscillator (DVCO), inspired by an already existing topology. Oscillations onset was initially checked with linear analysis techniques. Subsequently Auxiliary generators assisted Harmonic Balance simulations allowed to get complete spectral information, including tuning function, DC current consumption, and the power level at the fundamental, across the tuning range. Furthermore, a different biasing scheme was proposed and checked, in order to reduce output power variations. A prototype was fabricated resorting to online facilities, tested and measured.

Journal Paper

[iii] A. Collado, A. Acampora, and A. Georgiadis, "Nonlinear analysis and synthesis of distributed voltage controlled oscillators," *Cambridge International Journal of Microwave and Wireless Technologies* , vol.2, no.2, pp.159-163, April 2010.

Results obtained in [ii] motivated a deeper investigation of the four sections DVCO previously designed. The author has contributed in designing, implementing and measuring a DVCO. In particular, he has verified some DVCO tuning function simulation results, which were assessed in a dual manner with respect to the previous publication [ii]. Two neighboring gate voltages were considered as parameters, and tuning curves were found by performing double parametric sweeps, in harmonic balance auxiliary generator driven simulations.

Book Chapter

[iv] A. Acampora and A. Georgiadis, "Wideband Voltage Controlled Oscillators for Cognitive Radio Systems,"in *Advances in Cognitive Radio Systems* [On-line], Cheng-Xiang Wang and Joseph Mitola III, Ed. InTech, pp. 1-23, Jul. 2012. Available: http://www.intechopen.com/books/advances-in-cognitive-radio-systems/wideband-voltage-controlled-oscillators-for- cognitive -radio-systems [Mar. 19, 2013].

The author has reviewed some of the possible applications for DVCOs, pointing out the importance of their wideband feature in the context of emerging wireless communication paradigm. A critical and in-depth review of the reverse mode DVCO's linear and nonlinear simulation process was made, based on the results obtained in [ii] and [iii]. Flow diagrams elucidated the analysis and design algorithms. The DVCO tuning function, its output power level and DC current consumption were shown. The main findings presented in [ii] and [iii] where discussed.

LIST OF FIGURES

LIST OF TABLES

LIST OF ABBREVIATIONS

ADC	Analog to Digital Converter
ADS®	Advanced Design Systems (simulation suite from Agilent Tech.)
AG	Auxiliary Generator (or Harmonic Probe)
AM	Amplitude Modulation
AT	Access Technologies
BiCMOS	Bipolar-CMOS (device or process)
CAD	Computer Aided Design
CCRO	Cyclically –Coupled Ring Oscillator
CMOS	Complementary Metal Oxide Semiconductor (device or process)
CR	Cognitive Radio
DA	Distributed Amplifier
DFT	Discrete Fourier Transform
D-HBT	Double Heterojunction Bipolar Transistor
DVCO	Distributed Voltage Controlled Oscillator
EDA	Electronic Design Automation
EDFA	Erbium Doped Fiber Amplifier
EDGE	Enhanced Data-rates for GSM Evolution
EMC	ElectroMagnetic Compatibility
EMI	ElectroMagnetic Interference
Ev-DO	Evolution- Data Optimized
FET	Field Effect Transistor
FFT	Fast Fourier Transform
FM	Frequency Modulation
FT	Fourier Transform
GPRS	General Packet Radio Service

GSM	Global System for Mobile communications
HB	Harmonic Balance
HBT	Heterojunction Bipolar Transistor
HEMT	High Electron Mobility Transistor
HJ-FET	Heterojunction FET
HSPA	High Speed Packet Access
IDFT	Inverse Discrete Fourier Transform
IFT	Inverse Fourier Transform
ILFD	Injection-Locked Frequency Dividers
ILO	Injection-Locked Oscillator
LNA	Low Noise Amplifier
LTE	Long Term Evolution
MEMS	Micro-Electro-Mechanical Systems
MESFET	Metal-Semiconductor FET
MMIC	Monolithic Microwave Integrated Circuit
MOSFET	Metal-Oxyde-Semiconductor FET
NEMS	Nano- Electro-Mechanical Systems
n-FET	*n*- type FET
pHEMT	Pseudomorphic HEMT
PLL	Phase Locked Loop
PM	Phase Modulation
RFIC	Radio-Frequency Integrated Circuit
RF/μW	Radio Frequency /Microwave range
RTWO	Rotary Travelling Wave Oscillator
SDR	Software Defined Radio
SMC	Surface Mount Component
SOM	Self-Oscillating Mixer

THF	Tremendously High Frequency
TWA	Travelling Wave Amplifier
TWOA	Travelling Wave Optical Amplifier
TX/RX	Transmitter/Receiver
UMTS	Universal Mobile Telecommunication System
VCO	Voltage Controlled Oscillator
Wi-Fi	IEEE 802.11x WLAN protocol
WiMAX	Worldwide Interoperability for Microwave Access
WLAN	Wireless Local Area Network

TABLE OF CONTENTS

CHAPTER I. INTRODUCTION

1.1 GENERAL OVERVIEW. MOTIVATIONS AND SCOPE

Since more than a century ago, when first electromagnetic waves were put into use to the radio transoceanic transmission in the famous Marconi's experiment, the role of *wireless communication technology* has become so relevant and pervasive to such an extent, that it represents a difficult exercise to imagine how the world would look without it. Aside to the conventional *broadcasting communications* (radio & TV) the last century had witnessed the deployment of *wireless networked communication*, the most important example being the cellular phone infrastructure, which led to a profound modification, a real *paradigm shift, the way* people worldwide interact *exchanging information*. On the other hand, a parallel revolution took place due to what originally was aimed at being a distributed computing platform for facilitating the collaboration among labs and faculties across the US, and ultimately became known as the *Internet*, which nowadays delivers a variety of multimedia audiovisual content, and interconnects billions of computing devices across the world.

Comprehensibly enough then, in the last ten years several research proposals dealt with the interplay among *computing and communications* targeting more efficient ways to improve the existing network infrastructure and users' equipments, in order to guarantee the end user content delivery with an unprecedented fidelity, utilizing the wireless transmission framework. This goal clearly sets a constraint on the mapping between the *class of services/ content-type* being requested and the *streaming rates* of the *digital baseband signal* to be transmitted. Surely, from the point of view of *performance optimization*, adopting better engineered transmission protocols and modulation and coding schemes would help in achieving a good compromise between the two conflicting requirements (*quality of service* vs. *achievable bitrates*), based on many ad-hoc solutions tailored for the specific software application, media type, and traffic patterns. At the end of the day, the fact remains: higher quality is associated to higher bitrates, and thus (according to Nyquist Theorem) to a *wider spectral occupancy* of the baseband signal around the frequency of the carrier (a given *radio channel*). This constitutes a problem in the *overcrowded electromagnetic licensed spectrum, where a plethora of coexisting standards have been allocated in frequency, with pre-established physical layer parameters*, due to the possibility of mutual channel interference. This issue can be addressed by having recourse to two options, in order to efficiently allocate radio resources. The signal transmission *could be shifted in the unlicensed band employing higher frequencies carriers*, taking advantage of still available *unused portions of the electromagnetic spectrum* to achieve higher bitrates and making the interference constraint appear as a minor issue; e.g. transmissions at 100 Mbit/s—1Gbit/s have been demonstrated in the 60 GHz bandwidth [1]. Otherwise the *electromagnetic spectrum could be managed in a more flexible way,* according to the recently introduced Cognitive Radio paradigm [2], by requiring both user devices and the network infrastructure are endowed with advanced software functionalities that dynamically map the telecommunication services of a given user to the *locally and temporarily idle* bands (i.e. *not being used at the moment, in the immediate surroundings by other users*) of the licensed spectrum, pursuing *load balancing* on the network side, and *interference minimization* among users.

However, in order to fully exploit these benefits, a significant advance in the enabling hardware technology implemented on the transceiver handsets is required. If the first option is considered, *high frequency oscillators* will be needed. However, generating an oscillating signal at frequencies greater than 30 GHz is made difficult by the active devices parasitics, which significantly impair the final performance. A more efficient solution would be to realize higher frequency sources by suitably combining the output of several lower frequency oscillators, giving rise to the *N-push oscillator topology* [3], delivering additional benefits in terms of phase noise reduction, decrease in modeling/simulation complexity, and improvements in the overall cost effectiveness, since a difficult *high frequency oscillator* design is brought back to the design of lower frequency oscillating sub-units, adequately inter-connected by a coupling network.

Alternatively, should the Dynamic Spectrum access be considered (according to the new Cognitive Radio paradigm), the user terminal would need to be endowed with a very wideband oscillator, capable to scan multi-GHz segments of the electromagnetic spectrum, to detect a *spectrum hole* and altering its physical layer parameters, initiate an *opportunistic transmission.* A promising candidate for a free-running wideband voltage controlled oscillator needed to perform this task, derives in turn from an old invention, the Distributed Amplifier [4]. In contrast with the conventional *lumped design*, the distributed configuration offers an increase in signal power gain without being affected by a bandwidth reduction caused by high frequency currents shunting effect (due to active devices' parasitic capacitances).Thus introducing a feedback path and implementing a suitable biasing strategy in a distributed amplifier, a wideband tunable oscillator is obtained, which could conveniently be used as a subsystem in envisioned cognitive radio equipments [5].

Being so relevant to practical purposes in the foreseen scenarios, both the *N*-Push oscillator topology and Distributed (voltage controlled) oscillator are investigated in this thesis. Many works, based on a linear analysis/small signal models approach, have successfully dealt with the problem of deriving the conditions for which the oscillations can be triggered in the aforementioned topologies. Nevertheless, resorting only to linear analysis /small signal models for such intricate configurations often leads to oversimplified results, running the risk of obtaining high discrepancies with the measurements performed on a real prototype. Moreover, linear analysis simulation techniques, as later will be seen do not allow to estimate important figures of merit; in the case of designing an oscillator for example, linear analysis could be used at a preliminary design stage, and just for detecting an estimate of the actual oscillation frequency.

The distinctive feature of this work relies in the application of *nonlinear simulation techniques*, which allow taking into account the complex dynamics governing *multi-device, distributed, autonomous active circuits,* to both shed new light into their operation and provide design hints. In the next sections, these aspects will be examined with greater detail.

1.1.1 N-PUSH OSCILLATORS AS EFFECTIVE FREQUENCY MULTIPLIERS /HARMONIC GENERATORS

The need for high frequency signal sources arises naturally in the context of practical application of microwave and millimeter wave systems, which span across radioastronomy/space

applications [6], radio transmission in the 60 GHz bandwidth [7], research for THz radiation sources [8].High frequency carriers could in principle be generated designing an oscillator (or an oscillator driven system, such as a PLL) that might provide the required signal without employing any sort of frequency conversion, or rather starting with a lower frequency source and then raising it via frequency multiplication. The former approach leads to added complexity, due to the presence of noise impairing the oscillation frequency stability [9], and modeling difficulties for high frequency (>30 GHz) microwave components and substrates (or processes, if dealing with MMIC). In contrast, adopting the second approach, a higher frequency signal is obtained as the output of a cascade of microwave multipliers from a more stable lower frequency source [10].

Frequency multipliers are roughly divided in two categories: passive and active multipliers [11]. In passive multipliers, usually the nonlinear output current or the nonlinear voltage across the junction capacitance of a diode is responsible for frequency multiplication, providing wideband operation but clearly presenting conversion losses; an amplifier stage is thus frequently needed to make up for them, introducing the required gain. Alternatively an active implementation, based for example on FET devices, is based on the harmonic generation due to operation near the pinch-off region of the output characteristics, delivering conversion gains on the order of 10 dB; however the noise in this case is a relevant issue, particularly when considering cascaded connections [6—11]. For all the aforementioned reasons, alternative approaches should be considered. To this aim, quiet recently much attention has been devoted to the investigation of microwave *N*-push oscillators topologies [12—19] for their ability to act as effective frequency multipliers, being basically *harmonic generators*. Essentially, *N*-push oscillators are obtained by coupling *N* identical oscillator elements operating at the same oscillation frequency f_0 by means of a *linear passive combining network* which generally shows a high degree of symmetry (being it a star or ring network as shown in [12, 13]). Assuming that all oscillators are perfectly synchronized with a phase distribution of $2\pi/N$ among neighboring elements, the output waveform, which is usually taken at the node corresponding to the centre of symmetry of the network, will then present the harmonics up to the $(N\text{-}1)^{th}$ order virtually suppressed (highly attenuated in practice) and the N^{th} harmonic boosted, delivering the oscillation frequency Nf_0. Therefore, designing an *N*-push oscillator based frequency multiplier at a frequency $f_{out} = Nf_0$ would, by and large, consist in choosing a suitable topology which allows the *N*-th harmonic generation from *N* identical subunits operating at $f_0 = (1/N) \cdot f_{out}$. Each individual oscillator working frequency is therefore reduced by a factor of *N*, which brings relevant benefits to the phase noise of the output signal [12] and relieves noticeably the requirements in terms of high frequency behavior/modeling of the active device, electromagnetic coupling, values for loaded Q_L for microwave lumped inductor and capacitor of the *LC* tank [18]. Moreover as an additional benefit, in case of employing variable frequency sources (VCO) having a tuning range ΔB, the tuning range of the combined waveform *T* gets multiplied as well by the same factor *N* obtaining $T=N\Delta B$ [18]

In practical applications, due to increasing complexity of the passive coupling networks and to the attenuation due to losses the order *N* is limited to a small number; in fact examples of push-push (*N*=2) oscillators [20, 21], triple-push (*N*=3) oscillators [16, 17] and more recently

quadruple push (N=4) oscillator [22—24] are very common in the literature[1]. In particular, triple-push oscillators will be covered here since they represent a good tradeoff between the need for higher frequency operation, compact size requirements, still preserving an adequate DC to RF efficiency[2] [18]. Nevertheless, it is worth noting that the amount of lower order harmonics rejection depends strictly on component tolerances which are inevitably present in real world circuits. In fact, a perfect cancellation of lower order harmonics would require identical oscillating elements, which is impossible to achieve in practice[3]. Furthermore, the intrinsic symmetry in triple push oscillators in presence of delays[4] makes possible the appearance of different oscillating modes [25, 26] coexisting along with the intended one, that are simultaneously stable (therefore physically observable) to which the system, subject to different initial conditions, might evolve. Thus, for a first-pass design, it becomes vital performing a nonlinear analysis of the various oscillating modes, identifying observable states and monitoring their evolution in dependence of some *critical circuit parameters*, whose variations can determine their *multistability*, their partial cancellation or their total disappearance to a nonoscillatory rest state (a phenomenon called "amplitude death" [27]). As reported in [28], both the *delay* and the *coupling strength* among oscillating elements are essential parameters for the description of complex collective behavior in coupled oscillator systems. In [26], *the voltage magnitude of an oscillating element at the fundamental at a convenient node* ($|V_n^{(1)}|$) was chosen to be a suitable observable state, the *degree of coupling* was considered as the corresponding critical parameter and solution paths were traced by means of numerical continuation techniques [29] [30]. In a traditional triple push oscillator topology the coupling network (usually having a *star topology*) is essentially composed of transmission (microstrip) lines sections; hence only *coupling phase* (related to *distributed delays*) might be modified by controlling the length of each coupling arm[5]. In order to act upon the *coupling strength*, it's convenient to augment the network, cascading each elemental oscillator with resistive T or Π pad attenuator as in [25] or high-pass k-constant filters [26], tuning their internal lumped components values (resistances in case of pad attenuators, inductances/capacitances in case of lumped filters) in order to obtain a specified attenuation at each sub-oscillator's fundamental frequency. Using high pass filter section has the advantage of providing attenuation only at the fundamental frequencies, leaving higher order harmonics unchanged, which facilitates third harmonic boosting.

---

[1] An extreme case of implementation of an N-push oscillator has been reported in consisting in an "Octa-push" oscillator (N=8), designed for applications in the V band [3].

[2] In fact, if P represents the DC power consumed by a single oscillator, the N-push oscillator uses up roughly (as a first order estimate) *N times as much as P* [18]

[3] The ratio of the m^{th} order harmonic (power) to the Nth order harmonic (power) (with $m<N$) quantifying the harmonic rejection might be hard to estimate from numerical simulation due to component mismatches, and generally this quantity is exactly known after an experimental validation. For this reason, most of the times, achieving a prescribed rejection level for lower order harmonics necessitates a cut and try procedure with a-posteriori tuning of the circuit. Statistical Analysis or Sensitivity analysis tools included in most EDA software could help in extracting mean values, or best case/worst case values.

4 Due to the distributed nature of the coupling network, generally made up of transmission lines.

[5] For a given substrate, in a planar transmission line (microstrip line) two parameters could be simultaneously adjusted; its width and its length. The length is mainly responsible for a phase shift at the output (presenting the same values at multiples of the signal wavelength) while the width mainly controls the impedance. Assuming the impedance of the coupling network is matched to the 50 Ω load, only the length of the line can be altered.

Taking into account the previous considerations, this work illustrates the design of a 6 GHz Triple−Push Oscillator, following the works [25, 26]. Core oscillators operating at a nominal frequency of about 2 GHz are initially designed, and subsequently coupled by means of microstrip lines in a star configuration. Full nonlinear simulations based on the Harmonic Balance method have allowed tracking the evolution of each mode by taking advantage of auxiliary generator techniques for the synchronized regime [25, 31]. In order to provide different phase and amplitude conditions for each oscillator element which defined a particular oscillating mode, three different auxiliary generators have been used [14, 15]. Furthermore, the evolution of each mode has been tracked sweeping two distinct parameters, namely the *attenuation level* (provided by the high pass filter section and governing the coupling strength among oscillating subunits) and the *coupling line length* (in order to alter the amount of delay between coupled elements) and observing the solution path (parametric plot) for $|V_n^{(1)}|$. Numerical continuation techniques (branch switching) have been employed when dealing with many-valued function, as in the case of the local behavior of parametric curves in the neighborhood of a turning point [30]. Graphical results confirmed the theoretical prediction in [28] for the existence of "mode islands". Carefully selecting attenuation level and coupling line length, it was possible to avoid the spurious modes and to establish a progressive phase distribution of $2\pi/3$ among oscillator elements, which ensured the third harmonic generation. Simulation results were experimentally validated through the fabrication of a Triple Push Oscillator prototype [26] making use of standard microwave Surface Mount Components (SMC) and a microstrip printed circuit board layout.

1.1.2 Distributed Voltage Controlled Oscillators for Wideband Spectrum Sensing

Since when they appeared in the earliest FM demodulation schemes, Voltage Controlled Oscillators (VCOs) have been receiving much attention from the scientific community and this tendency still continues nowadays due to the exponential growth of data-intensive wireless communications [32−33]. In fact, high-performance RF front end is required to cope with increasing transmission rates, lower energy consumption, and enhanced compatibility with different wireless protocols/standard of the newest wireless devices/handsets. Voltage Controlled Oscillators (VCOs) represent ubiquitous key elements of modern transceivers [34], in which they commonly serve as variable carrier frequency synthesizers either in direct frequency synthesis, or when used in Phase-Locked Loops (PLL) [35−37] A great deal of research has been carried out, optimizing the VCOs to address specific issues, like reducing their phase noise, minimizing their power consumption, raise their operational frequency or extend their tuning bandwidth, just to name a few [38] [39] [40].

Moreover, the importance of wideband tuning capabilities for wireless mobile user terminals has been recently emphasized in the context of Cognitive Radio (CR) paradigm [41]. In a CR scenario, a secondary user[6] can access many legacy radio Access Technologies (ATs)[7] with

[6] In the Cognitive Radio paradigm, a fundamental distinction is made among the *primary users*, which can be thought as subscribers of a licensed telecommunication service, and *secondary users* which opportunistically exploit the portion of electromagnetic spectrum underutilized by the primary users, or rather communicate using *unlicensed bands*. In the literature, primary users are also named *spectrum owners* or subscribers, while secondary users are often called *cognitive radio users*. See [41].

higher degree of flexibility, depending on the spectral condition at a determined instant in time within a certain geographical area and on a maximum admissible mutual interference brought to primary users. Therefore a terminal needs no longer to be mapped to a single AT but instead, employing sophisticated *dynamic spectrum sensing/ spectrum management algorithms* a cognitive device selects and exploits locally unused portion of the electromagnetic spectrum, adapting the transmission parameters (i.e. carrier frequency, modulation and coding scheme, output power) in order to maximize the AT capacity, maintaining at an acceptable level the interference caused to other users [42]. It is understandable that *spectrum sensing procedures* are extremely important for these smart devices. Therefore, in order to span multi-gigahertz bandwidths and opportunistically access the free portion of electromagnetic spectrum, a wide tuning bandwidth VCO is required [43] [44].

Due to technological advancements in the MMIC components and processes[8] very high frequency oscillators and VCO have been implemented (as reported in [45—47]). It is worth noting that different design goals like compact size, low cost, low DC voltage supply, low power, low phase noise, wide tuning bandwidth, make one VCO more suitable than others depending on the specificity of the application; in general it turns out to be a rather difficult task to find a balanced tradeoff between conflicting design requirements, using conventional circuit techniques for LC oscillators [48—50]. Actually, the design of an analog VCO is commonly based on a suitably modified oscillator circuit core, obtained inserting an additional varactor in the LC tank resonator[9]. On the one hand, high frequencies, low phase-noise VCOs have been obtained using the aforementioned technique [51—57]. On the other hand, they generally[10] present a limited tuning capability (expressed in terms of fractional bandwidth[11]), and therefore inadequate for the spectrum sensing tasks to be performed by the foreseen cognitive radio devices [58—60].

One possible solution might be provided by employing Distributed circuits [5], which markedly fit to wideband operation. The foremost representative of this class is the Distributed Amplifier (DA) which was invented to overcome the restrictions imposed by the gain-bandwidth product in conventional topologies [61]. Allowing more stages to be connected by artificial

---

[7] GPRS, EDGE (2.5 G); UMTS, HSPA, Ev-DO , for mobile phones, IEEE 802.11 a/b/g/n (WiFi) in the case of wireless networks, WiMAX for broadband regional networks or their envisioned counterpart (LTE, Long Term Evolution framework [2] [32—33]). Notice how in general these standards define different transmission bands, carrier frequencies, modulation and coding schemes (that is, different *physical layers specifications*). Particularly, the TX/RX bands might be spaced by several GHz (ex EDGE-HSPA-WLAN (802.11b)).

[8] The possibility of attaining high frequency oscillation in an integrated version of a traditional LC tank oscillator, depends on the particular device (process) being used, and on inductors parasitics. If f_T is the *transition frequency of the intrinsic device* (after which its *current gain* drops below unity), the maximum oscillation frequency, f_{max} is proportional to f_T ; semiconductors process improvements lead to higher f_T and therefore to higher achievable f_{max}. Likewise, better miniaturization techniques in inductors fabrication technology, which are associated to a decreased impact on its high frequency limiting parasitics, is reflected in an higher operating frequency range for the oscillator circuit [45—47].

[9] Limited tuning of the oscillation frequency might also be achieved by changing the bias level of the active device.

[10] Lately, examples of very wideband LC tank oscillators have been shown, due to the aforementioned process improvements, especially in CMOS devices [58—60].

[11] Fractional Bandwidth is the ratio of the tuning bandwidth to its central frequency.

transmission lines sections the active devices' stray capacitances[12] get effectively decoupled, preventing bandwidth reduction observed in conventional topologies. Signal amplification is obtained in a concurrent fashion; as the signal progressively traverses the input line it is tapped at the active devices inputs and an amplified replica propagates down the output line. Consequently a linear increase with the number of active sections of gain is provided [62]. However, since the parasitic capacitances are absorbed in a *LC type interstage coupling networks, acting as low-pass filters* the amplifier bandwidth can be carefully selected, and made close to the intrinsic devices' frequency limit. Not surprisingly, soon after the introduction of the Distributed Amplifier, the effect of a distributed parameter network over a conventional oscillator circuit began to be studied [63, 64] as a new mean for increasing its oscillation frequency. In [65], for the first time it was proposed to implement a distributed oscillator as *derived by* the distributed amplifier topology *endowed with an internal feedback path* connecting the input/output lines. It was analyzed the possibility of achieving continuous tuning across a decade wide frequency range from a modified topology for distributed amplifier, employing p-HEMT devices in common source configuration, and varying their gate bias' levels. Having created a feedback path after the removal of the output line (drain line) matching resistor, and by taking advantage of the distributed amplifier's reverse gain, oscillations could be generated; their frequency was seen to depend on the specific bias configuration chosen for the *N* active devices. In particular, by individually activating each of them, while the other *N*-1 remain switched off, discrete resonances are triggered, whose frequency decrease as later stages are turned on [65], from the highest (when the first section is active) to the lowest (when the last section is active). Furthermore, considering the simultaneous biasing of two neighboring sections, oscillating signals with intermediate frequency could be generated, provided their voltage level is varied in a complementary manner [65]. Repeating this procedure with every pair of adjacent sections, the oscillation frequency spans the bandwidth comprised between the highest and the lowest resonant frequencies, which essentially depends (in a small-signal approximation, at least) on the *frequency response of the DA passive (linear) part,* which can be therefore optimized. Results were experimentally confirmed [66, 67]. This is circuit is seen to offer greater tuning performance, substantiating the theoretical analysis carried out in [65], delivering a multi-GHz tuning bandwidth (1 GHz—3.8 GHz), exceptional rejection of higher order harmonics, (ranging from -18 dBc to -44 dBc for second harmonic, -17 dBc to -55 dBc for third harmonic across the tuning band) and adequate phase noise levels[13], while simultaneously other different distributed oscillators were independently realized [68, 69]. The distributed oscillators reported in [67] and [69] present different tuning capabilities, owing to a different choice for the feedback loop insertion, together with different biasing strategies for the active sections. In [69] a distributed amplifier containing two paired active devices per section is provided with a feedback loop from the drain load resistor side, to the input line. Tuning is achieved by properly varying the active devices' bias voltage with the "current steering" technique [70] realizing a four sections 10 GHz VCO in CMOS technology delivering a 12% tuning bandwidth (9.3 GHz—10.5 GHz), with -7

[12] Parasitic capacitances are responsible for a lowpass filtering of the active devices' currents, due to shunting effect; therefore they degrade the bandwidth performance of an amplifier at high frequencies. By using transmission lines as an input/output transmission structure among each section, the shunting effect could be controlled by design and mitigated (see chapter II).

[13] Phase noise of the oscillator in [67] wasn't reported. In our implementation it was found to be around -100 dBc/MHz on average across the tuning range, see chapter VI.

dBm output power and a phase noise of -114 dBc/MHz (at 1 MHz from the 10.2 GHz carrier) exploiting the forward gain of the distributed amplifier.

The reverse mode Distributed Voltage Controlled Oscillator (DVCO), presented in [65—67] represents a valuable candidate in the light of possible applications as a subsystem in multi-standard cognitive device transceivers. Although intrinsically provided with wideband tuning capabilities this circuit lacked an adequate tuning algorithm, as the authors themselves stated [65—67]. The issue arose since the analytical framework used for explaining the VCO operation relied on small signal analysis in which the active devices' parameters are assumed not to depend upon signal strength [11, 29]. On one hand, this approximation surely enabled to shed some light on the biasing strategy of the active sections to provide tuning. On the other hand, linear signal analysis techniques fell short in predicting actual VCO behavior as they only made available just the oscillation frequencies estimates. In fact, authors in [67] had admittedly recourse to time domain simulations to analyze both the transient and steady state regime of the circuit in large signal conditions. Since the reverse mode distributed VCO tuning strategy involves the simultaneous variation of more than one parameter at a time (as later will be detailed), several time domain simulations would need to be sequentially run. Nevertheless, the numerical solution of differential equations [11, 29] governing the behavior of a DVCO requires exceedingly high computation times, since many cycles of a high frequency carrier (sampled with a very short time step) have to be integrated until the transient is extinguished and the periodic regime is finally settled. Moreover, distributed components (i.e. transmission line sections) which are natively frequency dispersive, are normally approximated by having their frequency domain relationships[14] expressed in the time domain by a convolution integral, which in turn needs to be reconstructed via interpolation at the sampling instants[15]. This procedure may introduce estimation errors which severely limit the solution accuracy, potentially causing convergence failure [11].

For these reasons, it has been chosen to study the DVCO by means of nonlinear Harmonic Balance (HB) techniques [71—74] which retain a simple description of distributed components in the frequency domain. Moreover, the use of frequency swept Auxiliary Generators techniques [31,75] enables a complete description of the tuning algorithm, delivering the voltage-frequency

[14] In frequency domain, the output signal emerging from a passive component (lumped or distributed) is simply given by the input signal times the transfer function of the passive block. Conversely, reconstructing the output signal in the time domain would involve evaluating the convolution of the input waveform with the time-varying impulse response [11].

[15] Usually the description of passive (lumped/distributed) components is given with high accuracy using frequency domain data (directly obtained from S-parameters measurements). In order to get the impulse response in the time domain, their frequency response undergoes an Inverse Fourier Transform (IFT). However, *non-causal functions could result (extending for negative values of time)* from IFT of certain spectra, lacking any physical significance. Assuming the result of the IFT computation is causal, its knowledge is limited to discrete samples which are evaluated at time instants which may not agree with those of a specific time domain simulation. Reconstruction of the missing samples is performed by means of interpolation [11].

graphs as in [76—78]. The same techniques might be used to study the parametric sensitivity of the DVCO to the aim of delivering optimal performance[16], thus serving as efficient design tools.

Based on the HB analysis, various prototypes have been implemented, taking advantage of the onsite facilities for printed circuit board manufacturing, showing good agreement with the simulation results. Two different DVCO topologies have been designed and tested. The first one, is inspired by the seminal work [43] and makes use of hybrid filter cells composed by transmission line sections and discrete inductors and capacitors [57]. The second one relies on periodically loaded uniform transmission lines which are coupled by the active devices.

1.2 THESIS STRUCTURE.

This thesis is organized according to a top-down scheme. After the introductory chapter, the subsequent ones deal with the following subjects:

Chapter II. Literature Review and Background, which covers the state of the art for coupled oscillators topologies (in relation to the specific case of *N-push oscillators*) and Distributed Circuits (in particular *Distributed Oscillators*), and describes the operation principles for Triple Push Oscillators and Distributed Oscillators. In the case of triple push oscillator, the phase amplitude-relationships among the core oscillating elements, needed for generating a high third order harmonic output signal, are derived resorting to a simple model of three identical oscillating waveform with different phase shifts. Linear analysis for Triple Push oscillator topologies is subsequently introduced. Finally, more advanced group theoretic results for symmetrically coupled systems of nonlinear oscillators are mentioned, which will constitute the basis for the discussion in chapter V. Following a *bottom-up approach,* the analysis of Distributed Oscillator starts after a thorough introduction on the Distributed Amplifier circuit, from which the former inherits many important features. Moreover, in order to provide a self-contained analysis, the properties of some simple distributed parameter networks, which constitute the key elements to distributed amplifier implementation, have been reviewed. After having recalled the properties of constant–*k* and *m*-derived sections, two distinct distributed amplifier topologies are analyzed; a distributed amplifier using *artificial transmission line sections* (made up of *cascaded* constant-*k or m*-derived sections) and a distributed amplifier using *uniform transmission line segments*. In both cases the gain function is computed and related to the circuital parameters, considering the realistic *lossy* case. Subsequently and based on the previous discussion, two distributed oscillators topology are introduced and compared. The first one is the forward mode distributed oscillator. Linear analysis results are shown to provide an estimate for the oscillation frequency, lending themselves to a straightforward physical interpretation. Finally the reverse gain mode DVCO is presented. Employing small signal analysis techniques, its operation principle is elucidated. In particular, considering an *N* section oscillator, the bias conditions leading to *N* discrete resonances (with one

[16] For instance, investigations of the effect of the feedback line length variations on DVCO performance (output power, tuning bandwidth, phase noise, harmonic power, etc.) can be simply embedded in the usual two tier harmonic balance optimization procedure [29]. The parametric plot, showing the oscillator relevant figures as a function of the chosen parameter, could be helpful in the design phase.

device active at a time), and the tuning capabilities (with a neighboring pair of devices being complementarily biased) are analyzed, making use of the *reverse gain function.*

Chapter III. Microwave Circuits Nonlinear Numerical Analysis, describing in great detail the numerical methods employed to analyze a microwave circuit. Three fundamental topics are reviewed the time domain methods, the frequency domain methods and the mixed domain methods. Time domain methods are related with the most general solution of the system of differential equations governing the circuit behavior; many techniques are compared, including the convolution method to account for circuit element which natively possess a frequency domain description, and for shooting methods when only the steady state information is relevant. Harmonic Balance, a frequency domain method, is introduced for the specific case of Non Autonomous circuits forced by a periodic signal by using a Fourier Series expansion of the unknown variables, and is seen to offer many advantages over the transient simulation when detecting periodic regimes. The convergence of the Harmonic Balance scheme is analyzed when some circuit parameters are altered, giving rise to Numerical Continuation Schemes. Parametric solutions arising from the Harmonic Balance are discussed, pointing out how to deal with multi-valued solution curves. Lastly, the Envelope Transient method is introduced with the purpose of analyzing circuits forced by (slowly) amplitude modulated (high frequency) carriers, giving rise to a mixed time-frequency analysis.

Chapter IV. Microwave Oscillators Nonlinear Simulation, in which it is shown how to simulate an autonomous circuits by means of the Harmonic Balance method in conjunction with the Auxiliary Generator Technique, consisting in a RF source introduced in the circuit schematic, the purpose of avoiding the misleading results an usual harmonic balance simulation may lead to. It is demonstrated how an harmonic balance optimization of both the amplitude and the frequency of the probe, with respect to suitable non-perturbation conditions, enable to obtain a complete spectral information. Techniques for correct algorithm initialization are covered in detail. Envelope Transient formulation is used for studying the stability of the solutions. Finally it is mentioned the application of this technique to the synchronized oscillators.

Chapter V. Phase-Locked Patterns Analysis and Control in Triple Push Oscillators, where the analysis and design of a Triple –Push oscillator configuration operating at 6 GHz is examined in detail. Numerical Continuation techniques in Auxiliary Generator-Driven Harmonic Balance Simulations framework, allow keeping track of the various oscillating modes this topology presents, according to very general group theoretic results applied to nonlinear systems showing symmetry. The parametric analysis of the nonlinear steady state solutions for each of these modes, obtained by tracing the curves of the first harmonic of the voltage at a suitable circuit node with respect to adequately chosen coupling factors, enables selecting only the "rotating-phase" solution which correctly delivers a high third-order harmonic, avoiding parasitic oscillations. These results were confirmed by measurements on a prototype implementation.

Chapter VI. Nonlinear Analysis and Design of Distributed Voltage Controlled Oscillators, which focuses on the application of nonlinear simulation technique in the frequency domain (Harmonic Balance) to the aim of investigating the tuning function of a particular reverse mode distributed VCO. A preliminary linear analysis design is carried out to the aim of determining the potential oscillations. Subsequently the circuit is analyzed in nonlinear term, showing how by the

introduction of suitable design parameters (resistors) parasitic oscillations can be quenched. The parametric variation of the four individual resonances with respect to the lumped capacitances and inductances in the embedded linear distributed network has been examined. The tuning curves are derived with the aid of an auxiliary generator, suitably connected to the circuit schematic (in order to avoid degenerate solutions of the Harmonic Balance routines), by varying its frequency in a certain band to observe the solution in terms of synthesized voltages which obey the oscillation condition at the probe port. In a dual manner, the same curves are traced by varying a set of voltages and observing the evolution of the frequency; in this case properly initialized envelope transient simulations allowed discriminating among stable and unstable solutions. A Multi-Objective Optimization is carried out to explore a better tuning strategy that fulfilled the constraint of output power minimum variation. Transient simulation is carried out to estimate the oscillator settling time. Phase Noise simulations have been used to evaluate the output waveform spectral purity. Distributed voltage controlled oscillator implementation is described in great detail; the measurement results performed on a experimental prototype matched well the numerical analysis. This chapter closes mentioning a different DVCO implementation, providing simulation and measurement results. Finally, the DVCO injection locking operation is empirically assessed.

Chapter VII. Conclusive Remarks. Main results are summarized, and the empirical validity of the results based on our implemented prototypes is discussed. A list of forthcoming research tasks is proposed.

1.3 PUBLISHED CONTRIBUTIONS

The main part of this thesis is based on published material, related to the analysis, simulation, design and optimization of triple-push oscillators and distributed voltage controlled oscillators. A brief description of the main findings follows.

- *Mode control in triple-push oscillator architectures* [26].

  A triple-push oscillator operating at 6 GHz was designed, and the stability of multiple coexisting modes was analyzed with regard to coupling strength and coupling phase. In order to modify the coupling strength, differently to what has been done in [44] three LC high-pass filters were placed at each oscillator output node. The coupling delay was controlled by the length of a microstrip line, representing the coupling arm of a star network topology. The experimental results indicated how, by controlling the values of the LC high pass network and the length of the coupling arm, a stable triple harmonic generation is achieved at the output.

- *Nonlinear analysis and optimization of a Distributed Voltage Controlled Oscillator for Cognitive Radio* [76]

  A reverse mode distributed voltage controlled oscillator, has been analyzed and designed by employing Harmonic Balance simulation techniques for microwave autonomous circuits. In particular, for the first time the DVCO tuning function was derived for a four section, microstrip-based DVCO, showing a qualitative agreement with earliest predictions. Furthermore, observing that the output power had significant variation throughout the

tuning band, it was proposed to optimize the tuning algorithm with the inclusion of a third gate bias voltage. The oscillator was implemented and tested taking advantage of on-site facilities, using four NE 3509 M04 HJ-FETs and lumped inductors and capacitors to implement artificial transmission lines, with a topology based on a microstrip layout on a dielectric substrate (H=0.52 mm, ε_r= 3.38 @ 10 GHz, tan d =0.0025). The measured prototype was in quantitative agreement with simulated results, showing a tuning range from 0.75 GHz to 1.85 GHz, an average dissipation of 59 mW, an average output power of 5.2 dBm and an average (across the tuning range) measured phase noise of is -111.2 dBc/Hz at 1 MHz offset from the carrier.

- *Nonlinear analysis and synthesis of distributed voltage controlled oscillators* [77]

  Harmonic Balance and Envelope Transient simulation technique were used to describe nonlinearly the DVCO previously designed. Particularly important with regard to design and optimization procedure are the parametric plots describing the evolution of the oscillation frequencies when the series inductances and the shunt capacitances of the embedded Π-type constant-*k* sections are varied. Stability analysis is performed employing Envelope Transient simulations. A new representation of the tuning curves is presented, in which are clearly classified stable and unstable oscillatory solutions. Using the proposed nonlinear tools, a DVCO operating in the frequency tuning range between 1 and 2 GHz was implemented in order to support the simulation results. The average output power and consumption along the frequency band for the designed DVCO were 5.2 dBm and 60.4 mW, respectively.

- *Wideband Voltage Controlled Oscillators for Cognitive Radio Systems* [78]

  Some of the possible applications for DVCOs are assessed, pointing out the importance of distributed electronics in terms of their wideband behavior in the context of emerging wireless communication paradigm. The Time Domain and the Harmonic Balance methods are discussed, in relation to their suitability in support of nonlinear and distributed microwave oscillator simulations. A critical and in-depth review of the reverse mode DVCO's linear and nonlinear simulation process was made, in order to derive its tuning algorithm, and the output power level and DC current consumption. The simulated curves are then contrasted with measurement results.

1.4 REFERENCES

[1] G.G. de Alwis and M. Delahoy, "60 GHz Band Millimetre Wave Technology," *Australian Communications Authority White Paper* [On-line], December 2004, Available: http://www.acma.gov.au/webwr/radcomm/frequency_planning/radiofrequency_planning_topics/docs/sp3_04_60%20ghz%20mwt%20-%20discussion%20 paper-final.pdf [Jan. 30, 2013].

[2] M. Muck, *et al*, "Evolution of Wireless Communication Systems Towards Autonomously Managed, Cognitive Radio Functionalities,"*Proceedings of the 64th IEEE Vehicular Technology conference (VTC-2006)*, pp.1-5, Sept. 2006.

[3] K. Kawasaki, T. Tanaka, and M. Aikawa, "V-band 8th harmonic push-push oscillator using microstrip ring resonator," *Proceedings of IEEE MTT-S Microwave Symposium 2009 (IMS 2009),* pp.697-700, Jun. 2009.

[4] T.T.Y Wong. *Fundamentals of Distributed Amplification*. London: Artech House, 1993.

[5] A. Hajimiri, "Distributed integrated circuits: an alternative approach to high-frequency design," *IEEE Communications Magazine*, vol.40, no.2, pp.168-173, Feb. 2002.

[6] G. Chattopadhyay, *et al*., "An all-solid-state broad-band frequency multiplier chain at 1500 GHz," *IEEE Transactions on Microwave Theory and Techniques*, vol.52, no.5, pp. 1538- 1547, May 2004.

[7] S. Emami, C.H. Doan, A.M. Niknejad, and R.W. Brodersen, "A Highly Integrated 60GHz CMOS Front-End Receiver," *Proceedings of. the 2007 International Solid State Circuits Conference (ISSCC 2007)*, pp.190-191, 11-15 Feb. 2007.

[8] I. Mehdi, G. Chattopadhyay, *et al*., "Terahertz Multiplier Circuits," *Proceedings of the IEEE MTT-S Microwave Symposium Digest*, pp.341-344, Jun. 2006.

[9] I. Kallfass *et al*, "A W-band active frequency-multiplier-by-six in waveguide package," *Proceedings of the 5th German Microwave Conference (GEMIC 2010)*, pp.74-77, Mar. 2010.

[10] K. Yuk and G.R. Branner, "Advances in active microwave frequency multipliers," *Proceedings of the IEEE 54th Mid-West Symposium on Circuits and Systems (MWSCAS 2011)*, pp.1-4, Aug. 2011.

[11] F. Giannini and G Leuzzi. *Nonlinear Microwave Circuit Design*, Wiley, 2004.

[12] C. Jonghoon and A. Mortazawi, "Design of push-push and triple-push oscillators for reducing 1/f noise upconversion," *IEEE Transactions on Microwave Theory and Techniques*, vol.53, no.11, pp. 3407- 3414, Nov. 2005.

[13] Yu-Lung Tang and Huei Wang, "Triple-push oscillator approach: theory and experiments," *IEEE Journal of Solid-State Circuits*, vol.36, no.10, pp.1472-1479, Oct. 2001.

[14] Shih-Chieh Yen and Tah-Hsiung Chu, "An Nth-harmonic oscillator using an N-push coupled oscillator array with voltage-clamping circuits," *Proceedings of the IEEE MTT-S Microwave Symposium 2003 (IMS 2003)*, vol.3, pp. 2169- 2172, Jun. 2003.

[15] Yu-Long Tang and Huei Wang, "A novel triple-push oscillator approach," *Proceedings of the IEEE MTT-S Microwave Symposium 2000 (IMS 2000)*, vol.2, pp.1201-1204 vol.2, Jun. 2000.

[16] B. Catli, and M.M. Hella, "A 30-GHz triple-push oscillator on silicon for mm-wave applications," *Proceedings of the 2009 IEEE International Symposium on Circuits and Systems (ISCAS 2009)*, pp.2037-2040, 24-27 May 2009.

[17] Tang, Yu-Lung and Wang, Huei, "A 24.6-GHz MMIC HBT Triple-Push Oscillator," *Proceedings of 31st European Microwave Conference (EuMC 2001)*, pp.1-4, Sept. 2001.

[18] B. Catli, and M.M. Hella, "Triple-Push Operation for Combined Oscillation/Divison Functionality in Millimeter-Wave Frequency Synthesizers," *IEEE Journal of Solid-State Circuits,* , vol.45, no.8, pp.1575-1589, Aug. 2010.

[19] U.L., Rohde, *et al*, "Low noise low cost ultra wideband N-push VCO," *Proceedings of the IEEE MTT-S Microwave Symposium Digest of Technical Papers (IMS 2005)* pp., 12-17 June 2005.

[20] Hyun-Wook Lee *et al*, "Design of a new K-band push-push oscillator improving output power," *Proceedings of the IEEE AP-S International Symposium 2008,* pp.1-4, 5-11 Jul. 2008.

[21] Sang-Woong Yoon *et al.*, "A compact GaAs MESFET-based push-push oscillator MMIC using differential topology with low phase-noise performance," *Proceedings on the 18th annual Technical Digest of Gallium Arsenide Integrated Circuit Symposium 2001*, (*GaAs IC 2001*) pp.45-48, 2001.

[22] H. Xiao, T. Tanaka and M. Aikawa, "A Ka-band quadruple-push oscillator," *Proceedings IEEE MTT-S Microwave Symposium Digest 2003, (IMS 2003)* vol.2, pp. 889- 892, Jun. 2003.

[23] S.Dongha *et al*, "553-GHz signal generation in CMOS using a quadruple-push oscillator," *Proceedings of the 2011 Symposium on VLSI Circuits (VLSIC 2011)*, pp.154-155, Jun. 2011.

[24] Sheng-Lyang Jang *et al.*, "A 0.18 mm CMOS Quadrature VCO Using the Quadruple Push-Push Technique," *IEEE Microwave and Wireless Components Letters*, vol.20, no.6, pp.343-345, Jun. 2010.

[25] A. Collado, and A. Georgiadis, "Nonlinear Mode Analysis and Optimization of a Triple-Push Oscillator," *IEEE Microwave and Wireless Components Letters*, , vol.18, no.8, pp.545-547, Aug. 2008.

[26] S.Via, A. Collado, A. Georgiadis, and A. Acampora, "Mode control in triple-push oscillator architectures," *Proceedings of the 2008 Workshop on Integrated Nonlinear Microwave and Millimetre-Wave Circuits. (INMMIC 2008),* pp.61-64, 24-25, Nov. 2008.

[27] S. H. Strogatz, "Nonlinear dynamics: Death by delay," *Nature*, no. 394, pp.316-317, 23 July 1998.

[28] D. V. Ramana Reddy, A. Sen, and G. L. Johnston, "Time Delay Induced Death in Coupled Limit Cycle Oscillators,"*Phys. Rev. Lett.* no.80, pp. 5109–5112, Jun. 1998.

[29] A. Suarez, and R. Quéré. *Stability Analysis of Nonlinear Microwave Circuits*, Artech House publishers, January 2003.

[30] E.L. Allgower and K. Georg, "Continuation and path following," *Acta Numerica*, no. 2 , pp 1-64, 1993.

[31] C.-R.Chang, M.B. Steer, S. Martin, and E. Jr. Reese, "Computer-aided analysis of free-running microwave oscillators", *IEEE Transactions on Microwave Theory and Techniques*, vol. 39, no. 10, pp.1735-1745, Oct. 1991.

[32] R Wadekar and L. Fagoonee, "Evolution towards next generation wireless broadband communications challenges," *Proceedings of the IET International Conference on Wireless, Mobile and Multimedia Networks 2006*, pp.1-4, Nov. 2006.

[33] L.D. Olavarrieta and A.A. Nava, "Wireless communications: a bird's eye view of an emerging technology," *Proceedings of the 2004 IEEE International Symposium on Communications and Information Technology (ISCIT 2004)*, vol.1, pp. 541- 546, Oct. 2004.

[34] T.Y. Lin, T.Y. Yu, L.W. Ke, and G.K. Dehng, "A low-noise VCO with a constant KVCO for GSM/GPRS/EDGE applications," *Proceedings of the. 2008 IEEE Radio Frequency Integrated Circuits Symposium, (RFIC 2008),* pp.387-390, April-Jun 2008.

[35] Han-il Lee *et al.,* "A Σ-Δ fractional-N frequency synthesizer using a wide-band integrated VCO and a fast AFC technique for GSM/GPRS/WCDMA applications," *IEEE Journal of Solid-State Circuits*, vol.39, no.7, pp. 1164- 1169, July 2004.

[36] Tie Sun, Chun Hui, and Yun Wang, "A VCO with high supply noise rejection and its application to PLL frequency synthesizer," *Proceedings of the 2005 IEEE International Symposium on Communications and Information Technology (ISCIT 2005)*, vol.2, pp. 1027- 1030, Oct. 2005.

[37] Chun-Wei Kuo and Zhi-Ming Lin, "A single signal controlled dual-band VCO for WiMAX applications," *Proceedings of the 2009 IEEE International Symposium on Circuits and Systems* (*ISCAS 2009)*, pp.1787-1790, May 2009.

[38] R.K Pokharel, *et al.*, "Design of VCO for 2.4GHz Wireless Applications Using Transmission Line Resonators," *Proceedings of the 2007 Asia-Pacific Microwave Conference (APMC 2007)*, pp.1-4, Dec. 2007.

[39] N.H.W Fong *et al.*, "Design of wide-band CMOS VCO for multiband wireless LAN applications," *IEEE Journal of Solid-State Circuits*, vol.38, no.8, pp. 1333- 1342, Aug. 2003.

[40] D. Solanki, R.Chandel, T. Alam, and A. Nishad, "Design of LC-VCO for low power narrowband electronic applications," *Proceedings of the 2nd International Conference on Wireless Communications, Vehicular Technology, Information Theory and Aerospace & Electronic Systems (Wireless VITAE 2011),* pp.1-4, Feb.- Mar. 2011.

[41] I. F.;Akyildiz, W.Lee, M. C. Vuran, and S. Mohanty, "NeXt generation/dynamic spectrum access/cognitive radio wireless networks: a survey," *Elsevier Journal on Computer Networks,* vol. 50, no. 13, pp.2127 – 2159, May 2006.

[42] L. Hanzo, M. El-Hajjar, and O. Alamri, "Near-Capacity Wireless Transceivers and Cooperative Communications in the MIMO Era: Evolution of Standards, Waveform Design, and Future Perspectives," *Proceedings of the IEEE* , vol.99, no.8, pp.1343-1385, Aug. 2011.

[43] Wireless World Research Forum (WWRF), Working Group 6,. *Cognitive Radio, Spectrum and Radio Resource Management (white paper)* [On-line] Available: http://wg6.ww-rf.org/images/pdfs/WG6_WP4_CogRaSpeRRM-20041208.pdf [Mar. 20, 2013].

[44] Shumin Zhang *et al.*, "Comparison of VCO Topology for Wideband Multi-Standard Applications," *Proceedings of the IEEE Annual. Wireless and Microwave Technology Conference (WAMICON 2006)*, pp.1-4, Dec. 2006.

[45] Yan Zhao, B.Heinemann, and U.R. Pfeiffer, "Fundamental mode colpitts VCOs at 115 and 165-GHz," *Proceedings of the 2011 IEEE Bipolar / BiCMOS Circuits and Technology Meeting* (*BCTM 2011)*, pp.33-36, Oct. 2011.

[46] A.Katz, O. Degani, and E. Socher, "Design and optimization of a low-noise cross-coupled fundamental VCO in 90nm CMOS for 60GHz applications," *Proceedings of the IEEE 11th Topical Meeting on Silicon Monolithic Integrated Circuits in RF Systems (SiRF* 2011), pp.13-16, Jan. 2011.

[47] Tsung-Hsien Lin, *et al.*, "A 5 GHz, 192.6 dBc/Hz/mW FOM, LC–VCO System With Amplitude Control Loop and LDO Voltage Regulator in 0.18 μm CMOS," *IEEE Microwave and Wireless Components Letters*, vol.17, no.10, pp.730-732, Oct. 2007.

[48] Chung-Yu Wu and Hong-Sing Kao, "A 1.8 GHz CMOS quadrature voltage-controlled oscillator (VCO) using the constant-current LC ring oscillator structure," *Proceedings of the 1998 IEEE International Symposium on Circuits and Systems* (*ISCAS '98),* vol.4, pp.378-381, May- Jun 1998.

[49] V.Issakov *et al.,* "A 5.9-to-7.8 GHz VCO in 65 nm CMOS using high-Q inductor in an embedded Wafer Level BGA package," *Proceedings of the of the IEEE MTT-S Microwave Symposium Digest 2011, (IMS 2011)* pp.1-4, Jun. 2011.

[50] Sheng-Lyang Jang *et al.,* "A Dual-Band CMOS Voltage-Controlled Oscillator Implemented With Dual-Resonance LC Tank," *IEEE Microwave and Wireless Components Letters,* vol.19, no.12, pp.816-818, Dec. 2009.

[51] Young-Jin Moon *et al.*, "A 4.39–5.26 GHz LC-Tank CMOS Voltage-Controlled Oscillator With Small VCO-Gain Variation," *IEEE Microwave and Wireless Components Letters*, vol.19, no.8, pp.524-526, Aug. 2009.

[52] Liheng Lou *et al.*, "A 0.68–1.65GHz CMOS LC voltage-controlled oscillator with small VCO-gain and step variation," *Proceedings of the 2011 International Symposium on Integrated Circuits (ISIC 2011)*, pp.79-82, Dec. 2011.

[53] Siti Maisurah, *et al.*, "A low phase noise and large tuning range 2.4GHz LC voltage-controlled oscillator," *Proceedings of the 11th biennial Asia Pacific Conference on Circuits and Systems IEEE APCCAS 2010,* pp.931-934, 6-9 Dec. 2010.

[54] Ruey-Lue Wang *et al.*, "A 1.2V low-power CMOS voltage-controlled oscillator (VCO) using current-reused configuration with balanced resistors for IEEE 802.16e,"*Proceedings of the 9th International Conference on Solid-State and Integrated-Circuit Technology ICSICT 2008*, pp.1633-1636, 20-23 Oct. 2008.

[55] D.Ghai, S.P Mohanty, and E. Kougianos, "Parasitic Aware Process Variation Tolerant Voltage Controlled Oscillator (VCO) Design," *Proceedings of the 2008 International Symposium on Quality Electronic Design ISQED 2008,* pp.330-333, March 2008.

[56] Hong-Yeh Chang and Yuan-Ta Chiu , "K-Band CMOS Differential and Quadrature Voltage-Controlled Oscillators for Low Phase-Noise and Low-Power Applications," *IEEE Transactions on Microwave Theory and Techniques*, vol.60, no.1, pp.46-59, Jan. 2012.

[57] Dongmin Park and SeongHwan Cho, "Design Techniques for a Low-Voltage VCO With Wide Tuning Range and Low Sensitivity to Environmental Variations," *IEEE Transactions on Microwave Theory and Techniques*, vol.57, no.4, pp.767-774, April 2009.

[58] S.Zafar, *et al.*, "Design of Voltage controlled oscillator (VCO) for ultra wideband (UWB) CMOS frequency synthesizer," *Proceedings of the 2007 International Conference on Intelligent and Advanced Systems (ICIAS 2007),* pp.1383-1386, Nov. 2007.

[59] S.A.Osmany, F. Herzel, and J.C. Scheytt, "An Integrated 0.6–4.6 GHz, 5–7 GHz, 10–14 GHz, and 20–28 GHz Frequency Synthesizer for Software-Defined Radio Applications," *IEEE Journal of Solid-State Circuits,* vol.45, no.9, pp.1657-1668, Sept. 2010.

[60] Acharya Su Cui, *et al.*, "A low-power and wide tuning range frequency locked loop for a Cognitive Radio system," *Proceedings of the 2009 IEEE Radio and Wireless Symposium (RWS '09)*, pp.364-367, Jan. 2009.

[61] W. S. Percival, "Thermoionic Valve Circuits" British patent specification No. 460,562, Jan. 1937.

[62] E. L.; Ginzton, W. R. Hewlett, J. H. Jasberg, and J. D. Noe, "Distributed Amplification," *Proceedings of the IRE*, pp. 956-69, Aug. 1948.

[63] W.; Howard and H. Stellrecht, "Integrated voltage-controlled oscillators using distributed parameter phaseshift networks," *Proceedings .of the 1969 IEEE International Solid-State Circuits Conference* , vol.XII, no., pp. 102- 103, Feb 1969.

[64] A. Manolescu, "Single-transistor oscillators with distributed RC networks," *IEEE Electronics Letters* , vol.2, no.4, pp.151-152, Apr. 1966.

[65] Z. Škvor, S.R. Saunders and C.S. Aitchison, "Novel decade electronically tunable microwave oscillator based on the distributed amplifier," *IEEE Electronic Letters*, vol. 28, no. 17, pp. 1647-1648, Aug. 1992.

[66] L. Divina and Z. Škvor, "Experimental verification of a distributed amplifier oscillator," *Proceedings of the EuMC 1995*, pp. 1163–1167, Sept. 1995.

[67] L. Divina and Z. Škvor, "The Distributed Oscillator at 4 GHz," *IEEE Transactions On Microwave Theory And Techniques*, vol. 46, no. 12, pp 2240-2243, Dec. 1998.

[68] B. Kleveland. *et al.*, "Monolithic CMOS Distributed Amplifier and Oscillator," *Proceedings of the 1999 IEEE International Solid-State Circuits Conference*, Paper MP 4.3, Feb. 1999.

[69] H. Wu and A. Hajimiri, "A 10 GHz CMOS distributed voltage controlled oscillator", *Proceedings of the IEEE 2000 Custom Integrated Circuits Conference (CICC 2000)*, pp.581-584, May 2000.

[70] H. Wu and A. Hajimiri, "Silicon-Based Distributed Voltage-Controlled Oscillators", *IEEE Journal Of Solid-State Circuits,* vol. 36, no. 3, pp 493-402, Mar 2001.

[71] K.S. Kundert, "Introduction to RF simulation and its application," *IEEE Journal on Solid-State Circuit*, no.34, pp. 1298–1319, Sept. 1999. Available online also from: http://www.designers-guide.org/Analysis/rf-sim.pdf [Mar. 20, 2013]

[72] K.S. Kundert, "Simulation methods for RF integrated circuits," *Proceedings of the 1997 IEEE/ACM International Conference on Computer-Aided Design*, pp.752-765, Nov. 1997.

[73] V. Rizzoli and A. Neri, "State of the art and present trends in nonlinear microwave CAD techniques" *IEEE Transactions on Microwave Theory and Techniques*, vol. 36, pp. 343–356, Feb 1988.

[74] V. Rizzoli *et al.,* "State of the art harmonic balance simulation of forced nonlinear microwave circuits by the piecewise technique", *IEEE Transactions on Microwave Theory and Techniques*, vol. 40, pp. 12–28, Jan. 1992.

[75] E. Ngoya, *et al.,* "Steady state analysis of free or forced oscillators by harmonic balance and stability investigation of periodic and quasi-periodic regimes", *Wiley International Journal on Microwave and Millimeter Wave Computer Aided Engineering* ,vol. 5, no. 3, pp. 210–223, May 1995.

[76] A. Acampora, A. Collado, and A. Georgiadis, "Nonlinear analysis and optimization of a Distributed Voltage Controlled Oscillator for Cognitive Radio," *Proceedings of the 2010 IEEE International Microwave Workshop Series on RF Front-ends for Software Defined and Cognitive Radio Solutions (IMWS 2010)*, pp.1-4, Feb. 2010.

[77] A.Collado, A. Acampora, and A. Georgiadis, "Nonlinear analysis and synthesis of distributed voltage controlled oscillators," *International Journal of Microwave and Wireless Technologies*, vol.2, no.2, pp.159-163, Apr. 2010.

[78] A. Acampora, and A. Georgiadis, "Wideband Voltage Controlled Oscillators for Cognitive Radio Systems," *Advances in Cognitive Radio Systems* [On-line], Cheng-Xiang Wang and Joseph Mitola III Ed. InTech, Available from: http://www.intechopen.com/books/advances-in-cognitive-radio-systems/wideband-voltage-controlled-oscillators-for-cognitive-radio-systems [March, 20, 2013].

CHAPTER II. LITERATURE REVIEW & BACKGROUND

2.1 STATE OF THE ART IN COUPLED OSCILLATOR SYSTEMS AND N-PUSH OSCILLATOR TOPOLOGIES.

Coupled oscillators systems [1] have been long an intensely studied topic. Examples stem from biological applications [2] to theoretical investigations regarding networks of coupled oscillator exhibiting complex synchronization patterns [3]. A system of coupled oscillators is formed by joining together *N* identical oscillating elements; the nature of the coupling network connecting the individual sub-units, and the way the oscillating nodes are arranged (defining the network *symmetry*) largely determines the possible onset of diverse oscillating modes [4]. Possible interconnections among oscillating nodes are shown in Fig. 2.1.

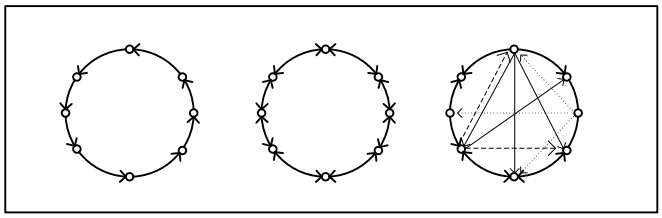

FIGURE 2-1. Coupled oscillators and interconnecting networks topologies. One-way nearest neighbor coupling, mutual nearest neighbor coupling, global mesh asymmetric coupling. The individual oscillating nodes resonate at the same frequency

More specifically, the (electrical) coupling among oscillating circuits started to be considered as early as sixty years ago from a purely theoretical point of view. Coupled nonlinear oscillators dynamics were studied in [5] utilizing the Hamiltonian formalism, and coupled-mode equations were written considering any number of harmonic components and any nonlinearity order, obtaining general results regarding the waves (power) amplification due to the interaction among the core elements. These results was particularized in [6] to coupled van der Pol oscillators, which present a third-order nonlinearity, investigating the stability of the oscillatory solution with the Lyapunov method, and determining specific bounds for avoiding aperiodic oscillations. In the context of radiofrequency and microwave engineering research on coupled oscillators was fostered by the need of obtaining high power radio waves by using of several identical oscillating low power units. In [7] 3-dB directional couplers were used to interconnect 2^n diode oscillators in a hierarchical structure, in order to get output power level increase. The result was validated using 32 identical oscillating units at 19 MHz, showing a 32– fold boost in the output power as compared to a single oscillator. However in [8], it was proven for the first time that coupling two *different* (possessing a different output power) oscillators would provide an output power level *greater than the sum of the powers* associated to the individual devices. A prototype built using two reflex klystron having output powers of 1.4 W and 1.2 W and coupled by an hybrid-tee produced an oscillation of 3.4 W at 7 GHz. Another example of multi-device oscillator is the Rucker's oscillator [9] used to combine the output of many devices symmetrically placed around the center of a star

topology coupling network. Conditions are derived to ensure stable operations resorting to eigenvector analysis. The result in [8] would be later interpreted correctly in [10] where a general formulation was introduced to study the power, noise, and synchronization properties of multiple devices coupled by a linear network described by scattering parameters. The analytical model allowed computing and plotting the relationship among power, oscillation frequencies for two T-magic coupled oscillators as a function of the coupling arm phase, as well as for the PM and AM noise. Two cases were considered. The synchronization behavior was studied by having two individual units operating at slightly different free running frequencies, but possessing the same amplitudes. Secondly, two oscillators were supposed to have the same nominal frequency but opposite phases. The nonlinear noise among synchronized oscillators has been investigated[11], in the context of injection locked oscillators, subharmonically injection locked oscillators and tightly coupled oscillators by a power combining network, demonstrating output phase noise reduction for moderate injection levels.

A one-dimensional ladder network constituted by inductances and capacitances and manifesting a low pass or high pass frequency selectivity to couple multiple van der Pol oscillating elements was examined in [12], determining the stability of the oscillation modes and discriminating among the single-tuned, double tuned and degenerate modes. An extension of this study was presented in [13] regarding two dimensional arrays of coupled van der Pol oscillators, and in [14] where ring coupling networks are considered. An example of high power microwave oscillator suitable for satellite communications (in the K_u band), was illustrated in [15] utilizing six high efficiency IMPATT diodes deployed in three coupled modules in push-pull configurations to achieve a total output power of 10 W. The impact of delays in the coupling networks was considered in detail in [16] and in [17] demonstrating how they affect the stability of certain oscillation modes, or the synchronization among nodes as the network becomes increasingly large. In [18] the conditions which assured a stable operation in multi-device MMIC power amplifiers were detailed, obtaining incidentally for the first time an enunciation of the possible resonating modes in *N-push oscillators* which would be subsequently developed.

A remarkable application of nearest neighbor coupled oscillators is presented in [19] [20] [21]. *N* identical oscillating units are coupled in a ladder network configuration, by means of RLC cells (employing series inductances and resistances, and shunt capacitances). When the first and the last element are fed with exactly the same driving signal, the network phase locks with it, and zero coupling phase are established among the oscillating elements. However, when a phase difference of the injection signal among the first and the last oscillator exists, the steady state oscillators' phases show a uniform progression from one element to the next, which can be exploited to drive a phased antenna array, without the need of deploying phase shifter circuitry. Experimental and theoretical confirmations of this intuition were later shown in [22] in which it is analytically proven (by having recourse to the van der Pol oscillator model) that a constant phase progression can in fact be established by slightly detuning the peripheral elements in the array when the oscillating elements are loosely coupled, and empirically demonstrated by using a four-element MESFET oscillators linear patch array suitable for beam steering applications. Referring to coupled oscillator array dynamics, significant contributions came from the works [23] [24].

In [23] the stability properties of strongly coupled oscillator arrays are explored and stable modes are identified using the averaged potential theory, allowing the designer to excite in-phase

contributions only, thus avoiding spurious modes. In [24] the Kurokawa decoupling approach for describing the phase and amplitude oscillator's dynamics is extended to linearly coupled oscillator network as described by N-port circuit parameters, obtaining a set of relationships for the derivatives of the individual oscillators' phases and amplitudes which supported the experimental approach in [22]. Parametric variation of coupling resistances in rings of mutually coupled oscillators was considered in [25], particularly referring to its impact over system synchronization. In [26] the beam steering technique (developed in [22]) was successfully applied to a receiver, consisting of a five element FET varactor tuned VCOs oscillating at 8.6 GHz and providing a 25° scan.

A different application of coupled oscillators is presented in [27]. The mutual phase locking characteristic of coupled oscillators is herein exploited to generate a robust and low cost clock distribution scheme for both printed and integrated circuits, drastically reducing the clock skew. The improvement in timing performance corresponds, on the frequency domain, to a phase noise reduction which was both theoretically and experimentally substantiated in [28], where it is shown that for certain values of the coupling phase, the near carrier phase noise is reduced by a factor of *N,* as much as the number of interrelated oscillating elements when reciprocal coupling network are employed. In [29], the delay in coupled oscillator systems subject to an external excitation is seen to produce simultaneously stable synchronized and desynchronized states. In synchronized states, multiple clusters in the network resonate with different collective frequencies, showing hysteresis versus the external driving signal as it increases or decreases, while in desynchronized states the oscillators' resonances are distributed uniformly. The poly-phase signal generation using coupled oscillators is addressed in [30] in which four capacitively coupled oscillators stably resonate at slightly different individual frequencies, obtaining a four phase oscillations. Circular polarized wave are obtained by coupling oscillators nodes in a ring with unidirectional coupling in [31]. A thorough study of the impact of delay in coupled oscillators is reported in [32], where analytical treatment and numerical simulation show the modification of stability property and the onset of various regimes, most notably phase locked states (synchronized), incoherent states (desynchronized), amplitude death (null oscillation). The results, shown for a two coupled oscillator system, are generalized to a linear array of *N* elements, quantifying the parametric dependence of amplitude death regions on coupling strengths and mean time delay among oscillating elements. A rather analytical approach is also used in [33] to pinpoint critical transitions between the incoherent state and a multitude of coherent states with different synchronization frequencies, showing multistable solutions as in [29] and analyzing the parametric variations on coupling strength and delay time as in [32]. Linear arrays of *N* oscillators are considered in [34], studying in detail the inter-injection locking mechanism [19-21, 22, 24], providing details of locking range, locking time, as well as accounting for the oscillators' unlocked spectra with regard to frequency spacing and amplitude variations.

The triple push oscillator was introduced in [35] demonstrating how, by suitably coupling three identical oscillating subcircuits resonating at the same oscillation frequency and establishing a phase progression of 120° among their output voltages at the fundamental frequency, the third harmonic output power level is boosted, while the fundamental and second harmonic are canceled, thus obtaining a higher harmonic generator, and experimentally validating the contributions [2] [4] [18] which expressed the possibility of achieving *N*-th harmonic boosting by coupling *N* oscillating nodes in a star network (or employing more sophisticated topologies)

whose phase difference is kept at $2\pi/N$. A prototype using MMIC technology and HBTs devices, realized by coupling three identical oscillators operating at 8.2 GHz with a phase shift of 120° among their output node voltages, was shown to provide a third harmonic (24.6 GHz) power level of 14.8 dBm, with a 20 dB of harmonic rejection for the fundamental and second harmonic. The concept of triple push oscillators was generalized in [36] considering *N*-push oscillators topologies employing linear passive networks (i.e microstrip lines) as combining networks. It is established that, by summing phase shifted replicas of the sub-oscillators output signals (provided a constant phase shift of $2\pi/N$ *is kept constant*), the output power level at the *N*-th harmonic is enhanced, while all the lower order harmonics are suppressed. The *N*-push oscillator concept is amenable to devise broadband and low noise VCOs starting from cheaper oscillator units as shown in [37], where a push-push (or double push) VCO covers the $1-3$ GHz bandwidth when the oscillating nodes operate in – phase (even oscillating mode) and $3-6$ GHz bandwidth when operating in the π out of phase mode (odd oscillating mode), with an exceptional noise figure better than -118 dBc/Hz at 100 KHz offset over the entire range $1-3$ GHz/$3-6$ GHz. Another example of implementation is demonstrated in [38] in which four oscillators are coupled by means of a common ring-resonator, realizing a quadruple push oscillator. According to the design principle expressed in [36] the quadruple push oscillator output provided a fourth harmonic output power of +1.67 dBm at 35.8 GHz, with a lower order harmonic rejection of -18 dBc (approx) and a measured phase noise performances at 35.8 GHz of -104.0 dBc/Hz and -82.3 dBc/Hz at the offset frequency of 1 MHz and 100 kHz, respectively. Up-conversion (flicker noise, $1/f$) noise reduction techniques for push-push and triple push configurations are addressed in [39] and in [40].In both the previous works it is proposed to couple the oscillating subcircuits in order to ensure their output waveforms possess the highest symmetry. Specifically, in [39] for push-push configuration it is suggested to make the phases of the Fourier coefficients equal at all harmonics, in order to reduce the waveform distortion induced by a high second harmonic power. For triple push configurations instead, it is advised to filter all even harmonic components. By taking this measures 15 dB phase noise improvement is observed at 100 kHz from the carrier. Similar results are obtained in [40], reaching a 12 dB improvement at 10 KHz from the 8 GHz carrier with respect to an asymmetrical circuit operating at the same nominal frequency. A very high frequency push-push oscillator, employing emitter coupled double heterojunction bipolar transistors (D-HBT) characterized by a very high f_{max} , has been reported to oscillate at 287 GHz with an output power greater than 0 dBm, using the harmonic tuning technique [41]. Harmonic balance simulation techniques have been applied to investigate push-push injection locked oscillators in [42] fed by low power driving signals, analyzing the circuit both in the time and the frequency domain and performing a parametric analysis to investigate the oscillation modes stability, validating the results with a prototype operating at 10 GHz, whose measurements showed good agreements with the analysis. A similar approach is used in [43] where it has been considered the stability analysis of the oscillating modes of Rucker's [9] and quadruple push oscillators, having oscillation frequencies of 3.9 GHz and 15.6 GHz respectively. A triple-push oscillator circuit at 13.8 GHz was illustrated in [44] . Harmonic Balance simulation techniques have been used to trace the parametric dependence on the possible oscillation modes [4] on the coupling strength and on the delay between the oscillators, having resorted to envelope transient simulation to discriminate stable and unstable solutions, and providing design hints for choosing the optimal coupling parameters ensuring the onset of the triple-push mode (odd mode, with voltages and currents having a mutual phase shift of 120°).

A 30 GHz silicon triple push oscillator was designed [45] using a fully monolithic 130 nm CMOS process, and observing the highest harmonic rejection ever achieved to date for integrated triple push oscillators. In [46] eight oscillators sub-circuits operating in the X-band were coupled by a ring resonator, obtaining an octa-push oscillator at the V-band. The elements are placed on an octagonal ring, such that their mutual phase shift (from one element to the next) is $2\pi/N$ (where $N= 8$) that is $\lambda_g/2$ at four times the oscillation frequency provided by a single element achieving an oscillation at the output node of -4 dBm at 51 GHz, with -100 dBc/Hz at 1MHz offset from the carrier. A combined VCO and frequency divider realized with CMOS process operating at 60 GHz and tunable in the 57 GHz—64 GHz band was shown [47], to provide more tuning bandwidth than conventional injection locked frequency dividers (ILFDs). In fact, reversing the operation principle, the N-push oscillators/ VCO can be seen as ILFDs; in the specific case, a divider-by-three is realized feeding the output of a triple push oscillators with a f_0 =60 GHz (representing the third harmonic of the triple-push oscillators) and extracting the divided frequency f_0 /3 = 20 GHz (representing the fundamental frequency of one core element) at one oscillator subcircuit. In a triple push oscillator, both the nominal and divided frequency are present, therefore it can be interpreted as a combined oscillator /divider, which would bring also important benefits in terms of phase noise reduction (due to N-push operation) and oscillator /divider tuning bandwidth alignment.

Recently, triple push oscillator have been shown to be capable to operate in the THF/ Terahertz range as detailed in [48] reaching frequencies as high as 482 GHz and delivering -7.9 dBm in a 65 nm CMOS process. Lastly, the technique of coupling together N ring oscillators (in turn containing M active stages) employing a cyclic-unidirectional coupling network was shown in [49], bringing relevant benefits compared with the traditional ring oscillator design, like the availability of several phase shifted outputs, and a noticeable phase noise reduction. Two cyclically coupled oscillators fabricated in a 90 nm digital CMOS process were illustrated. First, a wideband N-Push/M-Push cyclically coupled ring oscillator (CCRO) was shown to achieve an output frequency range of 3.16-12.8 GHz using a unit cell ring oscillator operating at 1-2.56 GHz. The measured phase noise at 1 MHz offset is -103.4 dBc/Hz and -101.6 dBc/Hz at 3.16 GHz and 12.8 GHz, respectively. Additionally, an mm-wave N-Push CCRO was illustrated, generating an output frequency of 13-25 GHz with a phase noise performance of -95 dBc/Hz at 1 MHz offset over the output frequency range.

2.2 TRIPLE PUSH OSCILLATOR OPERATION

In this section three different approaches are used to explain the basics of Triple Push Oscillator operation. In section 2.2.1, a simple mathematical model elucidates the reason of having a phase shift of $2\pi/k$ among oscillating elements for generating the k-th harmonic frequency. In section 2.2.2 different oscillating modes are analyzed via the eigendecomposition of the impedance matrix of the coupling network, a technique used in [18]. Finally, the results of group theoretical approach to rings of coupled oscillator for predicting the existence of unconventional oscillating modes due to symmetry are summarized in section 2.3.3.

2.2.1 PHASE CONSTRAINTS FOR OBTAINING THIRD HARMONIC GENERATION

Triple push oscillators are a special kind of coupled oscillator systems [50], employing three identical "core" oscillators having the same oscillation frequency f_0 and mutually operating in phase locking condition. If the oscillators waveforms present a mutual phase shift of $2\pi/3$, the voltage taken at output node O (Fig. 2.2) will present the harmonic series starting from the third harmonic[1] (3 f_0, 6 f_0, 9 f_0…) with the fundamental and second harmonics canceled. Analytically this could be seen by imposing a constraint on the output currents[2] from the oscillator elements I_α, I_β, I_γ entering the node O. The output current taken at O must be equal to the sum of the individual contributions I_ξ, (ξ = α, β, γ) which arrive at the output node with different time delays (or equivalently showing different phase lags). Considering the Fourier Series Expansion (in complex notation) of the three periodic waveforms, and retaining, without loss of generality, only the positive frequency terms up to the third order[3], the currents flowing out from the oscillator elements can be expressed as:

$$\begin{aligned} &I_\xi(\omega_0 t) = I_\xi^{(1)} e^{j\omega_0 t} + I_\xi^{(2)} e^{j2\omega_0 t} + I_\xi^{(3)} e^{j3\omega_0 t} + \ldots,\ \xi \in \{\alpha, \beta, \gamma\} \\ &where\ \ I_\xi^{(r)} = A_{\xi,r} \cdot e^{j\varphi_{\xi,r}};\ \ A_{\xi,r} = \left| I_\xi^{(r)} \right|;\ \ \varphi_{\xi,r} = \angle A_{\xi,r},\ \xi = \alpha, \beta, \gamma \end{aligned} \tag{2.1}$$

where every term $I_\xi^{(r)}$ is the *r^{th} order harmonic phasor, having amplitude* $A_{\xi r}$ and phase $\varphi_{\xi r}$.

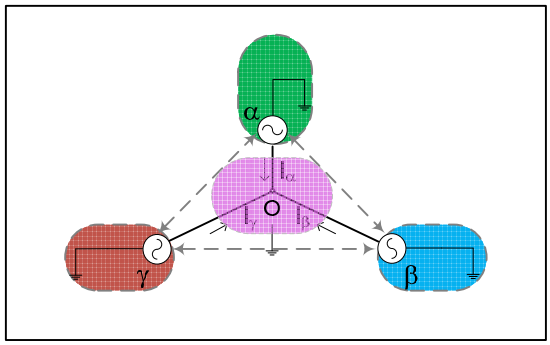

FIGURE 2-2 Composition of the oscillating currents in a Triple Push Oscillator Topology

When arriving at the output node, each current contribution possesses a different phase shift according to the following scheme:

[1] Higher harmonic terms get filtered out due to the low-pass nature of the coupling structure.

[2] A dual representation in terms of voltages is possible using the admittance coupling matrix and considering the inputs as voltages and the output as currents. Greek letter subscripts are used here to avoid confusion with the harmonic indices.

[3] The harmonics having order greater than three could be neglected, assuming their amplitudes is sufficiently close to zero.

$$\begin{aligned} I_\alpha(\omega_0 t) &\to I_\alpha(\omega_0 t + \Delta\varphi) \\ I_\beta(\omega_0 t) &\to I_\beta(\omega_0 t + \Delta\psi) \\ I_\gamma(\omega_0 t) &\to I_\gamma(\omega_0 t + \Delta\vartheta) \end{aligned} \tag{2.2}$$

due to different delays experienced by the signals when traversing the coupling network.

$$\begin{aligned} I_\alpha(\omega_0 t + \Delta\varphi) &= I_\alpha^{(1)} e^{j(\omega_0 t + \Delta\varphi)} + I_\alpha^{(2)} e^{j2(\omega_0 t + \Delta\varphi)} + I_\alpha^{(3)} e^{j3(\omega_0 t + \Delta\varphi)} + \dots \\ I_\beta(\omega_0 t + \Delta\psi) &= I_\beta^{(1)} e^{j(\omega_0 t + \Delta\psi)} + I_\beta^{(2)} e^{j2(\omega_0 t + \Delta\psi)} + I_\beta^{(3)} e^{j3(\omega_0 t + \Delta\psi)} + \dots \\ I_\gamma(\omega_0 t + \Delta\vartheta) &= I_\gamma^{(1)} e^{j(\omega_0 t + \Delta\vartheta)} + I_\gamma^{(2)} e^{j2(\omega_0 t + \Delta\vartheta)} + I_\gamma^{(3)} e^{j3(\omega_0 t + \Delta\vartheta)} + \dots \end{aligned} \tag{2.3}$$

Furthermore, since the oscillating elements are identical, the harmonics of the three output currents will also be the same, so that:

$$\begin{aligned} I_\alpha^{(1)} &= I_\beta^{(1)} = I_\gamma^{(1)} = I_O^{(1)} \\ I_\alpha^{(2)} &= I_\beta^{(2)} = I_\gamma^{(2)} = I_O^{(2)} \\ I_\alpha^{(3)} &= I_\beta^{(3)} = I_\gamma^{(3)} = I_O^{(3)} \end{aligned} \tag{2.4}$$

The total current flowing into the output node will then be the sum of these delayed contributions:

$$I_O = I_\alpha(\omega_0 t + \Delta\varphi) + I_\beta(\omega_0 t + \Delta\psi) + I_\gamma(\omega_0 t + \Delta\vartheta) \tag{2.5}$$

and our goal is to find the unknown phase shifts $\Delta\varphi$, $\Delta\psi$, $\Delta\theta$ *which fulfill the conditions:*

$$\begin{aligned} I_\alpha^{(1)}(\omega_0 t + \Delta\varphi) + I_\beta^{(1)}(\omega_0 t + \Delta\psi) + I_\gamma^{(1)}(\omega_0 t + \Delta\vartheta) &= 0 \\ I_\alpha^{(2)}(\omega_0 t + \Delta\varphi) + I_\beta^{(2)}(\omega_0 t + \Delta\psi) + I_\gamma^{(2)}(\omega_0 t + \Delta\vartheta) &= 0 \\ I_\alpha^{(3)}(\omega_0 t + \Delta\varphi) + I_\beta^{(3)}(\omega_0 t + \Delta\psi) + I_\gamma^{(3)}(\omega_0 t + \Delta\vartheta) &= 3I_O^{(3)} e^{j\cdot 3\omega_0 t} \end{aligned} \tag{2.6}$$

according to which the first and second harmonics become null and only the third harmonic components of the individual oscillator elements sum up in phase. Substituting the (2.4) into the (2.6):

$$\begin{aligned} &I_O^{(1)} e^{j\omega_0 t} \cdot \left(e^{j\Delta\varphi} + e^{j\Delta\psi} + e^{j\Delta\vartheta} \right) = 0 \\ &I_O^{(2)} e^{j2\omega_0 t} \cdot \left(e^{j2\Delta\varphi} + e^{j2\Delta\psi} + e^{j2\Delta\vartheta} \right) = 0 \\ &I_O^{(3)} e^{j3\omega_0 t} \cdot \left(e^{j3\Delta\varphi} + e^{j3\Delta\psi} + e^{j3\Delta\vartheta} \right) = 3 I_O^{(3)} e^{j\cdot 3\omega_0 t} \end{aligned} \tag{2.7}$$

which further simplifies to :

$$\begin{cases} e^{j\Delta\varphi} + e^{j\Delta\psi} + e^{j\Delta\vartheta} = 0 \\ e^{j2\Delta\varphi} + e^{j2\Delta\psi} + e^{j2\Delta\vartheta} = 0 \\ e^{j3\Delta\varphi} + e^{j3\Delta\psi} + e^{j3\Delta\vartheta} = 3 \end{cases} \tag{2.8}$$

Qualitatively, the first and second equations indicate that the sought-after phase shifts should compose vectorially to give a zero contribution at first and second harmonic, while at third harmonic the unitary vectors in the complex plane should be aligned. Analytically, since the zero sum of three complex numbers having unitary norm (lying on the unitary circle) correspond to the three cube roots of unity[4] it is found:

$$\begin{aligned} &e^{j\Delta\varphi} + e^{j\Delta\psi} + e^{j\Delta\vartheta} = 0 \Rightarrow \begin{bmatrix} e^{j\Delta\varphi} \\ e^{j\Delta\psi} \\ e^{j\Delta\vartheta} \end{bmatrix} = \begin{bmatrix} e^{j0} \\ e^{j2\pi/3} \\ e^{j4\pi/3} \end{bmatrix} \text{ or equiv. } \begin{bmatrix} e^{j\Delta\varphi} \\ e^{j\Delta\psi} \\ e^{j\Delta\vartheta} \end{bmatrix} = \begin{bmatrix} e^{j0} \\ e^{j(-2\pi/3)} \\ e^{j(-4\pi/3)} \end{bmatrix} \\ &e^{j2\Delta\varphi} + e^{j2\Delta\psi} + e^{j2\Delta\vartheta} = 0 \Rightarrow \begin{bmatrix} e^{j\Delta\varphi} \\ e^{j\Delta\psi} \\ e^{j\Delta\vartheta} \end{bmatrix} = \begin{bmatrix} e^{j0} \\ e^{j4\pi/3} \\ e^{j2\pi/3} \end{bmatrix} \text{ or equiv. } \begin{bmatrix} e^{j\Delta\varphi} \\ e^{j\Delta\psi} \\ e^{j\Delta\vartheta} \end{bmatrix} = \begin{bmatrix} e^{j0} \\ e^{j(-4\pi/3)} \\ e^{j(-2\pi/3)} \end{bmatrix} \end{aligned} \tag{2.9}$$

The two set of vectors in (2.9) are not independent, and can be obtained from one another by means of rotations of $2\pi/3$ or $4\pi/3$ in the complex plane. To the same conclusion one might

[4] A *n-th order* root of unity is a complex number for which holds $z^n = 1$. For the Fundamental theorem of Algebra there must be exactly n distinct complex numbers fulfilling the previous equation and they are a discrete set of complex exponentials which lie on the unit circle in the complex plane at evenly spaced angles multiples of $2\pi/n$. It turns out that the sum of the n roots of unity equals zero, in symbols:

$$\sum_{k=0}^{n-1} \varepsilon_{n,k} = 0 \Rightarrow \varepsilon_{n,k} = e^{j\cdot k(2\pi/n)}$$

be led by considering only the third equation and setting $\Delta\varphi = \Delta\psi = \Delta\theta$, *for reasons of symmetry in the coupling network*[5]*:*

$$\begin{cases} e^{j3\Delta\varphi} + e^{j3\Delta\psi} + e^{j3\Delta\vartheta} = 3 \\ \Delta\phi = \Delta\psi = \Delta\theta \end{cases} \Rightarrow \; e^{j3\Delta\varphi} = 1 \Rightarrow \Delta\varphi = \frac{2k\pi}{3},\ k=0,1,2 \tag{2.10}$$

A *progressive phase shift distribution* of $2\pi/3$ among the output currents (or voltages) of each oscillating element is thus required for cancelling the contributions from the first and second harmonics, maintaining only the ones coming from the third harmonics of the output currents. Jointly the (2.9) and (2.10) could be summarized in the pictures below (Fig. 2.3).

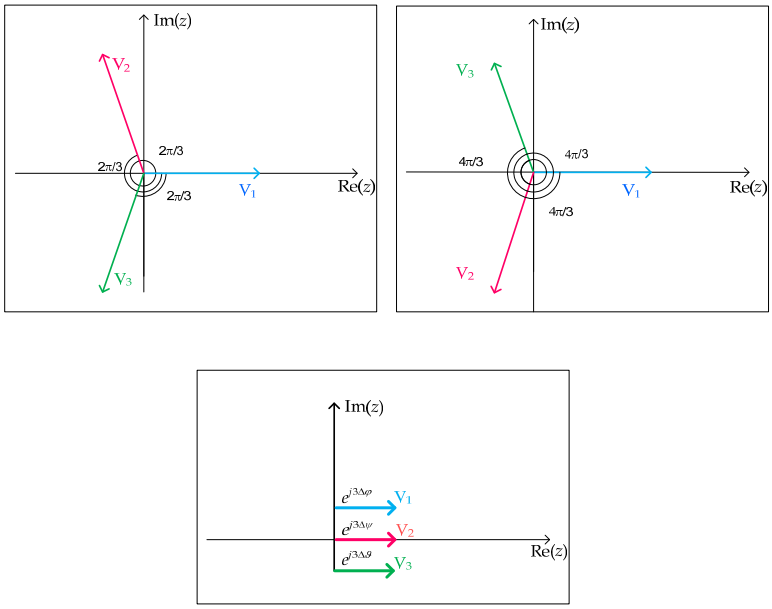

FIGURE 2-3. Triple Push third-harmonic resonance condition. If a phase progression of $2\pi/3$ is established among each oscillating node, the third harmonic contributions add in phase, while the lower order harmonics cancel out.

[5] Assuming the phase lag among each output waveform is the same, leads to a close solution expressed simply by the (2.9) and (2.10). However, this case is unrealistic in that it doesn't include the effect of inevitable mismatches in the coupling circuit modeled by different delay terms in the output signals. In that case the generic argument of the output current will be written $\Xi(t,\tau_\xi) = \omega_0(t-\tau_\xi) + \Delta\phi_\xi$, $\xi = \alpha, \beta, \gamma$. Introducing the delay terms in the equation brings new important phenomena, like *Multistability of the Solutions* (various oscillating modes other than the intended one are simultaneously observable) and *Amplitude Death* (for certain delays values, the currents interfere destructively, leading to a null output) [25] [26].

2.2.2 OSCILLATING MODES OBTAINED FROM EIGENDECOMPOSITION OF THE COUPLING NETWORK IMPEDANCE MATRIX

In the previous section, the basic approach for combining the different signals (taken at the outputs of the core oscillators) via the coupling network in order to achieve a third harmonic generation was outlined. However, a question still unanswered is whether a triple push oscillator could present other possible oscillating modes; if so, a careful design strategy is needed to quench the unwanted ones, by selecting properly the circuit parameters. In this section, an answer will be given by employing linear analysis techniques by means of eigendecomposition of the coupling network **Z** matrix.

Following Freitag seminal work on the (linear) stability of microwave amplifiers [18] [35] [51] in which the same concepts were applied to triple push oscillator operation, an impedance matrix representation of coupling network is given, and condition for triggering oscillations are sought in terms of eigenvalues analysis of the **Z** matrix [9]. In fact, if (I_1, I_2, I_3) are the small signal currents emerging from the output nodes (following the naming conventions in [18]) and **Z** represents the impedance matrix of the coupling structure the output voltages will be given by

$$\begin{aligned} \mathbf{ZI} = \mathbf{V} \Rightarrow & \begin{bmatrix} Z_{11} & Z_{12} & Z_{13} \\ Z_{12} & Z_{22} & Z_{23} \\ Z_{13} & Z_{12} & Z_{33} \end{bmatrix} \cdot \begin{bmatrix} I_1 \\ I_2 \\ I_3 \end{bmatrix} = \begin{bmatrix} V_1 \\ V_2 \\ V_3 \end{bmatrix} \\ Z_{ij} = & \left. \frac{V_i}{I_j} \right|_{I_k=0,\ k\neq j} = \left. \frac{V_j}{I_i} \right|_{I_k=0,\ k\neq i} = Z_{ji},\ 1 \le i, j, k \le 3 \end{aligned} \tag{2.11}$$

where the last expression refers to the reciprocity of the coupling network, stating the equality of mutual impedances. Actually, due to the geometrical symmetry of the star configuration (Fig. 2.4) the self-impedances Z_{ii} and the transfer-impedances Z_{ij} do not depend upon the specific port being considered and **Z** matrix in (2.11) becomes:

$$\begin{bmatrix} Z_s & Z_t & Z_t \\ Z_t & Z_s & Z_t \\ Z_t & Z_t & Z_s \end{bmatrix} \cdot \begin{bmatrix} I_1 \\ I_2 \\ I_3 \end{bmatrix} = \begin{bmatrix} V_1 \\ V_2 \\ V_3 \end{bmatrix}, \quad \begin{matrix} Z_{ii} = Z_s,\ Z_{ij} = Z_t \\ (i \neq j)\ \ 1 \le i, j \le 3 \end{matrix} \tag{2.12}$$

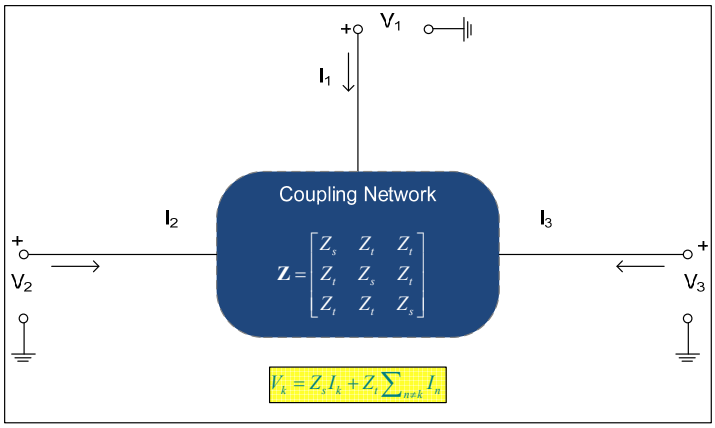

FIGURE 2-4. Impedance Matrix representation of the coupling network.

In order to look for the possible oscillating modes, it is convenient to express the set of possible currents in the eigenvectors basis for the impedance matrix [28] [52], each eigenvalue representing the impedance correspondent to each mode. In other terms we wish that:

$$\begin{bmatrix} V_1 \\ V_2 \\ V_3 \end{bmatrix} \in \text{Span}\left\{ \begin{bmatrix} I_1 \\ I_2 \\ I_3 \end{bmatrix} \in \mathbb{R}^3 \text{ s.t. } \begin{bmatrix} Z_s & Z_t & Z_t \\ Z_t & Z_s & Z_t \\ Z_t & Z_t & Z_s \end{bmatrix} \begin{bmatrix} I_1 \\ I_2 \\ I_3 \end{bmatrix} = \zeta \cdot \begin{bmatrix} I_1 \\ I_2 \\ I_3 \end{bmatrix}, \zeta \in \mathbb{R} \right\} \tag{2.13}$$

and solving the characteristic equation det (**Z** - ζ·**I**) = 0 we find two distinct roots (one having double multiplicity) [18, 35] and the associated eigenvectors[6]:

$$\begin{vmatrix} Z_s - \zeta & Z_t & Z_t \\ Z_t & Z_s - \zeta & Z_t \\ Z_t & Z_t & Z_s - \zeta \end{vmatrix} = (Z_s + 2Z_t - \zeta) \cdot (Z_s - Z_t - \zeta)^2 = 0 \tag{2.14}$$

[6] The rows (columns) of the **Z** matrix are obtained by cyclic permutation of the first row (column). A matrix presenting such structure is called *circulant* and presents the following structure:

$$\mathbf{C}(\mathbf{v}) = \begin{bmatrix} v_0 & v_1 & \cdots & v_{n-2} & v_{n-1} \\ v_{n-1} & v_0 & \cdots & v_{n-3} & v_{n-2} \\ \vdots & \vdots & \ddots & \vdots & \vdots \\ v_2 & v_3 & \cdots & v_0 & v_1 \\ v_1 & v_2 & \cdots & v_{n-1} & v_0 \end{bmatrix}$$

The eigenvalues and eigenvectors of the circulant matrix can be expressed in terms of the *n-th roots of unity* as

$$\begin{aligned} &\textit{If } \mathbf{x}_h \in \mathbb{C}^n,\ \eta_h \in \mathbb{C} \textit{ such that } \mathbf{C}(\mathbf{v}) \cdot \mathbf{x}_h = \eta_h \mathbf{x}_h, \textit{ then for } \varepsilon = e^{j\frac{2\pi}{n}},\ h \in \mathbb{N}\ 0 \le h \le (n-1): \\ &\mathbf{x}_h = \frac{1}{\sqrt{n}}\left[1, \varepsilon^h, \varepsilon^{2h}, \ldots, \varepsilon^{(n-1)h}\right] \text{ (normalized eigenvector)} \\ &\eta_h = v_0 + \varepsilon^h v_1 + \ldots + \varepsilon^{(n-1)h} v_{n-1} \text{ (eigenvalue associated with } \eta_h \text{)} \end{aligned}$$

According to eigenvalues analysis, as shown in (2.15) there exist two possible modes; one "even" in which the current fundamentals sum in phase and two "odd" modes for which the sum of the current contributions must equal zero, and arriving at the same results expressed in (2.8 – 2.10). The "odd" mode currents[7] $\mathbf{I}_{o1}$, $\mathbf{I}_{o2}$ are responsible for third harmonic generation, while the "even" $\mathbf{I}_e$ mode should be avoided.

$$\begin{cases} \zeta_e = Z_s + 2Z_t \ \text{(simple) s.t. } \mathbf{ZI}_e = \zeta_e \mathbf{I}_e \Rightarrow \mathbf{I}_e = \begin{bmatrix} 1 \\ 1 \\ 1 \end{bmatrix} \\ \zeta_o = Z_s - Z_t \ \text{ (double) s.t. } \mathbf{ZI}_o = \zeta_o \mathbf{I}_o \Rightarrow \mathbf{I}_o = \gamma \overbrace{\begin{bmatrix} e^{j0} \\ e^{j\frac{2\pi}{3}} \\ e^{j\frac{4\pi}{3}} \end{bmatrix}}^{\mathbf{I}_{o1}} + \xi \overbrace{\begin{bmatrix} e^{j0} \\ e^{j-\frac{2\pi}{3}} \\ e^{j-\frac{4\pi}{3}} \end{bmatrix}}^{\mathbf{I}_{o2}}, \gamma, \xi \in \mathbb{R} \end{cases} \tag{2.15}$$

The result expressed in (2.15) is remarkable since it allows understanding that, due to the symmetry in the coupling network, a Triple Push Oscillator supports more than one operating mode. Moreover, equations (2.15) provide the *small signal impedances associated with each mode* and enable a systematic *linear* design [18], [53]. In fact, the small signal conditions for triggering oscillations [54] should be verified *only for the "odd" mode impedances*:

$$\begin{gathered} \mathrm{Re}\left(\zeta_e(\omega)\right) = \mathrm{Re}(Z_s(\omega) + 2Z_t(\omega)) > 0 \text{ ("even mode" is suppressed)} \\ \begin{cases} \mathrm{Re}\left(\zeta_0(\omega)\right) = \mathrm{Re}(Z_s(\omega) - Z_t(\omega)) < 0 \\ \mathrm{Im}\left(\zeta_o(\omega)\right) = \mathrm{Re}(Z_s(\omega) - Z_t(\omega)) = 0 \end{cases} \text{ ("odd mode" oscillates)} \end{gathered} \tag{2.16}$$

The equations (2.16) can be rewritten in a more suitable manner for an easier interpretation in the design process. As it is shown in picture (Fig. 2.5) assuming a nominal impedance of Z_L = 50 Ω in the output load, since the "even mode" currents are adding themselves in phase, the equivalent load impedance $Z_L^{(e)}$ of the even mode *seen by a single sub-oscillator* will be three times greater than Z_L, i.e. $Z_L^{(e)}$=150 Ω. Analogously, in the "odd mode" the first harmonic currents cancel each other and the load becomes a virtual ground so $Z_L^{(o)}$=0 Ω. Considering only one device and the branch of the coupling network towards the output node, the eigenvalues $\zeta_{(e)}$, $\zeta_{(o)}$ are evaluated (at the nominal oscillation frequency f_0) by adding the partial contributions Z_{out} (looking into the active device), Z_{in} (looking towards the coupling network and depending on the load impedance Z_L , providing:

[7] Notice that $\mathbf{I}_{o2} = \mathbf{I}_{o1}^*$ that is, one eigenvector is obtained as the *complex conjugate* of the other.

$$\begin{aligned}
&\mathrm{Re}\left(Z^{(e)}_{out\ (\mathrm{device})}(\omega)+Z^{(e)}_{in\ (\mathrm{coupling})}(\omega)\right)\Big|_{\substack{Z_L^{(e)}=3Z_L \\ \omega=\omega_0\equiv 2\pi f_0}} > 0;\\
&\mathrm{Re}\left(Z^{(o)}_{out\ (\mathrm{device})}(\omega)+Z^{(o)}_{in\ (\mathrm{coupling})}(\omega)\right)\Big|_{\substack{Z_L^{(o)}=0 \\ \omega=\omega_0\equiv 2\pi f_0}} < 0\\
&\mathrm{Im}\left(Z^{(o)}_{out\ (\mathrm{device})}(\omega)+Z^{(o)}_{in\ (\mathrm{coupling})}(\omega)\right)\Big|_{\substack{Z_L^{(o)}=0 \\ \omega=\omega_0\equiv 2\pi f_0}} = 0
\end{aligned} \tag{2.17}$$

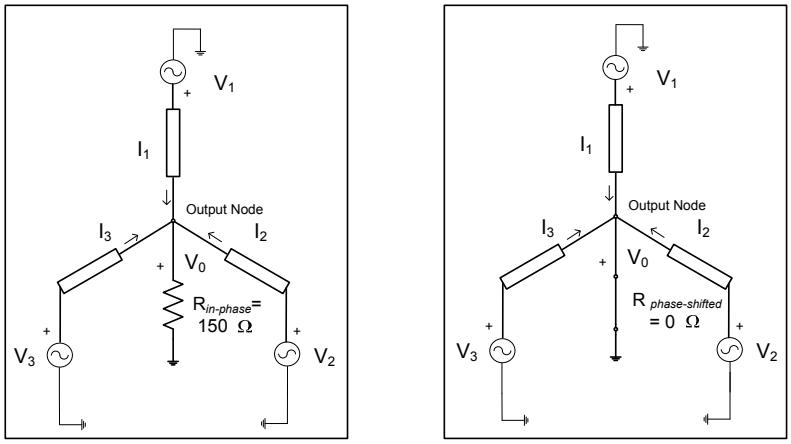

FIGURE 2--5. Small signal Oscillation condition for achieving third harmonic generation. Assuming a nominal impedance of 50 Ω, third harmonic generation can be checked by using a 150 W output resistor for the in-phase oscillations, and a virtual ground for the phase shifted resonances.

Employing the small signal conditions (2.17) might be helpful in choosing the bias conditions, the component values of the sub-oscillators, and to design the coupling network in order to trigger the odd oscillation mode, so to set the phase shift among neighboring elements to $2\pi/3$ and to combine the output currents' third harmonics in phase to obtain a power increase at a triple frequency (relative to the sub-oscillators fundamental). However, the major drawback of this approach is not considering the nonlinear coupled oscillator dynamics, which is essential for describing oscillation output power level, low order harmonic rejection, possible instabilities or spurious signals generation, sensitivity analysis with respect to circuital parameters, oscillator phase noise [54]. All of these issues have to be dealt by undertaking a rigorous full nonlinear analysis[8], as exposed in [44].

[8] On the contrary, equations (2.17) are valuable for determining roughly the fundamental frequencies of the core oscillators when coupled in the triple-push topology, so to obtain indirectly an approximate value for the frequency of the coupled oscillators system's output signal, which is three times as much. It has to be stressed that impedance functions are *evaluated for two different load conditions, at the same oscillation frequency*.

2.2.3 Triple Push Oscillator Modes Dictated by Group Theoretic Results[9]

A more general approach, based on some group theoretic findings [2], [4] applied to the system of ODEs governing the evolution of rings of nearest-neighbors coupled oscillators[10], allow one to predict the existence of more oscillating modes, due to mixed spatiotemporal symmetry in triple-push oscillator topologies, which are summarized in Fig. 2.6 and Table 2.1. In fact, it can be noticed that the "even" (*in phase output signals* with perfect synchronization, mode M_1) and "odd" modes (*discrete rotating wave with a progressive phase distribution of* $2\pi/3$ among individual oscillators, mode M_2) are only two out of four possible ones. In mode M_3 two oscillators are π out of phase and exhibit identical amplitudes, while the third oscillator freely resonates at a frequency double to the frequency of the other two; this mode is more difficult to detect experimentally. Finally, in mode M_4, two oscillators present the same amplitude and are mutually phase locked, while the third element has different amplitude and phase shift with respect to the others. M_2 enables third harmonic boosting.

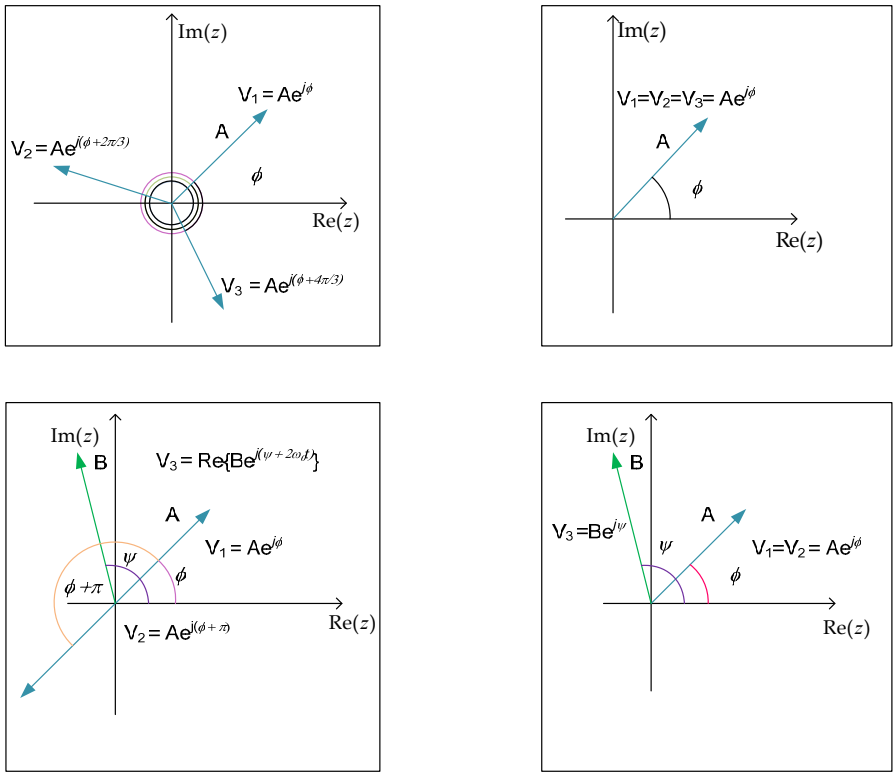

FIGURE 2-6 Phasors configuration for a ring of three identical oscillators, as derived from Group Theoretic results (summarized in table below).

[9] A systematic presentation of the background of the group theoretic approach of coupled nonlinear oscillator is beyond the scope of our research, and therefore the most important results will be here summarized. For further discussions, see the appendix A and the references at the end of the chapter.

[10] The results apply here in the case N=3, whether the coupling network is in the form a star or ring, since the two groups of symmetries are perfectly identical.

Mode M_i	Oscillators Phases			Oscillators Amplitudes		
	φ_1	φ_2	φ_3	A_1	A_2	A_3
M_1	φ	φ	φ	A	A	A
M_2	φ	$\varphi + 2\pi/3$	$\varphi + 4\pi/3$	A	A	A
M_3	φ	$\varphi + \pi$	$\psi(@2f_0)$	A	A	$B(@2f_0)$
M_4	φ	φ	ψ	A	A	B

TABLE 2-1. Set of *Phase Locked Periodic Solutions* for a triple push oscillator [2],[4].

2.3 STATE OF THE ART IN DISTRIBUTED OSCILLATORS AND VCO

Distributed Oscillators and Distributed Voltage Controlled Oscillators (DVCO) are commonly referred to those distributed circuits deriving from the Distributed Amplifier which was invented to overcome the gain bandwidth limitation in conventional multi-stages amplifiers caused by the presence of parasitic capacitances in the active devices [55–58]. By suitably coupling various active sections by means of two separate transmission line structures, (one for feeding the input signal, the other for extracting the output signal), purposely designed to mitigate the effect of stray capacitances, it is possible to obtain a wideband operation, such as a lowpass behavior extending from DC to a cutoff frequency ω_c which can be made very close to the active devices' intrinsic frequency limit.

A Distributed Oscillator is conceptually conceived as a distributed amplifier in which a feedback is created for building up and sustaining oscillations [59]. A DVCO in turn, consists in a distributed oscillator, in which some biasing voltage (or current, depending on the implementation) is used to alter the phase of the closed loop transfer function determining a modification of the oscillation frequency. It is interesting to notice that, though the aforementioned interpretation results valid for recently published works, historically the term "distributed oscillators" took different nuances of meaning. In fact, it generally indicated a class of oscillators in which the effect of distributed elements, may they be passive (i.e. microstrip lines resonators) or active (as Tunnel Diode, admitting a distributed parameter description) is relevant to the circuit analysis and design, in contrast to the simple low-frequency lumped counterparts. Moreover, in some works [60 – 62] a "distributed oscillators" refers to what is commonly now acknowledged as a coupled oscillator system (see previous section), that is a one or two dimensional array of oscillating elements coupled by a linear passive network.

The first attempt to use distributed parameter networks in oscillator design dates back to the work [63] in which is detailed a method to extend the frequency range of a phase-shift oscillator by using an artificial transmission line constituted by various resistances and capacitances. If a section impedance of the artificial RC line is made k times the previous one, the

minimum gain for having oscillations decrease, causing an increase in the maximum oscillation frequency. In [64] the effect of distributed resonant circuit for the range 300 MHz—3 GHz was accounted. Various works subsequently related to [63] and described single active device oscillator topologies (e.g., phase-shift, or Wien type) in which the feedback path was implemented with ladder RC networks or proper transmission lines [65-68]. Evidently the first contributions in which multiple active devices were periodically placed along a reactive multi-sections power combining distribution networks are [69, 70]. Specifically in [69] is indicated how the use of four Tunnel Diodes (a two port device) placed periodically on a quarter wave transmission line, would improve the output power level, analyzing the effect of series losses, and of the shunting capacitances. On the other hand, in [70] was firstly shown an integrated realization of a distributed oscillator using RC phase shift network and bipolar transistor using additional coupling among some sections, which markedly resembles the modern implementation. Finally an integrated quarter wave resonator coupled to n-type GaAs Schottky Diode was investigated in [71], deriving the oscillation conditions from the analysis of its physical behavior.

It was in [72] that for the first time was considered the possibility of placing an internal feedback path (after having removed unnecessary components) in the distributed amplifier topology, in order to trigger oscillations. Additionally, it was demonstrated (by means of linear analysis techniques) that by individually biasing each active device in a given section, a set of discrete resonances could be obtained, exploiting the so called *reverse gain mode*. These individual resonances were obviously bounded below and above, by the frequency characteristics of the embedded low-pass transmission network. Furthermore, it was suggested that by changing two adjacent sections active devices' bias voltage, the oscillation frequency shifted continuously between the two corresponding individual resonances; applying this procedure repeatedly, virtually the entire tuning band would be covered. Since the tuning band is inherited by the distributed amplifier passband, a very wideband VCO could thus be obtained, capable of scanning a decade – wide frequency band. These theoretical findings were experimentally verified. In [73] a low frequency (55.7 MHz—112.5 MHz) prototype was tested, using ATF 35376 discrete devices and a artificial transmission lines sections, showing a harmonic rejection (for second and third harmonic) better than 20 dB over the entire tuning bandwidth. Interestingly, it was noticed an ambiguity in the tuning function, for which many different tuning combinations provided the same oscillation frequency. However, the authors suggested that the tuning function non-uniqueness could offer some benefits, since it allowed selecting the best possible tuning strategy according to different specifications, like maximum output power, minimum harmonic distortion, minimum phase noise. A multi-GHz wide frequency range DVCO was successfully designed and tested in [74] confirming once more the theoretical framework described in [72]. The oscillator, realized on a microstrip board, made use of the periodically (actively) loaded transmission line concept, therefore no discrete (chip) components were used other than the active devices (same model as before), padding capacitors to provide phase equalization and broadband match, and the necessary lumped elements acting in DC block, DC feed networks. The authors reported to have reached a tuning range of almost 3 GHz, (1GHz—3.8 GHz) and obtained a very good spectral purity and harmonic rejection, with levels ranging from 18 to 44 dB for the second harmonic, and 17 to 55 dB for the third. Still, the tuning function was not shown, as the author notified again of its unclear multi-valued, non-smooth behavior.

Soon after the experimental confirmation illustrated in [74], more advanced research on Distributed Oscillators and VCO was carried out. In [75] a 16.6 GHz three segment distributed oscillator was realized with a CMOS process using coplanar striplines as inductive elements. This circuit had some differences with the one illustrated in [74] mostly due to a different biasing strategy and to a different choice for the feedback path layout. In fact, while in [74] the circuit exploited the reverse propagating waves on the output line of a distributed amplifier, in [75] feedback path is created by simply connecting the output line back to the input, utilizing a ring topology, and biasing the active devices at the same voltage level. The oscillation builds up as the signal traverses the loop structure, and settles at a frequency corresponding to transmission network delay plus one gate delay (needed to transfer it at the output line). Therefore, in [75] the forward propagating waves are continuously circulating and reentering the circuit, having no forward /backward wave interaction described in the previous works [72-74]. A thorough analysis of a similar *forward mode* distributed oscillator is exposed in [76] where a general oscillation condition is derived in order to predict oscillation amplitude and frequency. A distributed VCO operating at 12 GHz dissipating 13 mW of power was demonstrated, possessing a tuning range of 26% with a phase noise of -104 dBc/Hz at 1 MHz offset from the carrier; a second design illustrated 17 GHz bipolar distributed oscillator, which dissipates 9 mW of power. A novel tuning technique, called current- steering delay balanced tuning, was presented in [77] to obtain a DVCO from the previous invention. Essentially, each distributed oscillator segment comprises a pair of active devices whose gates are coupled by an additional transmission line, and whose drains are directly connected. By properly varying the biasing currents of the two active devices, a change in its transconductances will alter the phase loop response causing a shift in the oscillation frequency. This tuning technique was used to design a DVCO operating at 10 GHz in a 0.35 μm CMOS technology, continuously tunable between 9.9 and 10.3 GHz. Another example provided by the same authors is [78] illustrating a DVCO with a coarse/fine tuning selection. The DVCO was based on a BiCMOS process and achieved a tuning range of 12% (9.3 GHz to 10.5 GHz) with a phase noise of -114 dBc/Hz at 1 MHz offset from the 10.2 GHz carrier. Moreover, a critical review of the theoretical analysis and findings was summarized in [79].

New Clock Distribution Networks for circuits operating in the digital domain, based on the distributed oscillator concept, were conceived in [80] as "Rotary Travelling Wave Oscillators" (RTWO). Creating a rotating travelling wave within a closed loop differential transmission line, this circuit allows one to directly access a multi-phase signal, reduces noticeably the clock skew and can be scaled to cover large chip areas.

The oscillator phase noise was evaluated in [81] by identifying an effective capacitance equal to the total capacitance distributed along the transmission lines, and by accounting for the contributions of the various passive and active noise sources. In [82] a frequency domain first order distributed oscillator model is derived, with analytical treatment similar to [74] [79], and subsequently expanded to include the nonlinear noise contributions effects from each active device. The closed form expressions obtained analytically are then compared with a series of Harmonic Balance simulations using Agilent ADS© software for various distributed oscillator configurations, and demonstrating a good agreement with a maximum error of 5 dBc at 1 MHz offset. The DVCO injection-locked operation was illustrated in [83] in which a PLL controlled both the oscillation frequency of a 5.2 GHz three-segments, bipolar transistor DVCO and the ½ sub-harmonic signal at 2.6 GHz, obtaining a wide locking range frequency synthesizer (104 MHz @ 5.2

GHz for an injection power of -5 dBm @ 2.6 GHz), a noticeable improvement in phase noise (-121 dBc/Hz @ 1 MHz offset from the carrier), and a very low power consumption (supply voltage of 2.7 V, supply current of 14.5 mA). Similar to the previous design, an oscillator operating at 5.8 GHz and with a lower supply voltage was devised in [84] and included the presence of a varactor diode inserted in the feedback path for implementing tuning capabilities, achieving a 650 MHz tuning range.

Using low loss MEMS coplanar waveguide in a CMOS integrated distributed oscillator was demonstrated [85] to bring significant benefits in terms of phase noise reduction, reaching the lowest record (of that time) of -125.7 dBc/Hz at 1MHz offset from the 13.3 GHz carrier. A design using a folded coplanar waveguide concept, was illustrated to have good performance in terms of RF efficiency delivering 5.77 dBm at 12 GHz with a phase noise of -115.16 dBc/Hz at 1 MHz offset [86]. A particular layout technique, consisting in using closely packed (differential) pairs of input /output transmission lines, to the aim of minimizing chip area while maximizing the return losses (with respect to single ended realizations) was used to implement a BiCMOS distributed amplifier possessing a 25 GHz bandwidth and 7.5 dB of gain, and capable of operating as a distributed oscillator @ 9.2 GHz carrier, providing with -6 dBm single-ended output power, phase noise of -103 dBc/Hz at a 1 MHz offset, and a 17% tuning range[87]. The work in [88] analyzed the previous contributions regarding the reverse mode distributed voltage controlled oscillators [72-74] and extending the linear DVCO model previously developed for constant-*k sections* based artificial transmission lines, to the more general *m*-derived sections, obtaining the minimum transconductance needed for achieving oscillations at the output.

A different (modular) design approach is presented in [89]. A distributed voltage controlled oscillator is implemented connecting different sub-systems in a closed loop: a distributed amplifier, which provides a flat gain response over a wide pass-band; a varactor tunable band pass filter, responsible for frequency selection, and a variable phase shifter in the feedback loop, needed for meeting the oscillation condition at a given frequency. Additionally, a distributed feedback amplifier was included to accommodate for the gain factor needed for achieving oscillations, and a power splitter to extract the output signal. The oscillator was tunable in the band (1.59 GHz—2.29 GHz) offering (simulated) phase noise values better than -116 dBc. The last design methodology was also used in [90-93] *conceptually separating* the design of the frequency selective section (switched capacitor filter banks, providing coarse/fine tuning) from the amplifying section consisting in a wideband distributed amplifier, which are subsequently connected them through a feedback loop. In this manner, many complications regarding the tuning capabilities are avoided, though strictly speaking the resulting circuit cannot be qualified as a proper distributed oscillator.

Inspired by the distributed oscillator first presented in [75-76] a similar three section circuit was implemented in integrated form [94] achieving a 27 GHz (central frequency) tunable oscillator (26.4 GHz—27.4 GHz) with a 15 ± 0.9 dBm across the tuning range. Another contribution focused on an integrated DVCO exploiting MOS varactor pairs placed along the feedback path to provide frequency tuning, retaining a close analogy with a previously published work [86] for what concerns the layout technology (folded coplanar waveguides used as inductive elements) and the active devices used [95]. One DVCO realization comprised four sections, had an oscillation frequency of 20 GHz approx. and was tunable in the range (20.02 GHz—20.23 GHz) while another possessed three sections, and was reported to have a tuning range of 570 MHz (20.46 GHz—21.03

GHz). The two oscillators maintained a bounded power level variation of 2 dBm for the three sections DVCO and 1.5 dBm for the four sections DVCO. The same authors showed in [96] the feasibility of a (25.82 GHz— 27.1 GHz) DVCO using a change in the body terminal of n-FET devices providing a wider tuning range, compared to the previously published works. The aforementioned tuning techniques [95] [96] were simultaneously used in a successive DVCO implementation at 23.97 GHz [97]. In [98] a different "gain cell" module was devised for designing three different DVCOs. One of them was based on a three-section configuration, cascaded-common source n-FET stages (interconnected by a coplanar waveguide), to boost the active section transconductance. The other one, had five sections; the even numbered ones (sections 2 and 4), in which the elementary cell was constituted by two cascaded common source stage, and the odd numbered ones (sections 1, 3 and 5) in which the gain cell included an additional peaking inductor as a coupling element between the two common source FET, creating a high pass filtering at the lowest harmonics, resulting in a third harmonic power increase. The first oscillator resonates at frequencies comprises in the K- band, being tunable by changing the voltage of the intrinsic MOSFET body varactor (-1.5V—0.6V) to cover the 18.89 GHz—20.05 GHz bandwidth (tuning range of 1.16 GHz) an delivering an output power of 10.75 dBm, with a low phase noise of -126.857dBc/Hz at 1 MHz offset from the carrier. The second oscillator resonated at the 3rd harmonic frequency of 29.27 GHz in Ka-band offering a -0.3dBm power level, whereas the fundamental is of -12.828 dBm at 9.756 GHz and 2nd harmonics of -17.289 dBm. It is important to notice that the previous findings [95—98] are based only on simulations performed on the Harmonic Balance engine from Agilent ADS.

A different operation principle, based on the theory of Mode-Locked Lasers to generate ultra-short impulses, was proposed in [99]. Thanks to a nonlinear element inserted in the feedback path of a suitably modified reverse mode distributed oscillator topology [72-74] (making use of additional input line for injecting a supplementary external signal) and to an uneven distribution of the tap weights of the amplifying sections, pulsed operation is achieved. The exact values of tap weights depend on the required pulsating waveform specification and can be obtained by implementing a numerical optimization program.

Finally, a thorough theoretical analysis of phase noise for active circuits coupled to distributed resonant loads, and thus resulting in wave-based oscillators has been reported in [100]. Three cases were analyzed. In the first case, an active circuit, which amplifies small signals and attenuates large ones, is coupled to an open-end half wave transmission line creating standing wave resonance. Secondly, the same topology is used, but the nonlinear device attenuates the small signals and amplifies the large ones, giving rise to linear pulse in the output. In the last case, a nonlinear transmission line is employed, periodically loaded with varactors, to shape the linear pulse into a soliton pulse. The findings, after having accounted for the distributed noise sources along the transmission networks, revealed that the phase noise depends on the type waveform being considered (sinusoidal, linear pulse, soliton) providing design suggestions. Though very detailed, however this study doesn't directly relate to the distributed oscillators/VCOs concrete topologies presented earlier [74] [79].

2.4 DISTRIBUTED AMPLIFIER THEORY

The Distributed Amplifier [101-103] deserves attention for two main reasons. First, it is traditionally considered as the invention capable of overcoming the known *gain-bandwidth product constraint* which for every lumped realization of an amplifier remains constant, regardless of the interstage/end stage coupling network used and it is primarily affected by the input/output active devices' parasitic capacitive loading [104]. In distributed amplification instead, the increase in gain is not offset by a decrease in bandwidth. The wideband operation in a distributed amplifier is achieved by periodically displacing the active devices input/output ports stray (shunt) capacitances at each section, along two separate, input/output transmission networks. Hence, the output currents produced by the active devices at each section get superimposed, without being restrained by active devices' capacitive loading effect and delivering a voltage gain which is proportional to the number of sections. The distributed amplifier bandwidth is thus determined by the frequency response of the embedded transmission network[11] which can be conveniently designed, by carefully accounting for the effect of parasitic capacitances to have a flat low-pass response up to a cut-off frequency closer to f_T .

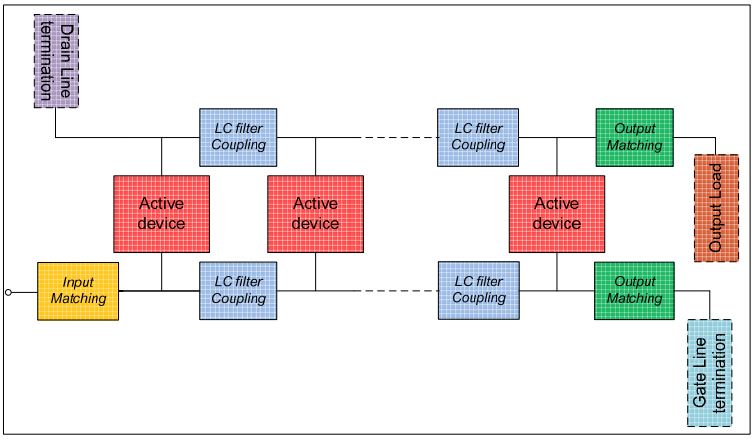

FIGURE 2-7 Distributed Amplification principle, using FET devices and artificial transmission lines sections.

Second, the distributed amplifier is the key element for understanding other relevant microwave circuit topologies, like distributed oscillators and VCOs, distributed mixers [105 --106], frequency synthesizers [83], signal generators /waveform shapers [99, 107], frequency multipliers / dividers [108]. In particular the distributed oscillators and VCOs can be viewed as positive feedback distributed amplifiers. Therefore, a discussion on distributed amplifiers' main features and design methodology proves to be essential.

This section is split into three parts. In 2.3.1 the distributed amplification technique is explained. It is shown how to increase the bandwidth of conventional lumped amplifiers, by using *N-sections distributed topologies*, in which several active devices are connected at two distinct (input/output) transmission networks. In section 2.3.2 different distributed amplifiers realizations

[11] Depending on the implementation, these transmission networks can be cast in a form of cascaded constant-*k filter sections* (*artificial transmission lines*) or in *periodically loaded transmission lines* [103].

are analyzed[12]. The first one employs artificial transmission lines formed by cascaded *constant-k* filter section, while the second one makes use of periodically loaded transmission lines. Generically, field effect transistors (FETs) are considered as active device taking part in the amplification of the RF/μW signals. The properties of distributed parameter networks are reviewed, studying the voltage response to multiple current sources, emulating the contributions coming from the active devices. This constitutes the basis for analyzing the distributed amplifier gain in section 2.3.3 where imperfect match at the terminations and the effect of losses are considered. The basic assumption made here is that the small signal FET models are unilateral, so that the wave propagation in the output line won't affect the voltage (current) distribution in the input line. The ensuing analysis is based on the works [101]—[102].

2.4.1 BROADBAND AMPLIFICATION UTILIZING DISTRIBUTED NETWORKS.

One of the most important features of an amplifier circuit is its *gain function*, describing its *frequency behavior* in terms of voltage (current, power) input/output *transfer ratio*. For many applications, it would be rather appealing to increase both the gain and the -3 dB bandwidth [109], but as long as the circuit realizations consist of lumped components these requirements are conflicting. These results have been theoretically substantiated for many topologies [104]. For instance, a bandpass FET amplifier could be considered (whose small signal model is depicted in Fig. 2.8). The voltage gain is:

$$A(\omega) = \frac{-g_m R}{1 + jQ\left(\frac{\omega}{\omega_0} - \frac{\omega_0}{\omega}\right)} \tag{2.18}$$

where A_0=-$g_m R$ represents the *maximum gain at the central frequency* $\omega_0 = 1/\sqrt{(LC)}$, $Q = \omega_0 RC$ *is the quality factor, and the -3dB bandwidth is* $B = \omega_0 / (2\pi Q) = 1/2\pi RC$. Therefore, the gain bandwidth product is readily computed:

$$|A(\omega_0)B| = \frac{g_m}{2\pi C} \tag{2.19}$$

and doesn't depend on the terminating resistance, but only on the shunt capacitance[13] seen at the tuned load and on the transconductance of the active device.

[12] A distributed amplifier could be more abstractly defined as a *distributed transmission structure* coupled to an *active medium*. Travelling Wave Optical Amplifier (TWOA), Erbium Doped Fiber Amplifier (EDFA), exploiting the interaction of a beam of light (EM radiation) with a properly gain medium for achieving its amplification see [101], fall into this category.

[13] Network Theorem from Bode states that in the high frequency limit, the output impedance of a two port devices is capacitive [101], [104].

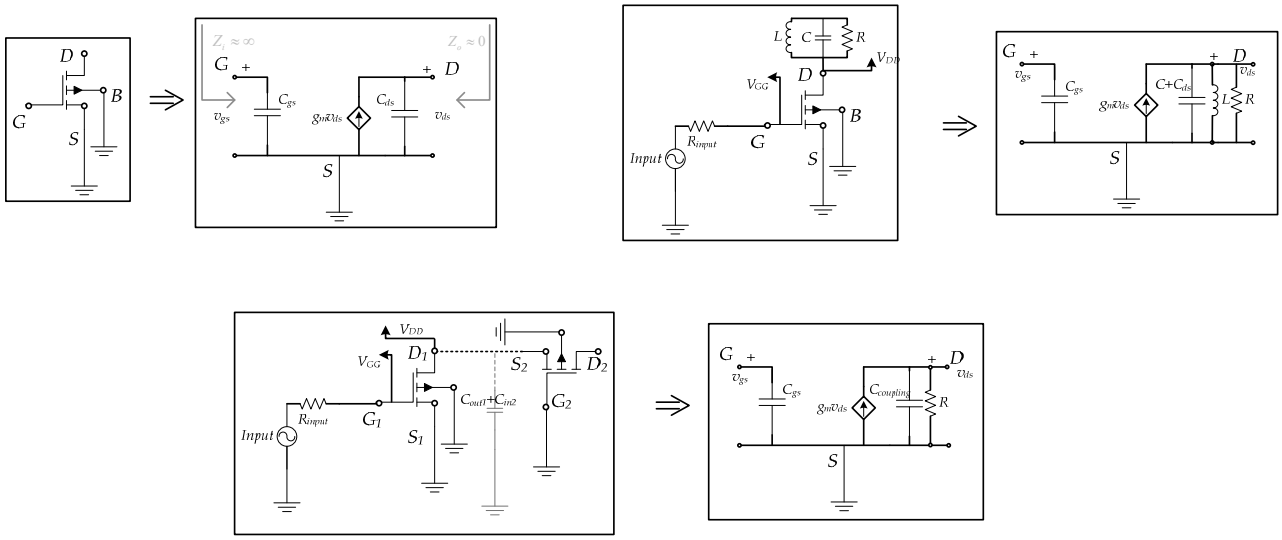

FIGURE 2-8. Small signal equivalent models of a FET amplifier. In the case of a tuned amplifiers and in cascaded stages the output capacitance loading bounds the maximum bandwidth.

Therefore, from (2.19) follows that for a given active device (g_m is fixed) one should reduce the loading effect of the output capacitance, in order to increase the bandwidth of the amplifier. However, this is not easy to achieve as long as the output capacitance remains lumped at the output port[14]. This is easily seen in the *RC* coupled amplifier in Fig. 2.8 where the *RC* coupling emulates the output impedance/next stages impedance. With a low-pass frequency response having a real pole on $\tau=RC$, *and thus a -3 dB bandwidth extending in* $[0, 1/\tau]$ the gain-bandwidth product is: $|A_0B| = g_m/C$. Once again the lumped capacitive loading at the output ports prevents the designer to fully exploit the maximum attainable bandwidth for a given device (which extends from zero frequency to f_T). Apparently there's no way of circumventing this issue. In fact, when cascading several stages a higher gain is achieved[15] but the bandwidth is reduced[16]. Nor the parallel connection is useful, since both the transconductances and the capacitances of the active devices get added, and the product $|A_0B|$ stays unaltered.

However, as shown in Percival patent [55], a higher bandwidth could be achieved by connecting several active devices through separate transmission networks, in such a way that the output currents could be accumulated, isolating the contribution from the capacitive loading of each section by using inductance coils. By doing so, the input/ output capacitances are absorbed in cascaded filter sections, giving rise to two artificial transmission lines. Choosing suitably the values for the inductances both at the input and at the output line and provided phase synchronization is kept in both lines, a lowpass frequency response can be obtained, which

[14] This result remains valid also in the case of multistage amplifiers, for the interstage capacitive loading. In that case the input capacitances of the subsequent stages should be accounted for.

[15] As an equivalent transconductance which is the product of the transconductances of the stages $g_m=g_{m1}g_{m2}$ [109].

[16] The equivalent bandwidth (in the *high frequency limit*) of a multistage amplifier *B* could be computed by considering the *dominant pole approximation*, and it is given by the reciprocal of the sum of the *open-circuit time constants:* $2\pi B=(\tau_1+\tau_2+\ldots+\tau_N)^{-1}$ where $\tau_k=R_kC_k$ *,accounting separately for the contribution of each capacitive branch* (supposing the capacitors are not interacting) [109].

broadens the achievable bandwidth, enabling operation close to the intrinsic devices frequency limit [4]. Although the original patent detailed the invention providing the actual schematics for implementing multi-stage tube-based distributed amplifier, it apparently passed unnoticed. It wasn't until ten years later that (in seminal Gintzon paper, 1948 [56]) the theoretical foundations for analyzing distributed amplification were laid. Since then, the scientific literature regarding distributed amplifier gained impetus, and many corrections to the first-order theory were provided [110-112], the transient response calculated, and the effect of unequal propagation constants in the transmission networks investigated [57], [58], [113]—[122]. A major boost came from the possibility of implementing very wideband microwave amplifiers in MMIC (microwave monolithic integrated circuits) form using MESFET active device [123]. Effective design methods were firmly established, that are still used nowadays even in the design of DA employing discrete components.

A distributed amplifier can be realized by connecting several FET devices by means of transmission lines, whose behavior has to be prominently inductive [110], [112]—[113], [118] in the frequency band of interest[17]. Since the FETs are normally arranged in a common source configuration, the input (output) line is alternatively termed *gate* (*drain*) *line* as shown in Fig. 2.9. A simplified analysis is possible, employing the unilateral approximation for the active devices' small signal models[18] ; an active device is simply represented by a capacitor at the gate port (C_{gs}), and by a parallel connection of a capacitor (C_{ds}) and a current source, controlled by the gate voltage (V_{gs}) at the drain port[19]. Since there is no internal feedback element in the FET model, the analysis of the wave propagation in the gate and drain lines is effectively decoupled[20].

[17] When the operating frequency is less than a few GHz, chip inductors can still be used for interconnecting sections, and together with the stray FET capacitances form cascaded *constant-k* filters, or *artificial transmission lines* [103].

[18] In general, the devices operate nonlinearly, when the voltage swing applied at the input port causes the FET output current not to respond proportionally, due to the saturation phenomena [109] determining a distortion of the output waveform (clipping of the signal). However, if the input signal remains bounded and *small* (*compared to the DC bias voltages*) the linear approximation gives satisfactory results. In an oscillator circuit, the small signal model is used for *estimating the oscillation frequencies*, during the oscillation build-up phase [50]. However, after the oscillating signal has grown in amplitude, the linear analysis is inappropriate in describing the circuit, due to the *large* (i.e. the *same order of* DC voltages, or *even greater*) high frequency self-sustaining voltages driving the active devices.

[19] In a small signal analysis moreover, this three parameters aren't dependent on the input voltage that is $C_{gs}(V)=C_{gs0}$; $C_{ds}(V)=C_{ds0}$, $g_m(V)=g_{m0}$; *they remain constantly at their nominal value (depending on the DC quiescent point).*

[20] A much simpler FET models retains only its essential features (*being a voltage controlled current source*), neglecting inductive effects, and resistive losses (due to drain, gate, source metallization, and packaging). More importantly the internal C_{gd} (gate-drain) *feedback capacitance* [50] is omitted, assuming the device is *unilateral thus simplifying the treatment.* A more detailed analysis is possible without overlooking the above mentioned details, leading to time domain coupled wave, full nonlinear formulation made possible by setting up partial differential equations [101].

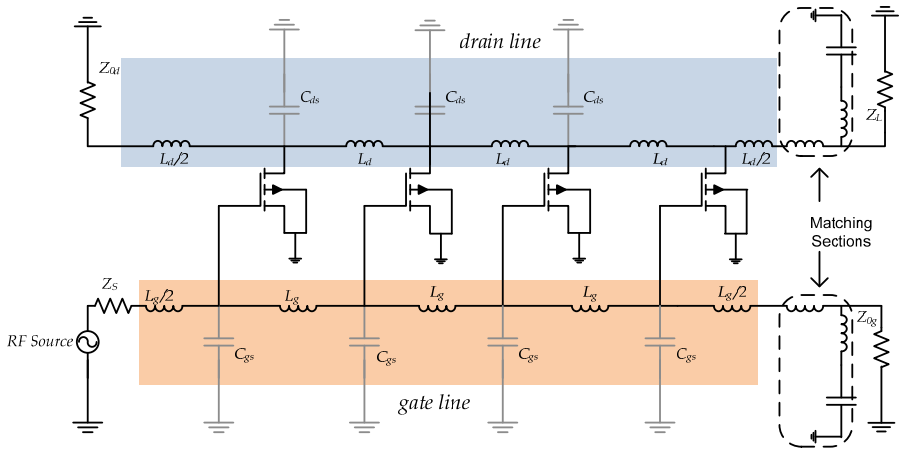

FIGURE 2-9. A simplified schematic of a distributed amplifier. The artificial transmission line is formed by connecting several active device with inductors (or prominently inductive components) and using the active devices parasitic capacitances.

It is noticed that, by approximating the transmission line with pure inductances, neglecting their losses (and the FET losses as well) and their capacitive behavior, the distributed amplifier is constituted by two artificial transmission line, which are unilaterally coupled by means of the transconductance of the active devices. As the input RF signal which is fed on the gate line traverses each section, it progressively excites the FETs so to give rise to an *N-fold* current contribution in the output line. The signal in the gate line is finally absorbed by a matched resistor, provided an adequate matching section is inserted, so to minimize spurious reflections. The currents produced in the drain line instead, travel in two opposite directions. In fact, forward propagating current waves keep summing in phase[21] so that an amplified version of the input signal is delivered to the output load (Fig. 2.9), matched to the output line by an appropriate ending section (as for the case of the gate line). At the same time, the backward travelling waves give rise to a highly frequency dependent signal which is absorbed by a drain line matching resistor.

In order to evaluate the performance of the distributed amplifier, it is necessary to pinpoint the frequency behavior of the cascaded two ports shown in picture. Therefore the properties of the constant-*k* filters and *m* -derived filters sections will be briefly reviewed.

2.4.2 TWO-PORTS NETWORKS: TRANSMISSION PROPERTIES

In the previous section, it has been outlined the distributed amplification phenomenon. Essentially to achieve a wideband operation it is vital to disperse the gate (drain) parasitic capacitances over an extended coupling network that maintains a constant impedance level. By

[21] As long as the *phase velocity* in the gate and drain line is equal *at each cell*, so that the wave propagation in the output line is *phase matched* to that of the input line. It is important to notice that phase propagation factors are allowed to vary from one section to another, as long as $\varphi_g^i = \varphi_d^i$ $(1 \leq i \leq N)$ *while impedance level of the gate (drain) line has to be kept constant across all sections to the greatest extent possible for proper operation* that is $Z_{0g}^i = Z_{0g}$; $Z_{0d}^i = Z_{0d}$ $(1 \leq i \leq N)$ (not needing to take the same values, i.e. $Z_{0g} \neq Z_{0d}$ *in general*). Usually the impedances of the gate and drain lines are quite similar; often they agree with $Z_0 = 50\ \Omega$ for convenience. In a distributed oscillator instead (as later will be explained) the existence of a *feedback path connecting the output and the input line* forces the condition $Z_{0g} = Z_{0d}$ *for achieving broadband matching* [101].

coupling together *N active cells* via *inductive transmission line sections* (or inductors)[22] the output currents are superimposed, bringing a linear increase in the output gain, while the parasitic capacitances get embedded in cascaded constant *k* filter sections, which (when properly designed) ensure a low-pass operation[23], with pass-bands reaching several gigahertz [124].

Constant-*k* and *m*-derived filters can be conveniently analyzed using two-port parameters [101]—[103]. Although in linear circuit theory two-ports are usually characterized by their impedance or admittance matrices, when dealing with cascaded structures consisting of interconnected two ports, it is easier to assign them *the chain matrix* defined by the relations[24]

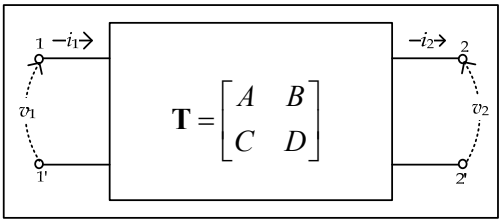

FIGURE 2-10. Chain Matrix representation of a two-port network, with associated signs for currents and voltages.

$$\begin{bmatrix} v_1 \\ i_1 \end{bmatrix} = \begin{bmatrix} A & B \\ C & D \end{bmatrix} \begin{bmatrix} v_2 \\ i_2 \end{bmatrix} \Rightarrow \begin{cases} v_1 = Av_2 + Bi_2 \\ i_1 = Cv_2 + Di_2 \end{cases} \tag{2.20}$$

$$A = \left.\frac{v_1}{v_2}\right|_{i_2=0}, B = \left.\frac{v_1}{i_2}\right|_{v_2=0}, C = \left.\frac{i_1}{v_2}\right|_{i_2=0}, D = \left.\frac{i_1}{i_2}\right|_{v_2=0}$$

The chain matrix of two-ports cascaded connection in that case is simply the matrix product of the individual chain matrices associated to each two-port [101]-[103]. The number of independent chain matrix parameters is reduced if the network is reciprocal[25].

[22] Real chip inductors present losses (resistive path) and spurious resonances (due to parasitic capacitance) which should be kept into account, by introducing vendor models, or by using two port S parameters extracted from measurements. The same holds true for chip capacitors.

[23] Not considering: *a)* the attenuation due to losses ; *b)* imperfect matching at the ending sections,.

[24] Unlike the expression for [Z] ([Y]) matrix relating the currents (voltages) at the two ports with the corresponding voltages (currents) by means of open-circuit impedance (short-circuit admittance) parameters, the chain matrix express both the voltage and currents at port "1" as linear combinations of voltage *and* currents at port "2". Moreover, the sign of the current at port "2" is positive, with the convention that the current is leaving the two ports.

[25] A two port network is reciprocal when exchanging stimuli (causes) at one port for effects (observations) at the other port produce identical results.

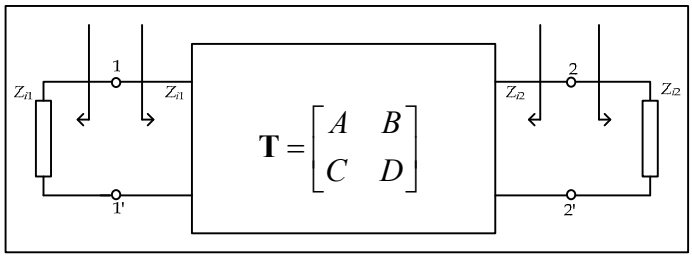

FIGURE 2-11. Image Impedances concept.

When considering the wave propagation along transmission structures in distributed amplifiers, it is very important to take into account the matching properties of the cascaded two-ports. In order to obtain a maximum power transfer [101]-[103] along the operating bandwidth is in fact required for each two port to operate with adequate impedance terminations. Making use of the image impedance concept helps in fulfilling this condition. The *image impedances* Z_{i1}, Z_{i2} of a two-port network are defined in relation with the impedance seen by looking into either direction of each port (Fig. 2.11). They can be expressed in terms of chain matrix parameters as [103]

$$Z_{i1} = \sqrt{\frac{AB}{CD}}\,; \qquad Z_{i2} = \sqrt{\frac{DB}{CA}}$$

$$Z_{i1} = \sqrt{\frac{B}{D}}\sqrt{\frac{A}{C}} = \sqrt{\frac{v_1/i_2\big|_{v_2=0}}{i_1/i_2\big|_{v_2=0}}}\sqrt{\frac{v_1/v_2\big|_{i_2=0}}{i_1/v_2\big|_{i_2=0}}} = \sqrt{Z_{sc1}Z_{oc1}} \tag{2.21}$$

$$Z_{i2} = \sqrt{\frac{D}{C}}\sqrt{\frac{B}{A}} = \sqrt{Z_{sc2}Z_{oc2}}$$

with Z_{sc1} (Z_{oc1}) the impedance calculated at port 1, when port 2 is short-circuited (open-circuited) and analogous definition holds for Z_{i2}. Image impedances Z_{i1}, Z_{i2} overlap when the two-port network is symmetrical; in that case the characteristic impedance Z_0 suffices for the description of its matching properties, being $Z_0 = Z_{i1} = Z_{i2}$.

When analyzing a two port network, is particularly interesting to evaluate the voltage, current, power transfer ratios. Using the chain matrix parameters [101]-[103], and noticing that the factor ($\sqrt{AD}$- $\sqrt{BC}$) is common to both the voltage and the current transfer ratio, it can be defined as a complex propagation factor[26] $\gamma = \alpha + j\beta$:

$$e^{-\gamma} = (\sqrt{AD} - \sqrt{BC}) \tag{2.22}$$

The propagation factor could be found using simple algebraic manipulations, taking into account that for a reciprocal network AD-BC=1:

[26] An intrinsic definition of the complex propagation factor is obtained by taking the square root of the power ratio at port 1 vs the power ratio at port 2: e^{γ} = sqrt(P_{in}/P_{out}).

$$
\begin{aligned}
&e^{-\gamma} = (\sqrt{AD} - \sqrt{BC}) \Rightarrow e^{\gamma} = (\sqrt{AD} + \sqrt{BC}) \\
&\cosh\gamma = \frac{e^{\gamma} + e^{-\gamma}}{2} \Rightarrow \gamma = \cosh^{-1}\sqrt{AD} \\
&\sinh\gamma = \frac{e^{\gamma} - e^{-\gamma}}{2} \Rightarrow \gamma = \sinh^{-1}\sqrt{BC}
\end{aligned}
\tag{2.23}
$$

The voltage and current transfer ratio can be therefore suitably expressed in terms of the images impedances and the complex propagation factor $\gamma = \alpha + j\beta$ as:

$$
\begin{aligned}
&\frac{v_2}{v_1} = \sqrt{\frac{Z_{i2}}{Z_{i1}}} \cdot e^{-\gamma}, \quad \frac{i_2}{i_1} = \sqrt{\frac{Z_{i1}}{Z_{i2}}} \cdot e^{-\gamma}, \quad (\gamma = \alpha + j\beta) \Rightarrow \\
&\frac{P_{out}}{P_{in}} = \frac{v_2 i_2^*}{v_1 i_1^*} = \sqrt{\frac{Z_{i2} Z_{i1}^*}{Z_{i1} Z_{i2}^*}} \cdot e^{-(\gamma+\gamma^*)} = e^{-2\alpha}\left(\sqrt{e^{2j(\angle Z_{i2} - \angle Z_{i1})}}\right) = e^{-2\alpha}(\arg(Z_{i2}) - \arg(Z_{i1}))
\end{aligned}
\tag{2.24}
$$

the power transfer ratio being computed, knowing the voltage and current transfer ratios. If the network is lossless, the attenuation factor α is zero and the image impedances are real therefore: $P_{out} = P_{in}$. In the following, the expressions (6.4)—(6.8) will be applied in the analysis of the filter sections usually employed in distributed amplifiers.

2.4.3 CONSTANT-*K* AND *M*-DERIVED FILTER SECTIONS

The most simple two-port network possessing a frequency selective behavior is a simple circuit containing an impedance ($z/2$) in the series arm and an admittance ($y/2$) in the shunt arm, generally referred to an *L* section or half–section (shown in Fig. 2.12) [101]-[103]. Two *L* sections can be interconnected in a back-to-back manner, giving rise to the *T* and *Π* networks[27] which are symmetrical networks possessing characteristic impedance of Z_{0T} , $Z_{0\Pi}$ respectively. From (6.4) and (6.7) the characteristic impedances Z_{0T} , $Z_{0\Pi}$ and the propagation factor γ are immediately obtained:

$$
Z_{0T} = \sqrt{\frac{z}{y}\left(1 + \frac{zy}{4}\right)}, \qquad Z_{0\Pi} = \sqrt{\frac{z}{y}\left(1 + \frac{zy}{4}\right)^{-1}}, \qquad \gamma = \cosh^{-1}\sqrt{1 + \frac{zy}{4}}
\tag{2.25}
$$

A lowpass network is implemented by introducing an inductor in the series arm and a capacitor in the shunt arm. By doing so, the impedances and the propagation constant becomes:

[27] *L* (*half*) sections are employed for converting the impedance from Z_{0T} to $Z_{0\Pi}$ and vice versa.

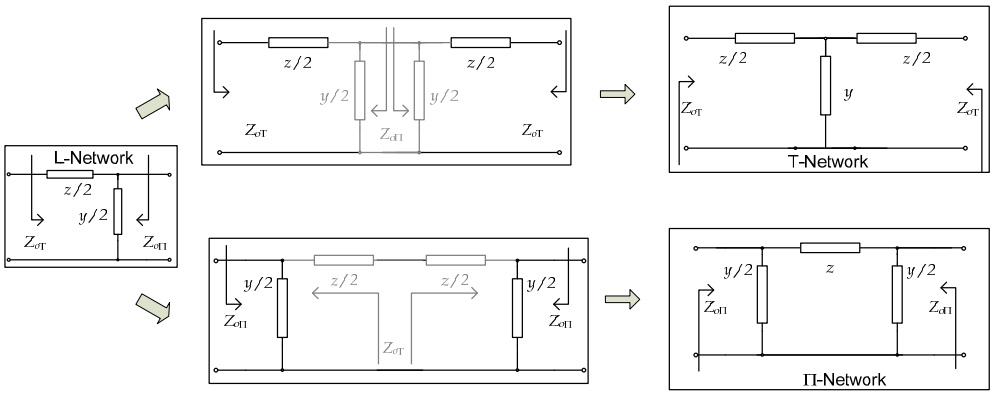

FIGURE 2-12. Half sections (L Section) topologies for a constant-k filter; cascaded interconnections give rise to T-network and Π networks.

$$Z_{0T} = \sqrt{\frac{L}{C}\left(1-\frac{\omega^2 LC}{4}\right)} = \sqrt{\frac{L}{C}\left(1-\frac{\omega^2}{\omega_c^2}\right)}$$
$$Z_{0\Pi} = \sqrt{\frac{L}{C}\left(1-\frac{\omega^2}{\omega_c^2}\right)^{-1}} \quad where \quad \omega_c = \frac{2}{\sqrt{LC}} \tag{2.26}$$
$$\gamma = \alpha + j\beta = \cosh^{-1}\sqrt{1-\frac{\omega^2}{\omega_c^2}}$$

where ω_c is the cut-off frequency of the section. Above ω_c the attenuation of the filter sets in, as evident in expression of α =Re(γ) for $\omega > \omega_c$, while the image impedances turn from real to imaginary [101]-[103]. Applying (2.25) it is noticed that throughout the passband of the filter (below the cutoff frequency), the power transfer ratio is constantly equal to one, after reaching the cutoff frequency when it starts to roll off as $e^{-2\alpha}$, emphasizing the inherent low-pass filtering property.

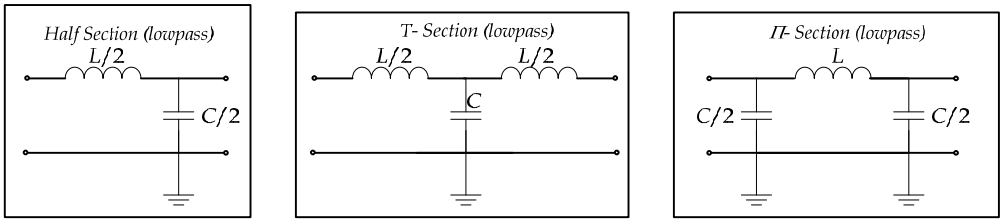

FIGURE 2-13 Low-pass constant –*k* sections.

The networks shown before are examples of constant–*k* (lowpass) filter sections, their name originating from the property: $z/y=R^2$ (*R is real*) meaning that the ratio of the series impedance to the shunt admittance is a constant. For constant-k section, from (2.26) results:

$$Z_{0T} \cdot Z_{0\Pi} = \frac{z}{y} = R^2 \tag{2.27}$$

Moreover, the propagation factors of the *T* and *Π* networks are the same, and twice[28] the one corresponding to a *L* network. Cascading adequately *L*, *T*, or *Π* sections, ladder network can be obtained, otherwise called *artificial transmission lines.*

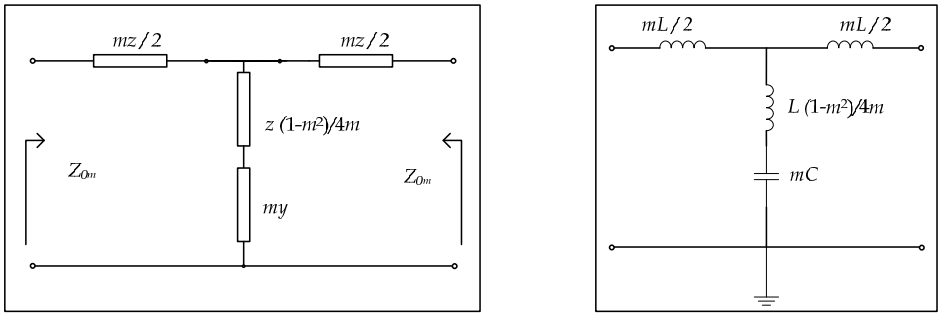

FIGURE 2-14 Example of *m*-derived T section lowpass filter**.**

An inconvenient of the constant-*k* filter is represented by the remarkable frequency dependence near the cutoff frequency which makes the broadband matching task more difficult. Furthermore the attenuation factor in the filter stopband grows slowly for $\omega > \omega_c$ [101]-[103]. In order to have a sharper lowpass response, *m*-derived sections are used. Essentially, they are obtained from *constant-k* filters introducing an impedance in the series arm [101]-[103] that is exactly *m* times ($0< m \leq 1$) that of the corresponding constant–*k* filter (Fig. 2.14), where *m* represents an adjustable parameter[29]. The admittance of the shunt arm y_m for a generic lowpass *T* section is found by imposing a perfect equivalence for the impedances of the constant-*k* and *m*-derived prototypes:

$$Z_{oT}^2 = \frac{z}{y}\left(1+\frac{zy}{4}\right) = \frac{z_m}{y_m}\left(1+\frac{z_m y_m}{4}\right) = \frac{mz}{y_m}\left(1+\frac{mzy_m}{4}\right) \Rightarrow$$
$$\frac{1}{y_m} = \frac{1}{my} + \frac{1-m^2}{4m} z \tag{2.28}$$

making it evident that the shunt arm consists of two element in series. In the case of an *m*-derived *low-pass* section, the series arm comprises two inductors of values $L_m = mL/2$ while one inductor $L_p = (1-m^2)L/4m$, and a capacitor $C_m = mC$ are included in the shunt arm. The propagation factor of the m-derived section is :

$$\gamma = \cosh^{-1}\left(1+\frac{z_m y_m}{2}\right) = \cosh^{-1}\left(1+\frac{2m^2(\omega/\omega_c^2)}{(1-m^2)(\omega/\omega_c^2)-1}\right) \tag{2.29}$$

[28] It can be proven by cascading two *L* sections and computing the resultant chain matrix parameters.

[29] The parameter *m* is such that for *m*=1 the *m*-derived section reduces to a *constant-k* filter.

which denotes a passband extended in the range [0, ω_c], as the constant k derived filter but with a much more abrupt transition above the cutoff frequency due to the action of the series LC circuit in the shunt arm providing a transmission zero at the resonant frequency $\omega_0=\omega_c/\sqrt{(1-m^2)}$ [103] as qualitatively indicated in Fig. 2.15. Moreover a smoother frequency response is obtained throughout the bandwidth, which justifies the use of m-derived half sections as buffer stage to match an artificial transmission line (constituted by cascaded constant-k filters sections) to a resistive load. The mid-shunt impedance function for the m-derived half section is given by:

$$Z_{0\pi m} = \sqrt{\frac{L}{C}} \cdot \frac{1-(\omega/\omega_0^2)}{\sqrt{1-(\omega/\omega_c^2)}}, \quad \omega_0^2 = \frac{\omega_c}{\sqrt{1-m^2}} \tag{2.30}$$

In fact, choosing m=0.6 the mid-shunt impedance is kept constant at the nominal value $Z_0=\sqrt{L/C}$ in more than 85% of the passband, improving the wideband matching.

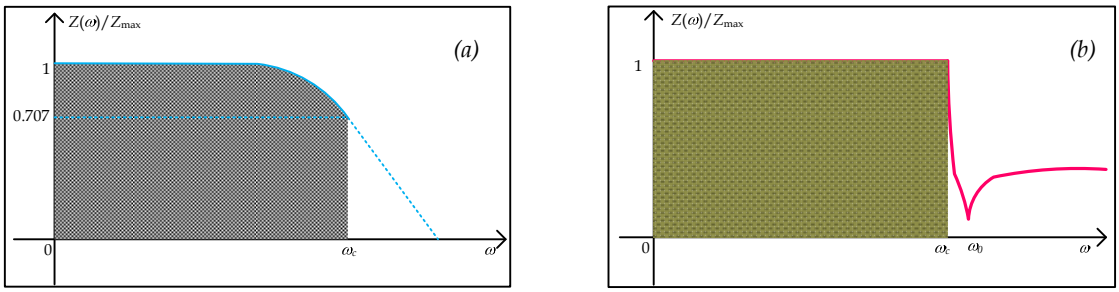

FIGURE 2-15. Qualitative filter response for constant-k (*a*) and m-derived (*b*) filter sections.

2.4.4 Distributed Amplifier Employing Artificial Transmission Lines

The transmission properties analyzed in the former section constitute the basis for the investigation of the distributed amplifier employing unilateral FET devices and lossless transmission networks. The distributed amplifier is seen to be composed by two artificial transmission lines[30], which are coupled by the action of the transconductance of the FETs. Due to the unilateral FET models here employed, once the signal is fed to the gate line, it progressively gets amplified in the drain line, as each section gets subsequently excited, but without any possibility for the output signal to be transferred back to the input line. Therefore the distributed amplifier analysis can be simplified by studying the signal propagation separately for the gate line and the drain line (decoupled analysis) separately shown in Fig. 2.16.

The input cell is formed by the C_{gs} capacitance (in the shunt arm) and the gate line inductance L_g (in the series arm), constituting a constant-k filter section with propagation factor γ_g. Analogously, the drain line comprises several sections with propagation factors γ_d made up of the

[30] Thanks to the scaling possibility they offer, periodically, capacitive-loaded, *uniform transmission line sections* are normally used in place of the cascaded *constant–k* or *m-derived* filters constituted by artificial transmission lines. Their analysis is carried out in [101]. Uniform transmission lines, are however designed in a manner such that the inductive effect prevails over the capacitive one. Using microstrip lines over a dielectric substrate, a good approximation is obtained by using electrically short ($l < \lambda/7$, λ is the wavelength corresponding to the highest frequency of the signal) sections possessing high impedance (compared with the nominal load impedance). The residual capacitance which is considered lumped at the two ends of each section, can be easily accounted for as detailed in next section.

C_{ds} capacitance (in the shunt arm) and the drain line inductance L_d in the series arm[31] . The output (voltage controlled) current sources at each section in the output line are responsible for conveying the signal from the input to the output line. The input signal is fed into the gate line and is distributed across the active devices, eventually vanishing in the gate line termination Z_{og}. Through the action of the FETs transconductance the voltage signal in the gate line is converted to a current and unilaterally coupled at the drain line, which propagates in opposite directions. Forward waves, which travel down the drain line, gets amplified as it passes through each section and finally are delivered two the output load. Backward waves instead interfere destructively ad are absorbed at the line termination[32] Z_{od} [125].

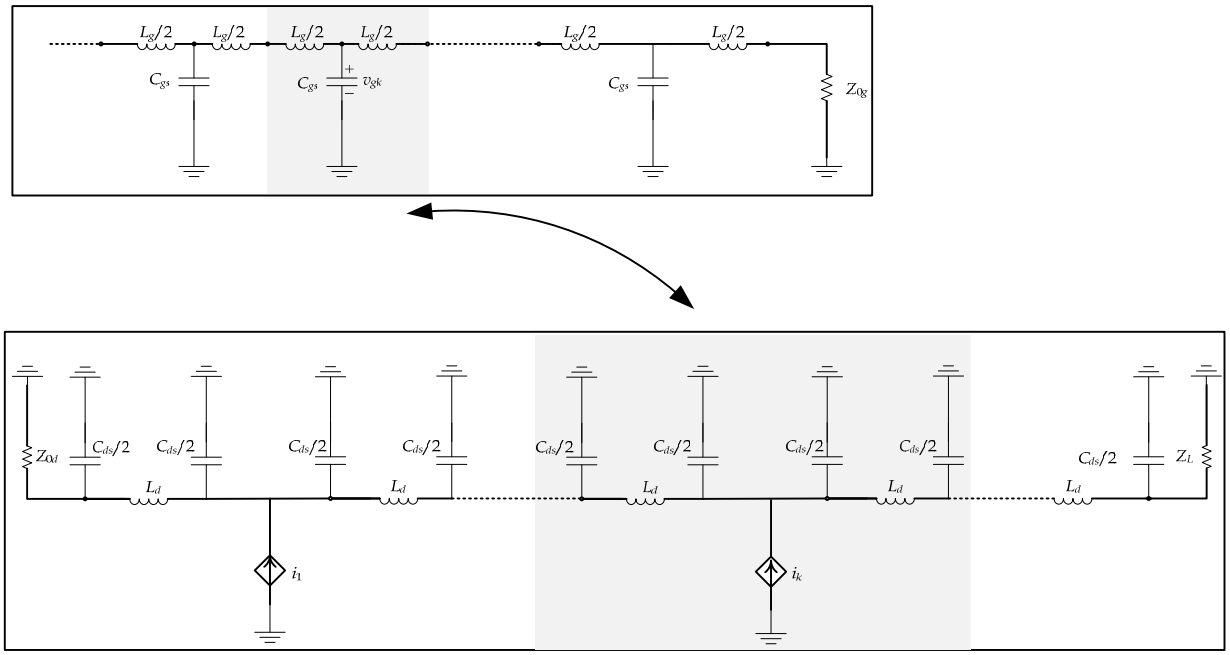

FIGURE 2-16. Small signal analysis of the FET distributed amplifier. Neglecting the internal FET C_{gd} feedback capacitance, the analysis can be effectively decoupled, considering the voltage at the *k*-th device, in the gate line exciting a current in drain line due to the action of transconductance, which superimpose with analogous contributions coming from the remaining devices.

Considering the input voltage at the *k*-th node of the input line from (6.8) follows that:

$$v_{gk} = V_{in}\sqrt{\frac{Z^g_{o\pi}}{Z^g_{oT}}}e^{-(k-1/2)\gamma_g} \tag{2.31}$$

which, due to the transconductance of the FET causes a current to flow in the output line given by:

$$i_k = -g_m v_{gk} \tag{2.32}$$

that propagates *to the left* (backward wave, *towards the absorbing termination*) and *to the right* (forward wave, *towards the load*) of the *k-th device*.

[31] In order to achieve the same propagation factors for both the gate and the drain line, is possible to choose L_g=L_d. However, since the gate(input) FET capacitance C_{gs} is higher than the drain (output) capacitance C_{ds} an additional capacitor needs to be placed in the drain line having a value of C_p=C_{gs}-C_{ds} to the aim of obtaining γ_g = γ_d.

[32] As a further simplification, let us assume that the input/output ATLs are perfectly matched. Mismatch analysis has been considered first by Ginzton in [56] and is reviewed in [101]. In practice, buffer (*m-derived*) sections are usually placed before any resistive termination to provide *broadband matching*.

The current in the output line is obtained by superposition of the individual contributions in (2.32). Considering only the currents wave travelling towards the load:

$$I_{out} = \frac{1}{2} \cdot \sum_{k=1}^{N} i_k e^{-\gamma_d (N-k)} \tag{2.33}$$

the corresponding voltage developed at the output load will be[33]

$$V_{out} = \frac{1}{2} Z_{od} I_{out} e^{-\gamma_d / 2} \tag{2.34}$$

Substituting (2.31—2.33) in (2.34) and considering (2.24), (2.26) the output voltage can be written as:

$$V_{out} = -\frac{V_{in} g_m}{2} \sqrt{\frac{Z_{o\pi}^g}{Z_{oT}^g}} \sqrt{Z_{o\pi}^d Z_{oT}^d} e^{(\gamma_g - \gamma_d)/2} e^{-N\gamma_d} \sum_{k=1}^{N} e^{(\gamma_g - \gamma_d)k} \tag{2.35}$$

The voltage gain can be easily obtained dividing the (2.35) by V_{in} and supposing that the two lines are phase synchronized with $\gamma_g = \gamma_d = \gamma$;

$$\begin{aligned} A_V &= \frac{V_{out}}{V_{in}} = -\frac{N g_m}{2} \frac{1}{\sqrt{1 - \omega^2 / \omega_c^2}} \sqrt{\frac{L_d}{C_d}} e^{-N\gamma_d} \\ \sqrt{\frac{Z_{o\pi}^g}{Z_{oT}^g}} &= \frac{1}{\sqrt{1 - \omega^2 / \omega_c^2}}; \quad \sqrt{Z_{o\pi}^d Z_{oT}^d} = \sqrt{\frac{L_d}{C_d}}; \; \gamma_g = \gamma_d, \; \sum_{k=1}^{N} e^{(\gamma_g - \gamma_d)k} = N \end{aligned} \tag{2.36}$$

From (2.36) is evident the main feature of the distributed amplifier voltage transfer function, which is to depend linearly on the active sections being used and exhibiting a passband that extends from DC to the cutoff frequency ω_c. The power gain can be obtained by definition as:

$$\begin{aligned} G &= \frac{P_{out}}{P_{in}} = \frac{\frac{1}{2} |I_{out}|^2 \, \mathrm{Re}(Z_L^d)}{\frac{1}{2} \left| \frac{V_{in}}{Z_{oT}^g} \right|^2 \mathrm{Re}(Z_{oT}^g)} = \frac{N^2 g_m^2}{4(1 - \omega^2 / \omega_c^2)} \sqrt{\frac{L_g L_d}{C_g C_d}} e^{-2N\gamma} \\ \gamma_g &= \gamma_d = \gamma; \quad \omega_c = 2 / \sqrt{L_g C_g} \\ Z_{oT}^g &= \sqrt{\frac{L_g}{C_g} \left(1 - \omega^2 / \omega_c^2\right)}; \; Z_L^d = \sqrt{\frac{L_d}{C_d}} \end{aligned} \tag{2.37}$$

in which the phase synchronization condition is required as before, but the two transmission networks may present different image impedances [101]-[103].The power gain is seen to depend *quadratically* on the number of sections, which would suggests that increasing N indefinitely would always be beneficial.

[33] The factor ½ in the magnitude derives from considering only the contributions due to *forward* currents flowing towards the load, neglecting the backward currents absorbed by the drain-line termination. The $\gamma_d/2$ factor for the phase is obtained accounting for the last half-section contribution in the drain line.

The analysis carried out so far was based on idealistic hypothesis, leading to an extremely simplified model in which it was assumed to operate with perfect match in the input/output line and loss-free transmission networks/devices. The impact of the mismatches[34] due to practical m-derived half section terminations and the losses in the lines/active devices on the performance of the distributed amplifier can be evaluated separately. To investigate on the effect of losses when conceiving a FET distributed amplifier, a more sophisticated transistor model is considered, in which the input ports contains the capacitance C_{gs} in series with a resistance R_{gs} and similarly at the output port, in which a resistance R_{ds} shunts the output capacitance C_{ds} and the voltage controlled current source (Fig. 2.17).

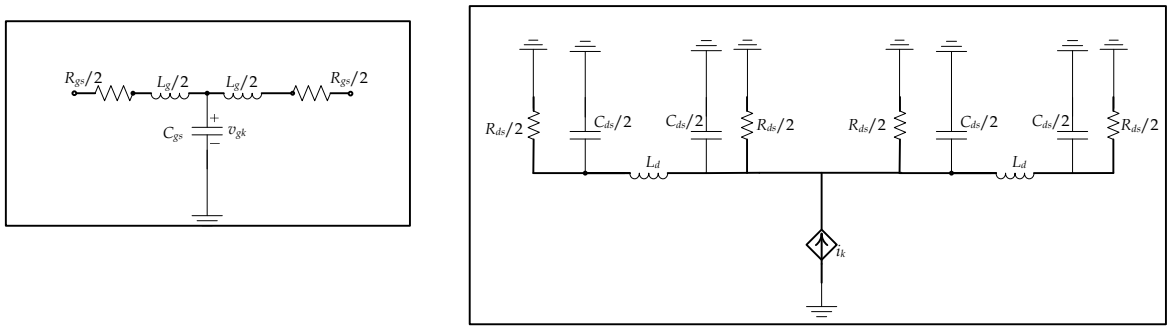

FIGURE 2-17. Lossy models of the input and output port for a generic FET device in a distributed amplifier.

Following the same line of reasoning that led to the loss-free expression for the distributed amplifier gain, the expression for v_{gk} is derived:

$$v_{gk} = V_{in}\sqrt{\frac{Z^g_{o\pi}}{Z^g_{oT}}}e^{-(k-1/2)\gamma_g}\cdot\frac{1}{1+j\omega C_{gs}R_{gs}} = \frac{V_{in}}{\sqrt{\left(1-\omega^2/\omega_c^2\right)\left(1+\omega^2/\omega_g^2\right)}}e^{-(k-1/2)\gamma_g - j\theta_g} \tag{2.38}$$

$$\omega_g = 1/(R_{gs}C_{gs}),\ \omega_c = 2/\sqrt{(L_gC_{gs})},\quad \theta_g = \tan^{-1}(\omega/\omega_g)$$

as the current in the drain line is related to (2.33) by the (2.34) and (2.35) and taking into account (2.26) (appendix B):

$$I_{out} = \frac{1}{2}\sqrt{\frac{Z^d_{o\pi}}{Z^d_{oT}}}\cdot\sum_{k=1}^{N} i_k e^{-(N-k+1/2)\gamma_d} = = -\frac{g_m V_{in}}{2\sqrt{\left(1-\omega^2/\omega_c^2\right)\left(1+\omega^2/\omega_g^2\right)}}\sqrt{\frac{Z^d_{o\pi}}{Z^d_{oT}}}e^{-j(N\beta_g+\theta_g)}e^{-(N/2)(\alpha_g+\alpha_d)}\frac{\sinh(N(\alpha_d-\alpha_g)/2)}{\sinh((\alpha_d-\alpha_g)/2)} \tag{2.39}$$

$$\gamma_g = \alpha_g + j\beta_g; \qquad \alpha_g \neq \alpha_d,\ \beta_g = \beta_d; \qquad \gamma_d = \alpha_d + j\beta_d$$

and recalling the definition of gain in (2.37) and substituting the values for the drain line image impedances we have the following approximation:

[34] Mismatches at the ending sections are known to deteriorate the "flatness" of the frequency response, creating peaks in the frequency response [113]-[122].

$$G \approx \frac{g_m^2\sqrt{\left(L_d/C_d\right)\left(L_g/C_g\right)}}{4\left(1-\omega^2/\omega_c^2\right)\left(1+\omega^2/\omega_g^2\right)} e^{-N(\alpha_g+\alpha_d)} \frac{\sinh^2[N(\alpha_d-\alpha_g)/2]}{\sinh^2[(\alpha_d-\alpha_g)/2)]} \tag{2.40}$$

Therefore, losses are shown to have a profound impact on the achievable gain. First, the gain depends *nonlinearly and non-monotonically* on the number of section through exponential functions. By maximizing the gain in (2.40) with respect to the variable N by looking for zeros of $\partial G/\partial N$, the optimal number of section is obtained:

$$\begin{gathered}\frac{\partial G}{\partial N} \approx -\frac{e^{-(\alpha_d+\alpha_g)N}\left(\left(\alpha_d+\alpha_g\right)\sinh^2\left(\frac{\left(\alpha_d-\alpha_g\right)N}{2}\right)+\left(\alpha_g-\alpha_d\right)\cosh\left(\frac{\left(\alpha_d-\alpha_g\right)N}{2}\right)\sinh\left(\frac{\left(\alpha_d-\alpha_g\right)N}{2}\right)\right)}{\sinh^2\left(\frac{\alpha_d-\alpha_g}{2}\right)} = 0 \\ \Downarrow \\ N_{opt} = \left\lfloor \frac{\ln(\alpha_d/\alpha_g)}{\alpha_d-\alpha_g} \right\rfloor\end{gathered} \tag{2.41}$$

clearly demonstrating that any additional section to N_{opt} results in worsening of the amplifier performances due to additional losses, which is detrimental to the amplifier gain. Second, the losses in the circuit deteriorate the frequency response at the low end of the passband, due to the term $\omega_d=(1/R_{ds}C_{gs})$ in the drain line for the amplifier having a low frequency pole determining an high pass behavior. Therefore, a careful selection of the parameters N, ω_{gl}, ω_d, ω_c is needed to have a flat frequency response from DC to the lowpass cutoff frequency

2.4.5 Distributed Amplifier using Periodically Loaded Transmission Lines

Usually a distributed amplifier is implemented having recourse to microstrip lines on a dielectric substrate as the input/output transmission networks, which are periodically loaded by the active devices [126]–[133] according to the schematic in Fig. 2.18. The effect of the *unilateral active coupling* between the two transmission networks can be studied analogously to the former case. The effect of the lumped parasitic FET capacitances is considered as if they were *continuously distributed across each section*. Therefore, given the length of each gate/drain section (l_g and l_d *chosen by design*), introducing the *associated parasitic capacitance per unit length* is $c_{gs}= C_{gs}/l_g$, $c_{ds}= C_{ds}/l_d$, (C_{gs} and C_{ds} are known by the manufacturer model) the *loaded* lines are propagation factors and image impedances are:

$$\begin{aligned}\gamma_g &= j\beta_g \cong j\omega\sqrt{L_g\left(C_g+\frac{C_{gs}}{l_g}\right)} \;\; ; \;\; Z_o^g \approx \sqrt{\frac{L_g}{C_g+C_{gs}/l_g}} \\ \gamma_d &= j\beta_d \cong j\omega\sqrt{L_d\left(C_d+\frac{C_{ds}}{l_d}\right)} \;\; ; \;\; Z_o^d \approx \sqrt{\frac{L_d}{C_d+C_{ds}/l_d}}\end{aligned} \tag{2.42}$$

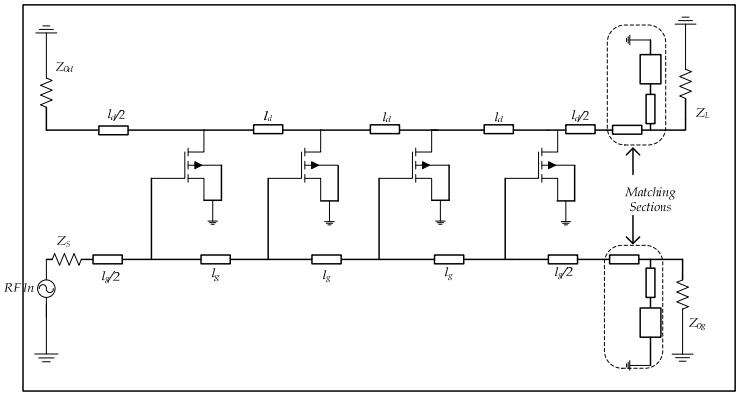

FIGURE 2-18. Distributed Amplifier employing uniform transmission lines

where (L_g, C_g, L_d, C_d) represent the *unloaded and lossless* lines distributed parameters, which can be derived by knowing the line *S*-parameters and apply a parameter extraction process/fitting algorithm [50]. The output current flowing through the load is obtained integrating the distributed current contributions on the drain line over the total output line length. To keep track of the propagation in the two lines, two different coordinates ξ_g and ξ_d are used. Since the input and output line length can be different, but the anchor points at which the FETs are attached are evenly spaced, therefore: $\xi_g/l_g = \xi_d/l_d$. Using this notation, the distributed current source evaluated at position ξ_d *in the drain line* due to the gate voltage measured at coordinate ξ_g *in the gate line* is (assuming a unitary voltage generator is in place):

$$i_s(\xi_d) = -\frac{g_m v_g(\xi_g)}{l_d} = -\frac{g_m e^{-j\beta_g \xi_g}}{l_d} = \frac{g_m e^{-j\beta_g (l_d/l_g)\xi_d}}{l_d} \tag{2.44}$$

and integrating all these elementary contributions we obtain the output current as:

$$I_{out} = \int_o^{N_{ld}} i_s(\xi_d) e^{-j\beta_d (N_{ld} - \xi_d)} d\xi_d \tag{2.45}$$

Knowing that the voltage appearing at the output load is due to the forward current component:

$$V_L = Z_o^d \frac{I_{out}}{2} \tag{2.46}$$

and computing the integral in (2.45) from (2.46) the voltage transfer ratio is readily obtained:

$$A_v = -\frac{g_m Z_o^d}{2}\left[\frac{e^{-jN\beta_g l_g} - e^{-jN\beta_d l_d}}{j(\beta_d l_d - \beta_d l_d)}\right] \tag{2.47}$$

If the phase synchronization condition is enforced ($\beta_g l_g = \beta_d l_d$)

$$A_v = -\frac{N g_m Z_o^d}{2} e^{-jN\beta_g l_g} \tag{2.48}$$

arriving at a conclusion analogous to (2.37), showing a linear increase for the amplification factor with the number of section, and a passband dictated by the *impedance frequency response* associated to the periodically loaded drain line [101]-[103]. Losses are taken into account as in the case of a distributed amplifier employing artificial transmission lines, leading to a modification of (2.40) in which the phase constants β_g, β_d have to be replaced by the complex propagation factors γ_g, γ_d. They are conveniently expressed in terms of *resistance or conductance per unit section*, and promptly included in the definition of the propagation factors of the gate and the drain lines (2.42):

$$\begin{aligned} \gamma_g &= \sqrt{j\omega L_g \left(j\omega \left(C_g + \frac{j\omega c_{gs}}{1 + j\omega r_{gs} c_{gs}} \right) \right)} \\ \gamma_d &= \sqrt{j\omega L_d \left(j\omega (C_d + c_{ds}) + 1/r_{ds} \right)} \end{aligned} \tag{2.49}$$

whereas the amplification factor given by (2.36), has to be modified to consider complex propagation factor $\gamma_g = \alpha_g + j\beta_g$, $\gamma_d = \alpha_d + j\beta_d$. Substituting them into (2.36) and provided that the phase matching condition is met in both the gate and the drain lines ($\beta_g l_g = \beta_d l_d$) is obtained:

$$A_v = -\frac{g_m Z_o^d e^{-jN\beta_g l_g}}{2} \left[\frac{e^{-N\alpha_g l_g} - e^{-N\alpha_d l_d}}{(\alpha_d l_d - \alpha_d l_d)} \right] \tag{2.50}$$

which represent the voltage transfer ratio of the distributed amplifier with losses. To obtain the gain function (expressing the input/output power gain), it is sufficient to take the square of the previous expression and multiply for the inverse ratio of the input to output impedances in the hypothesis of perfect match[35]:

$$G \cong \frac{g_m^2 Z_o^d Z_o^g}{4} \left| \frac{e^{-N\alpha_g l_g} - e^{-N\alpha_d l_d}}{(\alpha_g l_g - \alpha_d l_d)} \right|^2 \tag{2.51}$$

Deriving with respect to N and setting the derivative equal to zero, the optimal number of sections is found (constant terms are omitted in the derivative):

[35] $G = P_{out}/P_{in} = (V_{out} I_{out}/V_{in} I_{in})$ but $I_{out} = (V_{out}/Z_d)$; $I_{in} = (V_{in}/Z_g)$ then $G = (A_v)^2 * (Z_g / Z_d)$.

$$\frac{\partial G}{\partial N} = -\left(\left(-2\alpha_d l_d - 2\alpha_g l_g\right)e^{\left(\alpha_d l_d + \alpha_g l_g\right)N} + 2\alpha_g l_g e^{2\alpha_d l_d N} + 2\alpha_d l_d e^{2\alpha_g l_g N}\right)e^{-\left(2\alpha_d l_d + 2\alpha_g l_g\right)N} = 0$$
$$\Rightarrow \qquad N_{opt} = \frac{\ln(\alpha_d l_d) - \ln(\alpha_g l_g)}{\alpha_d l_d - \alpha_g l_g} \tag{2.52}$$

The optimum number of sections is determined by the attenuation characteristics in the input and output lines, analogously to the previous case.

2.5 DISTRIBUTED VOLTAGE CONTROLLED OSCILLATORS.

The distributed amplification concept has led to the development of different circuits/systems, which are particularly suitable in light of the applications for RF front ends[36] as well in high speed digital integrated circuits. Two considerations made immediately appealing the distributed oscillator topology as inherited from the distributed amplifier. First, the possibility of exploiting planar technology/process for implementing microwave oscillators in integrated form Second, the opportunity offered by the relaxed gain-bandwidth constraint of the Distributed Amplifiers (see §2.4), for which several active devices are enabled to concurrently operate at high-frequencies (with operational frequency close to the device transition frequency f_T), without trading-off the bandwidth for gain[37].

Schematically, a distributed oscillator (an example in Fig. 2.19) consists of a distributed amplifier provided with a feedback path which serves to inject output-line propagating waves back into the input line [75—77], [83—87]. There are essentially two options for devising it. A feedback loop for *forward travelling waves* is created by connecting the output line with the input line, after the removal of the load resistor Z_L, (picture) giving rise to the *forward gain mode distributed oscillator*. Conversely, an alternative feedback path could be conceived by taking advantage of the backward scattered waves towards the absorbing resistor Z_o^d forcing them to reenter the input line, having previously disconnected the resistive termination, thereby creating a *reverse gain mode distributed oscillator* [72—74], [88, 99].These two topologies will be subsequently analyzed. In particular, it will be shown that the reverse mode distributed oscillator could be converted to a very broadband VCO in a straightforward manner.

[36] For instance, after having envisioned the FET distributed amplifier in monolithic form, distributed mixer architectures requiring only slight modifications to the original distributed amplifier topology where fostered see §2.4

[37] A really important features in silicon CMOS devices is that they usually posses a smaller f_T when compared with FETs. As the operational frequency gets close to the device frequency limit f_T (transition frequency) the gain of each FET device approaches unity. If it is required to operate with frequencies $f > f_T$ *the gain would drop below unity*. However, since in a distributed amplifier the total gain corresponds to the sum of the individual sections gains, is still possible to have gain greater than one and yet operate near the maximum frequency threshold.

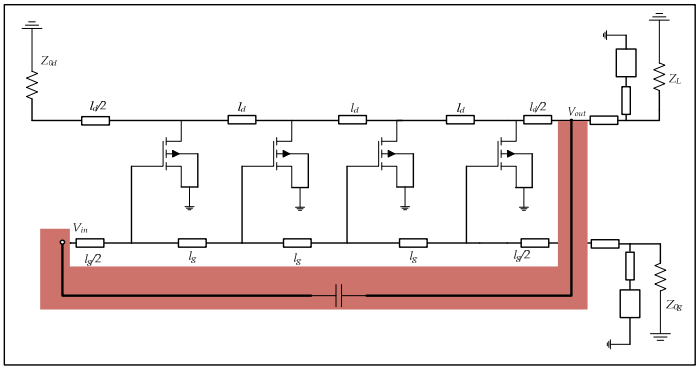

FIGURE 2-19. A forward gain mode distributed oscillator. Waves in the drain line re-injected into the gate line by means of a suitable feedback path.

2.5.1 FORWARD-GAIN MODE DISTRIBUTED OSCILLATOR THEORY

Although chronologically the first distributed oscillator was invented exploiting the reverse gain of a distributed amplifier, the forward gain mode distributed oscillator is introduced first, since it's operation principle could be inferred immediately from the considerations made in section 2.4

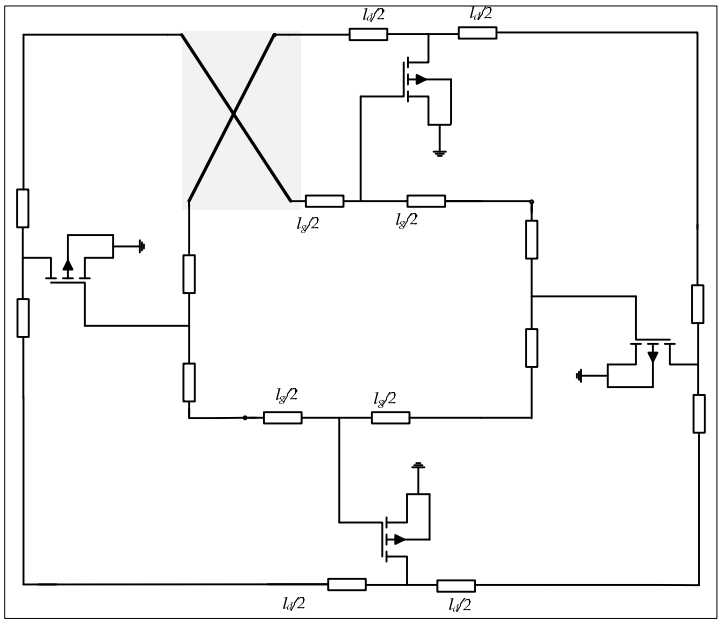

FIGURE 2-20. Forward Gain mode Distributed Oscillator based on a ring topology and presenting cross connected gate and drain line as a mean to establish a feedback path

As already observed, the forward gain mode distributed oscillator is almost entirely derived from the distributed amplifier structure, the only differences being the insertion of the feedback path between the input/output lines and the removal of unnecessary loading element, as sketched in Fig. 2.19. The active devices are generally biased choosing the same gate and drain voltage level and it is kept constant, ensuring that each FET device is working in the active zone [77—79]. Intuitively, oscillator operation is based on the regeneration of that signal *whose period results comparable with its round trip time* through the closed-loop circuit, and thus dependent upon its *feedback path length*; the shorter it is, the higher the attainable frequency [75] becomes. Laying this circuit out using the *conventional linear topology for the open-loop distributed amplifier (from which*

the distributed oscillator follows) while seeking its feedback path length minimization it's a nearly impossible task. For this reason *ring topologies* are preferred; in concrete implementations the distributed amplifier topology *is wrapped around itself*, creating an *annular loop* [75—76], [80], [86]. A feedback path then is simply created by connecting crosswise the output line with the input line, and vice versa (provided the two lines are perfectly matched, $Z_o^g = Z_o^d$ and all the resistive loads are effectively removed). This architecture is seen to provide benefits for high speed digital electronics (for clock-distribution circuits) [80] or RFIC circuit employing lower-f_T devices like silicon CMOS as highlighted in [75] .

The results presented on the work , relative to a BICMOS forward gain mode distributed oscillator[38] provide a first order estimate of the oscillation frequency and output signal amplitude, based on the calculation of the closed-loop transfer function for the feedback distributed amplifier [134]. Assuming the electrical length of the feedback path is sufficiently small, the output and the input voltage can be regarded as identical. Therefore using the formula (2.36) it can be stated that:

$$A_v\big|_{\text{closed-loop}} = -Ng_m(Z^b \,||\, Z^c)e^{-jN\gamma_c l_c} = 1 \tag{2.53}$$

which is derived from (2.36) substituting the factor $Z_o^d/2$ with the parallel impedance of the base line (input line, Z^b) and the collector line (output line, Z^c) and accounting for losses in the output line with a complex propagation factor $\gamma_c = \alpha_c + j\,\beta_c$. The (2.53) is a complex equation; hence it can be split in its real and imaginary part

$$\begin{aligned} &\text{Re}(A_v\big|_{\text{closed-loop}}) = Ng_m(Z^b \,||\, Z^c)\cdot e^{-jN\alpha l} = 1 \\ &\text{Im}(A_v\big|_{\text{closed-loop}}) = e^{-jN\beta l} = -1 \qquad\qquad (\gamma_b l_b = \gamma_c l_c \Rightarrow \gamma_b = \gamma_c = \gamma;\;\; l_b = l_c = l) \end{aligned} \tag{2.54}$$

in which both the complex propagation factors and the length of each transmission line sections in the base and collector line are for simplicity supposed to be identical. From the imaginary part of the closed loop function it follows that $N\beta l = \pi$. Recalling the definition of β *in terms of the group velocity and the frequency of the signal* [103], $\beta = 2\pi f / v_{group}$ the second equation of (2.54) provides:

$$f_{osc} = \frac{v_{group}}{2Nl} \tag{2.55}$$

showing that the *oscillation frequency is determined by the time the signal needs to return to the starting point, completing a cycle*. The real part in (2.54) determines the output voltage amplitude, as long as the relation $g_m = g_m(V_o)$ *is known and the bias currents* I_c *are kept fixed* [78, 79] The expression for $g_m(V_o) = 2I_c/V_o$ substituted in the first of (6.37) provides:

[38] In what follows the input line, will be named also *base line*, and the output line will be termed *collector line*, since bipolar devices are involved.

$$V_o = \frac{2I_c}{g_m} = 2NI_c(Z^b \,||\, Z^c)\cdot e^{-j\alpha Nl} \tag{2.56}$$

affected, as the intuition suggests, by the *losses in the line* and determined by the current bias level in the output line and equivalent impedances.

This oscillator is capable of being tuned by a patented method. Essentially, having more active devices per section and acting properly on their bias currents is possible to alter the electrical length of the signal path, thus modifying the oscillation frequency according to (2.55). Tuning ranges of up to 26% fractional bandwidth (9.6 - 12.45 GHz) have been reported, good phase noise figure (-104 dBc/Hz at 1 MHz offset from the 11.7 GHz carrier), and low DC voltage- currents (2.2 V, 1.6 mA).

Another possible solution to implement the tuning functionality in the forward gain mode distributed oscillator is to include a varactor in feedback loop [83, 84]. The voltage across the nonlinear capacitor has an impact on the imaginary part of the closed loop transfer function (*its phase*) and therefore on the oscillation frequency, which can be continuously swept in a narrow range.

Furthermore, it has been recently proposed to decouple the design of a Distributed Oscillator, considering two separate blocks (as the very elemental oscillator theory implies[39]) interconnected by a feedback loop; a distributed amplifier, providing gain across a wide frequency band and a capacitive filter bank, selecting the oscillation frequency by adjusting the phase at which the closed loop gain becomes one [135]. This technique has the advantage of the ease of implementation, and offers respectable tuning range as well as the possibility of having a coarse or fine tuning [90—93] mode selection, however it doesn't allow for compact designs as in [75—80].

2.5.2 Reverse-Gain Mode Distributed Oscillator Topology.

A different oscillator topology can be derived from the *N*-th sections distributed amplifier. It can be noticed that a feedback path for the backward travelling waves in the output line is immediately available, if one consider disconnecting the Z_o^d termination and connecting the input and the output line together as schematically shown in picture 2.21 [72]. The backward scattered waves in the output line are enabled to reenter the input line, and oscillations can be triggered if the *amplifier reverse gain*, defined as the ratio of *power reentering the input line*, to the available *power on the output line*, gets substantially greater than unity at a frequency for which the closed loop phase response equals 2π [72—74], [104] [109]. The reverse gain of the distributed amplifier increases as the sections are separately turned on [72—74]. Although the distributed amplifier topology is preserved, a *different biasing scheme*[40] is thus required for proper operation. Hence, activating consecutively each section and

[39] An oscillator is essentially constituted by an amplifier with a positive-feedback frequency selective network [109].

[40] In fact, a typical distributed amplifier (*in which all the sections are activated simultaneously*), presents a poor residual reverse gain due to the mutual cancellation of the backward travelling waves in the output line [4], which is made small by design.

leaving the remaining ones turned off[41], discrete resonances falling in the amplifier passband[42] can be excited, with oscillation frequencies depending *on the electrical length of the active feedback loop path*.

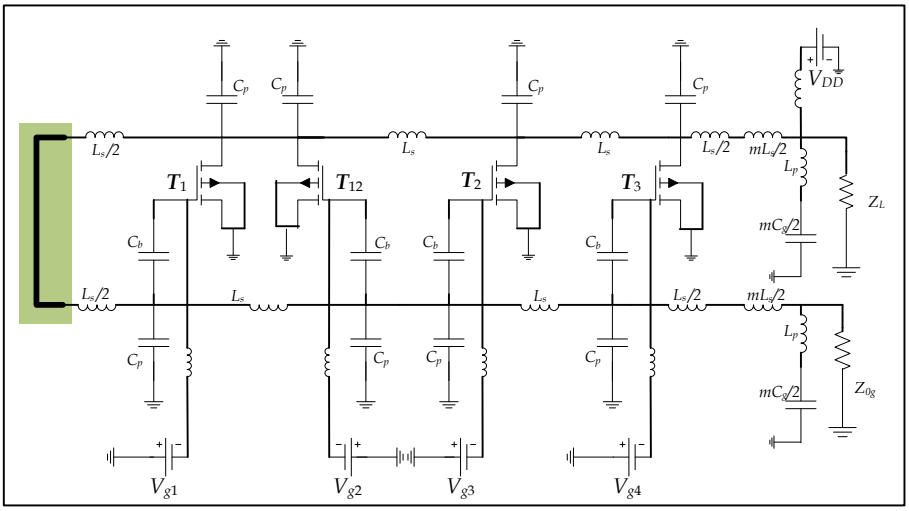

FIGURE 2-21. Reverse Gain based Distributed Voltage Controlled Oscillator Topology.

As a consequence, the *highest oscillation frequency* (*closer to the upper bound of the amplifier passband*) is obtained activating the *first section*, achieving a *minimum – length feedback path*; complementarily the *lowest oscillation frequency* (closer to the *lower bound of the amplifier passband*) is found when *turning on the last* (N^{th}) *section*, when the actual length of the feedback path is *maximum*. In between the oscillation frequencies associated with the first and the last, N-2 additional resonances are observed in the output spectrum, obtained by *turning on each section* $\boldsymbol{T}_k$ (k=2, 3,…,N-1) at a time, with a decreasing frequency (from the *second* to the *second to last*) according to the following scheme $f_1 > f_2 > \ldots > f_{k-1} > f_k > f_{k+1} > \ldots > f_{N-1} > f_N$. Moreover, as it was demonstrated in [72] using small signal equivalent FET models, linear analysis and CAD models, this circuit is seen to deliver a continuous tuning across the distributed amplifier passband, making it a multi-GHz distributed VCO (DVCO). The tuning is obtained by differentially biasing the active section in pairs ($\mathbf{T}_k$, $\mathbf{T}_{k+1}$), in such a way that one device is led towards interdiction and concurrently the subsequent one is driven to saturation. As a result of the net change in total transconductance, the small signal, reverse gain phase

[41] Activating a device means biasing it with adequate DC voltage levels at the input (gate) and at the output port to cause its transconductance g_m to become (much) greater than one. Since the devices used are FET connected in common source configuration, the voltages considered are V_{DS}, V_{GS}. One could choose to activate a section: *i)* by changing V_{GS}, keeping V_{DS} fixed; *ii)* by changing V_{DS}, keeping V_{GS} fixed; *iii)* by changing both V_{GS} and V_{DS}. In the following, only the option *i) will be considered;* the drain voltage is kept constant (and *positive*) and distributed at the active devices via the output line The gate voltage (*which is usually negative, for depletion FET*) thus determines the activation or the interdiction of each section; for a positive V_{DS} (typically +2V) the values of gate voltages V_{GS} ranges (normally) in [-1V, 0V].

[42] Amplifier passband is determined by the Impedance function associated with the *periodically loaded transmission structure*, as pointed out in earlier section.

condition for triggering oscillation is fulfilled[43] at an intermediate frequency within the interval $[f_{k+1}, f_k]$.

The reverse gain distributed oscillator analysis is based on the assumption that, at oscillation buildup, the signals exciting the active devices could be regarded as small perturbation around a *quiescent point* (biasing point). Therefore all the parameters of the intrinsic active devices (generally pHEMT or MESFETs) can be considered constant[44]. Moreover, for simplicity, the active devices will be considered lossless and unilateral. The transistor is modeled taking only into account its ability to transfer an input voltage (at its gate) to an output current (flowing through its drain) by means of its transconductance, and the reactive elements at the input /output port describing the parasitics due to the internal capacitances and the external inductances due to the active devices' packaging. The FETs periodically load the input/output line, determining a transmission network made up of cascaded *m*-derived filter sections[45] having a propagation factor that is purely imaginary[46] and equal for both the gate and the drain lines[47] to θ_m. Moreover, let us suppose that an extra element is inserted in the feedback loop, providing a phase shift[48] of ψ as illustrated in Fig. 2.22.

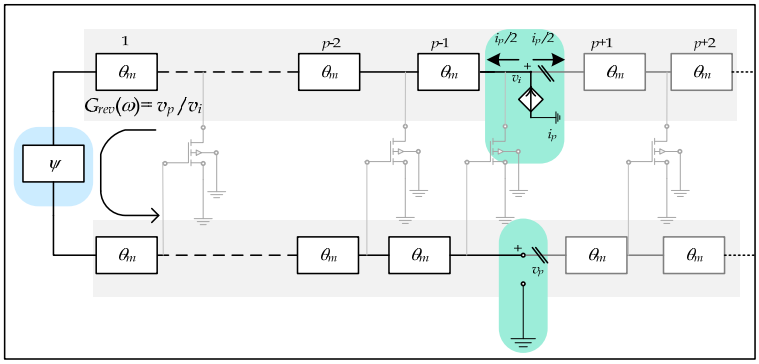

FIGURE 2-22. Reverse-mode Distributed Oscillator resonances small signal analysis, when only one section is active at a time.

[43] At the oscillation frequency, closed loop gain has to be unity, and the phase turns have to be an integer multiple of 2π.

[44] At oscillation start-up, the signal can be considered so small that simple linear relationships hold, involving currents flowing through the device and voltage at its ports. Moreover, the intrinsic parameters (most noticeably, g_m) are considered *constant;* in other terms they are not affected by the voltage/currents level at the device ports. *This argument does not stand* in normal operation (steady state oscillations) when a large-swing oscillating signal at microwave frequency is superimposed to a DC bias voltage, and more sophisticated nonlinear analysis tools are needed.

[45] If the FET parasitic inductance is not considered, the input/output line reduces to cascaded constant-k filter sections network.

[46] Since losses in this FET model are not accounted for, the waves in the gate/drain line can only experience a phase shift when passing through each section.

[47] Provided L_g=L_d it could be made equal for both lines by loading them with additional capacitances or choosing different width for the transmission line in each sections.

[48] This term accounts for additional phase rotation in the loop, due to a purposely inserted transmission line element providing a feedback path among the terminating half sections (on the left).

The small signal drain current[49] of the p-th ($1 \le p \le N$) FET i_p is a linear function of its input voltage v_p:

$$i_p = -g_{mp} v_p = g_{mp} v_p e^{-j\pi} \tag{2.57}$$

which gives rise to two symmetrical contribution ($i_p/2$ *flowing towards the load,* $i_p/2$ *flowing backwards through the feedback loop*) in the output line [72 — 74] [101, 102]. Each current contribution sees an impedance given by Z_{om}^{π}, *and therefore the voltage at the output port is:*

$$v_o\Big|_{\substack{\mathbf{T}_p \text{ on} \\ \mathbf{T}_q \text{ off} \\ p,q=1,\ldots,N \\ (q \neq p)}} = \frac{Z_{om}^{\pi}}{2} i_p \tag{2.58}$$

Cutting the loop as shown in picture, is possible to establish a relationship between the voltage v_i *at the input of the loop,* and the *p-th* gate voltage v_p ([50]) The total phase shift across the (p-1) sections[51] and the feedback loop is given by:

$$\vartheta = \sum_{h=1}^{(p-1)} \vartheta_h^d + \vartheta_f + \sum_{h=1}^{(p-1)} \vartheta_h^g \tag{2.59}$$

therefore, from the definition of the image propagation factor

$$\begin{aligned} & v_i = v_p e^{j(2p-1)\beta_m} \cdot e^{j\psi} \cdot e^{j(2p-1)\beta_m} \\ & \Rightarrow v_p = v_i e^{-j\left[2(2p-1)\beta_m - \psi\right]} \end{aligned} \tag{2.60}$$

which placed in (2.57) gives;

$$i_p = g_{mp} v_p e^{-j\pi} = g_{mp} v_i e^{-j\left[2(2p-1)\beta_m + \pi - \psi\right]} \tag{2.61}$$

and using the (2.60) the input and output voltage across the loop can be related:

$$v_o = \frac{Z_{om}^{\pi}}{2} i_p = \frac{Z_{om}^{\pi} g_{mp}}{2} v_i e^{-j\left[2(2p-1)\beta_m + \pi - \psi\right]} \tag{2.62}$$

which divided by v_i provides the reverse open loop voltage transfer ratio when only the *k-th* device is turned on:

---

[49] Different lowercase italics indices (*k,p,q,r,s)* every time denote *the active sections* ($\mathbf{T}_k$; $\mathbf{T}_p$; $\mathbf{T}_q$; $\mathbf{T}_r$; $\mathbf{T}_s$)with $k,p,q,r,s \le N$. According to the context, different sets of indices can be used to avoid ambiguous notations.

[50] The propagation factor of a cascaded connection of N-sections is equivalent to the sum of the individual propagation factors: $\theta_T = \theta_1 + \theta_2 + \ldots + \theta_N$. Notice that in general the propagation factors are frequency dependent (in case of lossless two ports they reduce to purely imaginary terms).

[51] Considering β_m as the propagation constant of an half section, a factor of 2 is needed to describe the phase change across a Π or T cell.

$$G_p^{rev}(\omega)=\frac{v_o}{v_i}\Big|_{\substack{\mathrm{T}_p\ \text{on}\\ \mathrm{T}_q\ \text{off}\\ p,q=1,\ldots,N\\ (q\neq p)}}=\frac{Z_{om}^{\pi}(\omega)g_{mp}}{2}e^{-j\left[2(2p-1)\beta_m(\omega)+\pi-\psi\right]} \tag{2.63}$$

and separating the magnitude and the phase components in (2.63) is obtained:

$$\begin{aligned} &G_p^{rev}(\omega)=\left|G_p^{rev}(\omega)\right|e^{-j\Theta(\omega)}\Rightarrow\\ &\left|G_p^{rev}(\omega)\right|=\frac{Z_{om}^{\pi}(\omega)g_{mp}}{2}\\ &\Theta(\omega)=\angle G_p^{rev}(\omega)=2\left(2p-1\right)\beta_m(\omega)+\pi-\psi \end{aligned} \tag{2.64}$$

From the last equation the small signal linear condition for triggering oscillations can be set as:

$$\begin{aligned} &G_p^{rev}(\omega)=\left|G_p^{rev}(\omega)\right|>1\\ &\Theta(\omega)=2a\pi\quad(a\in\mathbb{Z}) \end{aligned} \tag{2.65}$$

and plugging in the formulas giving the propagation factors for the *m*-derived section, the second of (2.65) which expresses the phase condition for achieving an oscillation, turns into:

$$2\left(2p-1\right)\arcsin\left(\frac{\omega}{\omega_c}\sqrt{\frac{m^2}{1-\frac{\omega^2}{\omega_c^{\,2}}(1-m^2)}}\right)+\pi-\psi=2a\pi\qquad(\omega\le\omega_c) \tag{2.66}$$

which can be used to find the oscillation frequencies:

$$\frac{\omega_{a,m,p,\psi}}{\omega_c}=\frac{\sin\left(\frac{(2a-1)\pi+\psi}{2(2p-1)}\right)}{\sqrt{m^2+(1-m^2)\sin^2\left(\frac{(2a-1)\pi+\psi}{2(2p-1)}\right)}} \tag{2.67}$$

The previous expression could be simplified in the case of a feedback loop obtained by joining the terminal half sections without inserting additional elements, setting $\psi=0$; in that case it could be shown that without loss of generality a=1 [72]

$$\frac{\omega_{m,p}}{\omega_c}=\frac{\sin\left(\frac{\pi}{2(2p-1)}\right)}{\sqrt{m^2+(1-m^2)\sin^2\left(\frac{\pi}{2(2p-1)}\right)}} \tag{2.68}$$

which depends only on the coefficient of the *m*-derived filter section, and on the position of the p^{th} device. Furthermore, neglecting the parasitic inductance in the shunt arm, the unit filter cell reduces to a constant-*k* filter which is the limit case of an *m*-derived section as *m* approaches one:

$$\frac{\omega_p}{\omega_c} = \sin\left(\frac{\pi}{2(2p-1)}\right) \qquad p = 1,\ldots,N$$
$$\left(\omega_c = 2\Big/\sqrt{L_g C_{gs}} = 2\Big/\sqrt{L_d C_{ds}}\right) \tag{2.69}$$

giving a first order estimate for the N *characteristic frequencies* (or *discrete resonances*) associated with *the various active paths obtained when turning on each transistor* $\mathbf{T}_p$ (p=1,…N) separately, provided that the cutoff frequencies in the drain/gate line are the same. It is worth mentioning that the (2.69) confirms the intuitive explanation regarding the appearance of discrete resonances proceeding in decreasing order as the various sections are gradually activated one at time, assuming that the magnitude of the loop voltage gain is always greater than one for that particular path.

2.5.3 Reverse-Gain Mode Distributed Oscillator Tuning: Linear Analysis.

In the previous section it was proven that it is possible to exploit the reverse gain of an N section feedback distributed amplifier to obtain a set of N discrete resonances, having characteristic frequencies allocated in the passband of the amplifier (from DC to the cutoff frequency ω_c), when each section is individually turned on, and whose frequencies decreases as each device T_p (p=1,2, …, N) get activated. Furthermore, in [72—74] was described the possibility of achieving a continuous tuning range by suitably biasing in the active region more than one device at a time. The tuning scheme is referred at *as complementary differential gate biasing*, since it operates among two *neighboring sections* in a such a way that if the section p is being activated, simultaneously the (p+1) section is being led to interdiction. As a result of this biasing strategy, it should be expected to observe *a continuously moving spectral line*, with a *frequency shift* from f_{p+1} to f_p. These statements can be demonstrated by having recourse to a first order analysis, analogously to the previous section.

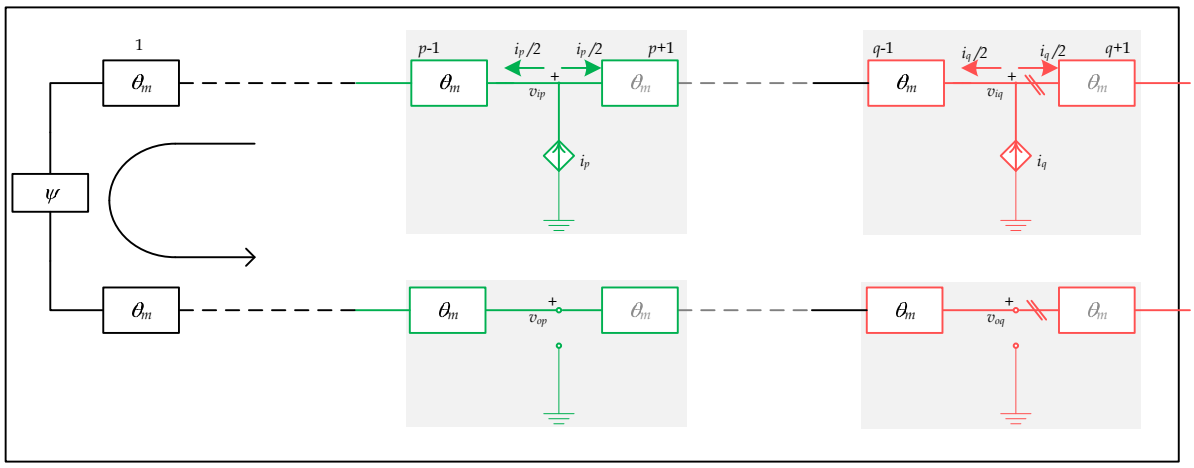

FIGURE 2-23. Linear analysis for evaluating DVCO tuning function.

Let us suppose that two transistors ($\mathbf{T}_p$,$\mathbf{T}_q$) are simultaneously operating while the other devices are interdicted (Fig. 2.23). The individual reverse voltage gain for $\mathbf{T}_p$ and $\mathbf{T}_q$ are obtained from (2.63) setting $2\beta_m=\beta$ and ψ=0:

$$G_p^{rev}(\omega)=\frac{v_o}{v_i}\Big|_{\substack{\mathbf{T}_p \text{ on}\\ \mathbf{T}_q \text{ off}\\ p,q=1,\ldots,N\\ (q\neq p)}}=\frac{Z_{om}^{\pi}(\omega)g_{mp}}{2}e^{-j\left[(2p-1)\beta(\omega)+\pi\right]}$$
$$G_q^{rev}(\omega)=\frac{v_o}{v_i}\Big|_{\substack{\mathbf{T}_p \text{ off}\\ \mathbf{T}_q \text{ on}\\ p,q=1,\ldots,N\\ (q\neq p)}}=\frac{Z_{om}^{\pi}(\omega)g_{mq}}{2}e^{-j\left[(2q-1)\beta(\omega)+\pi\right]} \tag{2.70}$$

and since the circuit behaves linearly, the superposition principle holds therefore:

$$G_{(p,q)}^{rev}(\omega)=\frac{v_o}{v_i}\Big|_{\substack{\mathbf{T}_p \text{ on}\\ \mathbf{T}_q \text{ on}\\ \mathbf{T}_r \text{ off}\\ p,q,r=1,\ldots,N\\ (r\neq q\neq p)}}=G_p^{rev}(\omega)+G_q^{rev}(\omega)\Rightarrow$$
$$G_{(p,q)}^{rev}(\omega)=\frac{Z_{om}^{\pi}(\omega)g_{mp}}{2}e^{-j\left[(2p-1)\beta(\omega)+\pi\right]}+\frac{Z_{om}^{\pi}(\omega)g_{mq}}{2}e^{-j\left[(2q-1)\beta(\omega)+\pi\right]} \tag{2.71}$$

i.e., the total reverse gain is the sum of the complex functions in (2.70). The magnitude and the phase are given by (see appendix C):

$$\left|G_p^{rev}(\omega)+G_q^{rev}(\omega)\right|=\frac{Z_{om}^{\pi}}{2}\sqrt{{g_{mp}}^2+2g_{mp}g_{mq}\cos\left(\beta(\omega)(p-q)\right)+{g_{mq}}^2}$$
$$\Theta_{(p,q)}(\omega)=\angle(G_p^{rev}(\omega)+G_q^{rev}(\omega))=\tan^{-1}\left(\frac{\left|G_p^{rev}(\omega)\right|\sin\Theta_p(\omega)+\left|G_q^{rev}(\omega)\right|\sin\Theta_q(\omega)}{\left|G_p^{rev}(\omega)\right|\cos\Theta_p(\omega)+\left|G_q^{rev}(\omega)\right|\cos\Theta_q(\omega)}\right) \tag{2.72}$$

and the oscillation condition is prescribed as usually (according to Barkhausen Criterion):

$$\left|G_p^{rev}(\omega)+G_q^{rev}(\omega)\right|\geq 1$$
$$\Theta_{(p,q)}(\omega)=2b\pi \quad (b\in\mathbb{Z}) \tag{2.73}$$

and a more simple expression of $\Theta_{(p,q)}$ is obtained in the hypothesis that Θ_p, Θ_q *are sufficiently close to* 2π*:*

$$\Theta_{(p,q)}(\omega)\cong\frac{\left|G_p^{rev}(\omega)\right|\Theta_p(\omega)+\left|G_q^{rev}(\omega)\right|\Theta_q(\omega)}{\left|G_p^{rev}(\omega)\right|+\left|G_q^{rev}(\omega)\right|}\Rightarrow$$
$$\Theta_{(p,q)}(\omega)\cong-\frac{g_{mp}\left[(2p-1)\beta(\omega)+\pi\right]+g_{mq}\left[(2q-1)\beta(\omega)+\pi\right]}{g_{mp}+g_{mq}} \tag{2.74}$$

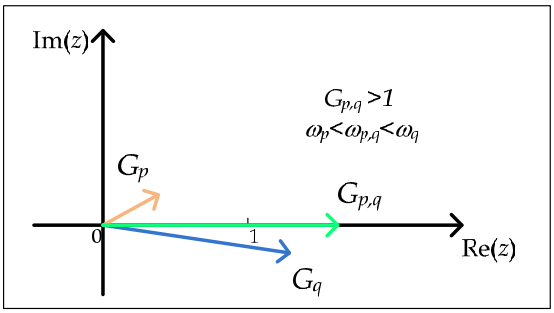

FIGURE 2-24. Total reverse gain when more than one section is active, obtained as a vector sum of the reverse gain associated with each section.

The previous equation show that the phase of the reverse loop voltage transfer ratio when two sections are simultaneously active, could be approximated as a weighted average of the two phases Θ_p, Θ_q when each section is being separately turned on, the weights being the individual transconductances of the *p-th* and *q-th* device. The formula (6.57) is consistent with the description of the biasing strategy mentioned earlier. As a *limiting case*, (6.57) reduces to (6.47) (with ψ=0) when g_{mp}, (g_{mq}) tends to zero, that is when only one device is activated (insert pictures):

$$\lim_{g_{mp}\to 0}\Theta_{(p,q)}(\omega)=\Theta_q(\omega)$$
$$\lim_{g_{mq}\to 0}\Theta_{(p,q)}(\omega)=\Theta_p(\omega) \qquad (2.75)$$

Additionally, (assuming $q > p$, *and therefore* $\omega_q < \omega_p$) when properly biasing the p^{th} and q^{th} device, *the vectors sum of the two reverse gains in the complex plane delivers a contribution lying on the real axis* ($\mathrm{Im}(G_p^{(rev)}+G_q^{(rev)})=0$, i.e. total phase turns $\Theta_{(p,q)}=2\pi$) with magnitude greater than unity at a frequency $\omega_q \le \omega_{p,q} \le \omega_p$ (as shown in Fig. 2.24). It turns out that the oscillation condition (2.73) is more easily satisfied if $q=(p+1)$ *(*see Appendix D for the details*) thus* biasing neighboring sections in a complementary fashion, such that when *transconductance of the device* $\mathbf{T}_p$ *is increased, the transconductance of the transistor* $\mathbf{T}_{p+1}$ *should decrease to keep the phase* $\Theta_{(p,p+1)}\approx 2\pi$ (insert pictures). By doing so, it is possible to continuously tune the distributed oscillator across the sub-bands $[\omega_q, \omega_p]$ (p,q = 1,…,N) whose lower and upper frequencies are defined by the individual characteristic frequencies associated to each active section. Therefore the tuning range, which spans from ω_N (*when only* $\mathbf{T}_N$ *is active*) to ω_1 (*when only* $\mathbf{T}_1$ *is active*), can be covered by differentially biasing a pair of adjacent transistors ($\mathbf{T}_s$,$\mathbf{T}_{s+1}$) (s=1,…,N-1) across the sub-bands $[\omega_N, \omega_{N-1}]$, $[\omega_{N-1}, \omega_{N-2}]$,…,$[\omega_{s+1}, \omega_s]$,…,$[\omega_2, \omega_1]$.

However, with the original schematic derived from a conventional distributed amplifier, it is possible to show that the tuning range cannot be swept uninterruptedly, due to a difference of π *among the phases of the reverse gains of the first two sections,* making it impossible to fulfill the condition $\Theta_{(1,2)}=2\pi$ (see appendix D). To solve this issue, in [72—74] *it was proposed to add an additional transistor placed crosswise among the first two sections* (insert pictures), which provided the adequate gain and phase conditions to *continuously trigger oscillations across the whole interval* $[\omega_N, \omega_1]$.

2.6 REFERENCES

References on Coupled Oscillators and N-Push Oscillators

[1] A. Georgiadis, A. Collado, and A. Suarez, "New Techniques for the Analysis and Design of Coupled-Oscillator Systems," *IEEE Transactions on Microwave Theory and Techniques*, vol.54, no.11, pp.3864-3877, Nov. 2006.

[2] J.J. Collins, and I.Stewart, "A group-theoretic approach to rings of coupled biological oscillators," *Springer Biological Cybernetics*,.vol.71, no. 2, pp. 95-103, 1994.

[3] M. Golubitsky and I. Stewart. "Nonlinear dynamics of networks: the groupoid formalism." *Bulletin of the American Mathematical Society,* vol. 43. no. 3, pp. 305-364, 2006.

[4] M.Golubitsky and I. Stewart. "Hopf bifurcation with dihedral group symmetry: coupled nonlinear oscillators" in *AMS Contemporary Mathematics*, *Multiparameter Bifurcation Theory* (Proceedings of the AMS-IMS-SIAM Joint Summer Research Conference Held July 14-20, 1985, with Support from the National Science Foundation), vol 56, pp. 131-173, 1986.

[5] A.E Siegman,. "Obtaining the equations of motion for parametrically coupled oscillators or waves," *Proceedings of the IEEE*, vol.54, no.5, pp. 756- 762, May 1966.

[6] J. Aggarwal, and C.Richie, "On Coupled van der Pol Oscillators," *IEEE Transactions on Circuit Theory*, vol.13, no.4, pp. 465- 466, Dec 1966.

[7] S. Mizushina, "2n oscillators combined with 3-dB directional couplers for output power summing," *Proceedings of the IEEE* , vol.55, no.12, pp. 2166- 2167, Dec. 1967.

[8] G.V. Welch, T.K. Ishii, "Hybrid-tee coupled oscillators," *IEEE Electronics Letters* , vol.6, no.22, pp.717-718, Oct. 1970.

[9] K. Kurokawa, "An Analysis of Rucker's Multidevice Symmetrical Oscillator (Correspondence)," *IEEE Transactions on Microwave Theory and Techniques*, vol.18, no.11, pp. 967- 969, Nov 1970.

[10] S. Okamura and Y. Okabe, "Power and Noise of Multiple Microwave-Oscillators," *Proceedings of the EuMC 1971*, vol.1, pp.1-4, Aug. 1971.

[11] K. Schunemann, "Nonlinear Noise Effects in Syncronized Oscillators," *Proceedings of the 4th EuMA European Microwave Conference (EuMC 1974)*, pp.309-312, Sept. 1974.

[12] Tetsuro Endo and S. Mori, "Mode analysis of a multimode ladder oscillator," *IEEE Transactions on Circuits and Systems*, vol.23, no.2, pp. 100- 113, Feb. 1976.

[13] Tetsuro Endo and S. Mori, "Mode analysis of a two-dimensional low-pass multimode oscillator," *IEEE Transactions on Circuits and Systems*, vol.23, no.9, pp. 517- 530, Sep. 1976.

[14] Tetsuro Endo and S. Mori, "Mode analysis of a ring of a large number of mutually coupled van der Pol oscillators," *IEEE Transactions on Circuits and Systems*, vol.25, no.1, pp. 7- 18, Jan 1978.

[15] F. Diamand, "Ku - Band Power Combining of Push-Pull Operated Impatt Diodes," *Proceedings of the Proceedings of the 9th EuMA European Microwave Conference (EuMC 1979)*, pp.566-570, Sept. 1979.

[16] A. Kouda and S. Mori, "Analysis of a ring of mutually coupled van der Pol oscillators with coupling delay," *IEEE Transactions on Circuits and Systems*, vol.28, no.3, pp. 247- 253, Mar 1981.

[17] H.J. Choi, and W.C. Lindsey, "Phase and Frequency Transfer Analysis of N Mutually Synchronized Oscillators," *IEEE Transactions on Aerospace and Electronic Systems*, vol.AES-20, no.6, pp.748-753, Nov. 1984.

[18] R.G. Freitag, "A unified analysis of MMIC power amplifier stability," *Proceedings of the IEEE MTT-S International . Microwave . Symposium . Digest 1992*, vol.1, pp.297-300,Jun 1992.

[19] K.D. Stephan, "Inter-Injection-Locked Oscillators with Applications to Spatial Power Combining and Phased Arrays," *Proceedings of the IEEE MTT-S International . Microwave . Symposium . Digest 1986,* pp.159-162, Jun 1986.

[20] K.D. Stephan, "Inter-Injection-Locked Oscillators for Power Combining and Phased Arrays," *IEEE Transactions on Microwave Theory and Techniques*, vol.34, no.10, pp. 1017- 1025, Oct 1986.

[21] K. Stephan and W. Jr. Morgan, "Analysis of interinjection-locked oscillators for integrated phased arrays," *IEEE Transactions on Antennas and Propagation*, vol.35, no.7, pp. 771- 781, Jul 1987.

[22] P.Liao and R.A. York, "Phase-shifterless beam-scanning using coupled-oscillators: Theory and experiment," *Proceedings of the 1993 Antennas and Propagation Society (AP-S) International Symposium 1993*, vol.2, pp.668-671, 28 Jun- 2 Jul 1993.

[23] S.Nogi, Jenshan Lin and T. Itoh, "Mode analysis and stabilization of a spatial power combining array with strongly coupled oscillators," *IEEE Transactions on Microwave Theory and Techniques*, vol.41, no.10, pp.1827-1837, Oct 1993.

[24] R.A. York, P.Liao and J.J. Lynch, "Oscillator array dynamics with broadband N-port coupling networks ," *IEEE Transactions on Microwave Theory and Techniques*, vol.42, no.11, pp.2040-2045, Nov 1994.

[25] Y. Setou, Y. Nishio, and A. Ushida, "Synchronization phenomena in many oscillators coupled by resistors as a ring," *Proceedings of the 1994 IEEE Asia-Pacific Conference on Circuits and Systems* (*APCCAS '94)*, pp.570-575, Dec 1994.

[26] Xudong Cao and R.A York, "Coupled-oscillator scanning technique for receiver applications," *Proceedings of Antennas and Propagation Society International Symposium 1995*, vol.2, pp.1311-1314, Jun 1995.

[27] I. Galton. *et al.,* "Clock distribution using coupled oscillators," *Proceedings of the 1996 IEEE International Symposium on Circuits and Systems (ISCAS '96)*, vol.3, pp.217-220, May 1996.

[28] Heng-Chia Chang, Xudong Cao, U.K. Mishra, and R.A York, "Phase noise in coupled oscillators: theory and experiment," *IEEE Transactions on Microwave Theory and Techniques*, vol.45, no.5, pp.604-615, May 1997.

[29] K. Seunghwan, S. H. Park, and C. S. Ryu, "Multistability in Coupled Oscillator Systems with Time Delay", *Phys. Rev. Lett., E*, vol. 79, pp .2911–2914, Oct. 1997.

[30] S. Moro, S. Mori, and I. Sasade, "Mutual synchronization in 4 coupled oscillators with different natural frequencies," *Proceedings of the 1998 IEEE International Symposium on Circuits and Systems (ISCAS '98)*, vol.3, no., pp.534-537, 31 May-3 Jun 1998.

[31] L. Dussopt and J.-M. Laheurte, "Coupled oscillator array generating circular polarization [active antenna]," *IEEE Microwave and Guided Wave Letters*, vol.9, no.4, pp.160-162, Apr 1999.

[32] D.V. Ramana Reddy, A. Sen, and G.L. Johnston. "Time delay effects on coupled limit cycle oscillators at Hopf bifurcation," *Physica D: Nonlinear Phenomena*, vol. 129, no. 1–2, pp. 15-34, May 1999.

[33] M. Y. Choi, H. J Kim,. D. Kim, and H. Hong, "Synchronization in a system of globally coupled oscillators with time delay" *Phys. Rev. E,* vol. 61, pp. 371–381, Jan. 2000

[34] A. Banai and F Farzaneh, "Locked and unlocked behaviour of mutually coupled microwave oscillators," *IEE Proceedings on Microwaves, Antennas and Propagation*, vol.147, no.1, pp.13-18, Feb 2000.

[35] Yu-Long Tang and Huei Wang, "A novel triple-push oscillator approach," *Proceedings of the IEEE MTT-S International . Microwave . Symposium . Digest 2000*, vol.2, pp.1201-1204, 2000.

[36] Shih-Chieh Yen, Tah-Hsiung Chu, "An Nth-harmonic oscillator using an N-push coupled oscillator array with voltage-clamping circuits," *Proceedings of the IEEE MTT-S International . Microwave . Symposium . Digest 2003* , vol.3, pp. 2169- 2172, Jun 2003.

[37] U.L. Rohde *et al*., "Low noise low cost ultra wideband N-push VCO," *Proceedings of the IEEE/MTT-S International . Microwave . Symposium . Digest 2005*, pp., 12-17, Jun 2005.

[38] X. Hai, T. Takayuki, and A. Masayoshi, "Basic Behavior of Quadruple-Push Oscillator Using Ring Resonator," *IEICE Trans. Electron*., vol.E88-C; no.7; pp.1502-1508, 2005.

[39] Jonghoon Choia and A. Mortazawi, "Design of push-push and triple-push oscillators for reducing 1/f noise upconversion," *IEEE Transactions on Microwave Theory and Techniques*, vol.53, no.11, pp. 3407- 3414, Nov. 2005.

[40] U.L. Rohde and A.K. Poddar, "Technological scaling and minimization of 1/f noise in SiGe HBTs coupled mode N-Push oscillator/VCO," *Proceedings of the 2006 Asia-Pacific Microwave Conference (APMC 2006)*, pp.623-626, Dec. 2006.

[41] Y.Baeyens *et al*, "Highly Efficient Harmonically Tuned InP D-HBT Push-Push Oscillators Operating up to 287 GHz," *Proceedings of the IEEE/MTT-S International . Microwave . Symposium 2007.*, pp.341-344, 3-8 Jun. 2007.

[42] M Ponton, E. Fernandez, A. Suarez, and F. Ramirez, "Harmonic-balance design and analysis of an injection-locked push-push oscillator," *Proceedings of the 2008 Workshop on Integrated Nonlinear Microwave and Millimetre-Wave Circuits (INMMIC 2008),* pp.53-56,Nov. 2008.

[43] F. Ramirez, M Ponton, S. Sancho, and A. Suarez, "Stability Analysis of Oscillation Modes in Quadruple-Push and Rucker's Oscillators," *IEEE Transactions on Microwave Theory and Techniques*, vol.56, no.11, pp.2648-2661, Nov. 2008.

[44] A. Collado and A. Georgiadis, "Nonlinear Mode Analysis and Optimization of a Triple-Push Oscillator," *IEEE Microwave and Wireless Components Letters*, vol.18, no.8, pp.545-547, Aug. 2008.

[45] B.Catli, and M.M. Hella, "A 30-GHz triple-push oscillator on silicon for mm-wave applications," *Proceedings of the 2009 IEEE International Symposium on Circuits and Systems (ISCAS 2009)*, pp.2037-2040,May 2009.

[46] K.Kawasaki, T. Tanaka, and M.Aikawa, "An Octa-Push Oscillator at V -Band," *IEEE Transactions on Microwave Theory and Techniques*, vol.58, no.7, pp.1696-1702, Jul. 2010

[47] B.Catli, and M.M. Hella, "Triple-Push Operation for Combined Oscillation/Divison Functionality in Millimeter-Wave Frequency Synthesizers," *IEEE Journal of Solid-State Circuits*, vol.45, no.8, pp.1575-1589, Aug. 2010.

[48] O.Momeni, and E. Afshari, "High Power Terahertz and Millimeter-Wave Oscillator Design: A Systematic Approach," *IEEE Journal of Solid-State Circuits,* vol.46, no.3, pp.583-597, March 2011.

[49] M.M Abdul-Latif and E. Sanchez-Sinencio, "Low Phase Noise Wide Tuning Range N-Push Cyclic-Coupled Ring Oscillators," *IEEE Journal of Solid-State Circuits*, vol.47, no.6, pp.1278-1294, June 2012.

[50] U. L.Rohde, A.K. Poddar and G. Böck. *The Design of Modern Microwave Oscillators for Wireless Applications : Theory and Optimization*, Wiley-Interscience, Jun 3, 2005.

[51] Yu-Lung Tang and Huei Wang; , "Triple-push oscillator approach: theory and experiments," *IEEE Journal of Solid-State Circuits*, vol.36, no.10, pp.1472-1479, Oct 2001.

[52] E.W Weisstein. "Circulant Matrix. Internet: http://mathworld.wolfram.com/"March 20, 2013 [March 20, 2013].

[53] R.G.Freitag, "A modal analysis of MMIC power amplifier stability," *Proceedings of the 35th Midwest Symposium on Circuits and Systems*, 1992., pp.1012-1015, vol.2, Aug. 1992.

[54] A. Suarez, and R. Quéré. *Stability Analysis of Nonlinear Microwave Circuits*, Artech House publishers, January 2003

References on Distributed Amplifiers and Oscillators

[55] W. S. Percival, "Thermoionic Valve Circuits" British patent specification No. 460,562, Jan. 1937.

[56] E. L Ginzton, W. R. Hewlett, J. H. Jasberg, and Noe, J. D, "Distributed Amplification" *Proceedings of the IRE*, pp. 956-69, August 1948.

[57] D.V.Payne, "Distributed Amplifier Theory," *Proceedings of the IRE* , vol.41, no.6, pp.759-762, June 1953.

[58] D.G. Sarma, "On distributed amplification," *Proceedings of the IEE - Part B: Radio and Electronic Engineering* , vol.102, no.5, pp.689-697, September 1955.

[59] A. Hajimiri, "Distributed integrated circuits: an alternative approach to high-frequency design,"*IEEE Communications Magazine*, vol.40, no.2, pp.168-173, Feb 2002.

[60] A. Scott, "Distributed multimode oscillators of one and two spatial dimensions," *IEEE Transactions on Circuit Theory*, vol.17, no.1, pp. 55- 60, Feb 1970.

[61] A. Scott, "Distributed multimode oscillators of one and two spatial dimensions," *IEEE Transactions on Circuit Theory*, vol.17, no.1, pp. 55- 60, Feb 1970.

[62] H.Aumann, "Standing waves on a multimode ladder oscillator," *IEEE Transactions on Circuits and Systems*, vol.21, no.3, pp. 461- 462, May 1974.

[63] R.W. Johnson, "Extending the Frequency Range of the Phase-Shift Oscillator," *Proceedings of the IRE* , vol.33, no.9, pp. 597- 603, Sept. 1945.

[64] F.C. Isely, "A New Approach to Tunable Resonant Circuits for the 300- to 3000-Mc Frequency Range," *Proceedings of the IRE* , vol.36, no.8, pp. 1017- 1022, Aug. 1948.

[65] W.A. Edson, "Tapered Distributed RC Lines for Phase-Shift Oscillators," *Proceedings of the IRE* , vol.49, no.6, pp.1021-1024, June 1961.

[66] A. Manolescu, "Single-transistor oscillators with distributed RC networks,"*IEEE Electronics Letters*, vol.2, no.4, pp.151-152, April 1966.

[67] Bang-Sup Song and T. Itoh, "A Distributed Feedback Dielectric Waveguide Oscillator with a Built-In Leaky-Wave Antenna,"*Proceedings of the 1979 IEEE/MTT-S International Microwave Symposium*, pp.217-219, April 30 1979-May 2 1979.

[68] V. Neprintsev, B. Koristin, and A. Kunaev, "Oscillator from the Wien-type two-port with distributed parameters," *IEEE Transactions on Circuits and Systems*, vol.32, no.4, pp.405-406, April 1985.

[69] A. Scott, "The Distributed Tunnel Diode Oscillator," *IEEE Transactions on Circuit Theory*, vol.10, no.1, pp. 53- 59, Mar 1963.

[70] W. Howard, and H. Stellrecht, "Integrated voltage-controlled oscillators using distributed parameter phaseshift networks," *Proceedings of the 1969 IEEE International Solid-State Circuits Conference (ISSCC 1969).*, vol.XII, no., pp. 102- 103, Feb 1969.

[71] A. Aishima and Y.Fukushima, "An Analysis of an Electronically Tunable N-GaAs Distributed Oscillator," *IEEE Transactions on Microwave Theory and Techniques*, vol.32, no.2, pp. 157- 164, Feb 1984.

[72] Z. Škvor, S.R. Saunders, and C.S. Aitchison, "Novel decade electronically tunable microwave oscillator based on the distributed amplifier", *IEEE Electronics Letters*, vol.28, no.17, pp.1647-1648, Aug. 1992.

[73] L. Divina and Z. Škvor, "Experimental verification of a distributed amplifier oscillator," *Proceedings of the 25th EuMA European Microwave Conference (EuMC 1995)*, pp. 1163–1167, Sept. 1995

[74] L. Divina and Z. Škvor, "The distributed oscillator at 4 GHz," *Proceedings of the International Microwave Symposium 1998 Digest*, vol.2, no., pp.865-868, Jun. 1998.

[75] B. Kleveland, *et al.*, "Monolithic CMOS distributed amplifier and oscillator," *Proceedings of the 1999 IEEE International Solid-State Circuits Conference (ISSCC. 1999)*, pp.70-71, 1999.

[76] A. Hajimiri and Hui Wu, "Analysis and design of silicon bipolar distributed oscillators," *Proceedings of the Symposium on VLSI Circuits 2000* , pp.102-105, 2000.

[77] Hui Wu; and A. Hajimiri, "A novel tuning technique for distributed voltage controlled oscillators," *Proceedings of the 2004 International Symposium on Circuits and Systems (ISCAS 2000)*, vol.3, pp.57-60, 2000.

[78] Hui Wu; and A. Hajimiri, "A 10 GHz CMOS distributed voltage controlled oscillator," *Proceedings of the 2000 IEEE Custom Integrated Circuits Conference (CICC 2000)*, pp.581-584, May 2000.

[79] Hui Wu; and A. Hajimiri, "Silicon-based distributed voltage-controlled oscillators," *IEEE Journal of Solid-State Circuits*, vol.36, no.3, pp.493-502, Mar 2001.

[80] J. Wood, T.C. Edwards, and S. Lipa, "Rotary traveling-wave oscillator arrays: a new clock technology," *IEEE Journal of Solid-State Circuits*, vol.36, no.11, pp.1654-1665, Nov 2001.

[81] C.J. White, and A. Hajimiri, "Phase noise in distributed oscillators," *IEEE Electronics Letters*, vol.38, no.23, pp. 1453- 1454, 7 Nov 2002.

[82] Jing Zhang, Haitao Mei, and T. Kwasniewski, "Prediction of phase noise in CMOS distributed oscillators," *Proceedings of the 2003 IEEE/SBMO International Microwave and Optoelectronics Conference (IMOC 2003)*, vol.1, pp. 157- 162, Sept. 2003.

[83] K.F. Tsang, and Chung Ming Yuen, "A 2.7 V, 5.2 GHz frequency synthesizer with 1/2 - subharmonically injection-locked distributed voltage controlled oscillator," *IEEE Transactions on Consumer Electronics*, vol.50, no.4, pp. 1237- 1243, Nov. 2004.

[84] Chung Ming Yuen and Kim Fung Tsang, "A 1.8-V distributed voltage-controlled oscillator module for 5.8-GHz ISM band," *IEEE Microwave and Wireless Components Letters*, vol.14, no.11, pp. 525- 527, Nov. 2004.

[85] Eun-Chul Park and Euisik Yoon, "A 13GHz CMOS distributed oscillator using MEMS coupled transmission lines for low phase noise," *Proceedings of the 2004 IEEE International Solid-State Circuit Conference, (ISSCC. 2004),* vol. 1, pp. 300- 530, 15-19 Feb. 2004

[86] K.Bhattacharyya, and T.H. Szymanski, "Performance of a 12GHz monolithic microwave distributed oscillator in 1.2V 0.18μm CMOS with a new simple design technique for frequency changing," *Proceedings of the 2005 IEEE Annual Conference Wireless and Microwave Technology (WAMICON 2005)*, pp. 174- 177, 2005.

[87] D. Guckenberger and K.T.Kornegay, "Design of a differential distributed amplifier and oscillator using close-packed interleaved transmission lines,"*IEEE Journal of Solid-State Circuits*, vol.40, no.10, pp. 1997- 2007, Oct. 2005.

[88] A.D.S. Barros, and F.S. Correra, "Analysis of reverse feedback distributed oscillators with m-derived artificial transmission lines," *Proceedings of the 2005 IEEE/SBMO International Microwave and Optoelectronics Conference (IMOC 2005)* pp. 74- 78, July 2005.

[89] Z.A. Shaik and P.N. Shastry, "A novel distributed voltage-controlled oscillator for wireless systems," *Proceedings of the 2006 IEEE Radio and Wireless Symposium (RWS '06)* pp. 423- 426, 17-19 Jan. 2006

[90] F. Cannone, G. Avitabile, and N. Lofu, "New wideband Distributed Voltage Controlled Oscillator with a coarse-fine tuning," *Proceedings of the 9th European Conference on Wireless Technology, 2006*, pp.302-305, 10-12 Sept. 2006

[91] F. Cannone, G. Avitabile and D. Cascella, "Fully integrated coarse-fine wideband distributed voltage controlled oscillator,"*Proceedings of the 2008 PhD Research In Microelectronics and Electronics (PRIME 2008)*, pp.165-168, June 22 2008-April 25 2008.

[92] F. Cannone and G. Avitabile, "Multi-band vco based on distributed VCO and switched-capacitors banks," *Proceedings of the 17th International Conference on Microwave, Radar and Wireless Communications (MIKON 2008)*, pp.1-4, 19-21 May 2008.

[93] F. Cannone, G. Avitabile and D. Cascella, "Multi-standard/multi-band distributed VCO based on the "switched-cells tuning techniques" for SDR applications," *Proceedings of the 2010 IEEE International Symposium On Circuits And Systems (ISCAS 2010)*, pp.1991-1994, May 30 2010-June 2 2010.

[94] Sheng-Fuh Chang *et al.*, "A Ka-Band Distributed Voltage-Controlled Oscillator With Constant 15-dBm Output Power," *Proceedings of the 16th IST Mobile and Wireless Communications Summit 2007,*pp.1-4, 1-5 July 2007

[95] K. Bhattacharyya, J. Mukherjee, and M.S. Baghini, "20GHz CMOS distributed voltage controlled oscillators with frequency tuning by MOS varactors," *Proceedings of the 2nd International Workshop on Electron Devices and Semiconductor Technology, (IEDST '09)*, pp.1-6, 1-2 June 2009.

[96] K. Bhattacharyya, J. Mukherjee, and M.S. Baghini, "27.1GHz CMOS distributed voltage controlled oscillators with body bias for frequency tuning of 1.28GHz," *Proceedings of the 52nd IEEE International Midwest Symposium On Circuits And Systems, 2009. (MWSCAS '09).*, pp.1034-1038, 2-5 Aug. 2009.

[97] K. Bhattacharyya, "23.97GHz CMOS Distributed Voltage Controlled Oscillators with Inverter Gain Cells and Frequency Tuning by Body Bias and MOS Varactors Concurrently,"*Proceedings of the 23rd International Conference On VLSI Design, 2010 (VLSID '10)*, pp.182-187, 3-7 Jan. 2010.

[98] K. Bhattacharyya, "CMOS Ku/K band distributed oscillators using cascade of CPW coupled n-FETs gain cells with record performance of phase noise and Ka-band third harmonic generation technique," *Proceedings of the 2010 IEEE 11th Annual Wireless And Microwave Technology Conference (WAMICON 2010)*, pp.1-4, April 2010.

[99] M. Yanez, and J.C. Cartledge, "Synthesis of Distributed Phase-Locked Oscillators," , *IEEE Transactions on Circuits and Systems I: Regular Papers*, vol.56, no.6, pp.1146-1159, June 2009.

[100] Xiaofeng Li, O.O. Yildirim, Wenjiang Zhu and Donhee Ham, "Phase Noise of Distributed Oscillators," *IEEE Transactions on Microwave Theory and Techniques*, vol.58, no.8, pp.2105-2117, Aug. 2010.

[101] T.T.Y Wong. *Fundamentals of Distributed Amplification*. London: Artech House, 1993

[102] B. S. Virdee, A. S Virdee, and B.Y. Banyamin. *Broadband Distributed Amplifiers*. Artech House, 2004.

[103] D. Pozar. *Microwave Engineering*. New York: Wiley, February 5, 2004.

[104] H.W.Bode. *Network Analysis & Feedback Amplifier Design*. Amsterdam: Van Nostrand, 1945, [On-line] http://archive.org/details/NetworkAnalysisFeedbackAmplifierDesign, [Nov 2, 2012].

[105] P. Heydari, D. Lin, A. Shameli, and A. Yazdi, "Design of CMOS distributed circuits for multiband UWB wireless receivers [LNA and mixer]," *Proceedings of the Radio Frequency Integrated Circuits (RFIC) Symposium 2005 Digest Of Papers, (RFIC 2005)*, pp. 695- 698, 12-14 June 2005.

[106] Y.K. Ramadass, and N.B Chakrabarti, "Design and implementation of CMOS distributed mixers and oscillators for wide-band RF front-end," *Proceedings of the 2004 IEEE International Symposium On Circuits And Systems (ISCAS '04)*, vol.4, pp. IV- 756-9 23-26 May 2004.

[107] Yunliang Zhu, J. D Zuegel, J.R. Marciante, and Hui Wu, "Distributed Waveform Generator: A New Circuit Technique for Ultra-Wideband Pulse Generation, Shaping and Modulation," *IEEE Journal of Solid-State Circuits*, vol.44, no.3, pp.808-823, March 2009.

[108] A.Q. Safarian, and P. Heydari, "Design and analysis of a distributed regenerative frequency divider using distributed mixer," *Proceedings of the 2004 IEEE International Symposium On Circuits And Systems (ISCAS '04)*, vol.1, pp. I- 992-5, May 2004.

[109] B. Razavi. *RF Microelectronics (2nd Edition)*. Prentice Hall Communications Engineering and Emerging Technologies Series, October 2, 2011.

[110] W.H Horton,. J.H. Jasberg, J.D Noe, "Distributed Amplifiers: Practical Considerations and Experimental Results," *Proceedings of the IRE*, vol.38, no.7, pp. 748- 753, July 1950.

[111] D. Pederson, "The Distributed Pair," *Transactions of the IRE Professional Group on Circuit Theory*, vol.PGCT-1, no., pp.57-67, December 1952.

[112] D.V. Payne, "Distributed Amplifier Theory," *Proceedings of the IRE* , vol.41, no.6, pp.759-762, June 1953

[113] H.G. Bassett, and L.C. Kelly, "Distributed amplifiers: some new methods for controlling gain/frequency and transient responses of amplifiers having moderate bandwidths," *Journal of the Institution of Electrical Engineers*, vol.1954, no.1, pp.31, January 1954.

[114] L. Enloe, and P. Rogers, "Wideband transistor distributed amplifiers," *Proceedings of the 1959 IEEE International Solid-State Circuits Conference*., vol.II, no., pp.44-45, 12-13 Feb. 1959

[115] P. H. Rogers, "Some .Useful Techniques for Overcoming the Frequency Limitations of Conventional Distributed Amplifiers," University of Michigan, Engineering Research Institute, Technical Memorandum No.32, November, 1956, [On-line] http://deepblue.lib.umich.edu/bitstream/2027.42/7305/5 /bad1385.0001.001.pdf, [Oct. 28, 2012]

[116] J. Hamasaki and K. Kurokawa, "A Wide-Band UHF Traveling-Wave Variable Reactance Amplifier," *IRE Transactions on Microwave Theory and Techniques*, vol.8, no.3, pp.351-361, May 1960.

[117] F. Thompson, "Broad-Band UHF Distributed Amplifiers Using Band-Pass Filter Techniques," , *IRE Transactions on Circuit Theory*, vol.7, no.5, pp. 8- 17, Aug 1960.

[118] W.K. Chen, "Distributed amplifiers: survey of the effects of lumped-transmission-line design on performance," *Proceedings of the Institution of Electrical Engineers*, vol.114, no.8, pp.1065-1074, Aug. 1967.

[119] W.K. Chen, "Distributed amplification: A new approach," *IEEE Transactions on Electron Devices,* vol.14, no.4, pp. 215- 221, Apr 1967.

[120] W. Jutzi, "Uniform distributed amplifier analysis with fast and slow waves," *Proceedings of the IEEE* , vol.56, no.1, pp. 66- 67, Jan. 1968.

[121] W.K. Chen, "Theory and Design of Transistor Distributed Amplifiers," *IEEE Journal of Solid-State Circuits*,vol.3, no.2, pp.165-179, June 1968.

[122] W. Jutzi, "A MESFET distributed amplifier with 2 GHz bandwidth," *Proceedings of the IEEE*, vol.57, no.6, pp. 1195- 1196, June 1969.

[123] Y. Ayasli, *et al.*, "A Monolithic GaAs 1-13 GHz traveling-wave amplifier", *IEEE Trans. Microwave Theory Tech.*, vol. MTT-30, pp.976-981, July 1982.

[124] Y. Ayasli, *et al.* "2-20 GHz GaAs traveling- wave power amplifier," *IEEE Trans. Microwave Theory Tech.*, vol. MTT-32, pp. 290-295, March 1984.

[125] K. Bowers, and R. Patrick. Design Guide: "Broadband Distributed Amplifiers" [On-line] Available: http://www.inst.eecs.berkeley.edu/~ee217/sp03/projectsSP99/ /Dist_Amp_b+r.pdf [Oct. 25, 2012]-

[126] J. A. Archer, F.A. Petz, and H. P. Weidlich, "GaAs FET distributed amplifier,"*IEEE Electronics Letters* , vol.17, no.13, pp.433, June 25 1981.

[127] E. W. Strid and K.R. Gleason, "A DC-12 GHz Monolithic GaAsFET Distributed Amplifier," *IEEE Transactions on Microwave Theory and Techniques*, , vol.30, no.7, pp.969-975, Jul. 1982.

[128] R. Pucel, "Wideband microwave/millimeter-wave solid-state amplifiers," *Proceedings of 1983 IEEE International Solid-State Circuits Conference*, vol.XXVI, no., pp. 142- 143, Feb 1983.

[129] K.B. Niclas *et al.,* "On Theory and Performance of Solid-State Microwave Distributed Amplifiers," *IEEE Transactions on Microwave Theory and Techniques*, , vol.31, no.6, pp.447-456, Jun. 1983.

[130] G. Nwaogu and C.S. Aitchison, "A Very Broadband Microwave Distributed Amplifier using FETs," *Proceedings of the EuMC 1981.*, pp.609-613, Sept. 1981.

[131] J.B Beyer, Prasad, S.N. *et al.*, "MESFET Distributed Amplifier Design Guidelines," *IEEE Transactions on Microwave Theory and Techniques*, vol.32, no.3, pp. 268- 275, Mar 1984.

[132] K. B. Niclas, "Reflective Match, Lossy Match, Feedback and Distributed Amplifiers: A Comparison of Multi-Octave Performance Characteristics,"*Proceedings of the 1984 IEEE MTT-S International Microwave Symposium*, pp.215-217, May 30 1984-June 1 1984.

[133] N. Nazoa-Ruiz, and C.S. Aitchison, "The Gain and Noise Performance of Lossy Distributed Amplifiers using MESFETs," *Proceedings of the 14th EuMA European Microwave Conference (EuMC 1984)*, pp.398-403, 10-13 Sept. 1984.

[134] T.H. Lee. *The Design of CMOS Radio-Frequency Integrated Circuits, Second Edition*. Cambridge University Press, December 22, 2003.

[135] M. Odyniec. *RF and Microwave Oscillator Design*. Artech House, October 15, 2002.

CHAPTER III. MICROWAVE CIRCUITS NONLINEAR NUMERICAL ANALYSIS

3.1 TIME DOMAIN METHODS.

The aim of circuit analysis using Time Domain Methods is to determine the time evolution (*waveforms*) of all the *branch currents* and *node voltages* (with respect to a reference node) in a suitable observation window identified with the closed interval $[t_0, t_1]$. In general, this involves setting up two different systems of equations. The first one is constituted by the *topological constraints,* dictated by the network interconnections among the circuit elements and expressed by the Kirchhoff Current Law (KCL) at each node (or at *cut-sets*) $\sum_{nodes} i(t)=0$, or Kirchhoff Voltage Law (KVL) at the loops or (meshes) $\sum_{loops} v(t)=0$. The second one, includes a set of physical constraints for each component in the circuit called Branch Constitutive Equations (BCE) which account for describing the voltage-current characteristics $i_k(t)=g(v_1(t), v_2(t),\ldots, v_l(t))$[1] of a nonlinear element. Whenever reactive elements (storing electric or magnetic energy) are present, the previous set of equations is augmented by using the *charge-voltage* $\{q_m(t) = q(v_1(t), v_2(t),\ldots, v_l(t))\}$ for *generalized capacitors* and *flux-current* relationships $\{\varphi_h(t) = \varphi(i_1(t), i_2(t),\ldots, i_k(t))\}$ *for generalized inductors* entailing the introduction of voltage (current) *time derivative* or *time integral*[2] in the system denoting the BCEs. Hence, it is necessary to deal with nonlinear differential systems of equations[3], and if the variables are properly chosen[4] [1], it could be cast into a system of Differential Algebraic Equations (3.1), where the unknown vector of functions $\mathbf{x}(t)$ *(n – dimensional)* represent the set of voltage through capacitors and currents through the inductors called *state vector*; $\mathbf{j}_s(t)$ *(p – dimensional)* denotes the inputs (in case of non-autonomous systems) expressed as a *Norton equivalent current sources*, $\mathbf{f}(\mathbf{x}(t))$, $\mathbf{g}(\mathbf{x}(t))$, $\mathbf{q}(\mathbf{x}(t))$ three nonlinear *vector-valued functions* of the state $\mathbf{x}(t)$. The functions $\mathbf{f}(\mathbf{x}(t))$ *(r – dimensional)*, $\mathbf{g}(\mathbf{x}(t))$ *(s – dimensional)* stands for the *generalized nonlinear currents* (*voltages*) while $\mathbf{q}(\mathbf{x}(t))$ *(r – dimensional)*represents a vector of *generalized nonlinear charges* (*fluxes*). In order to retrieve the unknown $\mathbf{x}(t)$ one must solve (3.1) implicitly for $\mathbf{q}(\mathbf{x}(t))$ and

---

[1] The current of the nonlinear element at the branch *k*, is dependent on a set of voltages $(v_1(t),\ldots,v_l(t))$ at the nodes $(1,\ldots,l)$ if the nonlinearity is *voltage controlled, the nonlinear function is dimensionally equivalent to a conductance.* Conversely, it is possible to deal with current controlled nonlinear resistances $v_p(t)= r(i_1(t), \ldots, i_s(t))$ from the branches $(1,\ldots,s)$.

[2] In fact, a current is obtained by deriving the charge function with respect to time; a voltage is obtained by deriving the flux linkage with respect to time. In case the reactive elements are *linear* there exist dual relationships for obtaining the voltage across a capacitor (current through an inductor) through integration of its branch current (node voltage) with respect to time.

[3] This mathematical framework doesn't include the description of distributed parameter elements. Subdividing a distributed element into infinitesimal slices (having negligible length, $\Delta x\rightarrow 0$) the lumped parameter formulation applies as well, leading to simplified formulations.

[4] The variables denoted with "*x(t)"may refer to voltages or currents indifferently.*

then apply the inverse function $\mathbf{x}(t)=\mathbf{x}(\mathbf{q}(t))$, (charge controlled state vector) in a suitable range(for which $\mathbf{q}(\mathbf{x}(t))$ is invertible).

$$\mathbf{x}(t_0)=x_0$$

nonautonomous systems:

$$\boxed{\frac{d\mathbf{q}}{dt}(\mathbf{x}(t))=\mathbf{F}(\mathbf{x}(t),t)=\mathbf{g}(\mathbf{x}(t))+\mathbf{j}_s(t)}$$

autonomous systems:

$$\boxed{\frac{d\mathbf{q}}{dt}(\mathbf{x}(t))=\mathbf{f}(\mathbf{x}(t))}\Rightarrow\boxed{\frac{d\mathbf{q}}{dt}(\mathbf{x}(t+\tau))=\mathbf{f}(\mathbf{x}(t+\tau))}$$

$$t\in[t_0,t_1]\subset\mathbb{R}\quad\forall\, t_0,t_1,\tau\in\mathbb{R}$$

$$\mathbf{x}=[x_1(t),\cdots,x_n(t)]^T$$
$$\mathbf{q}=[q_1(\mathbf{x}(t)),\cdots,q_r(\mathbf{x}(t))]^T$$
$$\mathbf{g}=[g_1(\mathbf{x}(t)),\cdots,g_s(\mathbf{x}(t))]^T$$
$$\mathbf{j}_s=[j_{s1}(t),\cdots,j_{sp}(t)]^T$$
$$\mathbf{f}=[f_1(\mathbf{x}(t)),\cdots,f_r(\mathbf{x}(t))]^T \qquad (3.1)$$

In the second equation in (3.1) describing the autonomous circuits dynamics, the functions $\mathbf{q}(\cdot)$ and $\mathbf{f}(\cdot)$ are seen not to depend *explicitly on time* which leads to the conclusion that arbitrary time shifted solutions are still valid solutions, defining the *time invariance properties for unforced circuits.*

3.1.1 Transient Analysis by means of Direct Integration.

Very rarely, however a closed form solution can be obtained analytically, hence time-domain methods are aimed at tackling this problem via numerical integration [2].The original problem (3.1) is reformulated in the *discrete time* domain, through sampling of the waveform vectors (sampling their components) with a sample period Δt in a certain time span $[t_0, t_1]$:

$$\frac{d}{dt}\mathbf{q}(\mathbf{x}(t_k))=\mathbf{F}(\mathbf{x}(t_k),t_k)$$
$$t_{k+1}=t_k+\Delta t=t_0+k\Delta t\subset[t_0,t_1] \qquad (3.2)$$

making sure that the time step Δt is chosen according to Nyquist sampling theorem in order to prevent aliasing in the frequency domain [3]. The derivatives appearing on the LHS of the (3.2) can be approximated with their *finite differences*, leading to the three alternative formulations:

$$\frac{\mathbf{q}(\mathbf{x}_{k+1})-\mathbf{q}(\mathbf{x}_k)}{t_{k+1}-t_k}=\mathbf{F}(\mathbf{x}_k,t_k)\qquad\text{Forward (Explicit) Euler Method}$$
$$\Rightarrow\boxed{\mathbf{q}_{k+1}=\mathbf{F}(\mathbf{x}_k,t_k)\cdot\Delta t+\mathbf{q}_k} \qquad (3.3)$$

$$\frac{\mathbf{q}(\mathbf{x}_{k+1})-\mathbf{q}(\mathbf{x}_k)}{t_{k+1}-t_k}=\mathbf{F}(\mathbf{x}_{k+1},t_{k+1})\qquad\text{Backward (Implicit) Euler Method}$$
$$\Rightarrow\boxed{\mathbf{q}_{k+1}=\mathbf{F}(\mathbf{x}_{k+1},t_{k+1})\cdot\Delta t+\mathbf{q}_k}\qquad\mathbf{q}_{k+1}=\mathbf{q}(\mathbf{x}_{k+1});\quad\mathbf{q}_k=\mathbf{q}(\mathbf{x}_k) \qquad (3.4)$$

$$\frac{\mathbf{q}(\mathbf{x}_{k+1})-\mathbf{q}(\mathbf{x}_k)}{t_{k+1}-t_k}=\frac{1}{2}\{\mathbf{F}(\mathbf{x}_k,t_k)+\mathbf{F}(\mathbf{x}_{k+1},t_{k+1})\}\qquad\text{Mixed (semi-Implicit) Euler Method}$$
$$\Rightarrow\boxed{\mathbf{q}_{k+1}=\frac{1}{2}\{\mathbf{F}(\mathbf{x}_k,t_k)+\mathbf{F}(\mathbf{x}_{k+1},t_{k+1})\}\cdot\Delta t+\mathbf{q}_k} \qquad (3.5)$$

From Forward Euler Method (3.3) a recurrence relation is obtained which relates $\mathbf{q}_{k+1}$ directly to $\mathbf{q}_k$, so the solution at the step s, $\mathbf{q}_s$ is obtained starting from the initial state $\mathbf{x}_0$ at the time t_0, iterating s times on equation (3.2) in a "marching forward" scheme. In the case of Backward Euler Method (3.4), it can be seen that the values of the current state depend both on the previous iteration $\mathbf{q}_k$ and on the value that the nonlinear function takes on the current iteration $\mathbf{F}(\mathbf{x}_{k+1}, t_{k+1})$, which is actually unknown. It should then be used a root-finding algorithm like the Newton-Raphson method [4] to solve the nonlinear system (3.4) that implicitly defines the new state $\mathbf{x}_{k+1}$. At each step, the solution is computed starting from an initial guess, derived from the explicit solution (3.3). It is possible to consider a mixed method too, obtaining by averaging the forward and backward differences computed in the interval $[t_k, t_{k+1}]$ giving rise to the semi-implicit scheme in (3.5). In spite of an increase of computation costs, these last two are numerically more stable[5]. In fact, inherently to every discretization process there is an unavoidable discrepancy due to the *truncation* (finite precision arithmetic) and to the numerical approximation of the derivatives with ratios. These discretization errors can be quantified as:

$$\begin{aligned} \varepsilon(\mathbf{x}_k) &= \mathbf{x}(t_k) - \mathbf{x}_k \\ \varepsilon(\mathbf{q}_k) &= \mathbf{q}(t_k) - \mathbf{q}_k \\ \varepsilon(\mathbf{F}_k) &= \mathbf{F}(t_k) - \mathbf{F}_k \end{aligned} \tag{3.6}$$

for each of the functions ($\mathbf{x}(.)$, $\mathbf{q}(.)$, $\mathbf{F}(.)$). They can be bounded only when using implicit methods (3.4) (3.5) and could become arbitrarily small by reducing the step size Δt [3].

A different approach consists in numerically evaluating the derivatives of the generalized charge in equation (3.2) and then using the aforementioned Newton method find a zero of the function:

$$\Xi\big(\mathbf{q}(\mathbf{x}(t_k)), t_k\big) = \frac{d}{dt}\mathbf{q}(\mathbf{x}(t_k)) - \mathbf{F}(\mathbf{x}(t_k), t_k) = \mathbf{0} \tag{3.6}$$

The charge derivative is computed taking into account that:

$$\begin{aligned} &\frac{d\mathbf{q}}{dt} = \dot{\mathbf{q}}(t) \Rightarrow \int d\mathbf{q} = \int \dot{\mathbf{q}}(t)dt \Rightarrow \mathbf{q}_{k+1} = \int_{t_k}^{t_{k+1}} \dot{\mathbf{q}}(t)dt + \mathbf{q}_k \\ &\big(\mathbf{q}_{k+1} - \mathbf{q}_k\big) = \int_{t_k}^{t_{k+1}} \dot{\mathbf{q}}(t)dt \approx \frac{\Delta t}{2}\big\{\dot{\mathbf{q}}_{k+1} + \dot{\mathbf{q}}_k\big\} \quad (\textit{trapezoidal rule}) \\ &\Rightarrow \boxed{\dot{\mathbf{q}}_{k+1} = \frac{2}{\Delta t}\cdot\big(\mathbf{q}_{k+1} - \mathbf{q}_k\big) - \dot{\mathbf{q}}_k} \end{aligned} \tag{3.7}$$

Of course generalizations of these two basic schemes are possible leading to linear multistep methods (i.e. Runge-Kutta, Gear's algortithm), in which at a single iteration, the function $\mathbf{F}(\mathbf{x}(t), t)$, the charge $\mathbf{q}(\mathbf{x}(t))$ and its derivative $\mathrm{d}\mathbf{q}(\mathbf{x}(t))/\mathrm{d}t$ are evaluated in more than one past time-point and a linear combination is produced [6]:

$$\dot{\mathbf{q}}_{k+1} = \alpha_0\mathbf{q}_{k+1} + \alpha_1\mathbf{q}_k + \alpha_2\mathbf{q}_{k-1} + \ldots + \alpha_k\mathbf{q}_{n+1-k} \tag{3.8}$$

Moreover, techniques to adjust the time step depending on the "stiffness" of the problem have been implemented [7]. In fact, is computationally more efficient not to use a *fixed* time step but

rather adapt it every time according to the circuit being considered (lumped vs. distributed) and to the signals being processed (continuous vs. sharp-edged).

Using time domain methods it is possible to obtain the "whole" solution, including the start-up transient and the steady state, in a fixed interval. This however imposes a computational burden in terms of simulation time when the integration step is small and the transient is long-lasting, as in oscillating waveform build-up [8]. In this case the integration step should be small enough to catch the rapid carrier wave variations, but a long time is needed for the transient to be over. Moreover examining circuits with distributed elements, is necessary to take into account the delays associated with the propagation of voltage or current waves inside the circuit, which leads to a Differential Delay Equation (DDE):

$$\boldsymbol{\Gamma}\left(\mathbf{x}(t),\quad \mathbf{z}(t-\tau_i),\quad \frac{d\mathbf{x}}{dt},\quad \mathbf{f}(\mathbf{x}(t),\mathbf{z}(t),t),\quad t\right)=\mathbf{0},\qquad \tau=\left[\tau_1,\tau_2,\cdots,\tau_l\right]^T \tag{3.9}$$

in which $\boldsymbol{\Gamma}(.)$ represents a nonlinear operator, $\mathbf{z}(t)$ expresses the state of the distributed elements and $\boldsymbol{\tau}$ is a vector containing all the delays associated with distributed elements, assuming they are independent of the state variables. It is clear that for stiff nonlinearities in a circuit with multiple distributed elements and containing very different frequency components, solving this set of equations could be very time consuming, so it is preferable to approach the problem in another way as it will be seen in the next subsection.

3.1.2 Transient Analysis via Convolution

In order to overcome the limitation of the time domain approach, outlined in the previous section the convolution technique is introduced [9]. It allows taking into account *linear, passive and dispersive elements* which natively possess a frequency domain description (i.e. S-parameters data from multi-port networks, distributed elements like transmission lines). Suppose a component is characterized by a frequency domain transfer function *H(ω); its impulse response can be obtained by a straightforward Inverse Fourier Transform:*

$$h(t)=\mathcal{F}^{-1}\{H(\omega)\}=\int_{-\infty}^{+\infty}H(\omega)\cdot e^{j\omega t}d\omega \tag{3.10}$$

and the input output relationship can be thus written as a *convolution integral:*

$$\begin{aligned} &y(t)=x(t)*h(t)=\int_{-\infty}^{t}x(t-\tau)h(\tau)d\tau \\ &\Rightarrow y_k=\sum_{m=o}^{M}h_m x_{k-m} \end{aligned} \tag{3.11}$$

conveniently approximated by a sum over the past *M* samples, starting from the *k*-th one. The equations (3.3)—(3.5) get modified by the introduction of this additional terms. For example, in the case of (3.4) considering for simplicity the one dimensional case (generalization is straightforward) it is obtained:

$$\frac{q(x_{k+1})-q(x_k)}{t_{k+1}-t_k}=F(x_{k+1},t_{k+1})+\sum_{m=o}^{M}h_m x_{k-m} \tag{3.12}$$

The computational cost as well as the storage requirements increase, since at each step the sum (3.11) involving M past values of the state variables need to be evaluated. Moreover, convolution integral is computed employing a constant time step. If the equation (3.12) needs to be solved with an adaptive time step, the time points needed for numerically evaluating the convolution integral in *x(t)*, might actually not overlap with those corresponding to the past values of the impulse response *h(t)*. They could be retrieved by using interpolation algorithms, at the expense of further complications, and increasing the error.

A major source of problems with the convolution approach lies in the fact that, being the impulse response $s(t)$ a time-limited signal, then necessarily the transfer function $S(\omega)$ must be defined across an infinite bandwidth [3], which is practically unfeasible, since all measurements/ models for every device/component are specified in relation to a limited frequency band. Conversely, a band-limited transfer function produces a non-causal impulse response. The impulse response non-causality could be removed by suitably windowing the transfer function in order for it to become null past a certain frequency ω_L (cascading a low pass filter), but this would inevitably cause a distortion in the phase response, invalidating the results. As indicated in [3] a solution to this problem is obtained by considering *the impulse response* $h(t)$ a *discrete function of time*, with *finite duration* and therefore *periodically extending the transfer function* $H(\omega)$ in the frequency domain. After the periodic extension of the function $H(\omega)$ is available, then it could be windowed, having care in choosing a frequency ω_L for which $X(\omega)$ (the spectrum of $x(t)$) presents negligible power.

The extension to multidimensional case consist in considering a multiport network with associated transfer functions $H_{pq}(\omega)$ p, q =1,…,n with an input output relationship:

$$\begin{aligned}
&Y_p(\omega)=H_{pq}(\omega)X_q(\omega)\xrightleftharpoons[\mathcal{F}\{.\}]{\mathcal{F}^{-1}\{.\}}y_p(t)=\int_{-\infty}^{t}x_q(t-\tau)h_{pq}(\tau)d\tau=h_{pq}(t)*x_q(t)\\
&Y_p(\omega)\xrightleftharpoons[\mathcal{F}\{.\}]{\mathcal{F}^{-1}\{.\}}y_p(t);\ H_{pq}(\omega)\xrightleftharpoons[\mathcal{F}\{.\}]{\mathcal{F}^{-1}\{.\}}h_{pq}(t);X_q(\omega)\xrightleftharpoons[\mathcal{F}\{.\}]{\mathcal{F}^{-1}\{.\}}x_q(t)\\
&\Rightarrow \mathbf{Y}(\omega)=\begin{bmatrix}H_{11}(\omega) & \cdots & H_{1n}(\omega)\\ \vdots & \ddots & \vdots\\ H_{n1}(\omega) & \vdots & H_{nn}(\omega)\end{bmatrix}\cdot\begin{bmatrix}X_1(\omega)\\ \vdots\\ X_n(\omega)\end{bmatrix}\xrightleftharpoons[\mathcal{F}\{.\}]{\mathcal{F}^{-1}\{.\}}\\
&\Rightarrow\ \mathbf{y}(t)=\begin{bmatrix}h_{11}(t) & \cdots & h_{1n}(t)\\ \vdots & \ddots & \vdots\\ h_{n1}(t) & \vdots & h_{nn}(t)\end{bmatrix}*\begin{bmatrix}x_1(t)\\ \vdots\\ x_n(t)\end{bmatrix}
\end{aligned} \tag{3.13}$$

and the equations (3.1) get modified accordingly with the addition of the convolution term:

$$\begin{aligned}
&\frac{d\mathbf{q}}{dt}(\mathbf{x}(t))=\mathbf{g}(\mathbf{x}(t))+\mathbf{j}_s(t)+\mathbf{y}(t)=\mathbf{g}(\mathbf{x}(t))+\mathbf{j}_s(t)+\mathbf{h}(t)*\mathbf{x}(t)\\
&\mathbf{x}(t_0)=\mathbf{x}_0
\end{aligned} \tag{3.14}$$

3.1.3 SHOOTING METHODS FOR DETECTING THE PERIODIC STEADY STATE.

The examples hitherto considered have shown the possibilities offered by time domain methods related with the analysis of the transient behavior in microwave circuit. In many cases it is of uttermost importance to quickly reveal if a circuit is capable of reaching a periodic steady state. In fact, this is often the case in oscillators; a pure transient simulation would be cumbersome if implemented with the direct integration/convolution methods, since many periods of the high frequency carrier wave need to be integrated before its amplitude settles to a constant value. A faster approach could be used to verify the onset of a periodic regime. Specifically an initial guess for both the initial state $\mathbf{x}_0=\mathbf{x}(t_0)$ and the fundamental period T must be provided[5]. Then the systems (3.1) is integrated with the schemes previously discussed in one period, obtaining a succession of values:

$$\mathbf{x}_0 = \mathbf{x}(t_0) \equiv \mathbf{x}(0) \rightarrow \mathbf{x}_1 = \mathbf{x}(t_1) \rightarrow ... \rightarrow \mathbf{x}_S = \mathbf{x}(t_S) \equiv \mathbf{x}(T) \tag{3.15}$$

the values of $\mathbf{q}(.)$ being determined accordingly. The value $\mathbf{x}(T)$ depends clearly on the choice of the initial guess $\mathbf{x}_0$, but since the function $\mathbf{x}(t)$ is periodic it should be:

$$\mathbf{x}(T) = \boldsymbol{\xi}(\mathbf{x}_0) = \mathbf{x}_0 \tag{3.16}$$

and in case a discrepancy between the boundary values occurred, the initial state is recomputed in order to fulfill the periodicity condition, by means of a nonlinear zero finding algorithm for the following function:

$$\Phi(\mathbf{x}_0) = \mathbf{x}(T) - \mathbf{x}_0 = \boldsymbol{\xi}(\mathbf{x}_0) - \mathbf{x}_0 = \mathbf{0} \tag{3.17}$$

Each iteration of the zero finding algorithm (i.e. Newton Raphson method), corresponds to an integration of the system (3.1) starting from a different initial state. Therefore, shooting methods represent a valid alternative when the computational time for solving the implicit system (3.17) is considerably less than the time required to integrate many periods via direct integration. Provided a good estimate for *the period T and the intial state* is given, shooting methods in general outperform the conventional time domain methods in terms of computation speed.

3.2 FREQUENCY DOMAIN METHODS. HARMONIC BALANCE.

A time domain simulation requires considerable computation effort. Nevertheless, the evaluation of the transient behaviour of a microwave circuit is often unnecessary, since in many cases it is solely required the steady state response to a given periodic excitation[6]. Supposing that the expected solution $\mathbf{x}(t)$ preserves the periodicity T_0 of the input signal $j_s(t) = j_s(t + pT_0)$, $p = \pm1, \pm2,\ldots$,

[5] In the case of forced (non-autonomous) circuits driven by a single frequency signal at f_0, $T=(1/f_0)$. In case of autonomous circuits, the period must be guessed, by having recourse to linear analysis techniques aimed at estimating the small signal oscillation frequency.

[6] As in the case of microwave power amplifiers, whose steady state response must be evaluated using a large signal approach.

a convenient choice would be to expand it by means of a Fourier series with unknown *harmonic terms* $\mathbf{X}_k$ ($\omega_0=2\pi/T_0$) :

$$\mathbf{x}(t)=\sum_{k=-\infty}^{+\infty}\mathbf{X}_k e^{jk\omega_0 t}\ ,\ \mathbf{X}_k=\frac{1}{T_0}\int_{-T_0/2}^{T_0/2}\mathbf{x}(t)\cdot e^{-jk\omega_0 t}dt \tag{3.18}$$

which replaced in the original system (3.1) or (3.4) delivers a *balance for the generalized currents* at *each harmonic* $\mathbf{X}_k$ (hence the name) in the form of a nonlinear algebraic system which is much more easy to solve, speeding up computation times for periodic steady state. This represents the essence of the *Harmonic Balance* method; compared to the time domain scheme, the information provided by *the forcing generators* is used for establishing the actual steady state solution, avoiding lengthy transient computation. Being the input signal periodic with angular frequency ω_0, the steady state will consist in a *replica of the driving signal but with a different spectral content*. The attention, is thus shifted from the knowledge of the entire waveform in a given temporal observation window, to the knowledge of its spectrum, assuming a periodic regime could be achieved under the action of the inputs.

Since it is based on a *frequency domain* description, the Harmonic Balance method is suitable for smoothly simulating large circuits containing distributed components which are natively characterized by frequency dependent parameters (i.e. multiport scattering parameters black boxes), without presenting the issues related to the convolution approach illustrated earlier.

However, this framework presents drawbacks too. In periodically forced circuits, very different regimes could be established, other than the periodic one for example subharmonic generation, or chaotic behaviour [3]; expressing the solution in terms of Fourier Series doesn't allow to analyze the most general steady state behaviour. Moreover, due to computing time vs complexity trade-off and to storage requirements, the series (3.18) needs to be truncated retaining only the first ($2N_h$ +1) terms:

$$\mathbf{x}(t)=\sum_{k=-N_h}^{+N_h}\mathbf{X}_k e^{jk\omega_0 t} \tag{3.19}$$

The *trigonometric partial sum* doesn't lend itself well to the analysis of periodic signal characterized by sharp/fast transitions[7], due to "ringing" or Gibbs' phenomenon near a discontinuity [10]. In order to reduce this effect, many harmonic terms must be included in the sum (3.19) complicating the calculations [11]. Finally, when dealing with autonomous circuits, noteworthy with oscillators, due to the absence of the input generators, the solution could erroneously converge to a zero frequency, nonoscillatory state, since the only available sources are given by DC generators.

In the following, two approaches are used to describe the Harmonic Balance method. The first, called *Nodal Harmonic Balance* replaces the time domain description (3.1), (3.14) with a system of nonlinear equations in the generalized phasors $\mathbf{X}_k$. This method presents the inconvenient of generating a large number of variables to solve the system; in fact taking into account that the state vector is n-dimensional, and that ($2N_h$+1) phasors characterize the periodic regime, a total of n*($2N_h$+1) variables should be found. In another approach called *Piecewise Harmonic Balance*, the network under investigation is split into a *linear part*, containing linear lumped reactive elements

[7] For example, in the case of a train of rectangular pulses modelling logical switching between two voltage levels.

and distributed parameters ones, and a *non linear part* containing the active devices. The interconnection among the two subsets takes place at q ports, with $q \ll n$ and thus requiring less variables for describing the steady state response. This framework is presented in relation to multi-tone driven circuits, exploring the Harmonic Balance capabilities of dealing with almost-periodic waveform, like the ones arising in two-tone test on a microwave amplifier for investigating the intermodulation products.

3.2.1 Single Input, Single-Frequency, Nodal Harmonic Balance for Periodic Steady State Analysis in Non-Autonomous Circuits.

The Fourier Series expansion for the vector $\mathbf{x}(t)$ (3.18) could be directly substituted in the governing equations in the time domain description (3.14) (containing the convolution term). However, the presence of nonlinear charge $\mathbf{q}(\mathbf{x}(t))$, and conductance $\mathbf{g}(\mathbf{x}(t))$ hinder a straightforward approach, since the Fourier series expansion doesn't commute with the composed functions $(\mathbf{q} \circ \mathbf{x})(t)$, $(\mathbf{g} \circ \mathbf{x})(t)$. Therefore, the nonlinear functions *must be evaluated in the time domain first* by applying the (3.18) to the functions $\mathbf{q}(.)$ $\mathbf{g}(.)$, and then derive the harmonic components $\mathbf{Q}_k$, $\mathbf{G}_k$ which will depend on the harmonic component of the state vector, $\mathbf{X}_k$:

$$
\begin{aligned}
&\mathbf{x}(t) \xrightarrow{\mathcal{F}} \{\ldots, \mathbf{X}_{-N}, \mathbf{X}_{-N+1}, \ldots \mathbf{X}_k, \ldots \mathbf{X}_{N-1}, \mathbf{X}_N, \ldots\}; \ \mathbf{X}_k = \left[X_{k1}, \ldots, X_{km}\right]^T \\
&\mathbf{q}(\mathbf{x}(t)) = \mathbf{q}\left(\sum \mathbf{X}_k e^{jk\omega_0 t}\right) = \sum \mathbf{Q}_k(\mathbf{X}_k) e^{jk\omega_0 t} \Rightarrow \mathbf{Q}_k(\mathbf{X}_k) = \frac{1}{T_0}\int_{-T_0/2}^{T_0/2} \mathbf{q}\left(\sum \mathbf{X}_k e^{jk\omega_0 t}\right) \cdot e^{-jk\omega_0 t} dt \\
&\mathbf{g}(\mathbf{x}(t)) = \mathbf{g}\left(\sum \mathbf{X}_k e^{jk\omega_0 t}\right) = \sum \mathbf{G}_k(\mathbf{X}_k) e^{jk\omega_0 t} \Rightarrow \mathbf{G}_k(\mathbf{X}_k) = \frac{1}{T_0}\int_{-T_0/2}^{-T_0/2} \mathbf{g}\left(\sum \mathbf{X}_k e^{jk\omega_0 t}\right) \cdot e^{-jk\omega_0 t} dt \\
&j_s(t) = \sum J_{sk} e^{jk\omega_0 t}, \quad \mathbf{y}(t) = \sum \mathbf{Y}_k e^{jk\omega_0 t}
\end{aligned}
\tag{3.20}
$$

Although an infinite number of harmonics is needed to synthesize the time domain waveform, to be of some use in practical circumstances, the Fourier Series (3.18) ought to be truncated after a certain order[8] N_h giving rise to the partial sum indicated in (3.19).The transformations (3.20) between time domain and frequency domain, which need to be performed numerically, require *time domain data in form of discrete sequences*, obtained by sampling the waveform $\mathbf{x}(t)$. If the bandwidth of $\mathbf{x}(t)$ is limited up to $f_m = N_h \cdot f_0$ (equation (3.19)), for the Nyquist Theorem, its reconstruction *is possible by* sampling it at regularly spaced points in time, with a *sampling period*[9] $T_s \leq (1/2f_m)$ obtaining the *discrete time* version of $\mathbf{x}(t)$:

[8] In order to take correctly into account the waveform distortion due to nonlinearities, the harmonic terms up to the third order should be included.

[9] In many commercial simulators, is given the possibility of choosing the *oversample* function, enabling a sampling frequency (period) which is a multiple (submultiple) of the minimum (maximum) Nyquist rate (Nyquist Period), allowing a more precise estimation of the nonlinear (active) devices in the time domain.

$$\tilde{\mathbf{x}}(t)=\sum_{m=-\infty}^{+\infty}\mathbf{x}(t)\delta(t-mT_s)=\sum_{m=-\infty}^{+\infty}\mathbf{x}(mT_s)\delta(t-mT_s)$$
$$\therefore\ \mathbf{x}(t)=\mathbf{x}(t+hT_0),\quad h\in\mathbb{Z} \tag{3.21}$$
$$\boxed{\tilde{\mathbf{x}}(t)=\sum_{m=0}^{M-1}\mathbf{x}(mT_s)\delta(t-mT_s)}$$

since the function $\mathbf{x}(t)$ is periodic, M samples suffice for describing its behaviour in time. Therefore the *k-th* harmonic terms corresponding to the function shown in (3.24) will be, after having normalized the fundamental period setting T_0=1;

$$\mathbf{X}_k=\mathbf{X}(jk\omega_0)=\frac{1}{T_0}\int_{-T_0/2}^{T_0/2}\tilde{\mathbf{x}}(t)\cdot e^{-jk\omega_0 t}dt=\frac{1}{T_0}\int_{-T_0/2}^{T_0/2}\left(\sum_{m=0}^{M-1}\mathbf{x}(mT_s)\delta(t-mT_s)\right)\cdot e^{-jk\omega_0 t}dt$$
$$if: T_s=\frac{T_0}{2N_h+1},\ then:\ M=(2N_h+1)\ samples\ in\left[-\frac{T_0}{2},\frac{T_0}{2}\right]\Rightarrow$$
$$\mathbf{X}_k=\frac{1}{T_0}\sum_{m=0}^{M-1}\mathbf{x}(mT_s)e^{-jk\omega_0\cdot mT_s}=\frac{1}{T_0}\sum_{m=0}^{M-1}\mathbf{x}(mT_s)e^{-j2\pi\frac{k\cdot m}{2N_h+1}} \tag{3.22}$$
$$\mathbf{x}_m=\mathbf{x}(mT_s)$$
$$setting: T_0=1\Rightarrow\boxed{\mathbf{X}_k=\sum_{m=0}^{M-1}\mathbf{x}_m e^{-j\frac{2\pi}{M}k\cdot m}},\quad \begin{matrix}-N_h\le k\le N_h\\ M=(2N_h+1)\end{matrix}$$

defining a transformation rule between a sequence of samples in the time domain known as *Discrete Fourier Transform* (DFT) [12] which can also be inverted providing the Inverse Fourier Discrete Transform (IDFT):

$$\boxed{\mathbf{x}_m=\frac{1}{K}\cdot\sum_{k=-N_h}^{N_h}\mathbf{X}_k e^{j\frac{2\pi}{K}m\cdot k}}\quad\begin{matrix}K=2N_h+1\\ m=0,1,...M-1\end{matrix} \tag{3.23}$$

offering the possibility to reconstruct the time sequence for $\mathbf{x}(t)$ from the knowledge of its harmonic terms[10]. Therefore operations carried out in (3.20) can be symbolically denoted by having recourse to the direct and inverse Discrete Fourier Transform operator:

$$\mathbf{X}_k=\mathcal{F}\{\mathbf{x}_m\},\ \mathbf{x}_m=\mathcal{F}^{-1}\{\mathbf{X}_k\};$$
$$\mathbf{Q}_k(\mathbf{X}_k)=\mathcal{F}\left\{\mathbf{q}\left(\mathbf{x}_m\right)\right\}=\mathcal{F}\left\{\mathbf{q}\left(\mathcal{F}^{-1}\{\mathbf{X}_k\}\right)\right\}$$
$$\mathbf{G}_k(\mathbf{X}_k)=\mathcal{F}\left\{\mathbf{g}\left(\mathbf{x}_m\right)\right\}=\mathcal{F}\left\{\mathbf{g}\left(\mathcal{F}^{-1}\{\mathbf{X}_k\}\right)\right\} \tag{3.24}$$
$$J_{s,k}=\mathcal{F}\{j_{s,m}\},\ \mathbf{Y}_k=\mathcal{F}\{\mathbf{y}_m\}=\left[\mathbf{H}(j\omega_0 k)\right]\cdot\mathbf{X}_k$$

Substituting (3.24) into (3.14), an equation involving infinite sum of complex exponentials is obtained, which is fulfilled by equating each harmonic term, due to the orthonormality of the basis of complex exponentials $\{e^{jk\omega_0 t}\}_{k\in\mathbb{Z}}$:

[10] In reality, Fast Fourier Transform (FFT) algorithms are used to efficiently switch between time and frequency domain data [3].

$$\boxed{-jk\omega_0\mathbf{Q}_k(\mathbf{X})=\mathbf{G}_k(\mathbf{X})+\mathbf{J}_{sk}+[\mathbf{H}(jk\omega_0)]\cdot\mathbf{X}_k} \quad k\in\{-N_h,...,0,...,N_h\}$$

where

$$\begin{aligned}
&\mathbf{X}=\left[\mathbf{X}_{-N_h},...,\mathbf{X}_k,...,\mathbf{X}_{N_h}\right]^T \quad \mathbf{X}_k=\left[X_k^1,...,X_k^i,...,X_k^n\right]^T\\
&\mathbf{J}_{sk}=\left[J_{sk},0,0,...,0\right]^T\\
&\mathbf{G}_k(\mathbf{X})=\left[G_k^1(\mathbf{X}),...,G_k^j(\mathbf{X}),...G_k^s(\mathbf{X})\right]^T=\left[G_k^1\left(\mathbf{X}_{-N_h},...,\mathbf{X}_k,...,\mathbf{X}_{N_h}\right),...,G_k^s(\mathbf{X}_{-N_h},...,\mathbf{X}_k,...,\mathbf{X}_{N_h})\right]^T\\
&\mathbf{Q}_k(\mathbf{X})=\left[Q_k^1(\mathbf{X}),...,Q_k^h(\mathbf{X}),...Q_k^r(\mathbf{X})\right]^T=\left[Q_k^1\left(\mathbf{X}_{-N_h},...,\mathbf{X}_k,...,\mathbf{X}_{N_h}\right),...,Q_k^r(\mathbf{X}_{-N_h},...,\mathbf{X}_k,...,\mathbf{X}_{N_h})\right]^T
\end{aligned} \tag{3.25}$$

in which the convolution term $\mathbf{y}(t)$ has been transferred in the frequency domain, and the derivation is performed by multiplying the charge term by $(-jk\omega_0)$. The system (3.25) is still *nonlinear but algebraic in the n-dimensional vector* $\mathbf{X}_k$; defining the *error function*:

$$\mathbf{E}(\mathbf{X}_k)=jk\omega_0\mathbf{Q}_k(\mathbf{X})+\mathbf{G}_k(\mathbf{X})+\mathbf{J}_{sk}+[\mathbf{H}(jk\omega_0)]\cdot\mathbf{X}_k \tag{3.26}$$

the unknown coefficients $\mathbf{X}_k$ must satisfy the condition:

$$\mathbf{E}(\mathbf{X}_k)=\mathbf{0} \tag{3.27}$$

and thus can be easily found by means of a *multidimensional zero finding algorithm*, like the *Newton-Raphson* method, which given a suitable initial guess $\mathbf{X}_k^{(0)}$ converges quadratically to the solution [13].This iterative method, starting from an initial state, computes the solution by means of a local approximation of the nonlinear function $\mathbf{E}(.)$ to its tangent hyperplane. For each harmonic component of $\mathbf{X}_h$ with $-N_h\le k,h\le N_h$:

$$\Delta\mathbf{E}(\mathbf{X}_k)=\mathbf{E}(\mathbf{X}_k^{(i+1)})-\mathbf{E}(\mathbf{X}_k^{(i)})\approx\frac{\partial\mathbf{E}}{\partial\mathbf{X}_k}\Delta\mathbf{X}=\left[\mathbf{J}_{\mathbf{E}}(\mathbf{X}_k)\right]^{(i)}\left(\mathbf{X}_k^{(i+1)}-\mathbf{X}_k^{(i)}\right)=\left[\frac{\partial E_h^r}{\partial X_k^s}\right]\Bigg|_{\substack{1\le r\le n\\1\le s\le n}}^{(i)}\cdot\left(\mathbf{X}_k^{(i+1)}-\mathbf{X}_k^{(i)}\right) \tag{3.28}$$

where $[\mathbf{J}_{\mathbf{E}}(\mathbf{X})]^{(i)}$ denotes the Jacobian matrix associated to the function defined in (3.26), evaluated at the *i*-th step[11]. Assuming that $\mathbf{X}_k^{(i+1)}$ is a better estimate than $\mathbf{X}_k^{(i)}$ results $\mathbf{E}(\mathbf{X}_k^{(i+1)})\approx\mathbf{0}$. Then it follows:

$$-\mathbf{E}(\mathbf{X}_k^{(i)})=\left[\mathbf{J}_{\mathbf{E}}^{(i)}(\mathbf{X}_k)\right]\cdot\left(\mathbf{X}_k^{(i+1)}-\mathbf{X}_k^{(i)}\right)\rightarrow\mathbf{X}_k^{(i+1)}=\mathbf{X}_k^{(i)}-\left[\mathbf{J}_{\mathbf{E}}^{(i)}(\mathbf{X}_k)\right]^{-1}\cdot\mathbf{E}(\mathbf{X}_k^{(i)}) \tag{3.29}$$

The heaviest part of the Newton Raphson algorithm is represented by the Jacobian Matrix inversion. In literature are presented many methods aimed at *directly* or *iteratively* solving the equivalent system:

$$-\mathbf{E}(\mathbf{X}_k^{(i)})=\left[\mathbf{J}_{\mathbf{E}}^{(i)}(\mathbf{X}_k)\right]\cdot\Delta\mathbf{X}_k^{(i+1)} \tag{3.30}$$

[11] The Jacobian is evaluated numerically based on FFT data [3] [8]. The notation $[\partial E_k^r/\partial X_h^s]$ refers to the derivative of the *the r-th component* of the error function $\mathbf{E}_h(.)$ at the *h-th harmonic*, with respect to the *the s-th component* of the vector $\mathbf{X}_k$.

which is a *linear system* of the form $\mathbf{A\xi} = \boldsymbol{\beta}$ in the difference vector $(\mathbf{X}_k^{(i+1)} - \mathbf{X}_k^{(i)})$. Many commercial HB simulators implement a *direct solver* for the system (3.30) employing the Gaussian Elimination Method [14]. However, for large circuits with many elements and higher harmonic orders iterative solvers, based on a *Krylov Subspace approach,* like the generalized minimal residual method (GMRES) are preferred [15].

Newton-Raphson iterations are stopped when the *error function norm*[12] takes value below a certain threshold $\| \mathbf{E}(\mathbf{X}_k^{(i)}) \| < \varepsilon$ or when the solution at a given step doesn't significantly differ from the solution at the previous one i.e. $\| \mathbf{X}_k^{(i+1)} - \mathbf{X}_k^{(i)} \| < \delta$ with ε, δ being pre-assigned tolerances. As the function $\mathbf{E}(.)$ has the dimension of a *current* and $\mathbf{X}$ is generally a vector of *voltages* a good choice might be setting ε=100μA, δ=1mV in practical implementations. When convergence is achieved, from the harmonic terms $\mathbf{X}_k$, $-N_h \le k \le N_h$ the samples $\mathbf{x}_m$ $m = 0, \ldots, 2N_h+1$ are obtained by an Inverse Fourier transform: $\mathbf{x}_m = \mathcal{F}^{-1}\{ \mathbf{X}_k\}$, enabling a complete characterization of the time domain steady state waveform over the fundamental period $T_0 = 2\pi/\omega_0$.

3.2.2 Multi-Input, Multi-Frequency Piecewise Harmonic Balance for Almost-Periodic Steady State Analysis in Non-autonomous circuits

As mentioned earlier, in the Nodal Harmonic Balance method the state vector is represented in terms of its spectral content $\mathbf{X}_k$ up to the order $K=2N_h+1$, and therefore $n*(2N_h+1)$ complex quantities need to be found by solving the nonlinear system $\mathbf{E}(\mathbf{X}_k)=\mathbf{0}$. The dimension of the Jacobian matrix used for obtaining the solution grows proportionally to the circuit dimension; thus for very large circuits employing many harmonic terms in the series (3.18), this approach turns out to be not very effective, in terms of computation time and storage requirements[13].

It is noteworthy to observe that microwave circuits are constituted for the most part by *linear blocks* representing *passive interconnections* (transmission lines), input/output *impedance matching sections*, hybrid lumped-distributed element used for *filtering purposes*, DC feed/ block networks, with *comparatively few active devices* (notably FETs) which are responsible for the nonlinear effects. Thus, it would be more convenient to split the network in two parts; a part containing only linear elements and another part containing the nonlinearities *represented by*

[12] Various vector norms are defined. The most used in commercial simulators are the L_1*-norm,* the L_2*-norm* and the $L\infty$ *-norm,* defined respectively as:

$$\|\mathbf{x}\|_1 = \sum_{i=1}^{\dim(\mathbf{x})} |x_i| \quad , \quad \|\mathbf{x}\|_2 = \sqrt{\sum_{i=1}^{\dim(\mathbf{x})} x_i^2} \quad , \quad \|\mathbf{x}\|_\infty = \max_{i=1,\ldots,\dim(\mathbf{x})} \{x_i\}$$

[13] Although the Jacobian Matrix size grows, it turns out to be very sparse, meaning that the nonzero entry are a few ones (comparatively with the matrix dimension). The system $\mathbf{E}(\mathbf{X}_k)=\mathbf{0}$, could then be more efficiently solved by having recourse to methods that exploit the *sparsity of* $[\mathbf{J}_\mathbf{E}(\mathbf{X}_k)]$ see [8] [11].

controlled sources. The *Piecewise Harmonic Balance* formulation is obtained by imposing the Kirchhoff Current Law among these last two subsets at every harmonic term [3] [8].

Let's suppose a generic microwave circuit is driven by S independent generators (represented by the vector $\mathbf{g}(t)$) which acting as *independent sources* (known terms), provide the *set of H fundamental incommensurable frequencies*[14] $\boldsymbol{\Omega} = (\omega_1, \omega_2, \ldots, \omega_H)$ with $H \le S$. The nonlinear devices outputs, treated as *controlled sources,* are identified with the Q- dimensional vector $\mathbf{y}(t)$ which depends upon the *controlling variables* expressed by the P-dimensional vector $\mathbf{x}(t)$, taken at P *ports* :

$$\begin{aligned} \mathbf{x}(t) &= (x_1(t), x_2(t), \cdots, x_P(t))^{\mathrm{T}} \\ \mathbf{y}(t) &= (y_1(t), y_2(t), \cdots, y_Q(t))^{\mathrm{T}} \\ \mathbf{g}(t) &= (g_1(t), g_2(t), \cdots, g_S(t))^{\mathrm{T}} \end{aligned} \qquad \mathbf{y}(t) = \boldsymbol{\Psi}\left(\mathbf{x}(t),\ \mathbf{x}(t-\tau),\ \frac{d\mathbf{x}}{dt},\ \cdots,\ \frac{d^m\mathbf{x}}{dt^m} \right) \tag{3.31}$$

The functional relationship between the nonlinear outputs $\mathbf{y}(t)$ and the controlling variables $\mathbf{x}(t)$ is the most general possible; in other terms, $\mathbf{y}(t)$ could depend also on delayed replicas of the controlling vector , and present a generalized memory effect up to the *m-th order* modeled by the inclusion of the derivatives $\mathrm{d}\mathbf{x}/\mathrm{d}t$, $\mathrm{d}^2\mathbf{x}/\mathrm{d}t^2$, ….$\mathrm{d}\mathbf{x}^m/\mathrm{d}t^m$.

Since the *frequency basis* $\boldsymbol{\Omega}$ is constituted by a set of incommensurable frequencies, all the *linear combinations* involving the ω_i with *integer coefficients* must be considered; thus the original Fourier Series expansion formulation requires a generalization to deal with almost-periodic functions. To that aim defining a *vector of integers* $\boldsymbol{\kappa}=(k_1, k_2, \ldots, k_H)$, and considering the scalar product with the frequency basis $\boldsymbol{\Omega}\cdot\boldsymbol{\kappa} = \omega_1 k_1 + \omega_2 k_2 + \ldots + \omega_H k_H$, the extension to almost periodic functions of the Fourier series reads:

$$\mathbf{x}(t) = \sum_{\boldsymbol{\kappa}\in\mathbb{Z}^H} \mathbf{X}_{\boldsymbol{\kappa}} e^{j\boldsymbol{\Omega}\cdot\boldsymbol{\kappa}\, t} = \sum_{k_1=-\infty}^{+\infty} \cdots \sum_{k_H=-\infty}^{+\infty} \mathbf{X}_{k_1 k_2 \cdots k_H} e^{j(k_1\omega_1 + k_2\omega_2 + \cdots + k_H\omega_H)t} \tag{3.32}$$

$$\mathbf{y}(\mathbf{x}(t)) = \sum_{\boldsymbol{\kappa}\in\mathbb{Z}^H} \mathbf{Y}_{\boldsymbol{\kappa}}(\mathbf{X}_{\boldsymbol{\kappa}}) e^{j\boldsymbol{\Omega}\cdot\boldsymbol{\kappa}\, t} = \sum_{k_1=-\infty}^{+\infty} \cdots \sum_{k_H=-\infty}^{+\infty} \mathbf{Y}_{k_1 k_2 \cdots k_H}(\mathbf{X}_{k_1 k_2 \cdots k_h}) e^{j(k_1\omega_1 + k_2\omega_2 + \cdots + k_H\omega_H)t}$$

$$\mathbf{g}(t) = \sum_{\boldsymbol{\kappa}\in\mathbb{Z}^H} \mathbf{G}_{\boldsymbol{\kappa}} e^{j\boldsymbol{\Omega}\cdot\boldsymbol{\kappa}\, t} = \sum_{k_1=-\infty}^{+\infty} \cdots \sum_{k_H=-\infty}^{+\infty} \mathbf{G}_{k_1 k_2 \cdots k_H} e^{j(k_1\omega_1 + k_2\omega_2 + \cdots + k_H\omega_H)t} = \sum_{i=1}^{H} \left(\sum_{k_i=-\infty}^{+\infty} \mathbf{G}_{k_i} e^{jk_i\omega_i t} \right)$$

which, as shown for the case of a single periodic excitation must necessarily be truncated, discarding higher order terms which produce neglectful effects. The truncated series reads, for a generic vector $\mathbf{f}(t)$:

$$\mathbf{f}(t) = \sum_{\boldsymbol{\kappa}\in\boldsymbol{K}} \mathbf{F}_{\boldsymbol{\kappa}} e^{j\boldsymbol{\Omega}\cdot\boldsymbol{\kappa}\, t} \tag{3.33}$$

[14] Two frequencies ω_1, ω_2 are said to be commensurable when there exist two integers $a < b$ such that $a\omega_1 = b\omega_2$, that is the quantity (ω_1/ω_2) is a rational number. The analysis of a two inputs circuit driven by signals at two commensurate frequencies, is thus reduced to the inspection of a *single frequency input* $\omega_r = (b/a)\omega_1$.

where $\boldsymbol{K}$ represent the set of admissible values for each vectors of integer numbers $\boldsymbol{\kappa}$ taking part in the linear combination $\boldsymbol{\lambda}= \sum k_i\omega_i$. Different truncation schemes are possible according to the definition of the *truncation order.* Defining the order of the truncation as the 1-norm of the vector $\boldsymbol{\kappa}$, a *diamond truncation scheme* of order d is obtained whenever $\|k\|_1=\sum |k|_i \leq d$, *as outlined in (3.34)* [3] [8].

H –tones, d – order *diamond* truncation scheme:

$$\begin{aligned}
&\boldsymbol{K} = \left\{ \boldsymbol{\kappa} \in \mathbb{Z}^H \mid \mathcal{D}(\Lambda) \leq d \ (d \in \mathbb{N}) \right\} \\
&where: \\
&\mathcal{D}(\Lambda) = \left\| \boldsymbol{\kappa} \right\|_1 = \sum_{i=1}^{H} |k_i| \\
&\Lambda = \left\{ \boldsymbol{\lambda} \in \mathbb{R}^H \mid \boldsymbol{\lambda} = \sum_{i=1}^{H} k_i \omega_i, \ \omega_i \in \mathbb{R}, \ \forall k_i \in \mathbb{Z} \right\}
\end{aligned} \tag{3.34}$$

A much more simple and intuitive method consist in retaining only N_i harmonic terms for each fundamental frequency ω_i supplied by the independent sources, giving rise to *the box truncation scheme*; exploiting the Hermitean symmetry[15] of the harmonic coefficients for real valued signals the negative indices terms could be neglected.

$$\begin{aligned}
&\text{box truncation:} \left\{ |k_i| \leq N_1, |k_2| \leq N_2, ..., |k_H| \leq N_H \right\} \\
&\mathbf{f}(t) = \sum_{k_1=-N_1}^{+N_1} \cdots \sum_{k_H=-N_H}^{+N_H} \mathbf{F}_{k_1 k_2 \cdots k_H} e^{j(k_1\omega_1 + k_2\omega_2 + \cdots + k_H\omega_H)t}
\end{aligned}$$

$$\begin{aligned}
&\text{reduced box truncation for real signals} \\
&\mathbf{f}(t) \in \mathbb{R}^l \Rightarrow \mathbf{F}^*_{k_1 k_2 \cdots k_j \cdots k_H} = \mathbf{F}_{k_1 k_2 \cdots (-k_j) \cdots k_H} \Rightarrow \\
&\mathbf{f}(t) = \sum_{k_1=0}^{N_1} \cdots \sum_{k_H=0}^{N_H} \mathbf{F}_{k_1 k_2 \cdots k_H} e^{j(k_1\omega_1 + k_2\omega_2 + \cdots + k_H\omega_H)t}
\end{aligned} \tag{3.35}$$

Whatever the truncation scheme used, the almost periodic Fourier Series generalization suffers from the difficulties in *time to frequency conversion.* In fact, for an almost periodic function the integration *period* is not well-defined; analytically the multi-harmonic coefficients $\mathbf{F}_{k_1 k_2 \cdots k_H}$ could be found by taking the limit [16]:

$$\mathbf{F}_{k_1 k_2 \cdots k_H} = \lim_{T_0 \to +\infty} \frac{1}{2T_0} \int_{-T_0}^{T_0} \mathbf{f}(t) e^{-j(k_1\omega_1 + k_2\omega_2 + \cdots + k_H\omega_H)t} dt \tag{3.36}$$

but this formulation would present the additional issue of performing an integration over an unbounded interval requiring thus a perfect knowledge of the time domain waveform.

[15]Fourier coefficients of a real valued function possess *Hermitian symmetry*, i.e. a series coefficient evaluated at a negative index (-k) is the complex conjugate of the same coefficient computed in its (symmetrical to zero) positive index (+k). Therefore, is possible to set up an Harmonic Balance only for positive frequencies and exploit the last property to compute the coefficients at negative frequencies by a straightforward conjugation, halving the computation time.

Recently many methods have been proposed in the literature to ensure an accurate frequency time conversion of the multi-harmonic Fourier series introduced in (3.32). Theoretically speaking in fact, it is always possible to reconstruct the time domain waveform, by choosing a number of samples equal to the number of unknowns to be found[16]. Nevertheless, since the DFT matrices associated to the operations (3.22) and (3.23) becomes ill conditioned, it is crucial to device efficient sampling techniques to guarantee numerical stability, choosing properly the sampling instants [17], or performing the waveform oversampling. Another approach, consist in using the multidimensional (multi-rate) Fourier Series defined as:

$$\begin{aligned}
&\mathbf{f}(t_1,t_2,...t_H)=\sum_{k_1=-\infty}^{+\infty}\cdots\sum_{k_H=-\infty}^{+\infty}\mathbf{F}_{k_1k_2\cdots k_H}e^{j(k_1\omega_1t_1+k_2\omega_2t_2+\cdots+k_H\omega_Ht_H)}\\
&\mathbf{F}_{k_1,k_2,...,k_H}=\frac{1}{\prod_{i=1}^{H}T_{0i}}\int_{\tau}^{\tau+T_{01}}\int_{\tau}^{\tau+T_{02}}\cdots\int_{\tau}^{\tau+T_{0H}}\mathbf{f}(t_1,t_2,...t_H)\cdot e^{-j(k_1\omega_1t_1+k_2\omega_2t_2+\cdots+k_H\omega_Ht_H)}dt_1dt_2\cdots dt_H
\end{aligned}\tag{3.37}$$

in which arbitrary time scales are introduced in relation to each independent frequency so that the original function $\mathbf{f}(t)$ can be recovered by simply setting $t_1 = t_2 = \ldots = t_H = t$. By sampling with respect to each time variable, with a sampling rate dictated by each angular frequency ω_i, an *H-dimensional grid of* $M=\prod_{i=1,\ldots,H}(2N_i+1)$*samples is obtained.* Extending to the multidimensional case the (3.22) and (3.23) assuming that the function obeys the Nyquist Sampling Theorem:

$$\begin{aligned}
&\mathbf{F}_{k_1k_2\cdots k_H}=\frac{1}{\prod_{i=1}^{H}T_{0H}}\sum_{m_1=-N_1}^{N_1}\sum_{m_2=-N_2}^{N_2}\cdots\sum_{m_H=-N_H}^{N_H}\mathbf{f}(t_{m_1},t_{m_2},\ldots,t_{m_H})e^{-j(k_1\omega_1t_{m_1}+k_2\omega_2t_{m_2}+\cdots+k_H\omega_Ht_{m_H})}\\
&if:\ t_{m_1}=\left(\frac{T_{01}}{2N_1+1}\right)m_1,\ t_{m_2}=\left(\frac{T_{02}}{2N_2+1}\right)m_2,\cdots,t_{m_H}=\left(\frac{T_{0H}}{2N_H+1}\right)m_H\\
&(-N_1\le m_1\le N_1;-N_2\le m_2\le N_2;\ldots;-N_H\le m_H\le N_H)\\
&\Downarrow\\
&\mathbf{F}_{k_1k_2\cdots k_H}=\frac{1}{\prod_{i=1}^{H}T_{0H}}\sum_{m_1=-N_1}^{N_1}\sum_{m_2=-N_2}^{N_2}\cdots\sum_{m_H=-N_H}^{N_H}\mathbf{f}(t_{m_1},t_{m_2},\ldots,t_{m_H})e^{-j2\pi\left(\frac{k_1m_1}{2N_1+1}+\frac{k_2m_2}{2N_2+1}+\cdots+\frac{k_Hm_H}{2N_H+1}\right)}\\
&\mathbf{f}(t_{m_1},t_{m_2},\ldots,t_{m_H})=\sum_{k_1=-N_1}^{N_1}\cdots\sum_{k_H=-N_1}^{N_H}\mathbf{F}_{k_1k_2\cdots k_H}e^{j2\pi\left(\frac{k_1m_1}{2N_1+1}+\frac{k_2m_2}{2N_2+1}+\cdots+\frac{k_Hm_H}{2N_H+1}\right)}
\end{aligned}\tag{3.38}$$

Of course, it is necessary to set an upper bound to maximum number of tones, given that the Jacobian matrix becomes increasingly large, and dense. In case the computational resources are a concern, other techniques can be applied (artificial frequency remapping [18]).

By applying the aforementioned techniques the problem is transformed into the frequency domain and the objective becomes the determination of the harmonic components of the *controlling variables* vector $\mathbf{X}(\omega)$ at each one of the *P ports, knowing the nonlinear outputs* $\mathbf{Y}(\mathbf{X}(\omega))$ and the *forcing term* $\mathbf{G}(\omega)$; in this context the variable ω denotes the linear combination of frequencies $\sum k_i\omega_i$ for *every* $\boldsymbol{\kappa}$ vector $(k_1, k_2, \ldots, k_H)$ included in the truncation scheme; assuming the multi-tone harmonics

[16] Which in turn depends upon the truncation scheme employed.

are ordered from the lowest to the highest, the frequency domain image of a generic *D-dimensional* vector $\mathbf{x}(t)$ (representing indifferently one among the $\mathbf{x}(t)$, $\mathbf{y}(\mathbf{x}(t))$, $\mathbf{g}(t)$) can be cast into a matrix:

$$\begin{aligned}&\mathbf{f}(t)\xrightarrow{\mathcal{F}}\mathbf{F}(\omega)=[-\mathbf{F}_{N_{\max}},\ldots,\mathbf{F}_h,\ldots\mathbf{F}_{N_{\max}}]^T\\&\mathbf{F}_h=[F_{h1},F_{h2},\ldots F_{hD}]\end{aligned}\tag{3.39}$$

being each column the *h-harmonic component* ($-N_{\max} \le h \le N_{\max}$) of the vector. Since nonlinearities don't admit a frequency representation in terms of transfer functions, a Discrete Fourier Transform is employed to toggle from time domain samples to the spectral representation to get the vector $\mathbf{Y}(\omega)$, after having evaluated $\mathbf{y}(t)$ in the time domain :

$$\begin{gathered}\mathbf{X}(\omega)\xrightarrow{\mathcal{F}^{-1}}\mathbf{x}(t);\ \ \mathbf{y}(t)\xrightarrow{\Psi(\cdot)}\mathbf{y}(\mathbf{x}(t));\ \ \mathbf{y}(t)\xrightarrow{\mathcal{F}}\mathbf{Y}(\omega)=\mathcal{F}\left(\mathbf{y}\left(\mathcal{F}^{-1}\left(\mathbf{X}(\omega)\right)\right)\right)\Rightarrow\\\mathbf{Y}(\omega)=\mathbf{Y}(\mathbf{X}(\omega))\end{gathered}\tag{3.40}$$

Finally, Kirchhoff Current Law equations are written at the P ports, balancing the harmonic contributions coming from the vectors $\mathbf{X}(\omega)$, $\mathbf{Y}(\omega)$, $\mathbf{G}(\omega)$ which takes the form of a linear relationship between these three vectors [19]

$$\mathbf{E}(\mathbf{X}(\omega))=[\mathbf{A}(\omega)]\cdot\mathbf{X}(\omega)-[\mathbf{B}(\omega)]\cdot\mathbf{Y}(\mathbf{X}(\omega))-[\mathbf{C}(\omega)]\cdot\mathbf{G}(\omega)=\mathbf{0}\tag{3.41}$$

and in which $[\mathbf{A}(\omega)]$, $[\mathbf{B}(\omega)]$, $[\mathbf{C}(\omega)]$ are frequency dependent block diagonal matrix of adequate dimensions. Finally, the nonlinear system of differential equations has been converted to a nonlinear system of algebraic equations (since the relationship between $\mathbf{X}$ and $\mathbf{Y}$ is nonlinear),in the unknown set of harmonic vectors $\mathbf{X}(\omega)$ which must satisfy $\mathbf{E}(\mathbf{X}(\omega))=\mathbf{0}$. The method for finding the solution is analogous to that outlined in the previous subsection; Newton's method iteratively founds the best approximation for $\mathbf{X}(\omega)$ seeking to minimize the norm $\|\mathbf{E}(\mathbf{X}(\omega))\|_2$.

For the convergence process to succeed, a suitable guess of the initial state $\mathbf{X}_0$ is needed. This could be obtained from (9) by letting $\mathbf{Y}(\mathbf{X}(\omega))=\mathbf{0}$, assuming initially *low amplitude driving terms*:

$$\mathbf{X}_0=[\mathbf{A}^{-1}(\omega)]\cdot[\mathbf{C}(\omega)]\cdot\mathbf{G}(\omega)\tag{3.42}$$

Having obtained $\mathbf{X}_0$, it is straightforward get the value of the nonlinear outputs of the device ($\mathbf{Y}_0$) first by means of (3.40). This value is inserted in (3.41) and if produces an error that is lower than the prescribed tolerance, the algorithm stops, otherwise continues as detailed.

$$
\begin{array}{l}
\textit{Initialization} \\
\text{for } \{-N_m \le h \le N_m\} \ \{ \\
\mathbf{X}^{(0)}(\omega) \leftarrow [\mathbf{A}(\omega)]^{-1} \cdot [\mathbf{C}(\omega)] \cdot \mathbf{G}(\omega) \\
\mathbf{Y}^{(0)}(\omega) \leftarrow \mathcal{F}\left(\mathbf{y}\left(\mathcal{F}^{-1}\left(\mathbf{X}_h^{(0)}(\omega)\right)\right)\right) \\
\mathbf{E}\left(\mathbf{X}_h^{(0)}(\omega)\right) := [\mathbf{A}(\omega)] \cdot \mathbf{X}_h^{(0)}(\omega) - [\mathbf{B}(\omega)] \cdot \mathbf{Y}\left(\mathbf{X}_h^{(0)}(\omega)\right) - [\mathbf{C}(\omega)] \cdot \mathbf{G}(\omega) \\
\text{evaluate } \left\|\mathbf{E}(\mathbf{X}_h(\omega))\right\|_2 \\
\} \\
\textit{Norm}-2 \ \ \textit{Error Minization} \\
\text{while } \left\{\left\|\mathbf{E}(\mathbf{X}_h(\omega))\right\| > \varepsilon\right\} \\
\text{for } \{-N_m \le h \le N_m\} \quad \{ \\
\quad \textit{do } \{ \\
\qquad \mathbf{X}_h^{(k)}(\omega) \leftarrow \mathbf{X}_h^{(k\text{-}1)}(\omega) - \left[\mathbf{J}_{\mathbf{H}}\left(\mathbf{X}_h^{(k\text{-}1)}(\omega)\right)\right]^{-1} \mathbf{H}\left(\mathbf{X}_h^{(k\text{-}1)}(\omega)\right) \\
\qquad \mathbf{Y}_h^{(k)}(\omega) \leftarrow \mathcal{F}\left(\mathbf{y}\left(\mathcal{F}^{-1}\left(\mathbf{X}_h^{(k)}(\omega)\right)\right)\right) \\
\qquad \mathbf{E}\left(\mathbf{X}_h^{(k)}(\omega)\right) := [\mathbf{A}(\omega)] \cdot \mathbf{X}_h^{(k)}(\omega) - [\mathbf{B}(\omega)] \cdot \mathbf{Y}\left(\mathbf{X}_h^{(k)}(\omega)\right) - [\mathbf{C}(\omega)] \cdot \mathbf{G}(\omega) \\
\qquad \text{evaluate } \left\|\mathbf{E}(\mathbf{X}_h(\omega))\right\|_2 \\
\qquad \} \\
\quad \text{if } \left\{\left\|\mathbf{E}(\mathbf{X}_h(\omega))\right\|_2 \le \varepsilon\right\} \\
\qquad \text{print the solution } \mathbf{X}_h(\omega) \qquad \}
\end{array}
\tag{3.43}
$$

3.3 NUMERICAL CONTINUATION IN HARMONIC BALANCE.

The convergence of the Newton Raphson algorithm largely depends on the distance of the first estimate $\mathbf{X}^{(0)}$ from the actual solution $\mathbf{X}^{(t)}$ obtained after t steps [20]; if the initial guess is not close enough, the procedure outlined in (3.43) may diverge. In this case, it's possible to make the convergence more robust by considering a circuit parameter[17] $0 \le \rho \le 1$ such that the original stiff problem (3.41) becomes tractable for $\rho = 0$, providing the solution $\mathbf{X}_0$ which can be then used as a first hint *for a succession of simpler problems* $\{\mathbf{S}(\mathbf{X}, \rho), \rho \in [0,1]\}$ based on incremental values of the real parameter $\{\rho_1 < \rho_2 < ... < \rho_t\} \subset [0,1]$. For each value of ρ, a Harmonic Balance simulation is carried out and the result is taken as initialization (*initial guess*) of the subsequent step following the scheme

$$
\begin{array}{l}
i-th \ \text{iteration} \\
\left[\begin{array}{l}
\rho^{(i)} \leftarrow \rho_i \\
\mathbf{X}_0(\rho^{(i)}) \ \leftarrow \ \mathbf{X}^{(i-1)} \\
\downarrow \\
\mathbf{S}(\mathbf{X}, \rho^{(i)}) = \mathbf{0} \\
\downarrow \\
\mathbf{X}^{(i)} \leftarrow \mathbf{X}(\rho^{(i)})
\end{array}\right]
\end{array}
\tag{3.44}
$$

[17] It could be a fictitious one or a real one like a generator amplitude. Without loss of generality, ξ can be scaled, to take values in the unitary interval [0,1].

Thus, as the parameter ρ *approaches the final value* $\rho_t = 1$ the desired solution to the original stiff problem is obtained.

$$
\begin{array}{l}
/HB\ \ continuation \\
Choose\ a\ parameter\ \rho \in [0,1] \\
Set-up\ \ a\ system\ \ \mathbf{S}(\mathbf{X},\rho)\ \ such\ that \\
\begin{cases} \mathbf{S}(\mathbf{X}_0,0) = \mathbf{0} & /\ the\ system\ converges\ for\ \rho = 0 \\ \mathbf{S}(\mathbf{X},1) = \mathbf{E}(\mathbf{X}) & /\ the\ system\ reduces\ to\ \mathbf{E}(\mathbf{X})\ for\ \rho = 1 \end{cases} \\
/notation: \mathbf{X}(0) = \mathbf{X}_0,\ \mathbf{X}(1) = \mathbf{X}^{(t)},\ \rho_t = 1 \\
\boxed{\begin{array}{l}
\text{solve } \mathbf{S}(\mathbf{X}_0,0) = \mathbf{0} \\
\mathbf{X}(0) \leftarrow \mathbf{X}_0 \\
for\ \{1 \le i \le t\}\{ \\
i \leftarrow 1 \\
\rho^{(i)} \leftarrow \rho_i \\
\mathbf{X}_0(\rho^{(i)}) \leftarrow \mathbf{X}\ (\rho^{(i-1)}) \\
solve\ \mathbf{S}(\mathbf{X},\rho^{(i)}) = \mathbf{0} \\
i \leftarrow i+1 \\
\}
\end{array}} \\
if\ \{\mathbf{S}(\mathbf{X},\rho^{(t)}) = \mathbf{0}\} \\
plot\ the\ solution\ \mathbf{X}^{(t)} = \mathbf{X}(1)
\end{array}
\tag{3.45}
$$

This technique which is called *numerical continuation* (an algorithm is sketched in (3.45)) proves to be very useful when convergence problems arise due to stiff nonlinearities, for example in the case of high amplitude of RF signal source generators; by increasing continuously their amplitude starting from low values, the final solution can be obtained according to the following scheme:

$$
\begin{array}{ll}
\mathbf{S}(\mathbf{X}^{(0)},\rho)_{\rho=0} = \mathbf{0} & \\
\rho_1 = 0 & \mathbf{X}_0(\rho_1) = \mathbf{X}^{(0)} \xrightarrow{HB} \mathbf{X}(\rho_1) = \mathbf{X}^{(1)} \\
\rho_2 & \mathbf{X}_0(\rho_2) = \mathbf{X}^{(1)} \xrightarrow{HB} \mathbf{X}(\rho_2) = \mathbf{X}^{(2)} \\
\vdots & \\
\rho_i & \mathbf{X}_0(\rho_i) = \mathbf{X}^{(i-1)} \xrightarrow{HB} \mathbf{X}(\rho_i) = \mathbf{X}^{(i)} \\
\vdots & \\
\rho_t = 1 & \mathbf{X}_0(\rho_t) = \mathbf{X}^{(t-1)} \xrightarrow{HB} \mathbf{X}(\rho_t) = \mathbf{X}^{(t)} = \mathbf{X}(1) \\
\mathbf{S}(\mathbf{X}^{(t)},\rho)_{\rho=1} = \mathbf{E}(\mathbf{X}^{(t)}) = \mathbf{0} &
\end{array}
\tag{3.46}
$$

3.4 SOLUTION PATH FOLLOWING BY PARAMETRIC SWEEPS. MULTI-VALUED SOLUTION CURVE TRACING BY PARAMETER SWITCHING.

The numerical continuation method exposed in the previous section is used to aid convergence. In other terms, the solution obtained at a given iteration is always used as a first guess for solving the harmonic balance system at the next iteration, corresponding to the analysis at the new parameter value. A similar scheme could be used also for *multi-parametric analysis*. If

the nonlinear circuit under analysis depends on a set of continuous parameters ξ_1, ξ_2,…, ξ_p the harmonic balance system will read (considering the single tone analysis, for simplicity):

$$\mathbf{E}(\mathbf{X},\boldsymbol{\xi})=\mathbf{0},\ \mathbf{X}\in\mathbb{R}^{n\times(2N_h+1)},\ \boldsymbol{\xi}=\left[\xi_1,\xi_2,\ldots,\xi_p\right]\in\mathbb{R}^p$$

The Implicit Function Theorem (references on [21], [22]), provides conditions to ensure that the error function $\mathbf{E}(\mathbf{X},\boldsymbol{\xi})=0$ could be expressed as the graph of the function $\mathbf{X}=\mathbf{X}(\boldsymbol{\xi})$, which represent the multidimensional solution path, in a bounded region of the parameter space. In particular, the *Jacobian matrix of the function* $\mathbf{E}(.)$ with respect to the circuit variables $\mathbf{X}=[X_1, X_2,..., X_K]^T$ should *be continuous and nonsingular:*

$$\begin{aligned}
&\mathbf{X}\in\mathcal{A}\subset\mathbb{R}^K\ \ \boldsymbol{\xi}\in\mathcal{B}\subset\mathbb{R}^p,\ (\mathbf{a},\mathbf{b})\in\mathcal{A}\times\mathcal{B},\ \mathbf{E}\in\mathbb{R}^K, K=n(2N+1)\\
&\text{then } \mathbf{E}(\mathbf{X},\boldsymbol{\xi})=0\Leftrightarrow\mathbf{X}=\mathbf{X}(\boldsymbol{\xi}) \text{ iff } \det\left[\frac{\partial\mathbf{E}}{\partial\mathbf{X}}\right](\mathbf{a},\mathbf{b})\neq 0, \text{ where}\\
&J_{\mathrm{E}}(\mathbf{a},\mathbf{b})=\begin{bmatrix}
\frac{\partial E_1}{\partial X_1}(\mathbf{a},\mathbf{b}) & \cdots & \frac{\partial E_1}{\partial X_K}(\mathbf{a},\mathbf{b}) & \frac{\partial E_1}{\partial \xi_1}(\mathbf{a},\mathbf{b}) & \cdots & \frac{\partial E_1}{\partial \xi_p}(\mathbf{a},\mathbf{b})\\
\vdots & \ddots & \vdots & \vdots & \ddots & \vdots\\
\frac{\partial E_K}{\partial X_1}(\mathbf{a},\mathbf{b}) & \cdots & \frac{\partial E_K}{\partial X_K}(\mathbf{a},\mathbf{b}) & \frac{\partial E_K}{\partial \xi_1}(\mathbf{a},\mathbf{b}) & \cdots & \frac{\partial E_K}{\partial \xi_p}(\mathbf{a},\mathbf{b})
\end{bmatrix}\\
&=\left[\frac{\partial\mathbf{E}}{\partial\mathbf{X}}\quad\frac{\partial\mathbf{E}}{\partial\boldsymbol{\xi}}\right](\mathbf{a},\mathbf{b})=\left[J_{\mathrm{E}}(\mathbf{X}),\quad J_{\mathrm{E}}(\boldsymbol{\xi})\right](\mathbf{a},\mathbf{b})
\end{aligned}\tag{3.47}$$

Provided the non-sigularity condition for the Jacobian matrix is met, the solution of the system depends *explicitly* on the parameter vector ξ and thus can be analyzed by performing *parametric sweeps*, that is adequately varying each parameter in a suitable range and tracking the evolution of the solution ($\mathbf{X}$ vector). Parametric Sweeps allow then to trace the vector valued function:

$$\begin{aligned}
&\mathbf{X}:\mathcal{A}\mapsto\mathcal{B} && \mathcal{A}\subset\mathbb{R}^p\\
&\boldsymbol{\xi}\xrightarrow{\mathbf{X}(.)}\mathbf{X}(\boldsymbol{\xi}) && \mathcal{B}\subset\mathbb{R}^{n\times(2N_h+1)}
\end{aligned}\tag{3.48}$$

In commercial simulators, parametric sweep tools allow to trace the solution with respect to a single circuit parameter. However they can be combined to perform *multidimensional parameter analysis of the solution* by using *nested cycles*. Since the multidimensional solution path tracking could be very hard to tackle, both numerically and analytically, the continuation scheme will be provided here for the case of a single parameter dependence $\mathbf{E}(\mathbf{X},\beta)=\mathbf{0}$. This corresponds to tracing the solution curve *sequentially p times*, keeping constant from time to time the remaining (p-1) parameters:

/Multidimensional Solution Tracking by Nested Cycles

$$
\begin{array}{l}
for\,(\xi_1^{\min} \le \xi_1 \le \xi_1^{\max})\{ \\
\quad for\,(\xi_2^{\min} \le \xi_2 \le \xi_2^{\max})\{ \\
\qquad\qquad \ddots \\
\qquad\qquad\quad for\,(\xi_p^{\min} \le \xi_p \le \xi_p^{\max})\{ \\
\qquad\qquad\qquad\qquad\qquad\qquad solve: \mathbf{E}(\mathbf{X}, \xi_1, \xi_2, ..., \xi_p) = \mathbf{0} \\
\qquad\qquad\qquad\qquad\qquad\qquad \mathbf{X} \leftarrow \mathbf{X}(\xi_1, \xi_2, ..., \xi_p) \\
\qquad\qquad\qquad\qquad\qquad\qquad \xi_p \leftarrow \xi_p + \Delta\xi_p \\
\qquad\qquad\qquad\qquad\qquad\qquad\qquad\qquad\qquad\qquad \} \\
\qquad\qquad\qquad\quad \vdots \\
\qquad\qquad \xi_2 \leftarrow \xi_2 + \Delta\xi_2 \\
\qquad\qquad\qquad\quad \} \\
\xi_1 \leftarrow \xi_1 + \Delta\xi_1 \\
\}
\end{array}
\tag{3.49}
$$

Although the information obtained it is not equivalent to the multidimensional approach in which *p parameters are simultaneously swept,* it is deemed adequate for practical purposes [18].

In order to find the parametric solution curve **X=X** (β), a *predictor corrector scheme* could be used. In the first step (*predictor*) the variation of the function **E**(**X**,β) through two successive iterations is approximated by momentarily neglecting the nonlinear contributions, obtaining a recurrence relations expressing an estimate of the circuit variables **X**, in terms of the result obtained at the previous step[19]:

$$
\begin{aligned}
&\Delta\mathbf{E} = \left[\frac{\partial \mathbf{E}}{\partial \mathbf{X}}\right]_{(n)} \left(\hat{\mathbf{X}}^{(n+1)} - \hat{\mathbf{X}}^{(n)}\right) + \left.\frac{\partial \mathbf{E}}{\partial \beta}\right|_{(n)} \left(\beta_{n+1} - \beta_n\right) = 0, \\
&\Rightarrow\ \hat{\mathbf{X}}^{(n+1)} = \hat{\mathbf{X}}^{(n)} - \left[\mathbf{J}_{\mathbf{E}}(\mathbf{X})\right]_{(n)}^{-1} \left.\frac{\partial \mathbf{E}}{\partial \beta}\right|_{(n)} \left(\beta_{n+1} - \beta_n\right) \\
&\text{where} \quad \left[\mathbf{J}_{\mathbf{E}}(\mathbf{X})\right]_{(n)} = \left[\frac{\partial \mathbf{E}}{\partial \mathbf{X}}\right]_{(n)} = \left[\left(\frac{\partial E_{p,q}}{\partial X_{r,s}}\right)^{(n)}\right]_{\substack{p,r=1,2,...,M \\ q,s=1,2,...,(2N+1)}} \\
&\textit{and} \quad \det\left(\left[\mathbf{J}_{\mathbf{E}}(\mathbf{X})\right]_{(n)}\right) \neq 0
\end{aligned}
\tag{3.50}
$$

Subsequently (*corrector step*), these estimates are set right by entering them in the nonlinear system of equations (5.26), which is solved at each step to find a solution to **E**(**X**, β)=**0**, with a multidimensional nonlinear root finding algorithm, in most cases the Newton-Raphson

[18] This approach is applied in examining the oscillating modes, keeping constant, from time to time, either the attenuation or the coupling line length, according to the decoupled analysis reported in chapter IV.

[19] The size of the n-th step (β_{n+1}-β_n) is actually unknown. A practical technique to improve the predictor-corrector method consists in choosing the step adaptively, depending on the convergence at the corrector phase. Then it could be doubled if the convergence at the previous step was successful, or halved if problem were experienced (see [21,22])

$$\mathbf{E}(\hat{\mathbf{X}}^{(n+1)},\beta_{n+1})=\mathbf{0}\xrightarrow[(corrector\ step)]{\text{solve }\mathbf{E}(\hat{\mathbf{X}}^{(n+1)},\beta_{n+1})=\mathbf{0}}\mathbf{X}^{(n+1)}=\mathbf{X}(\beta_{n+1}),\quad n=0,1,...,S \tag{3.51}$$

The succession of points $\{(\mathbf{X}^{(1)},\beta_1), (\mathbf{X}^{(2)},\beta_2),..., (\mathbf{X}^{(S)},\beta_S)\}$ thus defines the parametric solution $\mathbf{X}=\mathbf{X}(\beta)$. However, for successfully applying the predictor-corrector continuation scheme the Jacobian matrix of the function **E(.)** relative to the variables $\mathbf{X}(\beta)$ should be invertible. Therefore, convergence failure may occur in case of reaching a parameter value $\beta_T \in [\beta_n, \beta_{n+1}]$ for which the determinant of the Jacobian matrix $\mathbf{J_E(X(\beta))}=(\partial\ \mathbf{E}/\partial\ \mathbf{X})(\beta)$ approaches zero; this singularity condition *determines the occurrence of a turning point* [23]. Let us assume that this happens while tracing the parametric solution curve of a particular harmonic component at a specific port[20] $X_p=X_p(\beta)$, among the P available. Then, from (3.50) it's easy to show that in the neighborhood of the point $(X_p(\beta_T),\beta_T)$ the curve $X_p(\beta)$ presents infinite slope:

$$\left.\frac{\partial\hat{X}_p}{\partial\beta}\right|^{(n+1)}=\frac{\hat{X}_p^{(n+1)}-\hat{X}_p^{(n)}}{\beta_{n+1}-\beta_n}=-\overbrace{\frac{1}{\det\left[\mathbf{J_E}(X_p(\beta))\right]}\left[\frac{\partial X_p}{\partial E_r}\right]_{r=1,2,...,M(2N+1)}}^{\text{row vector of the form:}}\cdot\underbrace{\left.\frac{\partial\mathbf{E}}{\partial\beta}\right|_{(n)}}_{\text{column vector of the form: }\left[\frac{\partial E_r}{\partial\beta}\right]_{r=1,2,...,M(2N+1)}}$$
$$=\frac{1}{\det\left[\mathbf{J_E}(X_p(\beta_n))\right]}\sum_{r=1}^{M(2N+1)}\left(\frac{\partial X_p}{\partial E_r}\frac{\partial E_r}{\partial\beta}\right)\xrightarrow{\det[\mathbf{J_E}(X_p(\beta))]\to 0}\infty \tag{3.52}$$

In that case, a *parameter switching procedure is invoked*. At the predictor stage (3.51), it is selected the circuit variable or parameter possessing the largest increment; to fix our ideas suppose it is X_p:

$$\left|\Delta\hat{X}_p^{(n)}\right|>\max\left(\left|\Delta\beta^{(n)}\right|,\left|\Delta\hat{X}_1^{(n)}\right|,\ldots,\left|\Delta\hat{X}_{p-1}^{(n)}\right|,\left|\Delta\hat{X}_{p+1}^{(n)}\right|,\ldots,\left|\Delta\hat{X}_K^{(n)}\right|\right) \tag{3.53}$$

Then, *X_p it is chosen as the new parameter and the solution curve is traced with respect to it.* This step constitutes the essence of the parameter switching. Unbounded growth of circuit variables during the continuation procedure is thus effectively prevented [8], since X_p is assigned a finite step size:

$$\Delta X_p^{(n)}=\text{sign}\left(\Delta X_p^{(n)}\right)\cdot h \tag{3.54}$$

and the analysis of the solution path proceeds, considering the *inverse relation* $\beta=\beta(X_p)$ (instead of the direct relation $X_p=X_p(\beta)$), avoiding the singularity in the Jacobian shown in (3.52) with the following update rule:

[20] In order to simplify the notation we set $X_p=\text{Re}(X_{h,k})$ for $h=1,\ldots,(2N+1)$, $k=1,\ldots,P$, picking up the real part of one of the different $P(2N+1)$ harmonic terms (using the Piecewise Harmonic Balance).

$$\begin{bmatrix} X_p^{(n+1)} \\ \beta_{n+1} \end{bmatrix} = \begin{bmatrix} X_p^{(n)} \\ \beta_n \end{bmatrix} - \left[\tilde{\mathbf{J}}_{\mathbf{E}} \left(X_1, \ldots, X_{p-1}, X_{p+1}, \ldots X_K \right) \cdot \left(\frac{\partial \mathbf{E}}{\partial \beta} \right) \right]_{(n)}^{-1} \left(\frac{\partial \mathbf{E}}{\partial X_p} \right)^{(n)} \operatorname{sign}\left(\Delta X_p^{(n)} \right) \cdot h \qquad (3.54)$$

which shows a reduced order Jacobian matrix, obtained by eliminating the column corresponding to the variable X_p, which represent the new parameter for tracing the solution branch $\beta_{n+1} = \beta(X_p^{(n)})$; these estimates are once again corrected as in (3.52) – (3.54).

In commercial simulators, there exists no straightforward method to compute the determinant of $\mathbf{J}_E(\mathbf{X}(\beta))$, so the parameter switching strategy could be applied *a posteriori*, after convergence problem had arisen. In case the convergence of the harmonic balance system $\mathbf{E}(\mathbf{X},\beta)=\mathbf{0}$, in the neighborhood of a parameter value β_T for the observed variable $X_p(\beta)$, *is slow or problematic the role of the parameter and the variable are swapped*, tracing with a parameter sweep the inverse function $\beta = \beta(X_p)$ in a suitable range for the variable X_p. Switching back and forth trough the direct $X_p = X_p(\beta)$ and inverse relationship $\beta = \beta(X_p)$ every time a singularity is encountered, multi-valued solution curve be traced (i.e. *closed curves in the* (X_p, β) plane).

3.5 MIXED (TIME-FREQUENCY) DOMAIN. ENVELOPE TRANSIENT-HARMONIC BALANCE.

The harmonic balance analysis is essentially aimed at representing solutions in form of linear superposition of trigonometric (complex exponentials) functions, which restricts it's applicability to the periodic or almost periodic regimes. However many important radio communication signals, most notably *amplitude modulated ones,* consist of a *fast varying carrier wave* physically conveying the information provided by a *slower modulating signal* (*envelope*). This class of signal manifest *only a partial periodicity*, since the modulating waveform can be any arbitrary function of time, provided it is narrowband with respect to the carrier wave. As a consequence, an Harmonic Balance analysis would enable one to predict the steady state circuit response with respect to the carrier wave only neglecting the *time variant* contribution of the modulating signal. Nor a time domain analysis of the system (3.14) is more effective. In fact using direct integration, a *very small time step* should be used to analyze the fast phenomena, while to observe modulation effects *a large temporal window* would be needed, leading to big amount of data to be processed and therefore to an increase in memory requirements and CPU time.

These pitfalls can be overcome using a *mixed approach* (time- frequency) the most used of which is the Envelope Transient method [24]. This method aims at decoupling the analysis of circuits being driven by a signal in which two time scales are simultaneously present (*multi rate signal) distinguishing between the effects* of *slowly time varying, modulating signals* (envelopes) for which a time domain *transient analysis* (numerical integration/convolution) is performed, from the investigation of the response to *stationary high-frequency* carrier waves, which are analysed with the Harmonic Balance method, in the frequency domain.

Assuming a non-autonomous circuit is being driven by an amplitude modulated wave the expected response for each state variable (using the nodal approach) consists in the superposition of time varying spectral contributions at each harmonic term. Precisely, allowing a temporal dependence in the Fourier harmonic vectors in the expansion (3.18)-(3.19) the state vector will take the form

$$\mathbf{x}(t) = \sum_{k=-\infty}^{+\infty} \mathbf{X}_k(t) e^{jk\omega_0 t} \tag{3.55}$$

However the time scales involved in (3.55) are very different since, as mentioned earlier the modulating signals $\mathbf{X}_k(t)$ are very narrowband/slowly varying with respect to the high frequency carriers $\{e^{jk\omega_0 t}\}$. It would thus be beneficial to keep track of them separately by introducing two independent time variables (t_1, t_2) defining a new function related to (3.55)

$$\hat{\mathbf{x}}(t_1, t_2) = \sum_{k=-\infty}^{+\infty} \mathbf{X}_k(t_1) e^{jk\omega_0 t_2}, \quad \hat{\mathbf{x}}(t,t) = \mathbf{x}(t) \tag{3.56}$$

enabling to choose two different sampling rates for the according to the waveform being analysed; a lower sample rate for the modulating terms $\mathbf{X}_k(t_1)$ (t1 indicating *slow time*), an higher one for the harmonic carriers $\{e^{jk\omega_0 t_2}\}$. As indicated, the original vector is retrieved by setting $t_1=t_2=t$. Such a modification must hold also for the time domain description (3.14) briefly recalled in (3.57) in which the convolution is explicitly shown:

$$\begin{cases} \dfrac{d\mathbf{q}}{dt}\big(\mathbf{x}(t)\big) = \mathbf{g}(\mathbf{x}(t)) + \mathbf{j}_s(t) + \displaystyle\int_{-\infty}^{t} \mathbf{h}(t-\tau) * \mathbf{x}(\tau) d\tau \\ \mathbf{x}(t_0) = \mathbf{x}_0 \end{cases} \tag{3.57}$$

By applying the multi-rate vector defined in (3.56) the Differential Algebraic Equation (3.57) turns into a Multi Rate Partial differential Equation [25]:

$$\frac{\partial \mathbf{q}}{\partial t_1}\left(\hat{\mathbf{x}}(t_1,t_2)\right)+\frac{\partial \mathbf{q}}{\partial t_2}\left(\hat{\mathbf{x}}(t_1,t_2)\right)=\mathbf{g}\left(\hat{\mathbf{x}}(t_1,t_2)\right)+\hat{\mathbf{j}}_s(t_1,t_2)+\hat{\mathbf{h}}(t_1,t_2)*\hat{\mathbf{x}}(t_1,t_2)$$

where:

$$\hat{\mathbf{h}}(t_1,t_2)\equiv\sum_{k=-\infty}^{+\infty}\mathbf{h}_k(t_1)e^{jk\omega_0 t_2}\quad\text{impulse response}$$

$$\hat{\mathbf{j}}_s(t_1,t_2)=\sum_{k=-\infty}^{+\infty}J_{sk}(t_1)e^{jk\omega_0 t_2}\quad\text{driving signal}$$

$$\mathbf{q}\left(\hat{\mathbf{x}}(t_1,t_2)\right)=\sum_{k=-\infty}^{+\infty}\mathbf{Q}_k\left(\mathbf{X}_k(t_1)\right)e^{jk\omega_0 t_2}=\sum_{k=-\infty}^{+\infty}\mathbf{Q}_k\left(t_1\right)e^{jk\omega_0 t_2}\quad\text{nonlinear charge}$$

$$\mathbf{g}\left(\hat{\mathbf{x}}(t_1,t_2)\right)=\sum_{k=-\infty}^{+\infty}\mathbf{G}_k\left(\mathbf{X}_k(t_1)\right)e^{jk\omega_0 t_2}=\sum_{k=-\infty}^{+\infty}\mathbf{G}_k\left(t_1\right)e^{jk\omega_0 t_2}\quad\text{nonlinear }\textit{current}$$

$$\hat{\mathbf{h}}(t_1,t_2)*\hat{\mathbf{x}}(t_1,t_2)=\sum_{k=-\infty}^{+\infty}\mathbf{h}_k(t_1)e^{jk\omega_0 t_2}*\sum_{h=-\infty}^{+\infty}\mathbf{X}_h(t_1)e^{jh\omega_0 t_2}=\sum_{k=-\infty}^{+\infty}\left(\mathbf{h}_k(t_1)*\mathbf{X}_k(t_1)\right)e^{jk\omega_0 t_2} \tag{3.58}$$

Carrying out the partial derivatives in the expression above,

$$\frac{\partial \mathbf{q}}{\partial t_1}\left(\hat{\mathbf{x}}(t_1,t_2)\right)=\frac{\partial}{\partial t_1}\left(\sum_{k=-\infty}^{+\infty}\mathbf{Q}_k\left(\mathbf{X}_k(t_1)\right)e^{jk\omega_0 t_2}\right)=\sum_{k=-\infty}^{+\infty}\frac{\partial \mathbf{Q}_k}{\partial t_1}\left(\mathbf{X}_k(t_1)\right)e^{jk\omega_0 t_2}$$

$$\frac{\partial \mathbf{q}}{\partial t_2}\left(\hat{\mathbf{x}}(t_1,t_2)\right)=\frac{\partial}{\partial t_2}\left(\sum_{k=-\infty}^{+\infty}\mathbf{Q}_k\left(\mathbf{X}_k(t_1)\right)e^{jk\omega_0 t_2}\right)=\sum_{k=-\infty}^{+\infty}jk\omega_0\cdot\mathbf{Q}_k\left(\mathbf{X}_k(t_1)\right)e^{jk\omega_0 t_2} \tag{3.59}$$

$$\hat{\mathbf{h}}(t_1,t_2)*\hat{\mathbf{x}}(t_1,t_2)=\int_{-\infty}^{t_1}\int_{-\infty}^{t_2}\mathbf{h}(t_1-\tau_1,t_2-\tau_2)\mathbf{x}(\tau_1,\tau_2)d\tau_1 d\tau_2=$$

$$=\sum_{k=-\infty}^{+\infty}\mathbf{h}_k(t_1)e^{jk\omega_0 t_2}*\sum_{h=-\infty}^{+\infty}\mathbf{X}_h(t_1)e^{jh\omega_0 t_2}=\sum_{k=-\infty}^{+\infty}\left(\mathbf{h}_k(t_1)*\mathbf{X}_k(t_1)\right)e^{jk\omega_0 t_2}$$

and substituting in the previous expression (3.58), taking into account the orthonormality of the Fourier basis, an equation for the time varying harmonic term of order *k* is obtained:

$$\frac{\partial \mathbf{Q}_k}{\partial t_1}\left(\mathbf{X}_k(t_1)\right)+jk\omega_0\cdot\mathbf{Q}_k\left(\mathbf{X}_k(t_1)\right)=\mathbf{G}_k\left(\mathbf{X}_k(t_1)\right)+\mathbf{J}_{sk}(t_1)+\mathbf{h}_k(t_1)*\mathbf{X}_k(t_1) \tag{3.60}$$

and being t_1=*t and* t_2 *not involved,* the partial differentiation agrees with the derivative of a function of a single time variable:

$$\frac{d\mathbf{Q}_k}{dt}\left(\mathbf{X}_k(t)\right)+jk\omega_0\cdot\mathbf{Q}_k\left(\mathbf{X}_k(t)\right)=\mathbf{G}_k\left(\mathbf{X}_k(t)\right)+\mathbf{J}_{sk}(t)+\mathbf{h}_k(t)*\mathbf{X}_k(t)$$
$$-N_h\le k\le N_h,\quad t\in[t_a,t_b]\subset\mathbb{R} \tag{3.61}$$

The equation (3.60) is solvable with one of the numerical integration / convolution tools introduced earlier in section §3.1.to determine the evolution of the envelope associated with each

harmonic coefficient ($-N_h \leq k \leq N_h$) for a given observation window. Since the envelope evolves in time with at a low rate in comparison with the carrier, the (3.61) could be more easily integrated choosing a larger time step/sampling period. The envelope spectrum at an offset frequency Ω from the harmonic $\omega_k = k\omega_0$ is related to its time domain representation by an inverse Fourier Tranform:

$$\mathbf{X}_k(t) = \frac{1}{2\pi}\int_{-B_k/2}^{B_k/2} \mathbf{X}_k(\Omega) e^{j2\pi\Omega t} d\Omega \tag{3.62}$$

being B_k the bandwidth occupied by envelope spectrum, assuming $\omega_0 \gg B_k$ (narrowband modulating signal)[21].

Applying the Backward Euler integration scheme to (3.61) the differential equations turns to a one-step difference equation:

$$\begin{aligned} &t_m = m\Delta T \rightarrow \text{sampling instants} \\ &\frac{\mathbf{Q}_k(\mathbf{X}_k(t_m)) - \mathbf{Q}_k(\mathbf{X}_k(t_{m-1}))}{t_m - t_{m-1}} + jk\omega_0 \cdot \mathbf{Q}_k(\mathbf{X}_k(t_m)) = \mathbf{G}_k\left(\mathbf{X}_k(t_m)\right) + \mathbf{J}_{sk}(t_m) + \\ &\qquad\qquad + \sum_{s=0}^{m} \mathbf{h}_k(t_m - t_s)\mathbf{X}_k(t_s)\Delta T \end{aligned} \tag{3.63}$$

which depends only on harmonic terms, defined at specific time points; analogously to the Harmonic Balance formulation, is thus possible to define an error function:

$$\begin{aligned} \mathbf{F}(\mathbf{X}_k(t_m)) = &\frac{\mathbf{Q}_k(\mathbf{X}_k(t_m)) - \mathbf{Q}_k(\mathbf{X}_k(t_{m-1}))}{t_m - t_{m-1}} + jk\omega_0 \cdot \mathbf{Q}_k(\mathbf{X}_k(t_m)) - \mathbf{G}_k\left(\mathbf{X}_k(t_m)\right) - \mathbf{J}_{sk}(t_m) \\ &- \sum_{s=0}^{m} \mathbf{h}_k(t_m - t_s)\mathbf{X}_k(t_s)\Delta T \end{aligned} \tag{3.64}$$

so that:

$$\begin{aligned} &for[t_0 \leq t_m \leq t_1]\ \{ \\ &\quad \text{solve: } \mathbf{F}(\mathbf{X}_k(t_m)) = \mathbf{0} \quad (-N_h \leq k \leq N_h) \\ &\quad\quad t_m \leftarrow t_m + \Delta t \\ &\quad\quad \} \end{aligned} \tag{3.65}$$

which explicitly define a *sequence of Harmonic Balance problems (at the frequency of the carrier wave)* associated to the various sampling instants of the slowly varying envelope. Solving (3.65) a complete characterization of the modulated carrier is possible.

[21] If the generic modulating signal $a(t)$ has a lowpass frequency response $A(\omega)$, and modulates a carrier wave at frequency the bandpass signal will be represented by $a_{BP}(t)=\mathrm{Re}\{a(t)\cdot e^{j\omega 0 t}\}$. From the properties of Fourier transform, a product in time agrees with a convolution in frequency therefore $A_{BP}(\omega) = A(\omega) * \delta(\omega - \omega_0) = A(\omega - \omega_0)$. This low-pass equivalent representation, allow one to immediately identify the spectrum content of a bandpass signal, in terms of the spectrum content associated to the modulating signal, that is the envelope.

3.6 REFERENCES

[1] O.L. Chua, C.A. Desoer, and E.S. Kuh. *Linear and Nonlinear Circuits*. Mcgraw-Hill College, March 1987.

[2] M.I. Sobhy and A.K. Jastrzebski "Computer-aided design of microwave integrated circuits", *Proceedings of the14th European Microwave Conf*, pp. 705–710, Sep. 1984.

[3] F. Giannini, and G. Leuzzi. *Non-linear Microwave Circuit Design*, John Wiley & Sons, June 2004.

[4] P. Deuflhard. *Newton Methods for Nonlinear Problems: Affine Invariance and Adaptive Algorithms*. Springer Series in Computational Mathematics, 2011

[5] C.J. Butcher. *Numerical Method For Ordinary Differential Equations (Second Edition)*. John Wiley and Sons, June 2008.

[6] C.W. Gear, "Simultaneous numerical solution of differential algebraic equations", *IEEE Trans.Circuit Theory*, vol., no., 18(1), pp. 89–95, 1971.

[7] D.O. Pederson, "A historical review of circuit simulation", *IEEE Trans. Circuits Syst.*, vol., no. *CAS*-31,pp.103–111, 1984.

[8] A.Suarez, and R. Quéré. *Stability Analysis of Nonlinear Microwave Circuits*. Artech House publishers, January 2003

[9] C.F. Christoffersen, M. Ozkar, M.B. Steer, M.G Case, and M. Rodwell,"State-variable-based transient analysis using convolution", *IEEE Trans. Microwave Theory Tech.*, vol., no. MTT-47(6), pp. 882–889, 1999.

[10] A.J. Jerry. *The Gibbs Phenomenon in Fourier Analysis, Splines and Wavelet Approximations*. Springer Series on Mathematics and its Applications, 1998

[11] A. Suarez. *Analysis and Design of Autonomous Microwave Circuits*. Wiley Series in Microwave and Optical Engineering, 2009.

[12] J.F. James. *A Student's Guide to Fourier Transforms: with Applications in Physics and Engineering (third edition)*. Cambridge University Press, 2011

[13] V. Rizzoli, F. Mastri, C. Cecchetti, and F. Sgallari, "Fast and robust inexact Newton approach to the harmonic-balance analysis of nonlinear microwave circuits", *IEEE Microwave Guided Wave Lett.*, vol.,no, 7(10), pp. 359–361, 1997.

[14] "Agilent ADS 2008 Documentation on HB simulation" [On-line]. Available: http://edocs.soco.agilent.com/display/support/ADS+Product+Documentation [Mar. 20, 2013].

[15] R.W. Freund, "Krylov-subspace methods for reduced-order modeling in circuit simulation," *J. Comput. Appl. Math.*, vol. 123, pp. 395–421, 2000.

[16] A.S.Besicovitch. *Almost Periodic Functions.* Dover, 1954.

[17] K. Kundert, G.B. Sorkin, and A. Sangiovanni Vincentelli "Applying harmonic balance to almost-periodic circuits", *IEEE Trans. Microwave Theory Tech.*, vol, no., MTT-36, pp. 366–378, 1988.

[18] J.C. Pedro, and N. Borges de Carvalho, "Artificial Frequency-Mapping Techniques for Multi-Tone Harmonic Balance" [On-line], *IEEE, MTT-S International Microwave Symposium Dig.* Workshops,2000. Available: http://www.av.it.pt/nbcarvalho/docs/ws1.pdf [Mar. 21,2013].

[19] V. Rizzoli *et al.*, "State-of-the-art harmonic-balance simulation of forced nonlinear microwave circuits by the piecewise technique", *IEEE Trans. Microwave Theory Tech.*, vol.,no., MTT-40(1), pp. 12–28, Jan. 1992.

[20] L. R. Scott. *Numerical Analysis,* Princeton University Press, 2011.

[21] E. L. Allgower and K. Georg, "Continuation and path following", *Acta Numerica,*vol. 2 , pp 1-64, 1993.

[22] D. Hente, and R.H. Jansen, "Frequency domain continuation method for the analysis and stability investigation of nonlinear microwave circuits," *IEE Proceedings H (Microwaves, Antennas and Propagation)*, vol.133, no.5, pp.351-362, October 1986

[23] Y. Kuznetsov. *Elements of Applied Bifurcation Theory (Third Edition)*. Springer Series on Applied Mathematical Sciences, Vol. 112, 2004

[24] K. Kundert, "An envelope-following method for the efficient transient simulation of switching power and filter circuits Computer-Aided Design", *Proceedings of the 1988 IEEE/ACM International Conference on Computer Aided Design (ICCAD-88)* pp. 446 – 449, Nov 1988.

[25] J. Roychowdhury, "Multi-Time PDE for Dynamical System Analysis" in *Applied and Computational Control, Signals and Circuits: Recent Developments,* vol.629. B. N. Datta, Ed: Kluwer Academic Publishing, pp. 85-143, 2001

CHAPTER IV. MICROWAVE OSCILLATORS NONLINEAR SIMULATION

4.1 INTRODUCTION. NONLINEAR SIMULATION TOOLS.

This chapter deals with the application of a modified harmonic balance formulations, suitable to the analysis and design of microwave autonomous circuits including oscillators, injection-locked oscillators /synchronized oscillators, frequency dividers. This class of circuit is characterized by having the capability of generating self sustaining oscillations, whose frequency and power depend upon their circuital component/parameter values [1]. However, except for some idealized models or simple topologies, it doesn't exist a general analytical method which enables to predict the output oscillation spectral characteristics using a straightforward circuit inspection. The simple linear analysis methods, as the Barkhausen Criterion for positive feedback loop oscillator [2], the Nyquist stability theorem [1, 2], and the negative resistance approach stated by Kurokawa [1, 2] are useful design tools only at a *preliminary design stage* to check whether the circuit has *potential instabilities that could lead to oscillation onset* given a certain amount of gain (*negative resistance*, determined by the active deivices) and a phase response across the feedback loop (or *resonating reactances,* determining a frequency selectivity of the output signal). Nonetheless, when the turn-on transient is extinguished, the oscillator goes into a large signal regime [3] and the linear analysis is just oversimplified. In fact, many important oscillator figures of merit, like the harmonic rejection, its output power, its tuning function (in case of VCOs), the sensitivity with respect to parameter variations, can be reliably obtained only by considering the *active device model nonlinearities, arising when the signal level becomes comparable to the bias supply level,* so that the approximation based on small perturbation around a quiescent point (circuit at DC) is not valid anymore.

The aim of oscillator nonlinear analysis is thus to determine its most relevant features, without accepting the linear/small signal limitations. Notably, the oscillation frequency ω_o is an unknown of the system, together with the oscillator's output spectrum, defined by the harmonic vector $\mathbf{X}^p=[\mathbf{X}^p_0\ \mathbf{X}^p_1,\ldots,\ \mathbf{X}^p_k,\ldots,\ \mathbf{X}^p_{Nh}]$. The harmonic balance formulation presented in §3.2 *assumed* a periodic excitation as an input to the system, but this assumption does not apply in this case, since oscillators have no input sources. On the other hand since DC generators are present, to provide bias supply, they force a *degenerate*, *zero frequency*, non oscillatory solution [8]. Even though the oscillation frequency could be estimated by other means [1−3] and set as a tentative input frequency to perform a large signal HB simulation, since the degenerate solution always coexists with the oscillating one, there will always be the possibility of getting misleading results.

A remedy to flawed HB convergence is offered by the method of harmonic probes[1]/auxiliary generators [4-6]. Exploiting the non-autonomous HB formulation presented in

[1] These last two terms will be used interchangeably. As a *generator* it injects a voltage (current) signal, with definite values of amplitude, frequency and phase; as a *probe* it senses a current (voltage) signal, as later will be detailed. These Auxiliary generators are introduced for simulating purposes only; under no circumstances it can be part of the real circuit.

§3.2, *fictitious*, single-tone, generators are introduced at a convenient circuit node, injecting a voltage or current signal to the aim of triggering oscillations at a certain frequency[2], *forcing the Harmonic balance simulator to converge to the oscillating solutions,* thus avoiding the deceitful result of achieving a zero frequency solution. Their *amplitude*, *frequency* and *phase* could be chosen in order to fulfil a *non perturbation condition at the insertion node* [7]. Depending whether the circuit is operating in *free-running* (self starting oscillator) or in *synchronized mode* (injection locked oscillator) two among the three parameters of the harmonic probe can be found, when the third is kept constant. In particular, in case a free running oscillator is analyzed it is not relevant to specify its phase; due to time invariance properties of autonomous circuits, any phase-shifted (delayed) solution is a valid one; therefore without loss of generality it can be set to a constant value (ϕ=0°), while the amplitude and frequency of the harmonic probe are determined with a special Harmonic Balance formulation. In synchronized mode instead, assuming the frequency of the oscillator is equal to that of the input signal, the auxiliary generator frequency is fixed, while the auxiliary generator's amplitude and phase are the variables to be determined.

4.2 FREE RUNNING OSCILLATORS NONLINEAR ANALYSIS USING AUXILIARY GENERATORS.

Free running oscillator circuits analysis, is aimed at determining large signal spectral features, taking into account the nonlinear models of the active devices employed in the circuit by means of a suitably modified Harmonic Balance formulation.

As mentioned earlier, Auxiliary Generators need to be placed at a convenient node[3] in order to avoid ambiguous effects deriving from the Harmonic Balance formulation for non-autonomous circuits. There are two different kind of generators; one is based on *Thevenin equivalent voltage source,(*voltage generator with a series impedance) another on *Norton equivalent current source;* (current generator with a shunt admittance) these two representations are dual, and at least in principle perfectly equivalent.

A *voltage type* auxiliary generator is always inserted *in a parallel connection* with respect to the insertion node *(n)* (adding one more branch to the original circuit) where it injects a pure sine wave voltage having in principle *undetermined* amplitude A_p, frequency ω_p and phase ϕ_p defined by (Fig. 4.1):

$$e_n(t) = A_p \sin(\omega_p t + \phi_p) \tag{4.1}$$

[2] In case a frequency divider is analyzed, the auxiliary generator frequency agrees with a subharmonic (divided frequency) of the input signal. Analogously, when investigating sub-harmonic injection locking, the auxiliary generator frequency is set to superharmonic (frequency multiple) of the source signal.

[3] See [4].

where the notation $e_n(t)$ refers to the node voltage at "n" while the subscripts "p" *indicate probing quantities (amplitude, frequency and phase).* Considered that in free running oscillators all possible phase shifted solutions are equivalent due to time invariance, it is convenient to choose ϕ_p=0° in the equation (4.1).

Since a voltage generator is a short circuit at all frequencies except for the one delivered, it is necessary to prevent spurious shorting of RF signals entering the auxiliary generator branch[4]. To that aim, an ideal *impedance based band-pass filter* component, is connected in series with the auxiliary generator, having the transfer function:

$$Z_p(\omega) = \begin{cases} 0 & if\ \omega = \omega_p \\ \infty & if\ \omega \neq \omega_p \end{cases} \tag{4.2}$$

being the impedance a short circuit (zero resistance) to the nominal auxiliary generator frequency, and an open circuit (infinite resistance) otherwise. Additionally, to act like an *harmonic probe*, a *current meter* block must be inserted in series to the auxiliary generator, enabling to sense the current signal flowing through it, expressed as:

$$i_n(t) = I_{n,1}(A_p, \omega_p)\sin(\omega_p t + \psi_{n,1}(A_p, \omega_p)) \tag{4.3}$$

due to the series impedance filtering. Notice that the amplitude and phase of $i_n(t)$ both depend on the amplitude A_p and frequency ω_p of the injected signal. The ratio among the *injected voltage phasor* and the *detected current phasor*, defines the *admittance function* for the voltage type auxiliary generator at the frequency ω_p at the insertion node:

$$\mathbf{Y}_p^{(n)}(A_p, \omega_p) = \frac{I_{n,1}(A_p, \omega_p)e^{j\psi_{n,1}(A_p,\omega_p)}}{A_p} \tag{4.4}$$

[4] In fact, when the oscillator circuit is forced by the harmonic voltage probe $e_n(t)$, due to the nonlinearities present in the active devices, a multi-harmonic current is produced at the node "n"

$$i_n(t) = \sum_{k=0}^{\infty} I_{n,k}(A_p, \omega_p)\sin(k\omega_p t + \psi_{n,k}(A_p, \omega_p)) =$$
$$= I_{n,0}(A_p, \omega_p) + I_{n,1}(A_p, \omega_p)\sin(\omega_p t + \psi_{n,1}(A_p, \omega_p)) + I_{n,2}(A_p, \omega_p)\sin(2\omega_p t + \psi_{n,2}(A_p, \omega_p)) + \ldots$$

whose terms at a frequency other than ω_p *could be shorted to ground.*

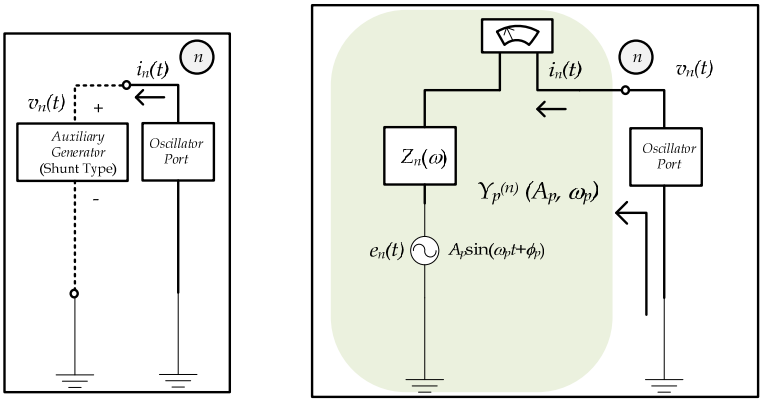

FIGURE 4-1. Voltage Type Auxiliary Generator, connected between a specified oscillator node *(n)* and the ground

As the auxiliary generator drives the oscillator circuit, *its amplitude and frequency are related to the final oscillating solution's amplitude and frequency at the circuit node (n)*. Precisely, at the steady state, a self sustained oscillation of amplitude A_p and frequency ω_p can be obtained if and only if *the auxiliary generator admittance reduces to zero*, letting the circuit evolve autonomously without any external influence:

$$\mathbf{Y}_p^{(n)}(A_p,\omega_p)=\mathbf{0}\Rightarrow\begin{cases}\mathrm{Re}\left(Y_p^{(n)}(A_p,\omega_p)\right)=0\\ \mathrm{Im}\left(Y_p^{(n)}(A_p,\omega_p)\right)=0\end{cases} \tag{4.5}$$

as if the steady state had been reached when the auxiliary generator was disconnected. The equation (4.5) defines a *non perturbation condition* being represented by two equations ($\mathrm{Re}Y_p(\cdot)=0$, $\mathrm{Im}Y_p(\cdot)=0$) in two unknowns (A_p,ω_p) such that, when solved jointly within an Harmonic Balance routine, completely specify the oscillatory solution, avoiding the zero-frequency degeneracy.

As will be described later with greater details, the system (4.5) can be very effectively solved by an *optimization routine jointly with an auxiliary generator driven harmonic balance simulation*, so that at each step of the optimization process, the best values of amplitude and frequency fulfilling (4.5) are selected; the underlying harmonic balance simulation engine then, considering the stimulus coming from the Auxiliary generator as if it was a *real single tone sine-wave voltage generator,* performs a *forced* nonlinear analysis of the oscillator circuit, calculating the harmonic vectors $\mathbf{X}_k=\mathbf{X}(j\omega_p k)$ with the scheme presented in §3.2. Then, the current flowing through the harmonic probe (4.4) will be computed, and *passed to the optimization algorithm* which iteratively will adjust the probe amplitude and frequency until (4.5) are met.

If the combined optimization process and Harmonic Balance simulation converges, the output will be a periodic signal whose *voltage magnitude at the fundamental* and *fundamental frequency* at the selected node "*a*" in the circuit agree with the outcomes of the optimization process A_{opt}, ω_{opt}, as if the circuit was driven by a real single tone generator inserted at that node.

As previously stated, a current-type auxiliary generator can be used, and it's characterized in a dual manner with respect to the voltage-type one. In particular it has to be inserted in series at

a branch "*b*" of the circuit (augmenting the total nodes by one) and consists in a pure tone sine wave current generator injecting the signal (the phase variable can be neglected):

$$j_b(t) = B_p \sin(\omega_p t + \phi_p) \tag{4.6}$$

which is connected in parallel to an admittance block which prevent the opening of the circuit branch at the frequencies different from ω_p:

$$Y_b(\omega) = \begin{cases} 0 & if\ \omega = \omega_p \\ \infty & if\ \omega \neq \omega_p \end{cases} \tag{4.7}$$

and to a voltmeter, to sense the voltage variations through it:

$$v_b(t) = V_{b,1}(B_p, \omega_p) \sin(\omega_p t + \psi_{b,1}(A_p, \omega_p)) \tag{4.8}$$

Defining the impedance of the probe as the ratio of the detected voltage to the injected current at the circuit branch "*b*":

$$\mathbf{Z}_p^{(b)}(B_p, \omega_p) = \frac{V_{b,1}(B_p, \omega_p) e^{j\psi_{b,1}(A_p, \omega_p))}}{B_p}$$

and the non-perturbation condition can be reformulated in terms of the harmonic probe impedance as:

$$\mathbf{Z}_p^{(b)}(A_p, \omega_p) = \mathbf{0} \Rightarrow \begin{cases} \mathrm{Re}\left(Z_p^{(b)}(A_p, \omega_p)\right) = 0 \\ \mathrm{Im}\left(Z_p^{(b)}(A_p, \omega_p)\right) = 0 \end{cases} \tag{4.9}$$

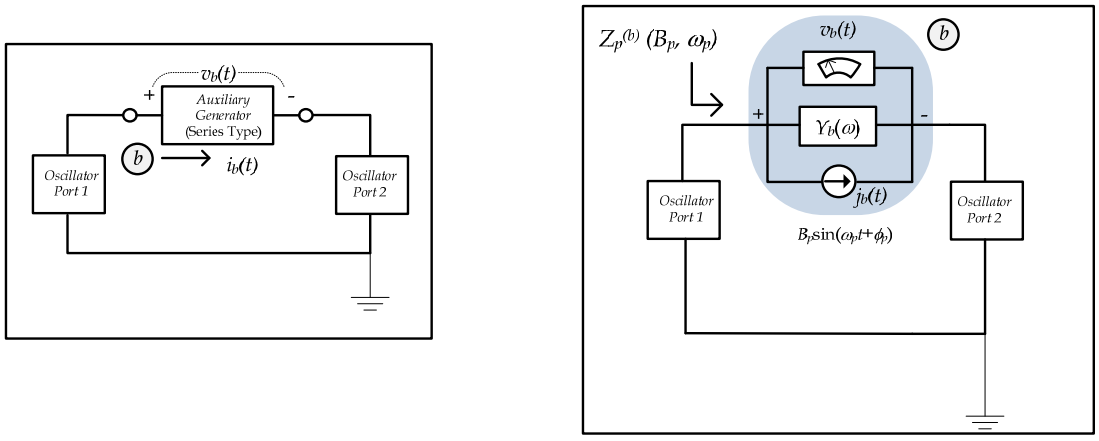

FIGURE 4-2. Current type Auxiliary Generator, connected in series to a branch (*b*) of the oscillator circuit.

In this work, only the voltage-type auxiliary generators/harmonic probes have been considered. In single ended (unbalanced) oscillator implementation, it is always connected among a selected node in the circuit and the ground.

4.2.1 Two-Tiers Harmonic Balance Analysis and Synthesis for Free-Running Oscillators.

In order to proceed to an oscillator harmonic balance analysis, the voltage probe (4.1) needs to be placed at a convenient circuit node[5]. It can easily be implemented with built-in simulator components, available from the "RF sources palette" available in many commercial simulators (i.e. Agilent ADS® 2008), and consisting in a single tone sine wave source, having as input parameters its amplitude frequency and phase. . The impedance ideal band pass filter can be synthesized as a Z one-port component, specifying a conditional statement to describe its ideal frequency transfer:

$$Z_p[1,1] = R_p + j0 = \{if \;\; f = f_p \;\; then : R_p \leftarrow 1\,\mathrm{p}\Omega \;\; else \;\; R_p \leftarrow 1\,\mathrm{T}\Omega\}$$

and a *current-meter* block is inserted in series to the voltage generator and the impedance filter. Moreover, the probe admittance defined in (4.5) is measured by the ratio of the first harmonic component of the current to the amplitude of the voltage probe and stored in the variable Y_p.

The equation (4.5) is solved in a two tier approach by means of an optimization algorithm, suitable to a quick implementation in commercial simulators. At first, tentative values for the candidate oscillating solutions in terms of amplitude and frequency[6] ($A_p^{(0)}$, $f_p^{(0)}$) have to be provided to the auxiliary generator; as detailed later *a preliminary linear and quasi-linear analysis* generally deliver candidate values which are very close to the outcome of the nonlinear simulation. Assuming an *initial guess for the two values is available* the search spaces for the two variables (A_p, f_p), defined as the set of admissible values, and represented by the intervals $\mathcal{A}$= [A_{min}, A_{max}], $\mathcal{F}$=[f_{min}, f_{max}], are declared. Reasonable reference ranges[7] (at the outset, without any other specific information on the oscillator circuit) for the amplitudes go from $0.2 - 0.4$ V to $0.8 - 1$V; regarding the frequencies ,a decade wide range centered at the expected oscillation frequency [5] yields often good results.

The assignment of an *adequate*[8] value for the large signal probe amplitude could be initially based on a simple *trial and error approach*. Usually good initial estimates for the probe amplitude A fall

---

[5] Suitable nodes to inject the probe signal depend on the circuit topology. Usually they are chosen to be at *the active devices* output port, or at *the oscillator output port* [2,7].

[6] From this section on, the angular frequency notation is dismissed in favor of the conventional notation.

[7] At this point, it is important to notice that the *wider the search space (feasible set) the better the convergence properties of the search (optimization) algorithm.* In the case of the amplitude range, however a lower bound is determined by the minimum signal that has to be injected for the nonlinearities in the active devices come into play. As an empirical rule of thumb, this value is no less than a tenth of the bias voltage; if lower the linear approximation still holds. An upper bound to the amplitude reference range is dictated by convergence issues in the HB algorithm, which becomes problematic for high-amplitude forcing generators. A reasonable upper bound for the auxiliary generator voltage is therefore dictated by the *highest* DC bias voltage in the circuit; from empirical evidence best results are obtained when A_{max} is comparable (on the same order of magnitude) with it.

[8] The term "adequate" might appear somewhat ambiguous, but it simply refers to a value for the probe amplitude (expressed in volt) for which the nonlinear effects (e.g. the appearance of higher order terms in the harmonic series of the output waveform) becomes relevant.

within the interval [0.1 V, 1 V]. In any case, a best practice recommendation to avoid *convergence issues* is to set the initial candidate values for A *at a fraction of the drain bias voltage that is* $A := V_{DD}/\eta$ ($\eta > 1$), attempting to run the optimization process first *with lower values for* η (*closer to* V_{DD}), and subsequently with higher ones, in case the convergence should fail[9].

The non perturbation conditions, expressed in terms of the voltage probe admittance at the insertion node should be expressed *as optimization goals*. To that aim (4.5) can be reformulated as:

$$\begin{cases} \mathrm{Re}\, Y_p(A,f) = 0 \\ \mathrm{Im}\, Y_p(A,f) = 0 \end{cases} \Rightarrow \begin{cases} \left|\mathrm{Re}\, Y_p(A,f)\right| < \varepsilon \\ \left|\mathrm{Im}\, Y_p(A,f)\right| < \varepsilon \end{cases} \qquad \varepsilon \to 0 \tag{4.10}$$

Non-perturbation conditions are fulfilled when the real and imaginary part of the probe admittance differ from zero for less than a given tolerance (for example $\varepsilon = 10^{-18}$ S), which is expressed by two inequalities involving the absolute values of a function of the two variables A_p, f_p. Precisely two real *objective functions* are defined as $c_1(A_p, f_p)$ =Re $Y_p(A_p, f_p)$, measuring the real part of the auxiliary generator admittance and $c_2(A_p, f_p)$ =Im $Y_p(A_p, f_p)$ which evaluates the imaginary part. Two separate optimization goals (4.10) have to be simultaneously met:

$$\begin{gathered} c_1(A_p, f_p) = \mathrm{Re}\, Y_p(A_p, f_p) \\ c_2(A_p, f_p) = \mathrm{Im}\, Y_p(A_p, f_p) \\ \textit{such that}: \\ \begin{cases} \arg\min\limits_{\substack{A_p \in \mathcal{A} \\ f_p \in \mathcal{F}}} c_i(A_p, f_p) = -\varepsilon \\ \arg\max\limits_{\substack{A_p \in \mathcal{A} \\ f_p \in \mathcal{F}}} c_i(A_p, f_p) = \varepsilon \end{cases} \qquad \begin{gathered} \mathcal{A} = [A_{\min}, A_{\max}] \\ \mathcal{F} = [f_{\min}, f_{\max}] \\ (\varepsilon = 1 \cdot 10^{-18}) \end{gathered} \end{gathered} \tag{4.10}$$

The *Gradient* method is chosen as default optimizer [8]. At each step the objective functions are evaluated at a candidates values $(A_p, f_p)^{(i)}$ and compared with the targets (4.10) by creating a *Cost Function* (also termed Error Function) which measures the *distance* of the *achieved goals from the desired ones* at a given iteration, using a *quadratic norm;*

$$\mathcal{C}(A_p, f_p) = \sum_{i=1}^{2} w_i \left| c_i(A_p, f_p) - \varepsilon \right|^2 = w_1 \left(c_1(A_p, f_p) - \varepsilon \right)^2 + w_2 \left(c_2(A_p, f_p) - \varepsilon \right)^2 \tag{4.11}$$

in which is also offered the possibility of weighting the optimization goals, depending on their relevance. The *gradient* of the cost function is evaluated and therefore a *direction* in the bidimensional search space $\mathcal{A} \times \mathcal{F}$ in order to reduce the cost function is obtained, agreeing with $-\nabla\mathcal{C}(A_p, f_p)$, which leads to the following update rule:

[9] A *dichotomous approach* can be very useful in this case. The first tentative is done setting $A = V_{DD}/2$; if convergence isn't achieved the simulation is restarted halving the value to $A' = V_{DD}/4$ and if even in this case convergence fails the value is halved to $A'' = V_{DD}/8$ and the optimization is run one more time, until a solution is found or the values for the probe amplitude become unacceptably low (below 0.1 V) indicating that the circuit cannot sustain a free running oscillation at that particular candidate frequency.

$$\begin{bmatrix} A_p \\ f_p \end{bmatrix}^{(i+1)} = \begin{bmatrix} A_p \\ f_p \end{bmatrix}^{(i)} - \alpha^{(i)} \cdot \nabla C(A_p, f_p)^{(i)} \tag{4.12}$$

At each gradient iteration (*outer tier*), *the current best choices for the amplitude and frequency* $(A_p, f_p)^{(i+1)}$ *are passed to the Harmonic Balance* simulation engine (*inner tier*), *driven by the voltage probe*. Therefore, because at each gradient optimizer iteration the HB simulator computes the output spectrum of the circuit solving the when it is forced by the generator:

$$e_n(t) = A_p^{(i+1)} \sin(2\pi f_p^{(i+1)} t) \tag{4.13}$$

avoiding the ambiguity regarding *the choice of the frequency basis* or the *degenerate convergence to a DC steady state*. The output of the harmonic balance simulation consist in the spectrum[10] $\mathbf{X}_k$ obtained as a solution of the equation $\mathbf{E}(\mathbf{X}_k)=\mathbf{0}$ obtained with the methods outlined in the section 3.2. In order to catch the nonlinear phenomena, the harmonic order is usually set up to N_h=3, and an oversampling factor of four is selected for evaluating the time domain waveform.

If the simulator doesn't succeed in finding such good values for the error function the reason is usually twofold. It might get stuck with improving the solution around a *local minimum (or maximum),* and consequently one observes very little improvement in the final *error norm*, compared with the initial values, with *slightly changing probe amplitude and frequency values*. Or rather, *a vanishing solution can be encountered*, for which the probe's amplitude values keep decreasing towards $A_{min,}$ indicating that the output signals get quenched. In the first case, is sufficient to *restart the simulation from a different point, perturbing slightly* the *probe amplitude and frequency initial values*. In the second case, it might be necessary to alter some circuital parameter.

Generally a hundred iterations suffice to minimize the cost function; its final values should be on the order of a tenth of a billionth (C_f = 1.0 ·10^{-10} or less), corresponding to negligible currents (on the order of 1 μA) flowing through the probe[11].

The complete algorithm is described below.

[10] Depending on the implementation, $\mathbf{X}_k$ denotes either the harmonic vector of the state variables (in Nodal Harmonic Balance) or the harmonic vector of the controlling variables for nonlinear elements (in Piecewise Harmonic Balance).

[11]Since the removal of the triggering signal doesn't have to affect the large signal steady state solution, an oscillating voltage is present at the probe terminals, but no current has to flow through the probe, resulting in a zero probe admittance

/*Free Running Oscillator Analysis*

/*General Set – up*

/introduce *the auxiliary generator at node"n"*

$e_n(t) = A\sin 2\pi ft$ / * large signal probe $(\varphi = 0)$

introduce a *current meter at node M to evaluate* $I_p^{1,(n)}(A,f)$

/introduce the impedance filter

$Z_p[1,1] = R_p + j0 = \{if\ f = f_p\ then: R_p \leftarrow 1\,\mathrm{p}\Omega\ \ else\ R_p \leftarrow 1\,\mathrm{T}\Omega\}$

/*define the ranges for the unknowns* (A,f)

$A \in [A_{\min}, A_{\max}] = \mathcal{A}$

$f \in [f_{\min}, f_{\max}] = \mathcal{F}$

$A \leftarrow A_0 (\equiv aV_{DD}, 0 \le a \le 1)$ / *tentative amplitude value

$f \leftarrow f_o^{lin}$ /*derived from lin. analysis

/*Formulate the Non Perturbation Conditions*:

$Y_p^{(n)}(A,f) \leftarrow \dfrac{I_p^{1,(n)}(A,f)}{A}$ / *evaluate* the probe admittance

$c_1(A,f) \leftarrow \mathrm{Re}\{Y_p^{(n)}(A,f)\}$
$c_2(A,f) \leftarrow \mathrm{Im}\{Y_p^{(n)}(A,f)\}$ / *define the objective functions*

$|c_i(A,f)| < \varepsilon,\ i = 1,2$ / *set the optimization goals*

$\varepsilon \leftarrow 1\cdot 10^{-18}\,S$ / select the desired tolerance

$N_{opt} \leftarrow 100$ / choose the maximum number of iterations

/*probe parameters optimization*

/*Outer – tier*

$\begin{bmatrix} A \\ f \end{bmatrix}^{(0)} \leftarrow \begin{bmatrix} A_0 \\ f_0 \end{bmatrix}$

for $(i = 1,\ldots,N_{opt})$ {

evaluate $\mathcal{C}^{(i)}(A,f) \leftarrow \left(\sum_{j=1}^{2} |c_j(A,f) - \varepsilon|^2\right)^{(i)}$

update $\begin{bmatrix} A \\ f \end{bmatrix}^{(i+1)} \leftarrow \begin{bmatrix} A \\ f \end{bmatrix}^{(i)} - \alpha^{(i)} \cdot \nabla \mathcal{C}^{(i)}(A,f)$

/*inner – tier*
solve the HB system
$\mathbf{E}(\mathbf{X}_k, A^{(i+1)}, f^{(i+1)}) = \mathbf{0}$
$\forall k \in \mathbb{Z} \cap [-N_h, N_h]$

advance: $i \leftarrow i + 1$

}

(4.14)

Moreover, the auxiliary generator model allow also to effectively *tune the oscillator circuit parameters, in order to have to have a specific power at the fundamental, at the node where the probe is inserted*, enabling a *full nonlinear* oscillator design. To that end non perturbation conditions are utilized, but this time the amplitude[12] and the frequency (A_0, f_0) of the probe signal, which agree with the specified amplitude and fundamental oscillation frequency for the circuit to be synthesized, are regarded as design targets and kept fixed; instead a set of adjustable parameters $\boldsymbol{\eta}=[\eta_1, \eta_2,\ldots,\eta_p]$ is introduced in the system (4.10) which is modified as follows;

[12] The probe amplitude is set according to the required output power that the oscillator has to deliver at the fundamental. See appendix E.

$$\begin{cases} \mathrm{Re}\, Y_p(A_0, f_0, \eta_1, ..., \eta_p) = 0 \\ \mathrm{Im}\, Y_p(A_0, f_0, \eta_1, ..., \eta_p) = 0 \end{cases} \Rightarrow \begin{cases} \left|\mathrm{Re}\, Y_p(A_0, f_0, \boldsymbol{\eta})\right| < \varepsilon \\ \left|\mathrm{Im}\, Y_p(A_0, f_0, \boldsymbol{\eta})\right| < \varepsilon \end{cases} \tag{4.15}$$

$$\boldsymbol{\eta} = [\eta_1, ..., \eta_p]^T \in \boldsymbol{\mathcal{P}} \subset \mathbb{R}^p \quad \varepsilon \to 0$$

and a two tier harmonic balance optimization is run with the aim of finding the best values to fulfill. (4.15). However in this case , if p > 2 the system is *underdetermined, and therefore the uniqueness of the final solution cannot be guaranteed,* therefore great care must be exerted when interpreting the results. The synthesis algorithm is shown in (4.16)

/Free Running Oscillator Design
/General Set – up

/introduce *the auxiliary generator at node"n"*

$e_n(t) = A\sin 2\pi ft$ /* large signal probe $(\varphi = 0)$
introduce a *current meter at node M to evaluate* $I_p^{1,(n)}(A, f)$
/introduce the impedance filter
$Z_p[1,1] = R_p + j0 = \{if\ f = f_p\ then: R_p \leftarrow 1\,\mathrm{p}\Omega\ \ else\ R_p \leftarrow 1\,\mathrm{T}\Omega\}$

$A \leftarrow A_0$ /*amplitude specification
$f \leftarrow f_0$ /*frequency specification
/define the ranges for the design parameters $(\eta_1, ..., \eta_p)$
$\boldsymbol{\eta} = [\eta_1, ..., \eta_p]^T \in \mathcal{P}$
$\mathcal{P} = [\eta_1^0, \eta_1^1] \times [\eta_2^0, \eta_2^1] \times \cdots \times [\eta_p^0, \eta_p^1]$
$\boldsymbol{\eta} \leftarrow \boldsymbol{\eta}_0 = [\eta_{10}, ..., \eta_{p0}]^T$ */ initialization*

/Formulate the Non Perturbation Conditions :

$Y_p^{(n)}(\boldsymbol{\eta}) \leftarrow \dfrac{I_p^{1,(n)}(A_0, f_0, \boldsymbol{\eta})}{A_0}$ */ evaluate* the probe admittance
$c_1(\boldsymbol{\eta}) \leftarrow \mathrm{Re}\{Y_p^{(n)}(\boldsymbol{\eta})\}$
$c_2(\boldsymbol{\eta}) \leftarrow \mathrm{Im}\{Y_p^{(n)}(\boldsymbol{\eta})\}$ */ define the objective functions*
$|c_i(\boldsymbol{\eta})| < \varepsilon,\ i = 1,2$ */ set the optimization goals*
$\varepsilon \leftarrow 1 \cdot 10^{-18} S$ / select the desired tolerance
$N_{opt} \leftarrow 100$ / choose the maximum number of iterations

/probe parameters optimization

/Outer – tier
for $(i = 1, ..., N_{opt})$ {
evaluate $C^{(i)}(\eta_1, ..., \eta_p) \leftarrow \left(\sum_{j=1}^{2} \left|c_j(\eta_1, ..., \eta_p) - \varepsilon\right|^2\right)^{(i)}$
update $\begin{bmatrix} \eta_1 \\ \eta_2 \\ \vdots \\ \eta_p \end{bmatrix}^{(i+1)} \leftarrow \begin{bmatrix} \eta_1 \\ \eta_2 \\ \vdots \\ \eta_p \end{bmatrix}^{(i)} - \alpha^{(i)} \cdot \nabla C^{(i)}(\eta_1, ..., \eta_p)$

/inner – tier
solve the HB system
$\mathbf{E}(\mathbf{X}_k, A_0, f_0, \boldsymbol{\eta}^{(i+1)}) = \mathbf{0}$
$\forall k \in \mathbb{Z} \cap [-N_h, N_h]$

advance : $i \leftarrow i + 1$
}

(4.16)

Due to the very nature of the Harmonic Balance method, the existence of an oscillatory solution is no guarantee for its stability (*physical observability*) which should be checked with different methods, like *transient/convolution method* or properly initialized *envelope transient simulations* [9].

4.2.2 LOW-AMPLITUDE AUXILIARY GENERATORS ANALYSIS FOR ESTIMATING OSCILLATIONS FREQUENCIES.

A first guess of the oscillation frequency must be provided to the optimization routine described in the previous section. To that aim, a linear analysis technique, based on small signal voltage type auxiliary generators can be employed. In particular, the Kurokawa oscillation condition for a negative resistance oscillator [10] must be fulfilled at the probe port. The voltage probe supplies a low amplitude signal between the node "n" and the ground:

$$\gamma_n(t) = a_p \sin(2\pi f_p t) \tag{4.17}$$

where $a_p = 1-10\text{mV} \ll V_{bias}$ justifies the small signal (linear) approximation. Then, by altering the auxiliary generator frequency to scan a wide frequency range, the probe conductance $Y_p^{(n)}(f_p)$ is measured, looking for potential oscillations which arise at those frequencies exhibiting *negative conductance* $G_p^{(n)}(f_p) = \text{Re}(Y_p^{(n)}(f_p))$ values *and resonating susceptance* $S_p^{(n)}(f_p) = \text{Im}(Y_p(f_p))$. The linear frequency estimate, provided the aforementioned conditions are met, is found at the frequency value for which the susceptance crosses the frequency (abscissa) axis:

$$\boxed{\begin{aligned} &G_p^{(n)}(f_{osc}) < 0 \\ &\frac{\partial S_p^{(n)}(f_{osc})}{\partial f_p} > 0 \\ &S_p^{(n)}(f_{osc}) = 0 \end{aligned}} \qquad \begin{aligned} G_p^{(n)}(f_p) &= \text{Re}\{Y_p^{(n)}(f_p)\} \\ S_p^{(n)}(f_p) &= \text{Im}\{Y_p^{(n)}(f_p)\} \end{aligned} \tag{4.18}$$

To implement this *linear search method* to retrieve estimates of the possible oscillation frequencies, *small-signal driven*, *frequency swept* Harmonic Balance simulation are run, measuring both the real and the imaginary part of the auxiliary generator admittance at its port. The visual inspection of the two graphs $\{(G_p^{(n)}(f_p), f_p) / f_p \in \mathcal{F}\}$ and $\{(S_p^{(n)}(f_p), f_p) / f_p \in \mathcal{F}\}$ allow a quick verification, allowing to extract a suitable *candidate frequency value* for properly initializing the Auxiliary Generator.

/* *Linear Analysis set - up*
introduce *the probe at a measurement node "n"*
set the small probing voltage (constant): $a = 1mV$
$\gamma^{(n)}(t) = a \cdot \sin 2\pi ft$ /* *small amplitude, frequency swept voltage signal*
/*Frequency Analysis*
for $f \in [f_{\min}, f_{\max}]$ /
{
$\mathbf{H}(\mathbf{X}, a, f, \mathbf{V}) = \mathbf{0}$ /* *solve* the HB equations
$Y_p^{(n)}(f) \leftarrow \dfrac{I_p^{1,(n)}(f)}{a}$ /* *evaluate* the probe admittance
$f \leftarrow f + \Delta f$ /* *frequency advance*
}
/* *Oscillation Condition check*

$$if \left(\begin{array}{l} \mathrm{Re}(Y_p^{(n)}(f_o)) < 0 \\ \dfrac{\partial \mathrm{Im}(Y_p^{(n)}(f_o))}{\partial f} > 0 \\ \mathrm{Im}(Y_p^{(n)}(f_o)) = 0 \end{array} \right) \quad \text{then} \quad \hat{f}_{osc} \leftarrow f_o \ / \text{estimated osc. frequency } (f_o \in [f_{\min}, f_{\max}]) \tag{4.19}$$

4.2.3 A Describing Function (Quasi-Linear) Approach Based on Amplitude Tracking to Estimate Oscillation Amplitudes

A search method based on a quasi-linear approach for finding good auxiliary generator's candidate *amplitude values* proves to be adequate when all attempts with the trial and error method previously exposed aren't effective. In fact, a satisfactory approximation for the non perturbation conditions when only a *single harmonic analysis is carried out* is:

$$\begin{cases} \mathrm{Re}\, Y_p(A, f) \cong \mathrm{Re}\, Y_p(A, f_o)\big|_{f_o = const} = \mathrm{Re}\, Y_p(A) = 0 \\ \mathrm{Im}\, Y_p(A, f) \cong \mathrm{Im}\, Y_p(A_o, f)\big|_{A_o = const} = \mathrm{Im}\, Y_p(f) = 0 \end{cases} \tag{4.20}$$

being the probe admittance real part mainly dependent on the probe amplitude, while the imaginary part mainly dependent on its frequency; this approximation relies on the so called Describing Function (DF) method [11] which consist in neglecting the contributions of the higher harmonics in the current generated in response to the periodic excitation $e_n(t)$.

It is immediately noticed[13] that the second equation of the system (4.20) – *when evaluating it at a constantly small amplitude value (*$A=A_{lin}$ *=10 mV)* – is solved by the *linear estimate* $f_{lin}^{(i)}$. Evaluating the first equation at $f_{lin}^{(i)}$ – thus reusing the linear estimate – a *zero finding algorithm* for the function $\mathrm{Re}Y(A, f_{o,lin})$ is invoked, by using the *amplitude tracking procedure* as described in (4.21). Essentially, probe driven HB simulations are run at a constant frequency $f_{lin}^{(i)}$ while the probe amplitude is

[13] The system of equation gets decoupled, by evaluating $\mathrm{Re}(Y_p(A,f))$ *at a constant frequency* and $\mathrm{Im}(Y_p(A,f))$ at *a constant amplitude.* Instead of solving a 2x2 system of equation jointly dependent on the pair (A,f), the two equations are solved sequentially. From the second equation evaluated at a small amplitude, the linear frequency estimate $f_{lin}^{(i)}$ is calculated, which in turn, is plugged into the first equation from which the probe amplitude is derived.

swept in the reference range [A_{lin}, V_{DD}/η]; at each step the probe admittance is evaluated, and by inspecting the graph {A, Re($Y_p(A)$)} and the value A_0 *fulfilling the first equation of the system* (4.20) can be found, which provides a candidate value for the probe amplitude to be used in the process (4.5) as an initial estimate.

$$
\begin{aligned}
&\textit{Amplitude Tracking}\\
&\boxed{\begin{array}{l} V_g^i \leftarrow V_{0i} \ / \ \textit{tuning voltages are initialized} \\ p(t) = A\sin 2\pi ft \ / * \text{ voltage probe} \\ A \leftarrow A_{lin} = 10\,mV \\ f \leftarrow \hat{f}_{lin}^i \ / * \text{derived from lin. analysis} \end{array}}\\
&\text{for } \ A_{lin} \le A \le (V_{DD}/\eta)\{\\
&\boxed{\begin{array}{l} solve: \mathbf{H}(\mathbf{X},\ A, \hat{f}_{lin}^i, \mathbf{V}) = \mathbf{0} \ \ / harmonic\ balance\ equations \\ Y_p(A, \hat{f}_{lin}^i) \leftarrow \dfrac{I_p^{(1)}(A, \hat{f}_{lin}^i)}{V_p^{(1)}} = \dfrac{I_p^{(1)}(A, \hat{f}^i)}{A} \ / \text{ probe admittance} \\ A \leftarrow A + \Delta A \end{array}}\\
&plot\{A, \mathrm{Re}(Y_p(A, \hat{f}_{lin}^i)\}\\
&\qquad\qquad \}\\
&if\,(\mathrm{Re}\,Y_p(A, \hat{f}_{lin}^i) = 0 \ at\ A = A_0)\\
&\quad then\ \hat{A} \leftarrow A_0 \ (assignment\ of\ the\ candidate\ amplitude)
\end{aligned}
\tag{4.21}
$$

4.3 Auxiliary Generators-Driven, Envelope Transient Analysis for Inspecting the Stability of Oscillating Solutions

The Harmonic Balance simulation process relies on the assumption that when an external periodic excitation of frequency ω_0 forces a nonlinear circuit, the latter would eventually reach the periodic steady state. Due to the nonlinearities present in the active devices, the output waveform will be a distorted replica of the input signal; thus by expanding the unknown variable by means of Fourier Series up to certain harmonic order, it is possible to account for this effects, and completely characterize the circuit *periodic steady state* in nonlinear terms. This *working hypothesis* is mantained even in the case of oscillator analysis, which is performed by having recourse to artificial forcing terms, the harmonic probes (auxiliary generators).

However, the underlying assumption is a *very strong one*. In fact, as previously pointed out, very different regimes could be established when dealing with nonlinear circuits. For example, a circuit driven by a signal at a frequency ω_0 could generate subharmonic resonances ω_0/k, *as in the case of frequency dividers* [12]. Another possibility, is that the forcing signal at (ω_0) interacting with an autonomously generated spurious oscillation at frequency ω_s generates an almost periodic output waveform, like the one encountered in *self oscillating mixers* [13]. Or even very complicated *chaotic* steady states are possible, and they are of interest for secure communication [14].The harmonic balance method, being restrained to the expression of the solution as a trigonometric polynomial, turns out not to capture the most general nonlinear circuit behavior.

Even when setting aside the most complicated nonlinear phenomena, a serious consequence arising from the Harmonic Balance framework, is that although a *complete numerical description of the periodic steady state is possible,* meaning that the system $\mathbf{E}(\mathbf{X}_k)=\mathbf{0}$ *converges* it doesn't necessarily imply that *the physical solutions are observable in reality*. In the jargon of nonlinear systems theory, the *observable* solutions are called *stable*, the stability being a measure of *robustness of a solution with respect to perturbations. Unstable solutions aren't observable in physical experiments since they decay in a very small time* [2,7].If the circuit under investigation is an *oscillator*, unstable solutions does not show up in an a laboratory experiment with a prototype; *the circuit simply does not oscillate.*

In order to inquire into the solution stability, it is necessary to perturb the circuit with a disturbance (for example, a small duration *voltage pulse*) and follow the time domain evolution of the response to the perturbation; stable solutions are those which quickly recover their periodic behavior. Transient /Convolution analysis could therefore be used, but that may lead to lengthy/inefficient simulations as seen before.

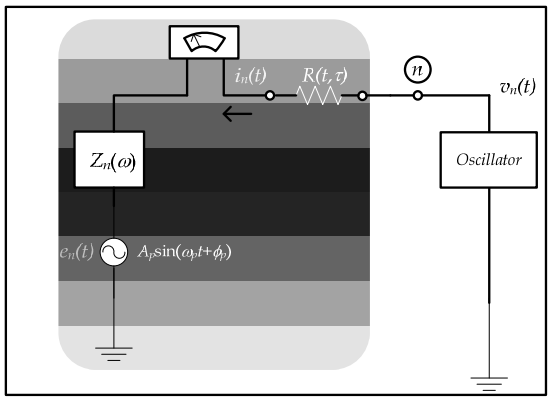

FIGURE 4-3. Voltage Type Auxiliary Generator augmented with a gating resistor to investigate oscillators transient behavior**.**

In this case, a mixed time domain /frequency domain approach pursued by Envelope Transient formulation could provide better results [15]. In the case of oscillator circuits analysis, it constitutes in fact a generalization of the previously exposed auxiliary generators technique to the time varying case. To that aim the harmonic probe is connected to a *time varying series resistor*, modeling *the effect of a gating signal* (insert picture) $R(t,\tau)$ which *disconnects the voltage probe after* a time[14] τ. As a result, the probe signal gets injected into the oscillator circuit only during the interval [0, τ]. As (4.22) suggest, $R(t,\tau)$ offers the probe an *arbitrarily high* series *resistance* outside the observation interval (which can be obtained by setting $R(t,\tau)$ = 1 MΩ for $t>\tau$), and a zero resistance otherwise (insert picture of the modified probe)

$$v(t) = R(t,\tau)\cdot A\sin(2\pi ft)$$
$$where\ R(t,\tau) = \begin{cases} \infty & t \in]\tau, +\infty[\\ 0 & t \in [0,\tau] \end{cases} \qquad (4.22)$$

[14] Gating time parameter has to be greater than the inverse of the oscillation frequency to catch the envelope variations, so a reasonable lower bound could be $(10/f_{osc}) \leq \tau$. Considering frequencies of a few GHz, τ *is usually chosen to be 5 ns to 10 ns.*

In order to check the stability of a given solution, first the values (A, f) must be initialized with the values obtained after an Harmonic Balance simulation has been carried out (A^*, f^*). Subsequently, an envelope transient simulation driven by the time-varying auxiliary generator is performed, allowing one to follow the solution amplitude, and doing so to check their stability. In case of stable solutions, the output *signal's amplitude grows and reaches eventually its steady state* value; otherwise the output signal *exponentially decreases over time*.

4.4 SIMULATION OF SYNCHRONIZED (INJECTION LOCKED) OSCILLATORS

In modern receivers architectures, a local oscillator is used in the RF stage feeding the TX/RX antenna to up-convert (when transmitting) or down-convert (when receiving) a baseband signal[15]. Free-running oscillators are rarely used as stand-alone components for generating (detecting) carrier waves since its nominal oscillation frequency may drift due to inevitable mismatches, components aging, temperature variations, mechanical vibrations, causing a deterioration of the receiver performance [1]. A much more reliable operation is obtained through the adoption of Phase Locked Loops [16], which essentially aim at tracking the received signal (*reference*) frequency by means of a control loop, constituted by a phase detector, a low-pass filter, and a voltage controlled oscillator. The phase detector reads the input phase and converts it to a voltage, which is low-pass filtered (to prevent spurious high frequency terms from affecting closed loop operation) and adjust the frequency VCO so to reduce the *phase error between the incoming signal phase and the reference one*. The input (reference) signal gets synchronized when the difference among the input phase and the output (VCO) becomes constant, and the VCO frequency is equal to that of the (reference) input signal.

Nonetheless, the phase locking condition (between a reference signal and the VCO output signal) could be more easily satisfied by means of a technique known as *injection locking* [17-20]. When the reference signal V_{inj} (at frequency ω_{inj}) is fed directly to an *additional* VCO *input port* (insert picture), the VCO output signal V_o *(at the VCO free-running frequency* ω_o) as a *result of nonlinear interactions synchronizes with the injected one*, provided its frequency falls within the *locking range* $\Delta\omega_L$. In simple *LC tank* oscillator configurations, the locking range is easily computed by using the simple result from Adler's differential equation at the steady state:

$$\Delta\omega_L = \frac{\omega_0}{2Q}\frac{V_{inj}}{V_o} \tag{4.23}$$

[15] Whether the signal is analogue or digital, the standard receiver architecture has been long based on the heterodyne and super-heterodyne approach. Although in the latest years, a new transceiver paradigm has been suggested, for the purpose of processing the information directly in the digital domain (after having it sampled with ADCs), and employing *general purpose processor instead of relying on conventional hardware* (Software Defined Radio), still technological limitations residing in the accuracy of high speed analog to digital conversion have hindered its deployment, thus making the analog components of the basic receiver RF chain (LNA, filters, mixers, oscillators) irreplaceable at present.

which depends *upon the relative strength of the injection signal*, and it's *inversely related* to the oscillator *frequency selectivity* around ω_o, expressed by the *Q*-factor (therefore lower *Q* resonators provide broader locking ranges). The Adler formula for the oscillator locking range is quite insightful; nevertheless the dependence upon the *Q*-factor limits its applicability to LC-tank oscillators, for which *Q* is rigorously defined[16] [21-24]. Moreover higher order issues are forgotten in the simple, Adler formula (3.87). First, there exist *a threshold input power level* which once exceeded might quench the free running oscillating solution at ω_0 (regardless about the vicinity of ω_{inj} with ω_0, i.e., regardless whether the injected signals possess a frequency falling within the oscillator (VCO) locking range $\Delta\omega_L$). Symmetrically, it can be shown that some oscillators which are biased at a sub-threshold voltage and not producing any oscillation in normal operation, when (adequately) driven by an input signal, phase-lock to it, and an increase of gain is observed in a very narrow band around the injected carrier (the circuit operates essentially as an *Injection Locked Amplifier or* ILA). Lastly, at the border of the locking range synchronization is not achieved since the input signal at ω_{inj} mixes with the oscillating signal at ω_0, giving rise to intermodulation products in the output spectrum which characterize a *self-oscillating mixer* behavior[17] [25-27].

In order to overcome this issue, a generalization of the Adler equation relying on the nonlinear systems theory framework and the *perturbation projection vector* (PPV) approach originally developed for investigating the oscillator phase noise [28], has recently been proposed in [29] . However, it might be hard to implement from a numerical standpoint since it calls for a *detailed knowledge of the time domain model of the circuit*, via *phase domain macro-models* [30] which for the specific case of Distributed Oscillators (VCOs) are unattainable.

A more suitable approach consists in evaluating the oscillator injection locking characteristics based on the modified Harmonic Balance method for autonomous circuits[18] [7]. An analogous setting is used for evaluating the injection locking properties; the auxiliary generator (harmonic probe) frequency is thus fixed at the injection frequency and the same two-tier procedure elucidated in the earlier paragraphs is used to obtain the output power and the coupling phase (described by the two unknowns (A, φ) of the harmonic probe). This simulation technique is

[16] In fact, many nonequivalent quality factor definition could be provided depending on the specific circuit being examined (a filter, an oscillator, an amplifier) giving rise to numerical discrepancies among them [24]. One topology independent definition sets the quality factor at half the resonant (oscillation) frequency times the derivative of the oscillator (closed loop) phase response in the frequency domain, in a neighborhood of ω_o, that is: $Q = \omega_0/2 * (\partial\Phi/\partial\omega)$, but also in this case quantitative differences for different circuits have been found and to inconsistencies for specific classes of oscillators which produce non-sinusoidal waveforms (recalcitrant oscillators, for example, for which a quality factor is not defined).

[17] This could be approximated by using the Adler differential equation for the phase variation, assuming specific (and simple) circuit topologies are given [20]. A more complete picture is however obtained by means of nonlinear analysis techniques in the frequency domain, jointly with a parametric analysis of the circuit, to extrapolate the oscillator synchronization regions regardless of the topology being examined.

[18] In fact, conceptually the harmonic probe (auxiliary generator) *is all in all equivalent to an external sine-wave* RF generator driving the circuit; *a free-running oscillating solution* (specified by the two unknowns (A, f) of the harmonic probe) is found when the *test circuit is injection locked to the auxiliary probe* and fulfills at the same time the non-perturbation conditions, so that the output power and fundamental oscillation frequency can be recovered by using a two-tier harmonic balance scheme.

illustrated in (6.88) where an additional design parameter μ has been considered. The advantage of using the harmonic balance formulation for analyzing the injection locking process resides in its flexibility. In fact, a complete synchronization profile of the oscillator can be obtained by sweeping both the input power (amplitude)[19] , and the phase of the auxiliary generator probe, with one or more design parameters varying in admissible ranges, to fulfill the oscillation conditions at the probe port as illustrated in (3.75).

[19] Considering a nominal impedance Z_0 (for example, 50 Ω) a one to one mapping among the amplitude expressed as peak voltage and corresponding power levels in dBm, is established, see appendix E.

Injection Locking Design (parameter dependent setting)

$f \leftarrow f_0$ / *injected signal requency*

$A \leftarrow A_0$ / *injected signal amplitude*

initializaztion

/introduce *the auxiliary generator at node* "n"

$e_n(t) = A_0 \sin(2\pi f_0 t + \varphi)$ / * large signal probe – φ *dependent*

introduce a *current meter at node* M *to evaluate* $I_p^{1,(n)}(A, f)$

/introduce the impedance filter

$Z_p[1,1] = R_p + j0 = \{if\ \ f = f_p\ \ then: R_p \leftarrow 1\,\mathrm{p}\Omega\ \ \ else\ R_p \leftarrow 1\,\mathrm{T}\Omega\}$

$\varphi \in [0, 2\pi]$ / *phase range*

$\mu \in \mathcal{U}$ / *design parameter range*

$\mu \leftarrow \mu_0$

$\varphi \leftarrow 0$

/*Formulate the Non Perturbation Conditions*:

$$Y_p^{(n)}(\varphi, \mu) \leftarrow \frac{I_p^{1,(n)}(A_0, f_0, \varphi, \mu)}{A_0} \text{ / } evaluate \text{ the probe admittance}$$

$c_1(\varphi, \mu) \leftarrow \mathrm{Re}\{Y_p^{(n)}(\varphi, \mu)\}$
$c_2(\varphi, \mu) \leftarrow \mathrm{Im}\{Y_p^{(n)}(\varphi, \mu)\}$ / *define the objective functions*

$|c_i(\varphi, \mu)| < \varepsilon$, $i = 1, 2$ / *set the optimization goals*

$\varepsilon \leftarrow 1 \cdot 10^{-18} S$ / select the desired tolerance

$N_{opt} \leftarrow 100$ / choose the maximum number of iterations

/*probe parameters optimization*

/*Outer – tier*

$$\begin{bmatrix} \varphi \\ \mu \end{bmatrix}^{(0)} \leftarrow \begin{bmatrix} \varphi_0 \\ \mu_0 \end{bmatrix}$$

for $(i = 1, ..., N_{opt})$ {

evaluate $\mathcal{C}^{(i)}(\varphi, \mu) \leftarrow \left(\sum_{j=1}^{2} |c_j(\varphi, \mu) - \varepsilon|^2 \right)^{(i)}$

update $\begin{bmatrix} \varphi \\ \mu \end{bmatrix}^{(i+1)} \leftarrow \begin{bmatrix} \varphi \\ \mu \end{bmatrix}^{(i)} - \alpha^{(i)} \cdot \nabla \mathcal{C}^{(i)}(\varphi, \mu)$

/*inner – tier*
solve the HB system
$\mathbf{E}(\mathbf{X}_k,\ A_0, f_0, \varphi^{(i+1)}, \mu^{(i+1)}) = \mathbf{0}$
$\forall k \in \mathbb{Z} \cap [-N_h, N_h]$

advance: $i \leftarrow i + 1$

}

(4.24)

Synchronization Profile. Injection-Locking Analysis

$$/\ find\ an\ \ oscillating\ solution\ described\ by \begin{cases} A = A(\varphi,\mu) \in \mathcal{A} \\ f = f(\varphi,\mu) \in \mathcal{F} \end{cases}$$

where φ *is the phase,* μ *is a parameter*

$$\boxed{\begin{array}{l} A \in \mathcal{A} = [A_{\min}, A_{\max}]\ /\ amplitude\ search\ range \\ f \in \mathcal{F} = [f_{\min}, f_{\max}]\ /\ frequency\ search\ range \\ \varphi \in [0, 2\pi] /\ phase\ range \\ \mu \in \mathcal{U} = [\mu_{\min}, \mu_{\max}]\ /\ parameter\ range \end{array}}$$

/introduce the large signal harmonic probe:

$$\boxed{\begin{array}{l} e_n(t) = A\sin(2\pi ft + \varphi)\ /\ *\ \text{large signal probe} - \varphi\ dependent \\ \text{introduce a } current\ meter\ \ at\ node\ M\ to\ \ evaluate\ I_p^{1,(n)}(A, f) \\ /\text{introduce the impedance filter} \\ Z_p[1,1] = R_p + j0 = \{if\ \ f = f_p\ \ then: R_p \leftarrow 1\,\text{p}\Omega\ \ \ else\ \ R_p \leftarrow 1\,\text{T}\Omega\} \end{array}}$$

$\varphi \leftarrow \varphi_0$ / *initial phase*

$\mu \leftarrow \mu_0$ / *initial parameter choice*

$$run\ HB\ \ analysis\ at\ (\varphi_0, \mu_0)\ to\ \ find \begin{cases} A_0 = A(\varphi_0, \mu_0) \in \mathcal{A} \\ f_0 = f(\varphi_0, \mu_0) \in \mathcal{F} \end{cases}$$

$A \leftarrow A_0$

$f \leftarrow f_0$

set $\Delta\varphi$

set $\Delta\mu$

$$\boxed{\begin{array}{l} /\ nested\ sweeps \\ for\ (\mu_{\min} \le \mu \le \mu_{\max})\ \{ \\ \quad for\ (0 \le \varphi \le 2\pi)\{ \\ \quad\quad solve\ \mathbf{HB}(\varphi, \mu) \\ \quad\quad\quad \varphi \leftarrow \varphi + \Delta\varphi \\ \quad\quad\quad \} \\ \quad\quad \mu \leftarrow \mu + \Delta\mu \\ \quad\quad\quad\quad \} \\ save\ \&\ display\{\ A(\varphi,\mu), f(\varphi,\mu) \in \mathcal{A} \times \mathcal{F},\ \forall (\varphi,\mu) \in [0, 2\pi] \times \mathcal{U}\} \end{array}} \qquad (4.25)$$

HB(φ,μ)

/ double tier system of Harmonic Balance Equations

$f \in \mathcal{F} = [f_{\min}, f_{\max}]$ / *range for the injection frequencies*

$A \in \mathcal{A} = [A_{\min}, A_{\max}]$ / *search range for the amplitude*

$\varphi \in [0, 2\pi]$ / *phase range*

$\mu \in \mathcal{U}$ / *additional design parameter*

set max *iteration number* $N_{\max}$

set max *harmonic order* N_h

set tolerance ε

$\varphi \leftarrow \varphi_0$

$\mu \leftarrow \mu_0$

set max *iteration number* $N_{\max}$

Formulate the Non Perturbation Conditions

/ (φ,μ) *are the external – parameters in the nested loop* (*fixed*):

$$Y_p^{(n)}(A(\varphi,\mu), f(\varphi,\mu)) \leftarrow \frac{I_p^{1,(n)}(A(\varphi,\mu), f(\varphi,\mu))}{A(\varphi,\mu)} \text{ / evaluate the probe admittance}$$

$$\begin{aligned} c_1(A(\varphi,\mu), f(\varphi,\mu)) &\leftarrow \mathrm{Re}\{Y_p^{(n)}(A(\varphi,\mu), f(\varphi,\mu))\} \\ c_2(A(\varphi,\mu), f(\varphi,\mu)) &\leftarrow \mathrm{Im}\{Y_p^{(n)}(A(\varphi,\mu), f(\varphi,\mu))\} \end{aligned} \quad \text{/ define the objective functions}$$

$\left|c_i(A(\varphi,\mu), f(\varphi,\mu))\right| < \varepsilon$, $i = 1,2$ / *set the optimization goals*

$\varepsilon \leftarrow 1 \cdot 10^{-18} S$ / select the desired tolerance

$N_{opt} \leftarrow 100$ / choose the maximum number of iterations

/ *probe parameters optimization* : *the* variables are (A, f)

/ *Outer – tier*

$$\begin{bmatrix} A(\varphi,\mu) \\ f(\varphi,\mu) \end{bmatrix}^{(0)} \leftarrow \begin{bmatrix} A(\varphi_0,\mu_0) \\ f(\varphi_0,\mu_0) \end{bmatrix}$$

for $(i = 1,\ldots,N_{opt})$ {

evaluate $\mathcal{C}^{(i)}(A,f) \leftarrow \left(\sum_{j=1}^{2} \left|c_j(A,f) - \varepsilon\right|^2\right)^{(i)}$

update $\begin{bmatrix} A \\ f \end{bmatrix}^{(i+1)} \leftarrow \begin{bmatrix} A \\ f \end{bmatrix}^{(i)} - \alpha^{(i)} \cdot \nabla \mathcal{C}^{(i)}(A,f)$

/ *inner – tier*

solve the HB system

$\mathbf{E}(\mathbf{X}_k, A^{(i+1)}, f^{(i+1)}, \varphi, \mu) = \mathbf{0}$

$\forall k \in \mathbb{Z} \cap [-N_h, N_h]$

advance : $i \leftarrow i + 1$

}

(4.26)

4.4.1 SUPERHARMONIC /SUBHARMONIC INJECTION LOCKING. APPLICATION TO FREQUENCY DIVIDERS.

Since the early discoveries related to the subject of driven oscillators, it was seen that the injection locking process could occur at rationally related frequencies[20] [17]. Specifically, let ω_o be the oscillator autonomous frequency and ω_{inj} the injected one, synchronization could be achieved in the following cases:

- $\omega_{inj} = p\omega_o$ ($p \in \mathbb{N}$, $p > 1$) , *superharmonic injection locking* (1:*p synchronization*): the RF injected signal (ω_{inj}) phase-locks the circuit at *an higher order harmonic of the autonomously generated oscillation* at ω_o (provided adequate input power is delivered and the injected frequency falls close enough to $p\omega_o$); therefore the output will be a *divided frequency* (of *p-th* order) $\omega_o = (1/p)\omega_{inj}$

- $q\omega_{inj} = \omega_o$ ($q \in \mathbb{N}$, $q > 1$), *subharmonic injection locking* (*q*:1 *synchronization*): higher order harmonics of the RF driving signal phase-locks the autonomously generated oscillation at ω_o (provided adequate input power is delivered and the autonomous frequency is close enough to $q\omega_{inj}$); the output oscillation will be a *multiplied frequency of q-th order*. Notice that the injection frequency is a subharmonic $\omega_{inj} = (1/q)\omega_o$ *of the free-running oscillation frequency.*

- $q\omega_{inj} = p\omega_o$ ($p \in \mathbb{N}$, $q \in \mathbb{N}$, $p \neq q$ $p,q > 1$), *ultra-subharmonic injection locking* (*q:p synchronization)*: achieved when an harmonic of order *q* of the injected signal at frequency ω_{inj} locks with an harmonic of order *p* relative to the autonomous oscillation frequency

The Harmonic Balance simulation framework analyzing the superharmonic or subharmonic injection locking is *equivalent* to the 1:1 synchronization analysis; it is sufficient to adequately specify the *frequency of the Auxiliary Generator, as if it was the injection source, and consider it as a constant*; the optimization process explained above will find the most suitable *locking amplitude* and *phase*.

[20] Two frequencies (ω_α, ω_b) are said to be *rationally related* if for some integers *m*,*n* results: $m\omega_a = n\omega_b$.

4.5 REFERENCES

[1] A. Grebennikov. *RF and Microwave Transistor Oscillator Design*, John Wiley and Sons, May 2007.

[2] F. Giannini, and G Leuzzi. *Non-linear Microwave Circuit Design*, John Wiley & Sons, June 2004

[3] M. Odyniec. *RF and Microwave Oscillator Design*, Artech House, October 15, 2002.

[4] A. Brambilla, G. Gruosso, and G.S. Gajani, "Robust Harmonic-Probe Method for the Simulation of Oscillators," *IEEE Transactions on Circuits and Systems I: Regular Papers*, vol.57, no.9, Sept. 2010, pp.2531-2541.

[5] C.R. Chang, M.B. Steer, S. Martin, E.,Jr. Reese, "Computer-aided analysis of free-running microwave oscillators", *IEEE Transactions on Microwave Theory and Techniques,* vol. 39 , no. 10, pp. 1735 – 1745, Oct. 1991.

[6] E. Ngoya, A. Suarez, R. Sommet and R.Quéré, "Steady state analysis of free or forced oscillators by harmonic balance and stability investigation of periodic and quasi-periodic regimes," *Wiley International Journal on Microwave and Millimeter Wave Computer Aided Engineering,* vol. 5, no. 3, pp. 210–223, May 1995.

[7] A. Suarez, and R. Quéré. *Stability Analysis of Nonlinear Microwave Circuits*, Artech House publishers, January 2003

[8] J. Snyman. *Practical Mathematical Optimization: An Introduction to Basic Optimization Theory and Classical and New Gradient-Based Algorithms*. Springer series on Applied Optimization, November 2005.

[9] E. Ngoya, J. Rousset, and D. Argollo, "Rigorous RF and microwave oscillator phase noise calculation by envelope transient technique,"*Proceedings of the 2000 IEEE MTT-S International Microwave Symposium Digest (IMS 2000)*, pp. 91–94, Jun. 2000.

[10] K. Kurokawa, "Some Basic Characteristic of Broadband Negative Resistance Oscillators," *Bell Systems Technical Journal,* [On-line] vol.48, June 1969, pp. 1937-1955, Available: http://www.alcatel-lucent.com/bstj/vol48-1969/articles/bstj48-6-1937.pdf [Mar. 21,2013].

[11] L. Gustafsson, G. H Bertil Hansson, and K. I. Lundström; "On the use of describing functions in the study of nonlinear active microwave circuits," *IEEE Trans. Microwave Theory Tech.,* vol. 20, pp. 402–409, 1972.

[12] J.C. Nallatamby, M. Prigent, J.C. Sarkissian, R. Quéré, and J. Obregon, "A new approach to nonlinear analysis of noise behaviour of synchronized oscillators and analog-frequency dividers," *IEEE Trans. Microwave Theory Tech., vol. 46*, pp.1168–1171, Aug. 1998.

[13] E. De Cos, A. Suarez, and S. Sancho, "Envelope transient analysis of self-oscillating mixers," *IEEE Trans. Microwave Theory Tech.*, vol. 52, pp. 1090–1100, April 2004.

[14] K.M Cuomo, and A.V. Oppenheim, "Circuit implementation of synchronized chaos with applications to communications," *Phys. Rev. Lett., no. 71*,pp. 65–68, July 1993

[15] H.G. Brachtendorf, G. Welsch, and R. Laur, "A time-frequency algorithm for the simulation of the initial transient response of oscillators," *Proceedings of the 1998 IEEE International Symposium on Circuits and Systems, (ISCAS '98),* vol.6, pp.236-239, 31 May-3 Jun 1998.

[16] F.M. Gardner. *Phaselock Techniques*. New York: John Wiley & Sons, July 29, 2005.

[17] R. Adler, "A Study of Locking Phenomena in Oscillators," *Proceedings of the IRE* , vol.34, no.6, pp. 351- 357, June 1946.

[18] L.J. Paciorek, "Injection locking of oscillators," *Proceedings of the IEEE*, vol.53, no.11, pp. 1723- 1727, Nov. 1965.

[19] K. Kurokawa, "Injection locking of microwave solid-state oscillators," *Proceedings of the IEEE*, vol.61, no.10, pp. 1386- 1410, Oct. 1973.

[20] B. Razavi, "A study of injection locking and pulling in oscillators," *IEEE Journal of Solid-State Circuits,* , vol.39, no.9, pp. 1415- 1424, Sept. 2004.

[21] T.O. Ohira, and K. Araki, "Active Q-Factor and Equilibrium Stability Formulation for Sinusoidal Oscillators," *IEEE Transactions on Circuits and Systems II: Express Briefs*, vol.54, no.9, pp.810-814, Sept. 2007.

[22] T. Ohira, "Rigorous Q-factor formulation for one- and two-port passive linear networks from an oscillator noise spectrum viewpoint," *IEEE Transactions on Circuits and Systems II: Express Briefs* , vol.52, no.12, pp. 846- 850, Dec. 2005.

[23] T. Ohira, "Extended Adler's injection locked Q factor formula for general one- and two-port active device oscillators," [On-line] *IEICE Electronics Express* vol. 7, no. 19, pp 1486-1492, 2010 : https://www.jstage.jst.go.jp/article/elex/7/19/7_19_1486/_pdf, [Mar. 21, 2013].

[24] T. Ohira, "Dedicated Q factor formulas stemming from oscillation frequency stability against source and load deviations," *IEICE Electronics Express* [On-line], vol. 9, no. 7, pp. 616-621, 2012, Available: https://www.jstage.jst.go.jp/article/elex/9/7/9_7_616/_pdf [Mar. 21, 2013].

[25] F. Ramirez, M.E. de Cos, and A. Suarez, "Nonlinear analysis tools for the optimized design of harmonic-injection dividers," *IEEE Transactions on Microwave Theory and Techniques*, vol.51, no.6, pp. 1752- 1762, June 2003.

[26] A. Suarez,J. Morales, and R. Quere, "Synchronization analysis of autonomous microwave circuits using new global-stability analysis tools," *IEEE Transactions on Microwave Theory and Techniques*, vol.46, no.5, pp.494-504, May 1998.

[27] V. Rizzoli, A. Neri, and D. Masotti, "The application of harmonic-balance methodology to the analysis of injection locking," *Proceedings of IEEE MTT-S International Microwave Symposium Digest, 1992,* vol. 3, pp.1591-1594,Jun 1992.

[28] A. Demir, and J. Roychowdhury, "A reliable and efficient procedure for oscillator PPV computation, with phase noise macromodeling applications," *IEEE Transactions on Computer-Aided Design of Integrated Circuits and Systems*, vol.22, no.2, pp. 188- 197, Feb. 2003.

[29] Xiaolue Lai and J. Roychowdhury, "Capturing oscillator injection locking via nonlinear phase-domain macromodels," *IEEE Transactions on Microwave Theory and Techniques*, vol.52, no.9, pp. 2251- 2261, Sept. 2004.

[30] P. Maffezzoni, "Analysis of Oscillator Injection Locking Through Phase-Domain Impulse-Response," *IEEE Transactions on Circuits and Systems I: Regular Papers,* , vol.55, no.5, pp.1297-1305, June 2008.

CHAPTER V. PHASE-LOCKED PATTERNS ANALYSIS AND CONTROL IN TRIPLE-PUSH OSCILLATORS

5.1 TRIPLE PUSH OSCILLATOR NONLINEAR ANALYSIS AND DESIGN

In the latest years much research effort was devoted to modeling complex self-organizing, coupled oscillator networks in which different delays and coupling strengths among elements determine complex pattern[1], which span from uncorrelated behavior to perfect synchrony [1-7] . The results can be summarized as follows. First, the delays in the coupling network, due to the distributed nature of the coupling elements, can severely affect the performance of the coupled oscillator, leading in some cases to a zero amplitude output (amplitude death). Second, the modes listed in Table 5.1 for certain combination of delay and coupling strength can be simultaneously stable, thus physically observable. As a consequence, when turning on the triple-push circuit at first, each one of the modes could possibly be settled, depending on the circuit initial conditions. Moreover, a slight perturbation applied at a specific instant in time might unexpectedly cause mode transitions $M_i \rightarrow M_j$. For these reasons, a nonlinear analysis of a Triple Push Oscillator is given here, considering the impact of the delays in the coupling network, and the variable coupling strength among oscillating elements. Specifically, three identical oscillators common gate HJ-FET oscillators are individually designed at the target frequency of 2 GHz (§5.3.1). The Triple Push Oscillator is formed by connecting them via a symmetrical coupling network, made up of three identical microstrip line sections. Furthermore, a LC high pass filter (§5.3.2) is inserted midway among each oscillator subunit and the coupling branch, to modify the attenuation level at the fundamental frequency of each oscillator. Taking advantage of Harmonic Balance simulations and numerical continuation techniques, the effect of variable coupling line length (which affects the delays among oscillating units) and variable attenuation (related to mutual coupling strength) is investigated (§5.3.3), by taking them as control parameters. A parametric plot of the output voltage magnitude at the fundamental for one of the core oscillators ($|V_n^{(1)}|$), is traced as the as the coupling line length and attenuation are varied. *In* (§5.3.4) the triple push oscillator is finally designed, by selecting attenuation and coupling length values which allow avoiding the undesired modes.

[1] In the work [4] dealing with rings of coupled oscillators presenting dihedral symmetry, the impact of delays in the coupling networks and the consequent issue of modes multi-stability were neglected, due to the complication of converting the analytical framework from an ODE (ordinary differential equations) setting to a PDE (partial differential equations, accounting for distributed elements) or DDE (differential-delay equations) setting [5][6].

5.2 DESIGN OF THE OSCILLATOR CORE

Individual oscillator elements are designed by choosing an active device providing enough gain to sustain oscillations, a feedback network that could resonate at the prescribed oscillation frequency (2 GHz), and adequate input—output matching networks for delivering maximum output power to the load [8-10]. To this term the NEC NE3509M04 transistor connected *in a common gate configuration* has been found suitable, taking the oscillator output voltage on the HJ-FET source side, choosing the ARLON A25 N as a substrate with a thickness of 0.762 mm (30 mil) with a loss tangent $\tan\delta = 0.0025$. The feedback path is provided by the inductor L_{fg} (approx. 7 nH) connected in series with the gate, and two open stubs at the source and drain ports with different aspect ratio (width/length) are responsible selecting the oscillation frequency and for matching the input/output impedance to 50 Ω nominal impedance [10], as shown in Fig. 5.1. A preliminary design[2] involved only the most basic elements, the vendor's nonlinear model of the active device itself, a reduced number of transmission line elements and simplified bias networks to check whether the oscillation conditions could be satisfied in the neighborhood of a suitable bias point by means of a linear analysis at a particular node of the circuit. To that aim, a variable frequency (in the range 0.1-5.0 GHz) small signal voltage probe (with an amplitude of 10 mV) was introduced in the circuit schematic (see chapter IV). Various simulations have been thus performed to examine the small signal admittance at various nodes of the oscillator, with different bias conditions at the source/drain port. Small signal condition for having an oscillatory solution was greatly fulfilled at the source port, which therefore turned out to be the selected node to get the oscillator output signal, that is, the signal that should be injected into the coupling network. The linear frequency search indicated an estimated oscillation frequency of 2.14 GHz, (Fig. 5.2) which is sufficiently close to the prescribed one. Subsequently, the large signal analysis was performed by taking advantage of this local solution, and employing a two tier harmonic balance simulation [9], in which the large signal frequency and amplitude of the oscillatory solution are regarded as additional unknowns and iteratively adjusted by means of an optimization routine. At this stage, the same harmonic probe was initialized with the estimated oscillation frequency previously sought and the amplitude was given an arbitrary value, on the same order of the bias voltage (0.1 V — 1 V) which reflected a reasonable output power level. A Harmonic Balance simulation was then run and the actual values of oscillation frequency and power were optimized to meet the large signal non-perturbation conditions $\mathrm{Re}(Y_o)=\mathrm{Im}(Y_o)=0$ [11].

[2] In this section our goal is not to describe in detail the design of a common gate transistor oscillator, which could also be tackled analytically, see [10]. The procedures and techniques for finding the oscillation frequency and power of a single frequency oscillator by means of a linear analysis search and subsequent nonlinear analysis optimization are just summarized without any claim of exhaustiveness, since they have been treated thoroughly in chapter IV.

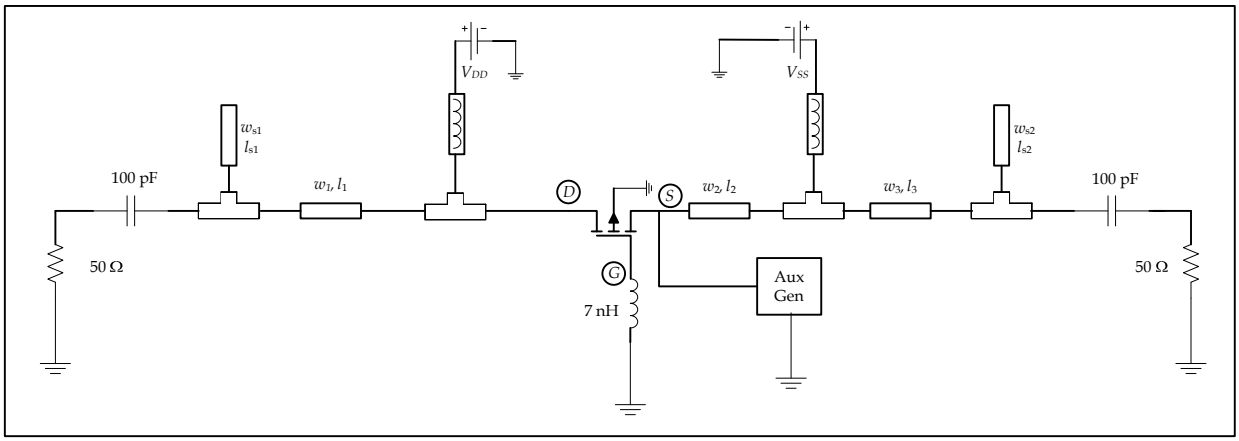

FIGURE 5-1. .Initial schematic of the individual oscillator at 2 GHz.

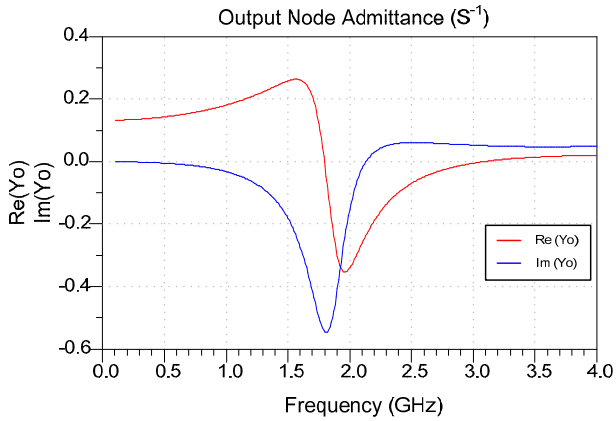

FIGURE 5-2. Small signal admittance computed at the oscillator output node, in the range [0.1 GHz, 4 GHz].

Finally, oscillator's layout was considered and the previous steps consisting in preliminary linear analysis and subsequent nonlinear probe analysis, were repeated a certain number of times to accommodate for variations due to the insertion of additional layout elements like T-junctions, cross-junctions, microstrip discontinuities, vendor's model for chip inductors and capacitors, transistor pads and via holes, whose S parameters were derived from electromagnetic simulations. Moreover, chip capacitors model from MURATA and two port S parameters for COILCRAFT inductors were introduced. A simplified schematic of the common gate transistor oscillator is shown in Fig. 5.3. The free running oscillator could be biased with two independent power supplies, to increase its flexibility and compensate for frequency detuning when inserted in the Triple Push Oscillator. The drain voltage V_{DD} is at 2V, and the source is connected to the ground (or to a negative potential). The output power spectrum proves that an oscillation was attained at a fundamental frequency of 2.34 GHz with an output power of 9.14 dBm (Fig. 5.4).

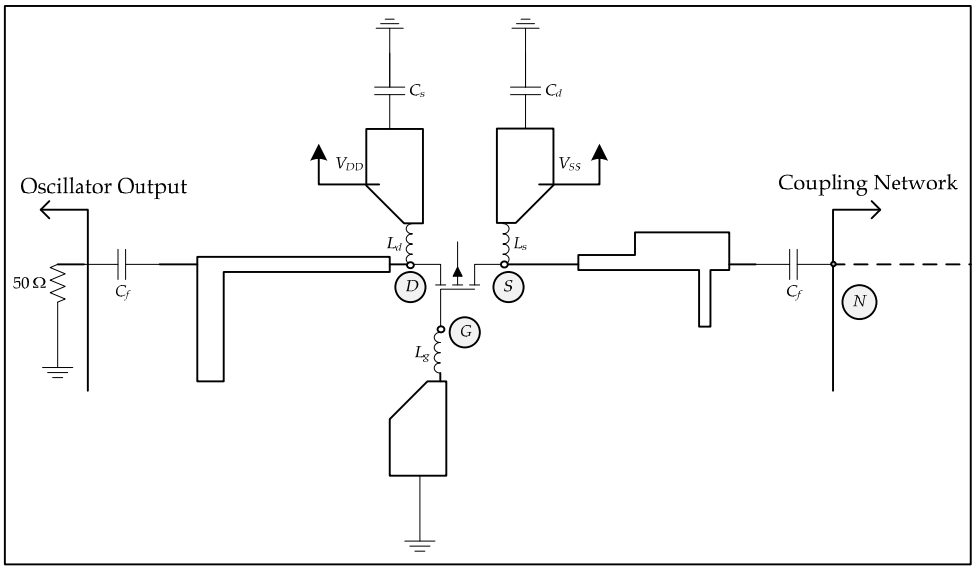

FIGURE 5-3. Final Oscillator Layout.

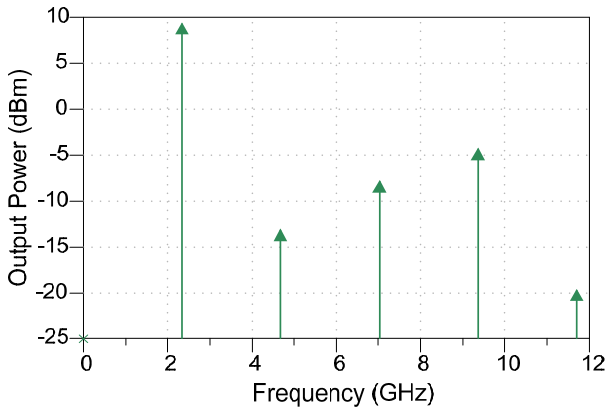

FIGURE 5-4. A single oscillator ooutput power spectrum. The fundamental frequency is 2.34 GHz.

5.3 Design of the LC High-Pass Filter Section

A high pass filter section is needed at the oscillator output in order to provide a prescribed amount of attenuation so to vary the coupling strength among the individual core oscillators[3]. It is simply a constant-*k* high-pass half section made up of a lumped inductor and capacitor (Fig. 5.4). Design formulas prescribe the values of inductance and capacitance needed to synthesize a filter with a specific impedance Z_0 and cut-off frequency f_c given by:

[3] A resistive T or Π pad attenuator could also be used but it would drop the power across all frequencies, consequently diminishing the third harmonic boosting. A high pass filter would instead provide a specific amount of attenuation at the first harmonic only, leaving third harmonics power unchanged. A triple push oscillator employing resistive attenuators to vary coupling strength was studied in [7].

$$C_s = \frac{1}{4\pi Z_0 f_c}$$
$$L_p = \frac{Z_0}{4\pi f_c} \tag{5.1}$$

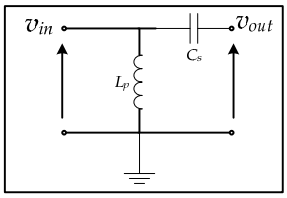

FIGURE 5-5. A simple LC high pass filter providing a specified attenuation at the fundamental oscillation frequency.

However, in (5.13) the attenuation in the stopband of the filter is left unspecified. From filter analysis via the image parameter method [10] is known that the attenuation factor is:

$$\alpha = \ln\left|\frac{V_{in}}{V_{out}}\right| = \ln\left|\frac{I_{in}}{I_{out}}\right| \Rightarrow \alpha = 2\text{arccosh}\left(\frac{f_c}{f}\right) \tag{5.2}$$

so fixing a specific frequency f_α whose output level has been lowered by α (Np) with respect to its input level, being the cutoff frequency of the filter expressed in terms of series capacitance and shunt inductance

$$f_c = \frac{1}{4\pi\sqrt{L_p C_s}} \tag{5.3}$$

and entering (5.15) in (5.14) is obtained:

$$\sqrt{(L_p C_s)} = \frac{1}{4\pi f_\alpha \cosh(\alpha/2)} \;\Rightarrow\; L_p(C_s,\alpha) = \frac{\kappa(\alpha)}{C_s}$$
$$\kappa(\alpha) = \frac{1}{16\pi^2 f_\alpha^2 \cosh^2(\alpha/2)} \tag{5.4}$$

where $\kappa(\alpha)$ is a rapidly decreasing function of the attenuation level. Following (4.4), in order to provide a prescribed attenuation level at a certain frequency f_α the inductance and capacitance of the filter have to be inversely proportional; in the plane described by (L_p, C_s) (5.16) represents a family of hyperbolas and a plot can be obtained via optimization technique. To that aim, initial values for L_p and C_s which fall in the range [0.5 nH, 10 nH] and [0.5 pF, 5.5pF] are introduced in the filter and the attenuation level is found by means of a single point S-parameter simulation at the frequency of interest f_α, which in our case agrees with the fundamental frequency of each oscillator core, evaluating the magnitude of the transmission parameter S_{21}. Subsequently the capacitance values are swept backwards (due to the inverse variation of L_p versus C_s) starting from the maximum value C_M = 5.5 pF and proceeding in decreasing order towards C_m = 0.5 pF (choosing ΔC = 0.1 pF) and at each step the inductance values are optimized to fulfill the attenuation constraint $\max(S_{21})=\min(S_{21})=-\alpha$ (dB) throughout the range 0.5 nH $\leq L_p \leq$ 10 nH (see Table V.I). This procedure is then repeated for different attenuation values to plot the family of hyperbolas $L_p(C_s, \alpha) = \kappa(\alpha)/C_s$ as shown in Fig. 5.6. These curves, giving a visual representation of the constraint $f(L_p(\alpha),C_s(\alpha))=0$, allow choosing the values of L_p and C_s providing a fixed attenuation level, at the fundamental oscillation frequency of each oscillator output.

$$
\begin{aligned}
&\text{for } k = 1,\ldots,n \\
&\quad \text{for } h = 0,\ldots,m \\
&\qquad C_s^{(h)} = C_M - h\cdot\Delta C \qquad /^*\ C_s^{(0)} = C_M = 5.5\ \text{pF};\ C_s^{(m)} = C_m = 0.5\ \text{pF}\ ^*/ \\
&\qquad \textbf{find } L_p\left(C_s^{(h)}\right) \text{ such that (at a specific frequency } f_0\text{):} \\
&\qquad\qquad \begin{cases} \max\limits_{L_m \le L_p \le L_M} S_{21}\left(f_0, L_p\left(C_s^{(h)}\right)\right) = -\alpha_k \ \text{(dB)} \\ \min\limits_{L_m \le L_p \le L_M} S_{21}\left(f_0, L_p\left(C_s^{(h)}\right)\right) = -\alpha_k \ \text{(dB)} \end{cases} \\
&\qquad\qquad /^*\ L_m = 0.5\ \text{nH};\ L_M = 10\ \text{nH}\ ^*/
\end{aligned}
\tag{5.5}
$$

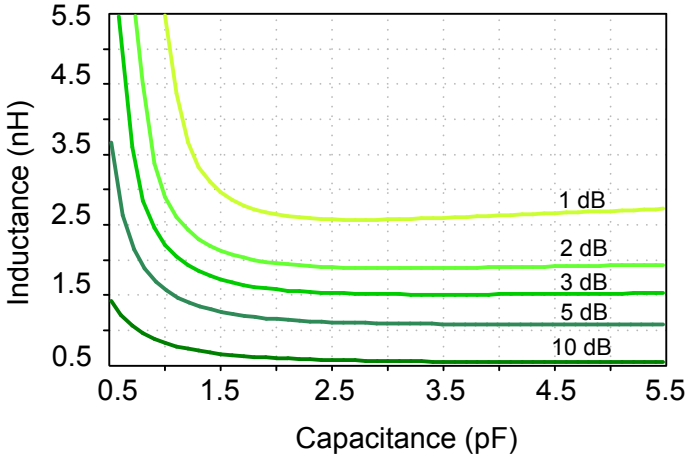

FIGURE 5-6. Constant attenuation curves used for synthesizing the LC high pass filter.

5.4 Nonlinear Mode Analysis

Starting from the core oscillators and the high pass filter sections, a triple push oscillator topology is readily synthesized by connecting together the three branches (*coupling arms)* shown in Fig. 5.7 each of them formed by a cascade of an elemental oscillator and an attenuator, by means of 50 Ω microstrip lines (line width is w_c=1.75 mm, for the chosen substrate). From circuit layout perspective, it has been found convenient to arrange the oscillators-high pass filter series connection around a star network (Fig. 5.7). In order to reduce space occupancy, microstrip coupling lines have been meandered. The oscillators' outputs are combined at the center of symmetry of the star network and the output voltage of the second oscillator (corresponding to the node N in the picture) is chosen to track the evolution of each mode (shown in Table 5.1) versus coupling lines length variation, to modify the delay/coupling phase among individual oscillators[4]. Moreover the coupling strength is

[4] In the following, it is assumed that the coupling network shrinks or expands symmetrically. In other terms, all coupling line sections are perfectly identical and a single variable (l_c) suffices to follow the solution path of the voltage V_n. The same holds true for the high pass LC filter inserted at each core oscillator output node, providing the same attenuation level.

varied by selecting adequate values for the attenuation provided by the high pass filter section (based on the proper choice of inductance and capacitance values, as exposed in section 5.3.2). For the nonlinear analysis of this circuit three different Auxiliary Generators are employed, which play the role of harmonic probes triggering the oscillating solutions for the two tier HB [9,11] simulations. Each of these harmonic probes are connected to the output node of each individual oscillator, and are initialized with a frequency value corresponding to the individual oscillators' fundamental frequency, while their amplitudes and phases are chosen accordingly to Table 5.1 for each of the oscillating modes.

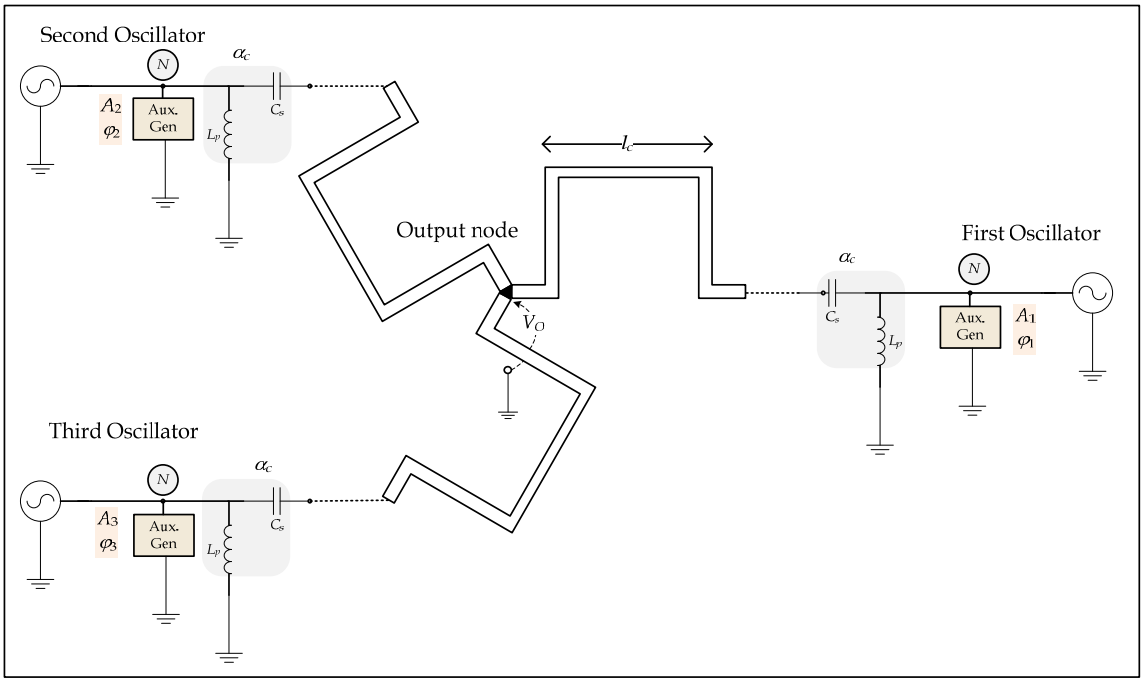

FIGURE 5-7. Triple Push Oscillator schematic for nonlinear analysis showing the nodes to which auxiliary generators are connected.

As stated before, M_1 represent the "in-phase" mode in which all core oscillators are perfectly synchronized with zero phase shift and possess the same amplitude. Mode M_2 represent the "discrete rotating wave" mode, in which all core elements are phase locked with a constant $2\pi/3$ phase progression among them and constant amplitude, which is responsible for triple harmonic generation. Given the complex amplitude phase-relationship for the mode M_3 in which one oscillator elements presents a frequency *double* to the frequency of the other ones and the fact that it hadn't appeared in first experimental validation of this topology [14], its analysis won't be addressed here. Mode M_4 shows two perfectly synchronized oscillators with the same amplitude, and the third one resonating with a different phase and amplitude; to the aim of simplifying the analysis, it will be assumed that the third oscillator is π out of phase with respect to the other two, having different amplitude. In Table 5.1 the values of frequency, amplitude and phase to be used for each auxiliary generator corresponding to each mode are summarized for ease of reference.

Oscillating Mode	1st *Aux. Gen.*	2nd *Aux. Gen.*	3rd *Aux. Gen.*
M_1, all oscillators are *in phase*	Amplitude= A_1 Frequency=f_0 Phase=0°	Amplitude= A_1 Frequency=f_0 Phase=0°	Amplitude= A_1 Frequency=f_0 Phase=0°
M_2, $2\pi/3$ *phase distribution among all the oscillators*	Amplitude= A_2 Frequency=f_0 Phase=0°	Amplitude= A_2 Frequency=f_0 Phase=120°	Amplitude= A_2 Frequency=f_0 Phase=240°
M_4, *two oscillators are in phase, one oscillator is* π *out of phase*	Amplitude= A_4 Frequency=f_0 Phase=0°	Amplitude= A_4 Frequency=f_0 Phase=0°	Amplitude= B_4 Frequency=f_0 Phase=180°

TABLE 5--1. Analysis of the various oscillating modes dictated by symmetry in a triple push oscillator

The objective of this section is to describe how to analyze the parametric variation of *the voltage at node N (depending both on the attenuation and on the coupling phase), for each of the modes M1, M2, M4, in order to quench the undesired ones.* This problem can be tackled in two successive steps, which will be referred to as the *consistency check*, and the *solution path tracking.*

5.4.1 CONSISTENCY CHECK

In the first step, *one must make sure that a solution for the triple push oscillator circuit is found when coupling line lengths and attenuation values are kept constant.* This solution will be subsequently used as a starting point for tracing the parametric solution curve. To fix our ideas, one can initially consider a fixed length of the coupling line l_c=40 mm and a zero attenuation (α=0 dB), which would ease the convergence speed of the HB simulator due to the reduced complexity of the network since no filter section needs to be introduced. At this point, three different harmonic balance simulations must be run, in order to find the steady state solution for the three different modes. For each of the modes M_i, three auxiliary generators, placed in the vicinity of the individual oscillator output nodes, needs to be initialized with the values of amplitude, frequency, and phase given in Table 5.1. Then a non-perturbation condition has to be satisfied at each port where the auxiliary generators are connected[5] [9] [11] [14]:

[5] If the formulation for the harmonic balance equations is the piecewise harmonic balance, then **H(.)=0** represent an M-dimensional current balance between the linear and nonlinear sub-networks (for each $(2N+1)$ harmonic components) and the complex vector **X** represents the $(2N+1)$ harmonic components of the M voltages at the interconnecting ports. Therefore we have, **E**=$\{E_{r,s}\}$, **X**=$\{X_{r,s}\}$, r = 1,…,$(2N+1)$, s=1,…m. See [9]

$$\begin{cases} \mathrm{Re}\left(Y_j^i\left(A_j,\phi_j,f_o\right)\right)=0 & \text{Oscillation Condition for the } i\text{-th mode at } j\text{-th probing port (outer tier)} \\ \mathrm{Im}\left(Y_j^i\left(A_j,\phi_j,f_o\right)\right)=0 & i\in\{M_1,M_2,M_4\},\ j=1,2,3 \\ \mathbf{E}(\mathbf{X},A_j,\phi_j,l_c,\alpha,f_o)=\mathbf{0} & \text{Harmonic Balance Equations (inner tier)} \\ \begin{cases}\mathbf{L}_i\left(A_1,A_2,A_3\right)=0 \\ \mathbf{K}_i\left(\phi_1,\phi_2,\phi_3\right)=0\end{cases} & \begin{matrix}\text{Amplitude Constraints for the } i\text{-th mode} \\ \text{Phase Constraints for the } i\text{-th mode}\end{matrix} \\ Y_j^i=\dfrac{I_{j,1}^i}{V_{j,1}^i} & \text{Admittance for the } i\text{-th mode at the } j\text{-th probing port} \end{cases} \tag{5.6}$$

The equations (4.6) consist of a set of six *nonlinear equations* $\mathrm{Re}(Y^i_j)=0$, $\mathrm{Im}(Y^i_j)=0$, the *linear constraint* for the amplitudes $\mathbf{L}_i(A_1, A_2, A_3)=0$ and the phases $\mathbf{K}_i(\phi_1, \phi_2, \phi_3)=0$ which are related to the symmetry of each mode, and the harmonic balance system of equations. The system (5.18) can be conveniently solved with the classical two tier Harmonic Balance algorithm for autonomous circuits, in which the outer tier iteratively adjust the values for amplitudes and oscillation frequency via a gradient-type optimizer, while the inner tier solves the Harmonic Balance equations for the other circuit variables [9]; if convergence is achieved, the spectral information of $|V_n{}^1|$ is known, up to the third order harmonic, which is sufficient for our purposes. It should be noted that the actual number of optimization variables get drastically reduced thanks to the linear constraints for the amplitudes, and that the phases do not enter the optimization process but rather must be kept constant, so as to fulfill the phase locking condition for each specific mode.

If convergence isn't achieved, then the values of l_c, α, need to be modified in order to find a solution to the Harmonic Balance Equations. Then, it could be performed *a tuning of the Triple Push Oscillator*, by entering the same l_c, α, *into the system* (5.6) and solve it for the additional optimization variables, for a fixed oscillation frequency f_o:

$$\begin{cases} \mathrm{Re}\left(Y_j^i\left(A_j,\phi_j,l_c,\alpha\right)\right)=0 & i\in\{M_1,M_2,M_4\} \\ \mathrm{Im}\left(Y_j^i\left(A_j,\phi_j,l_c,\alpha\right)\right)=0 & j=1,2,3 \end{cases} \quad \textit{subject to} \quad \begin{cases}\mathbf{L}_i\left(A_1,A_2,A_3\right)=0 \\ \mathbf{K}_i\left(\phi_1,\phi_2,\phi_3\right)=0\end{cases} \tag{5.7}$$

A concrete example will now be given, for the consistency check of M_2. Three auxiliary generators satisfying the conditions indicated for M_2 in Table 5.2, are connected to the outputs of the core oscillators and a value of l_c=40 mm and α = 0 dB is chosen initially. Their amplitudes are constrained to be equal, and their mutual phase shift should be progressively increasing by $2\pi/3$ so:

$$\mathbf{L}_{M_2}\left(A_1,A_2,A_3\right)=0 \Rightarrow \begin{cases}A_1=A \\ A_2=A \\ A_3=A\end{cases};\ \mathbf{K}_{M_2}\left(\phi_1,\phi_2,\phi_3\right)=0 \Rightarrow \begin{cases}\phi_1=0^\circ \\ \phi_2=120^\circ \\ \phi_3=240^\circ\end{cases} \tag{5.8}$$

and the oscillation condition to be fulfilled at three individual oscillators output ports becomes:

$$\begin{aligned} \mathrm{Re}\left(Y_j^{M_2}\left(A, f_0\right)\right) &= 0 \\ \mathrm{Im}\left(Y_j^{M_2}\left(A, f_0\right)\right) &= 0 \end{aligned} \tag{5.9}$$

which has to be solved jointly with the Harmonic Balance simulation. If convergence is achieved, it provides the (common) amplitude of the three output voltages and oscillation frequency[6]; otherwise the parameters l_c *and* α should be tuned, as described earlier. In Fig. 5.8 the solution for mode M_2 is shown. The fundamental frequency at 2.6 GHz (which gets shifted due to the presence of the coupling network) is virtually suppressed, as well as the second harmonic, while the third harmonic only (at 7.8 GHz) has a sensible output power.

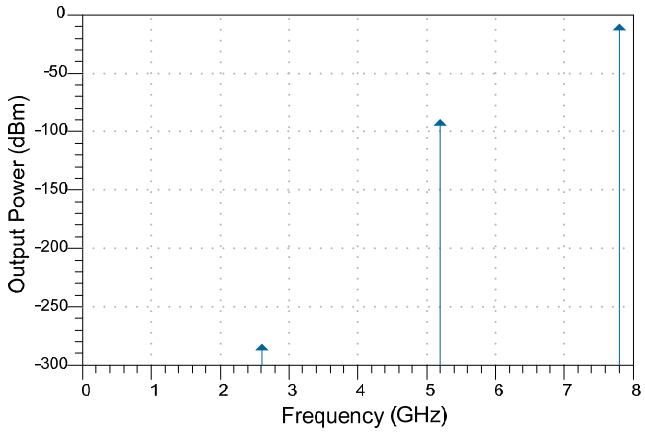

FIGURE 5-8. Nonlinear oscillating solution of the triple push oscillator obtained for constant values of coupling line length and attenuation. Lower order harmonics have negligible power, compared to the third harmonic at 7.8 GHz.

5.4.2 SOLUTION PATH TRACKING

Once the circuit has been analyzed for fixed values of line length and attenuation, the study of its parametric variation follows, examining the dependence of an oscillator output voltage's first harmonic component on the coupling line length and attenuation provided by the high pass filter section, hereinafter referred to *solution path tracking* [12][13]. To that aim, starting from the solution provided by the consistency check, both the length of the line and the attenuation values are iteratively swept across an admissible range [l_{min}, l_{max}] and [α_{min} , α_{max}][7] choosing an adequate step size Δl_c, $\Delta\alpha$[8]*;* at each step the (5.6) are then solved, jointly with the harmonic balance system of equations.

Though conceptually simple, this method involves a number of issues. First, the attenuation is a function of the values of inductances and capacitances of the high pass filter section, therefore it cannot be swept as an independent variable (as in the case of l_c). This could be

[6] It should be recalled that this solution depends also on the bias voltage which have to be considered fixed at V_{DD}=2V, Vss=0V.

[7] The admissible range is [30 mm, 120 mm] for the coupling line length and [0 dB, 10 dB] for the attenuation.

[8] The step size has to be carefully selected in order to facilitate the solution path tracking process at each step. In fact too many iteration points (small step size, relative to the admissible range) increase the computation times, too few (large step size, relative to the admissible range) might cause convergence failure. Very often, a solution path is tracked choosing adaptively different step size in different parameter regions, depending on the "stiffness" of the problem [12, 13]

circumvented, by placing ideal built-in attenuator components, which are available in most commercial EDA software, specifying the amount of attenuation in dB directly which enables to track the solution path analogously to the case of the varying line length. This approach makes the problem easier to solve, although the linear phase response of the triple push oscillator is altered due to the substitution of reactive elements with ideal passive components [14].

Second, the way the parameters are swept is crucial. In fact, a nested sweep (double sweep):

$$
\begin{aligned}
&i \in \{M_1, M_2, M_4\} \\
&\text{for } l_{\min} \le l_c \le l_{\max} \ \{ \\
&\quad \text{for } \alpha_{\min} \le \alpha \le \alpha_{\max} \ \{ \\
&\quad \begin{cases} \mathrm{Re}\left(Y_j^i\left(A_j, \phi_j, f_o\right)\right) = 0 \\ \mathrm{Im}\left(Y_j^i\left(A_j, \phi_j, f_o\right)\right) = 0 \end{cases} \text{ subject to: } \begin{cases} \mathbf{L}_i\left(A_1, A_2, A_3\right) = 0 \\ \mathbf{K}_i\left(\phi_1, \phi_2, \phi_3\right) = 0 \end{cases} \quad j = 1,2,3. \\
&\quad \mathbf{E}(\mathbf{X}, A_j, \phi_j, l_c, \alpha, f_o) = \mathbf{0} \\
&\qquad\qquad \alpha \to \alpha + \Delta\alpha \\
&\qquad\qquad \} \\
&\qquad l_c \to l_c + \Delta l_c \\
&\qquad\quad \}
\end{aligned}
\tag{5.10}
$$

could lead to cumbersome computation times. Instead, it is possible to take advantage of the independence of the two parameters, the coupling strength (α) and the coupling phase (l_c), to efficiently decouple the solution path length into two separate problem, one related to the parametric analysis of the effect of the attenuation (maintaining l_c *constant*), and another related to the effect of the variation of the coupling line length (keeping α fixed) :

$$
\begin{aligned}
&i \in \{M_1, M_2, M_4\} \ (l_c \text{ is kept fixed}) \\
&\text{for } \alpha_{\min} \le \alpha \le \alpha_{\max} \ \{ \\
&\quad \begin{cases} \mathrm{Re}\left(Y_j^i\left(A_j, \phi_j, f_o\right)\right) = 0 \\ \mathrm{Im}\left(Y_j^i\left(A_j, \phi_j, f_o\right)\right) = 0 \end{cases} \text{ subject to: } \begin{cases} \mathbf{L}_i\left(A_1, A_2, A_3\right) = 0 \\ \mathbf{K}_i\left(\phi_1, \phi_2, \phi_3\right) = 0 \end{cases} \quad j = 1,2,3. \\
&\quad \mathbf{E}(\mathbf{X}, A_j, \phi_j, \alpha, f_o) = \mathbf{0} \\
&\qquad\qquad \alpha \to \alpha + \Delta\alpha \\
&\qquad\qquad \}
\end{aligned}
\tag{5.11}
$$

$$
\begin{aligned}
&i \in \{M_1, M_2, M_4\} \ (\alpha \text{ is kept fixed}) \\
&\text{for } l_{\min} \le l_c \le l_{\max} \ \{ \\
&\quad \begin{cases} \mathrm{Re}\left(Y_j^i\left(A_j, \phi_j, f_o\right)\right) = 0 \\ \mathrm{Im}\left(Y_j^i\left(A_j, \phi_j, f_o\right)\right) = 0 \end{cases} \text{ subject to: } \begin{cases} \mathbf{L}_i\left(A_1, A_2, A_3\right) = 0 \\ \mathbf{K}_i\left(\phi_1, \phi_2, \phi_3\right) = 0 \end{cases} \quad j = 1, 2, 3. \\
&\quad \mathbf{E}(\mathbf{X}, A_j, \phi_j, l_c, f_o) = \mathbf{0} \\
&\quad\quad l_c \to l_c + \Delta l_c \\
&\quad \}
\end{aligned}
\tag{5.12}
$$

Third, despite the simplifying assumptions being made, the parametric variation of a nonlinear circuit variable often involves the use of numerical continuation techniques, in order to allow the graphical representation of multi-valued solution curves [9,13]. In fact, although a parameter is changed smoothly in a certain neighborhood of the admissible range, abrupt variation could arise in the solution due to a sudden variation of its stability properties [12].This phenomenon is referred to as the occurrence of a *turning point* [12]. In the vicinity of a turning point, the solution curve tends to fold over itself, thus making possible the existence of solution curves possessing more than one value in a certain region of the parameter space. When encountering a turning point during the solution path tracking, the simulator halts and report an error due to the singularity of the Jacobian matrix of the Harmonic Balance system of equations, which instead needs to be invertible to solve nonlinearly the system (5.6) with the Newton-Raphson algorithm[9,11] To deal with the occurrence of turning point, a procedure called *parameter switching* (or *branch switching*) needs to be employed. Loosely speaking, this procedure *detects* the occurrence of turning points, *swaps* the role of the parameter and observation variable by passing to the inverse function [12,13], and provides an adequate update of the solution path tracking[9].

All the earlier remarks have been taken into account for tracing the solution curves for the modes M_1, M_2, M_4, versus the coupling line length and attenuation. The circuit was initially analyzed performing separate (according to the decoupled scheme (5.24, 5.25)) two tier Harmonic Balance parameter swept simulation for α, l_c for each oscillating mode. The attenuation was held constant at first, and only the coupling line length was varied. Subsequently, α was changed in discrete steps to see its effect on the parametric analysis obtained for the coupling line length, for each mode.

One example of this approach is shown in Fig. 5.9 where the voltage magnitude of the second oscillator node "*N*" ($|V_n^{(1)}|$) at the fundamental frequency for M_1 is analyzed versus l_c for two different attenuation values[10] α_1*=1.6 dB,* α_2*=4.6 dB*; an Auxiliary Generator was directly connected at that node setting $|V_n^{(1)}|=A$, $\varphi_n=\varphi$. This curve presented turning points, therefore a parameter switching strategy was needed while performing the sweeps. Every time a turning point occurred the *role of the parameter* l_c *and of the observation variable* $A=|V_n^{(1)}|$, were exchanged. For example for α_1*=1.6 dB,* 32 mm $\le l_c <$ 63mm, and considering the first closed curve, the magnitude of the output voltage of the oscillator it is entirely tracked with one parameter sweep

[9] The procedure for tracing multi-valued solution curves is illustrated on Chapter III, Section 4.

[10] Obtained synthesizing two different LC high pass filters, according to § 5.3.2 For α_1*=1.6 dB* L_1 *=2.3 nH,* C_1*=3.3 pF;* for α_2*=4.6 dB* L_1 *=1.2 nH,* C_1*=3.3 pF;*

using Δl_c= 3 mm. For l_c =63mm, $|V_n^{(1)}|$= 0.1 V convergence failure arises, due to the presence of a turning point. Thus, the amplitude of the auxiliary generator connected at node N and representing $|V_n^{(1)}|$, is taken as the new parameter for tracing the solution curve, observing the evolution of the coupling line length. By doing so, a second branch of the curve could be followed (choosing an amplitude step of ΔA=50 mV) until a second turning point was reached at $|V_n^{(1)}|$=A=1.12 V l_c=50 mm and the procedure was repeated[11].

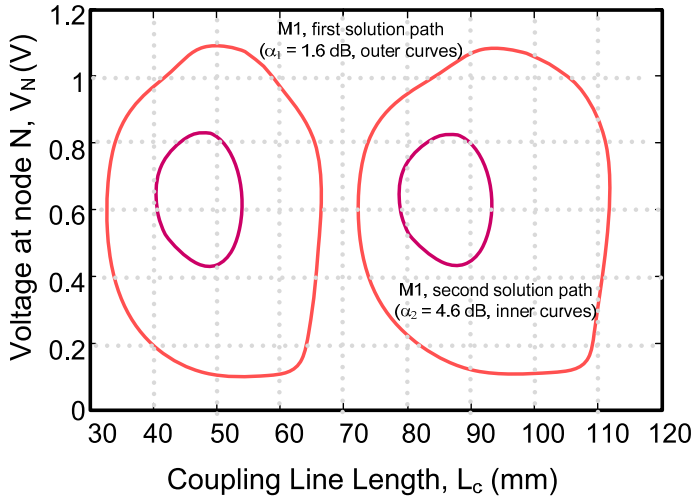

FIGURE 5-9. Multivalued solution curve corresponding to mode M_1 onset, as a function of the coupling line length, for two distinct values of attenuation. These oscillating solutions give rise to closed cycle in the parameter space, called *mode islands* [14]

I. Consistency Check

for $j = 1,2,3$

$l_c \leftarrow l_{c0}$; /* *line length* initialization

$A_j \leftarrow A$; ($\frac{1}{10} V_{DD} \le A \le V_{DD}$) /*Auxiliary Generators initialization: amplitudes

$\phi_j \leftarrow 0°$ /*Auxiliary Generators initialization: phases (constant)

$f_{oj} \leftarrow \hat{f}_o$; ($\frac{1}{10}\hat{f}_o \le f_{oj} \le 10 f_{oj}$) /*Auxiliary Generators initialization: frequencies

$$\hat{\mathbf{E}}(\mathbf{X}, A, f_o, l_c) \leftarrow \begin{cases} \mathrm{Re}\left(Y_j\left(A_j, \phi_j, f_o\right)\right) \\ \mathrm{Im}\left(Y_j\left(A_j, \phi_j, f_o\right)\right) \\ \mathbf{E}(\mathbf{X}, A_j, \phi_j, f_o, l_c) \end{cases} \quad /*Double-tier \text{ HB Equations}$$

while $\left(\left\|\hat{\mathbf{E}}(\mathbf{X}, A, f_o, l_{c0})\right\| > 0\right)$ {

$(A, f_o, l_{c0}) \leftarrow (\tilde{A}, \tilde{f}_o, \tilde{l}_{c0})$ /*Variables update – tuning

find (A^{opt}, f_o^{opt}) such that $\mathbf{E}(\mathbf{X}, A, f_o, l_{c0}) = \mathbf{0}$

}

II. Solution Path Tracking

for $l_{\min} \le l_c \le l_{\max}$ { /* parametric analysis w.r.t l_c

find (A, f_o) such that $\hat{\mathbf{E}}(\mathbf{X}, A, f_o, l_c) = \mathbf{0}$

if ($\left\|\hat{\mathbf{E}}(\mathbf{X}, A, f_o, l_T)\right\| \to \infty$) /* convergence failure condition

{/* paramter switching

for $A_{\min} \le A \le A_{\max}$ {/* parametric analysis w.r.t A

find (l_c, f_o) such that $\hat{\mathbf{E}}(\mathbf{X}, A, f_o, l_c) = \mathbf{0}$

$A \leftarrow A + \Delta A$

if ($\left\|\hat{\mathbf{E}}(\mathbf{X}, A_T, f_o, l_c)\right\| \to \infty$)

goto *II*}

$l_c \leftarrow l_c + \Delta l_c$

}

5.5 NONLINEAR DESIGN.

The final solution curve for M_1 consisted of two disjoint connected components called mode island [14] which are periodically repeating with respect to the coupling line length. The separation among the two curves implies the nonexistence of M_1 for certain values of l_c. By employing an Envelope Transient simulation with adequate initial values [15], it might be shown

[11] Throughout the solution path tracking, a key factor was to properly select the signs (*backward or forward sweep*) and the size of step-lengths (Δl_c, ΔA); *as a rule of thumb the maximum step-length size affects accuracy, while minimum step-length size determines the convergence speed* of the continuation process.

[14] that the upper parts of the curve are stable while the lower ones are unstable. Furthermore, setting the attenuation to a higher level, the closed curves shrink and consequently the range of values of l_c for which M1 doesn't exist gets wider (Fig. 5.9). Thus selecting a minimum attenuation level of 4.6 dB, provided more robustness for the design, ensuring that the mode islands occupancy was minimized and therefore facilitating the avoidance of this undesired mode. The minimum line length for avoiding M_1 was taken from the graph illustrated in Fig. 5.9 , and it was l_c=40 mm. Subsequently, following an analogous procedure as the one detailed in the previous section (§5.3.3), the parametric solution curves with respect to the attenuation were studied, for both M_2 and M_4, for the purpose of finding attenuation value that would preserve the desired mode M_2 and quench M_4. The results are shown in Fig. 5.10 [14]. It can be seen that for an attenuation of 4.6 dB both M_2 and M_4 still exist. While tracking the parametric solution for M_2, only one turning point was found at α=8.6 dB, $|V_n^{(1)}|=A$=0.6V (approx.). Instead, the continuation technique applied to M_4 showed the presence of two connected components, each of them possessing two distinct turning point. (α=8.25 dB, $|V_n^{(1)}|=A$=0.65 V and α=8.25 dB, $|V_n^{(1)}|=A$=0.35V approx.) Again, with a suitable envelope transient simulation [15] it was shown that only upper sections of the curves were stable. For attenuation values 8.3 dB < α < 8.6 dB, only M_2 (the intended mode) is present; therefore the minimum attenuation allowing effective M_4 avoidance was selected (α = 8.3 dB) and the component values for the high pass filter were selected accordingly (L_p=0.7 nH, Cs=3.3 pF).

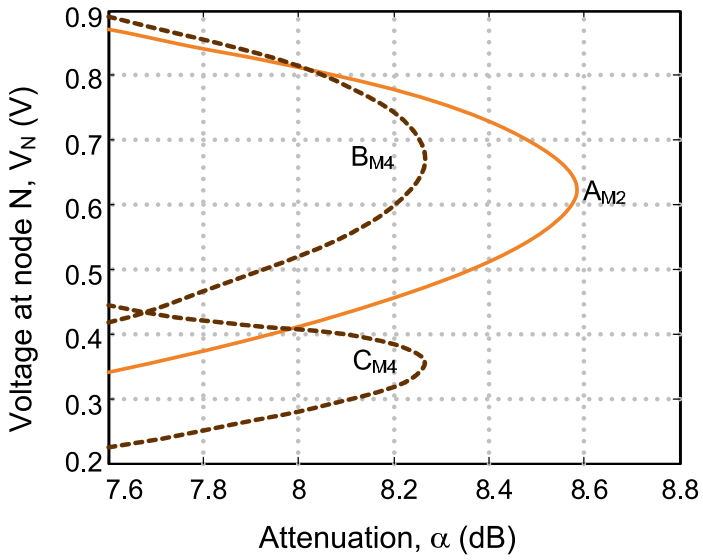

FIGURE 5-10. Parametric solution curves for the three modes (M_1, M_2, M_4) as a function of the attenuation provided by the high pass filter [14].

5.6 MEASUREMENT RESULTS

Taking advantage of the on-site facilities the Triple Push Oscillator was implemented and measured. Initially the circuit topology was laid out on Arlon 25 N substrate with H=0.76 mm, ε=3.38, with an LPKF Protomat C100-HF board plotter. After the excess copper removal, via hole connections to the bottom ground plane were drilled and metalized. Finally the circuit components were soldered and the circuit was tested. Specifically three HJ-FET from NEC were used, (NE3509M04), as active devices; TOKO chip inductors (size 1608,LL-FSH

series, various component values) MURATA chip capacitor (size 1608, GRM-18 series, various component values) were used for biasing the individual oscillators (dual voltage bias, at the source and at the drain), and for the three-high pass network inserted at each oscillator's output node (Fig. 5.11). The Triple Oscillator output node is taken at the center of the star network, by means of a SMA connector soldered at the bottom plane. Access to individual oscillators signals is provided by additional connectors mounted on the drain-side of each active device.

The measurements were carried out using both a spectrum analyzer, connected to the central output port of the triple-push circuit to evaluate the output power spectrum, and a multi-channel digital oscilloscope, to analyze the phase relationships between the first harmonic components of each oscillator so to identify each mode. Both the spectrum analyzer (E4445A, frequency band: 3Hz—13.2 GHz) and the four channel 10 GHz digital oscilloscope (DSO81004 Infiniium, maximum sample frequency: 40GSa/s) are from Agilent.

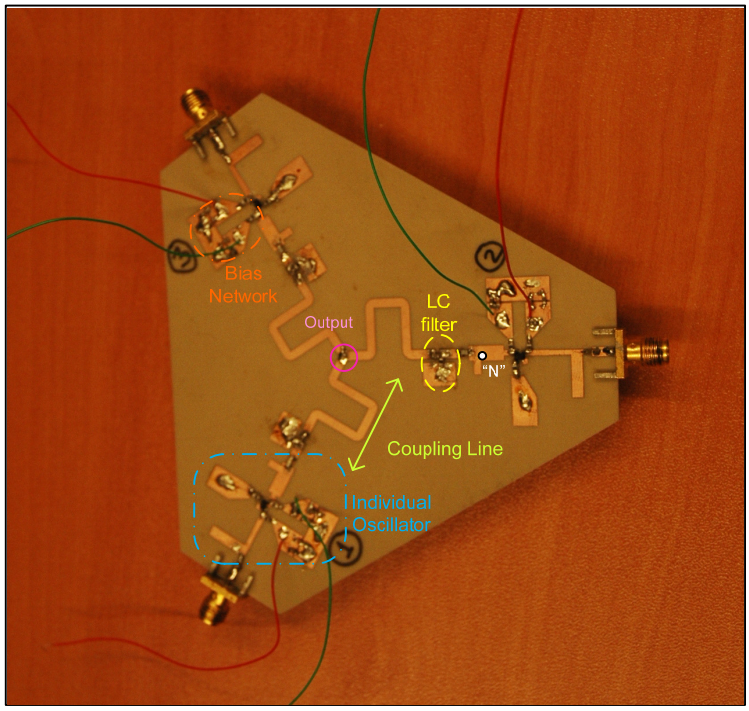

FIGURE 5-11. Triple Push Oscillator prototype, implemented using microstrip lines on a dielectric substrate and discrete components.

The circuit with l_c=40 mm, α=8.3dB, was measured. As expected, only the mode M2 was detected, providing a substantial increase in triple order harmonic output power, with a rejection ratio of 19.3 dB and 25.1 dB in comparison with the fundamental frequency (below 2 GHz) and the second order harmonic, respectively. However, changing the values of the LC filter network in order to provide less attenuation, the mode M4 still didn't appear in the measurement, possibly due to the fact that only unstable solutions were triggered (those corresponding to the lower sections of the curve shown in Fig. 5.12 [14]. For values of LC corresponding to α=4.6dB both the mode M2 and M4 are seen in the measurements, by

slightly changing the bias voltages. Finally, with an attenuation level of 1.6 dB all the modes (M1, M2, M4) coexist. It can be noticed, that the output oscillation frequency is the same for the modes M2 and M4, while it is higher for M1.

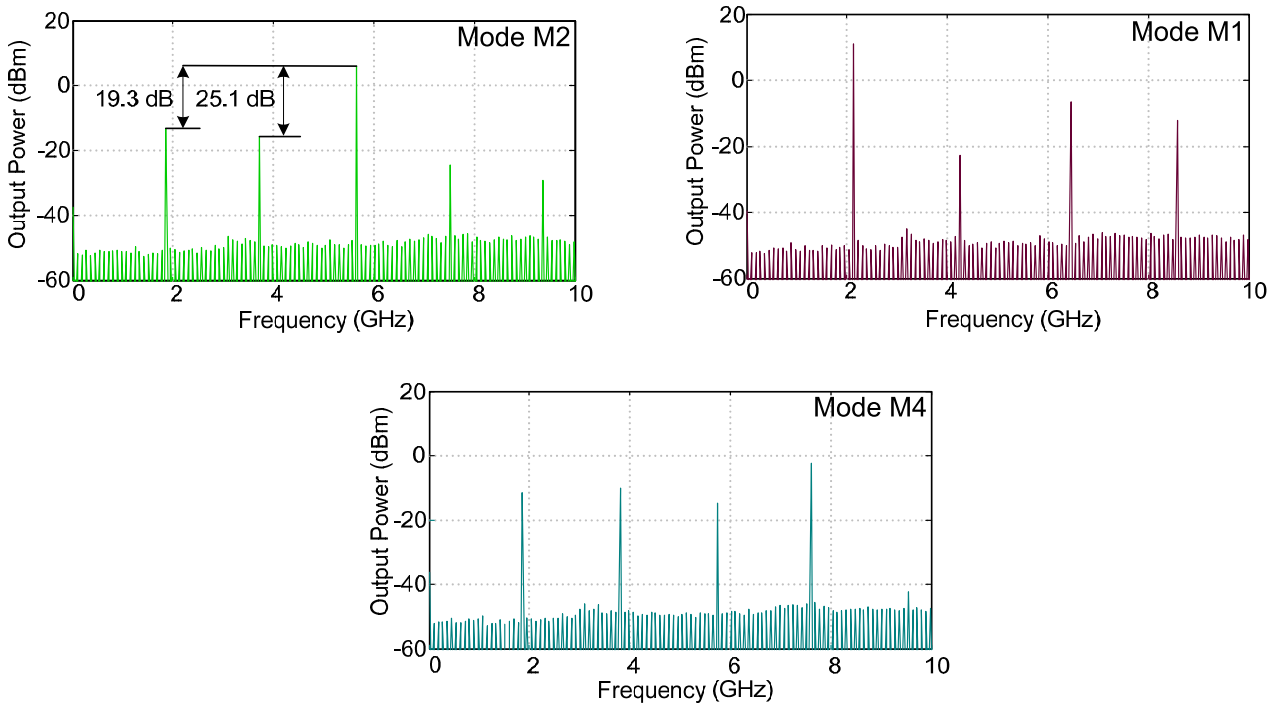

FIGURE 5-12. Measured Spectra corresponding to modes M1, M2, M4 [14].

5.7 CONCLUSIONS

In this chapter the analysis and design of a 6 GHz Triple Push Oscillator has been carried out by means of nonlinear techniques. By taking advantage of Harmonic Balance simulations and numerical techniques, various phase-locked patterns supported by this coupled oscillator topology have been analyzed, examining their dependence upon two circuit parameters, namely the coupling line length and attenuation provided at the output node of each core oscillator. Solution curves, expressing graphically the output voltage magnitude variation (at the fundamental frequency) versus the aforementioned parameters, have been traced. Regions of the parameters space for which only the mode enabling 3rd harmonic generation was excited have been identified, and the coupling network parameter have been selected accordingly. A prototype has been built, confirming the theoretical predictions.

5.8 REFERENCES

[1] S. Kim, S. Hee Park, and C.S. Ryu, "Multistability in coupled oscillator systems with time delay", *Physical Review Letters*, vol.79, no.15, pp. 2911–2914, Oct. 1997.

[2] D.V. Ramana Reddy, A. Sen, and G.L. Johnston, "Experimental Evidence of Time-delay-induced death in coupled limit-cycle oscillators," *Physical Review Letters*, vol.85, no.16, pp.3381-3384, Oct. 2000.

[3] R. Dodla, A. Sen, and G.L. Johnston, "Phase-locked patterns and amplitude death in a ring of delay-coupled limit cycle oscillators", *Physical Review E,* vol.69, 056217 (12 pages) May 2004

[4] M. Golubitsky, and I. Stewart, "Hopf bifurcation with dihedral group symmetry: coupled nonlinear oscillators," *AMS Contemporary Mathematics Multiparameter Bifurcation Theory*, vol. 56, pp. 131-173, 1986.

[5] S. H. Strogatz, "Nonlinear dynamics: Death by delay", *Nature,* no. 394, pp.316-317, 23 July 1998.

[6] D.V. Ramana Reddy, A. Sen, and G.L. Johnston, "Time Delay Induced Death in Coupled Limit Cycle Oscillators" ; *Phys. Rev. Lett.,* vol 80, pp. 5109–5112, June 1998.

[7] A. Collado, and A. Georgiadis, "Nonlinear Mode Analysis and Optimization of a Triple-Push Oscillator," *IEEE Microwave and Wireless Components Letters*,vol.18, no.8, pp.545-547, Aug. 2008.

[8] F. Giannini and G. Leuzzi. *Nonlinear Microwave Circuit Design*. Wiley, June 28, 2004.

[9] A. Suarez, and R. Quéré. *Stability Analysis of Nonlinear Microwave Circuits*. Artech House publishers, Jan. 2003.

[10] U.L. Rohde, A:K. Poddar, and G. Böck. *The Design of Modern Microwave Oscillator for Wireless Applications: Theory and Optimization*. John Wiley and Sons, June 2005

[11] C.-R.Chang, M.B. Steer, S. Martin, and E. Jr. Reese. "Computer-aided analysis of free-running microwave oscillators", *IEEE Transactions on Microwave Theory and Techniques*, vol. 39, no. 10, pp.1735-1745, Oct. 1991.

[12] D. Hente, and R.H. Jansen, "Frequency domain continuation method for the analysis and stability investigation of nonlinear microwave circuits," *IEE Proceedings H (Microwaves, Antennas and Propagation)*, vol.133, no.5, pp.351-362, Oct. 1986.

[13] E.L. Allgower and K. Georg, "Continuation and path following", *Acta Numerica*, vol. 2 , pp 1-64, 1993.

[14] S. Via, A. Collado, A. Georgiadis, and A. Acampora, "Mode control in triple-push oscillator architectures," *Proceedings of the 2008 Workshop on Integrated Nonlinear Microwave and Millimetre-Wave Circuits (INMMIC 2008)*, pp.61-64, Nov. 2008.

[15] E. Ngoya, and R. Larchevèque, "Envelope Transient Analysis: A New Method for the Transient And Steady State Analysis of Microwave Communication Circuits and Systems", *IEEE MTT-S Digest*, pp. 1365-1368, 1996

CHAPTER VI. NONLINEAR ANALYSIS AND DESIGN OF DISTRIBUTED VOLTAGE CONTROLLED OSCILLATORS

6.1 REVERSE MODE DVCO LINEAR DESIGN.

The *reverse mode* DVCO circuit previously introduced presents formidable challenges both from the analysis and from the design/implementation point of view. A convenient approach is to separate the overall circuit design in two parts, namely the *linear design* and the *nonlinear design*, [1-3] the former being an approximation of the latter. The aim of the linear design is to ensure that oscillations can be triggered when adequate reverse gain is provided throughout the oscillator loop, with low amplitude voltage probe driving the circuit[1]. Usually in this design phase, simple linear time invariant models for the discrete components (resistor, inductors, and capacitors) suffice, and ideal DC block and DC feed are used in placed of the actual bias networks. Moreover, the finest details regarding the real layout implementation (cross and T junctions, via holes, microstrip discontinuities and bends) are initially omitted for the sake of simplicity. Being the DVCO an *N* section distributed circuit, each section is designed independently of the others, making sure that the impedance matching among the section and the phase match between the drain and gate line are respected [4-5]. The resulting design cannot obviously be expected to be definitive, as it is merely used for detecting/checking the *possibility* of attaining oscillations[2] at certain frequencies. Hence, a full nonlinear analysis and design has to be performed subsequently to obtain a more precise evaluation of the resonant frequencies and to gather relevant information regarding the output power at the fundamental, the harmonic power content, the phase noise figure, the parametric sensitivity and so on. The schematic of the circuits used in nonlinear analysis/design makes use of the most accurate description, including all the details that were omitted in the linear design step.

6.1.1 DVCO PRELIMINARY DESIGN

The reverse mode DVCO is implemented according to the suggestions given in [6-7]. A first version of the circuit made use of a *ladder network constituted by lumped inductors and capacitors* (artificial transmission lines), with 50 Ω *microstrip line sections providing interconnection* among the sections and access to the gate and drain ports of the active devices.

---

[1] An equivalent analysis/design method would consist in measuring the open loop scattering parameter S_{loop} (evaluating *the reverse transfer ratio* across the loop for a DVCO means obtaining the reverse gain G_{rev}) and seek those frequencies at which $\text{mag}(S_{loop})>1$ with a linearly decreasing phase ($\varphi=\arg(S_{loop})$); the frequency corresponding to phase crossing the $\varphi=0$ axis then represents a potential oscillation frequency (according to the Nyquist Criterion, [1]).

[2] Additionally, there's no guarantee that a DC unstable point leads "simply" to an oscillation, being equally possible other phenomena like (sub-) superharmonic resonances, almost periodic waveform generation (self oscillating mixer behavior) and even chaotic behavior [1]. These diverse steady state regimes (which rely on the study of the bifurcation of dynamical systems as outlined in [3]) cannot be foreseen with a small signal linear analysis, which is useful only to get an *estimate* of the *possible* oscillation frequencies.

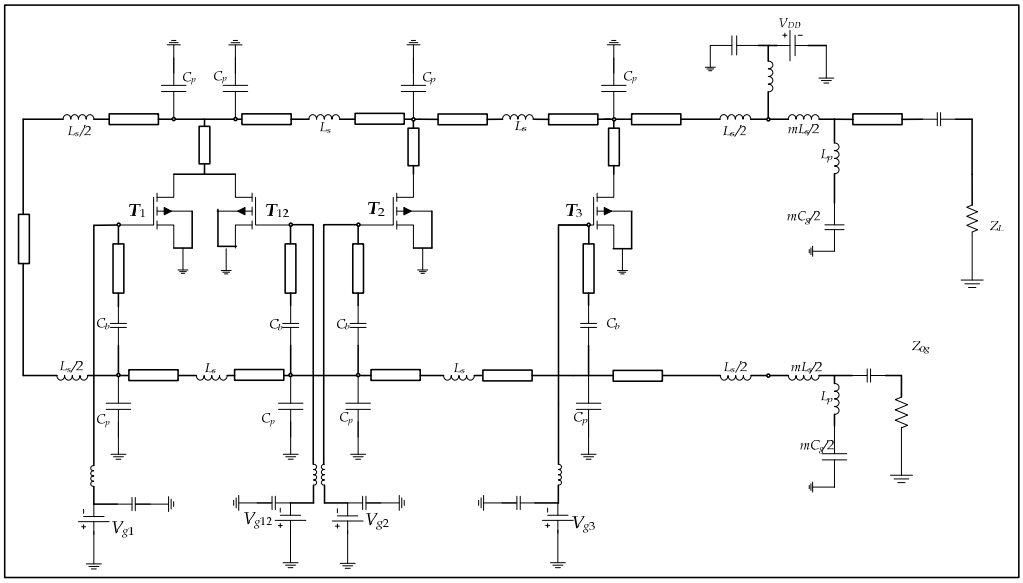

FIGURE 6-1. Schematic of the reverse mode DVCO, as derived from [6—7].

The initial design choice regarded the type of dielectric substrate to be used for the implementation of the DVCO in a microstrip line circuit board, and the active devices providing the necessary gain to build up and sustain oscillations. The oscillator was implemented on an ARLON 25 N (H=0.508 mm, ε = 3.38 @10 GHz) substrate [8], presenting a low and relatively constant dielectric permittivity over a wide frequency range. The active devices were four N3509M04 HJ-FETs from RENESAS (formerly NEC), presenting adequate transconductance values ($g_{m,min}$= 80 mS @ V_{DD}=2 V, I_D= 10 mA) [9], and an acceptable range for the voltage gate bias of 0.5 V (from -0.5V to 0V, since the HJ-FET operates in depletion mode, thus it is normally on when the gate to source voltage is zero) in the active zone.

Subsequently, a layout draft is sketched to estimate the spacing among the four sections striving for the most compact design possible[3]. Then, microstrip line sections of appropriate width and length are introduced[4] in the schematic. Since the output load impedance is by default 50 Ω, the microstrip lines interconnecting the *constant-k* filter section are designed to provide the same nominal impedance. The lines providing access to the gate and drain ports of the active device, doesn't necessarily fulfill this constraint, and their widths and lengths are dictated by purely

[3] Every additional line section for interconnecting the LC filter cells determines a decrease in the oscillation frequencies. This could be justified intuitively taking into account the additional transit time of the signal across the loop, or in a formal way by means of equations (2.66—2.69) (considering the case a=1, m=1, p, $\psi \neq 0$) where ψ is an additional phase.

[4] Microstrip lines width and length could be synthesized by entering the physical detail of the substrate (*dielectric permittivity, height of the dielectric, losses in the dielectric*) and by analyzing/synthesizing the maximum input-output phase shifts (related to the *length of the line*) and the nominal impedance (controlled by the *width of the line*) for the chosen substrate *at a given frequency*, which in the case of a multi-frequency device is usually chosen to be the highest. Many EDA microwave tools allow very easily designing microstrip line circuits. Generally speaking for a given substrate at a fixed frequency, the width of a line is inversely related to its nominal impedance (*narrow lines, higher impedances*), while the length of a line is directly related to the phase shift (longer lines, greater phase shifts) [11].

geometric[5] considerations (like *pad size* for transistors' pins, *length of the route* from the gate/drain line to the gate/drain active devices ports, etc.).

Lastly, the design of the basic constant-*k* filter sections is considered. The *inductive components* of the drain and gate line are chosen to be equal i.e. $L_g = L_d$. Nevertheless the *capacitive components* (represented by the input/output FET parasitic capacitances) *differ significantly*, being C_{ds} smaller than C_{gs}. In a distributed amplifier, in order to provide a good gate- line to drain-line phase match is mandatory to add a "padding" capacitor C_p on the drain line so that $C_{ds}+C_p = C_{gs}$ [10, 11] However in reverse distributed oscillators the input/output transmission networks are connected via the feedback loop, and an additional complication is represented by the presence of transistor $\boldsymbol{T}_{12}$ which needs to be placed crosswise and, exerting an additional capacitive loading on the gate line in the first section (together with T_1), and an additional capacitive loading on the drain line in the second section (together with T_2) (Fig. 6.1). An uneven capacitive loading on the two lines would vastly deteriorate the broadband impedance matching which is *essential for preventing the build-up of spurious oscillations* as the authors pointed out in [6,7]. Therefore the first choice to be made is how to balance the capacitive loading on the input/output lines taking into account the tradeoff between *phase* (*propagation constant of the LC sections*) *match* vs. *impedance match*. The solution to this problem affects the later design stages, and of course the DVCO behavior in terms of maximum attainable frequency, bandwidth, presence of spurious oscillations, discrete resonances distribution across the tuning bandwidth. Unfortunately, there's not a unique solution, but rather many ad-hoc solutions. In the schematic proposed by Skvor [7], the unequal capacitive loading is mitigated by placing *padding capacitors* in the gate/drain line, with different values in each section. In our first design [12], a slightly different topology it is used, were the additional transistor $\boldsymbol{T}_2$ (referred to as $\boldsymbol{T}_{12}$ in [6, 7]) isn't strictly placed crosswise, but rather connected to the adjacent stages using additional microstrip line segments, in order to simplify the final layout, ensuring an adequate spacing between each section. Moreover, since DC blocking capacitor C_b values can be selected to decrease the gate-to-source capacitance[6], fulfilling the relationship $(C_{gs}\ C_b) / (C_{gs} + C_b) = C_{ds}$ (), padding capacitors of constant value are inserted in the gate and the drain line assuming $C_{\underline{gp}} = C_{dp}$ *which constitute the basic LC filter sections*[7] *together with* $L_g = L_d$ *having* $Z_{od} \approx Z_{og}$ *and* $\omega_{og} \approx \omega_{od}$. Therefore, once the values of the cut-off frequency and image impedance are set, the values of the generic series inductor L_s and padding capacitor C_p are derived from (2.25-2.26) as :

[5] This is strictly valid if the "vertical dimension" of the circuit is much less than its "horizontal dimension", in other word unless the wave propagation across each active devices could be neglected, taking place primarily in the drain/gate lines) see [4], in the chapter regarding coupled wave analysis.

[6] The voltage the *p*-th section on the gate line, is applied to the series of the capacitors C_{gs} and C_b.

[7] This approximation is valid *if* $C_{\underline{gp}} = C_{dp} >> C_{gs} >> C_{ds}$, in other terms, if the DVCO is designed for frequencies up to a few gigahertz, in order to neglect the internal parasitics in comparison with the external padding capacitances. Moreover, in this preliminary phase inductors and capacitors are assumed ideal i.e without losses and/or additional parasitic (i.e. losses, spurious resonances due to stray reactive components) and *lumped. In this design inductive parasistics coming from the package and pins of the FET are neglected, thus the basic cell hereinafter being considered are constant K filters*

$$\begin{cases} Z_0 = \sqrt{\dfrac{L_s}{C_p}} \\ \omega_c = \dfrac{2}{\sqrt{L_s C_p}} \end{cases} \Rightarrow \begin{cases} L_s = \dfrac{2Z_0}{\omega_c} = \dfrac{Z_0}{\pi f_c} = Z_0^2 C_p \\ C_p = \dfrac{2}{\omega_c Z_0} = \dfrac{1}{\pi f_c Z_0} \end{cases} \tag{6.1}$$

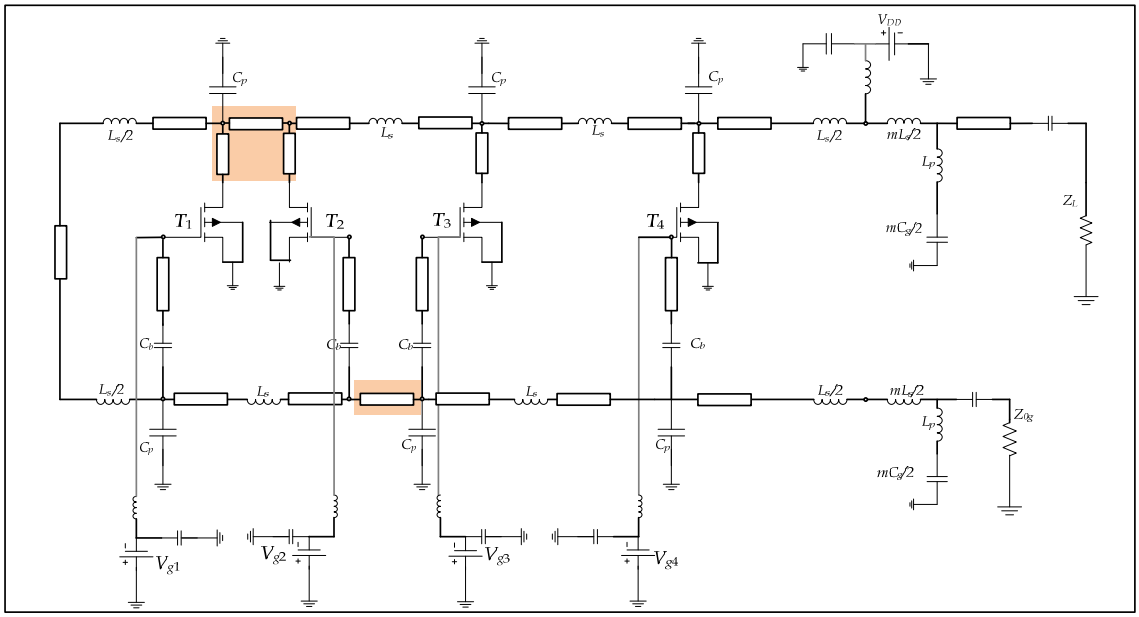

FIGURE 6-2. Proposed topology for a reverse mode DVCO.

Then the values of inductors and capacitors providing a 3 GHz cut-off frequency at 50 Ω nominal impedance are L_s=3.3 nH, C_p= 2.12 pF, which are introduced in the schematic (Fig. 6.2). The corresponding linear frequencies are indicated in Table 6.1, representing a limit case when the length of the feedback line approaches zero [8].

Moreover, for a successful design, it should be ensured an adequate impedance match in the input output line, in order to avoid signal reflections leading to potential instabilities or spurious oscillations [4], [7]. To that aim, *m*-derived sections (with m =0.6) are placed before the gate line terminating resistor (R_g= 50 Ω), and before the output load (R_L= 50 Ω), to match them to the nominal line impedance, across the 85% of the tuning bandwidth [11]. Their values are readily obtained by the previously designed constant k filters:

[8] The length of the feedback line influences the distribution of resonant frequencies across the tuning bandwidth since it adds an extra phase contribution which should be accounted for in the evaluation of the reverse gain phase response (indicated as ψ in equation (2.66)), which implies that the *integer number a in (2.66)* might be greater than unity. Significant discrepancies between the values obtained by linear analysis carried out in previous section and the numerical simulation can be expected.

$$\begin{cases} L_m = mL_s/2 = 0.3L_s \\ L_p = \left(\dfrac{1-m^2}{2m}\right)L_s = 0.533L_s \\ C_m = mC_p/2 = 0.3C_p \end{cases} \tag{6.2}$$

providing the values (approx.) L_m= 0.99 nH, L_p=1.76 nH, C_m=0.64 pF which need to be approximated by the closest practical available values for chip capacitor and inductors[9].

The distributed voltage controlled oscillator, appears as in Fig. 6.2 at this point. It has to be noted, that ideal *DC feeds* and *DC blocks* are used in place of the actual bias networks and blocking capacitors. Moreover, *via holes to the ground plane are neglected*, considering only ideal grounds as the effect of *discontinuities*, *bends, cross and T Junctions*, and will be considered when dealing with the nonlinear analysis. The discrete oscillation frequencies are then linearly estimated biasing adequately the active transistor $\mathbf{T}_i$, and then introducing a small sine wave voltage probing signal at a convenient node in the schematic to measure the output admittance variation across a reference frequency range (wider than the actual tuning range).

Active Device $\mathbf{T}_i$	Oscillation Frequencies
$\mathbf{T}_1$	3 GHz
$\mathbf{T}_2$	1.5 GHz
$\mathbf{T}_3$	927 MHz
$\mathbf{T}_4$	668 MHz

TABLE 6-1. Discrete Resonant Frequencies, as derived by the linear analysis performed in chapter II (eq. 2.69)

6.1.2 Low-Amplitude DVCO Probe Analysis for Estimating Individual Sections' Resonant Ferquencies.

The algorithm for finding the oscillation frequencies with the help of a small amplitude voltage probe has been described in chapters III, IV; it will be briefly reviewed here. Having designed the oscillator, a *small-signal voltage harmonic probe* (or small signal auxiliary generator) is

[9] A major source of disagreement among measured resonant frequencies and simulated ones, could partially be ascribed to an imperfect matching due to the non-ideality of the actual components employed in the *m-derived sections* (chip inductors/capacitors). Generally non-ideal lumped capacitors/inductors, include losses (modeled by series or shunt resistance) and additional resonances (modeled by series/parallel LC circuits) which worsen the broadband matching and introduce a source of instability (potential spurious oscillations might be triggered by this extra-resonances).

introduced between a convenient circuit node[10] and the ground. Small-signal-driven, Harmonic Balance, frequency-swept simulations are subsequently carried out for evaluating the *probe admittance*[11] $\mathbf{Y}_p$=[Re($\mathbf{Y}_p$), Im($\mathbf{Y}_p$)] at its port across a certain frequency range (e.g 0.1—10 GHz), for a specific biasing of the four active sections, determined by the values of the tuning control vector $\mathbf{V}$=[V_g^1 V_g^2 V_g^3 V_g^4] with $V_g^r = V_{GS}(\boldsymbol{T}_r)$ being the *r*-th gate bias control . A potential oscillation occurs[12] whenever the *probe conductance* G_p=Re($Y_p(f)$) *becomes negative* and while the *probe susceptance* S_p =Im($Y_p(f)$) crosses the frequency axis with a positive slope (i.e. $\partial S_p/\partial f>0$) [1] –[3] at the frequency f_o in the range [f_{min}, f_{max}]:

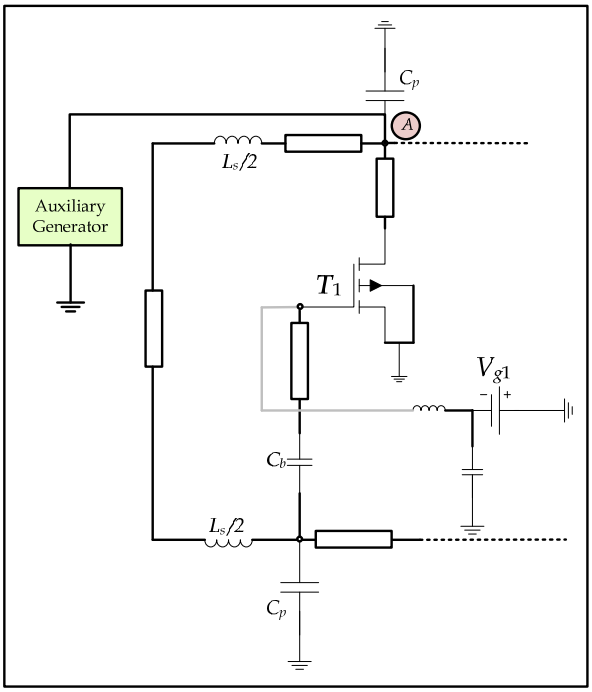

FIGURE 6-3. DVCO Linear Analysis using an auxiliary generator connected at the node *A*, just before the first section.

[10] Suitable nodes to inject the probe signal are immediately before the *DVCO feedback loop*, or at *i-th* ($\mathbf{T}_i$) drain port, or at *the DVCO output port* (picture 6.3).

[11] Or impedance Z_p, if a current sine wave generator $i(t)= I_p \sin(2\pi f_p t)$ is used (see chapter IV).

[12] Regardless of the actual circuit DVCO schematic, equations (6.61) (derived from the Kurokawa oscillation condition) show that the entire oscillator might be simply interpreted as a one-port element connected in parallel with the voltage probe, and that oscillations are possibly triggered when the probe is receiving RF power from the oscillator port (the admittance turns negative (Re(Y_p))<0) and simultaneously the reactive component resonate (expressed in the last two equation in (5.3)). The frequency at which (5.3) holds represent the linear estimate for the oscillation frequency.

LFS. Linear Frequency Search

/* *Linear Analysis set - up*

define the voltage range $\mathcal{V}=[V_{\min}, V_{\max}]$ / $V_{\min}=-1V$; $V_{\max}=0V$

define the tuning vector $\mathbf{V}=[V_g^1, V_g^2, V_g^3, V_g^4]\in\mathcal{V}^4$

set the tuning voltages: $V_{gi}\leftarrow V_{0i}$

introduce *the probe at a measurement node M*

set the small probing voltage (constant): $a=1mV$

$p_a(t)=a\cdot\sin 2\pi ft$ /* *small amplitude, frequency swept voltage signal*

introduce a *current meter at node M to evaluate* $I_{p,\mathbf{V}}^{1,M}(f)$

/*Frequency Analysis*

for $f\in[f_{\min}, f_{\max}]$ / $f_{\min}=0.1\text{GHz}$; $f_{\max}=10$ GHz;

{

$\mathbf{E}(\mathbf{X}, a, f, \mathbf{V})=\mathbf{0}$ /* *solve* the HB equations

$Y_{p,\mathbf{V}}^{M}(f)\leftarrow\dfrac{I_{p,\mathbf{V}}^{1,M}(f)}{V_{p,\mathbf{V}}^{1,M}(f)}=\dfrac{I_{p,\mathbf{V}}^{1,M}(f)}{a}$ /* *evaluate* the probe admittance

$f\leftarrow f+\Delta f$ /* *frequency advance*

}

/* *Oscillation Condition check*

$$if\left(\begin{array}{l}\text{Re}(Y_{p,\mathbf{V}}^{M}(f_o))<0\\ \dfrac{\partial\,\text{Im}(Y_{p,\mathbf{V}}^{M}(f_o))}{\partial f}>0\\ \text{Im}(Y_{p,\mathbf{V}}^{M}(f_o))=0\end{array}\right)$$

then $\hat{f}_{osc}\leftarrow f_o$ /estimated osc. frequency ($f_o\in[f_{\min}, f_{\max}]$) (6.3)

In the DVCO simulation executed on a commercial EDA software, ADS Agilent 2008® [13] the probe consists in a RF single tone generator, whose parameters are represented by its amplitude and frequency[13]. Its amplitude a is kept constant at a small value (a = 1—10 mV), while its frequency f is swept[14] in the range [$f_{\min}$, $f_{\max}$]. The output admittance at the probe port is measured as a ratio of the first harmonic of the probe current and the first harmonic of the voltage developed across its terminals: $Y_p = I_p^1 / V_p^1$ and depends on the frequency of the injected signal. The active devices are turned on (one after another) and for each of them, *small signal-driven, frequency-swept HB simulations are run* to check whether the (5.3) are fulfilled[15]. Results are shown in Table 6.2 while Fig. 6.4 shows the probe admittance versus the frequency of the injected signal. A relevant frequency shift is observed as a consequence of the inclusion of the layout elements whose electrical length affects the reverse loop phase response according to equation (2.69) (accounted for in the ψ variable).

[13] In a free running oscillator all the possible circuit solutions differ for an arbitrary phase. Without loss of generality, therefore, the phase of the voltage RF periodic probe could be set to zero .

[14] Amplitude and frequency of the probe are declared as circuit variables in the simulator, so for the gate voltages hereinafter referred. Iterations in a circuit variable are carried out by the "parameter sweep" block (see refs ADS 2008).

[15] The transistors are biased with a gate voltage of -0.2 V, in order to let them operate in the active region of their output characteristics; *vendor models for lumped capacitors and inductors have been used*. Via holes are modeled with a constant series inductance to the ground of value L_h= 0.2 nH. The DC gate bias blocking capacitors are chosen to be C_b=22 pF, while the terminating section capacitors in the gate and drain line are C_f = 100 pF.

Active Device $\mathbf{T}_i$	Oscillation Frequencies (f_c= 3 GHz)
$\mathbf{T}_1$	1.8 GHz
$\mathbf{T}_2$	1.31 GHz
$\mathbf{T}_3$	860 MHz, primary resonance (spurious resonance at 1.99 GHz)
$\mathbf{T}_4$	710 MHz, primary resonance (spurious resonance at 1.7 GHz)

TABLE 6-2. Discrete Resonant Frequencies derived by Linear DVCO Simulation

In the case of activation of the third and fourth devices there exists the possibility of having spurious resonances, which possibly coexist with the intended one. The oscillation condition is in fact *fulfilled at two distinct frequencies* (Fig.6.4); unfortunately, linear simulations do not succeed in predicting which of those *would be physically observable*. Therefore nonlinear analysis tools are needed to inspect the DVCO circuit in a more detailed manner.

Moreover, it is observed that by adequately biasing the FET gates, the frequency intervals for which the probe conductance goes negative extend way beyond a small neighborhood of the *i*-th discrete resonance, and in most cases they overlap. It follows (from the first of (6.48)) that these devices possess adequate gain to trigger oscillations across all the tuning bandwidth [6—7].

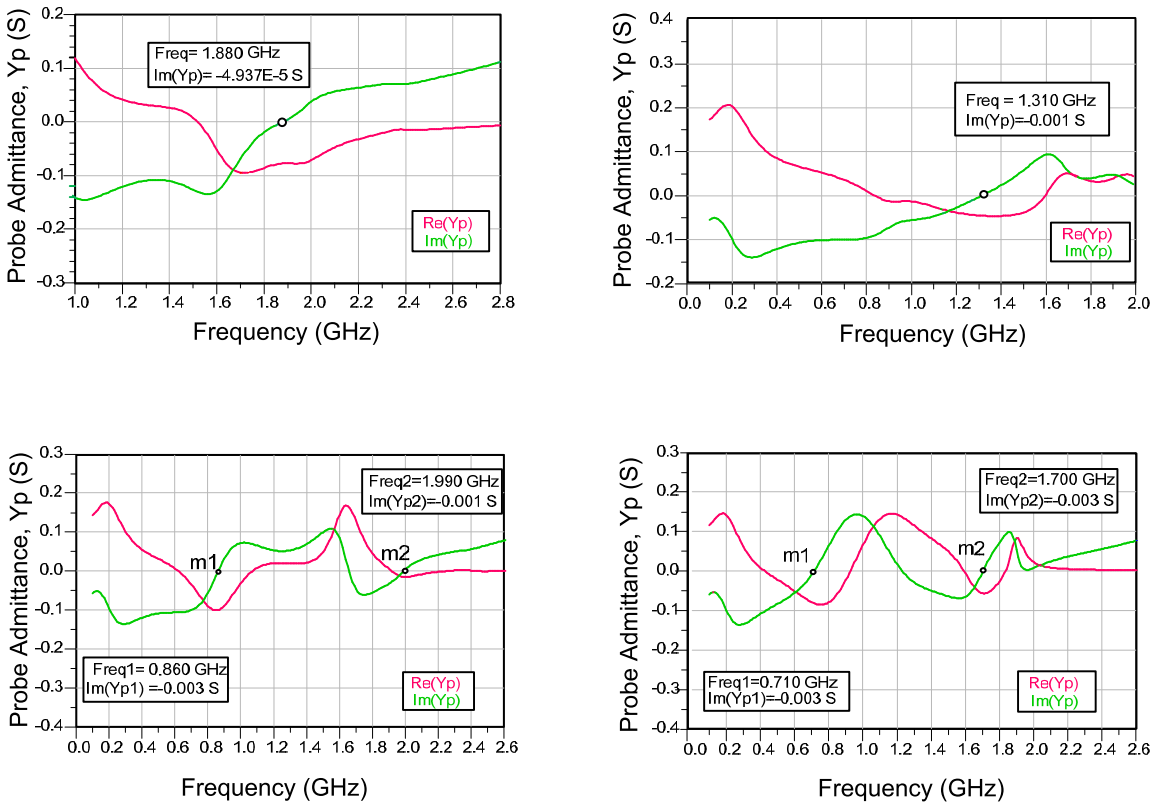

FIGURE 6-4. Small-Signal Auxiliary Generator Admittance plots as a function of auxiliary generator's frequency at four different bias settings, showing the possibility of attaining oscillations (whose frequencies are listed in Table 6.2). The lower graphs indicate that more than one resonance can be triggered.

6.2 REVERSE MODE DVCO NONLINEAR DESIGN.

The analysis of the individual discrete resonances is carried out by biasing adequately the four tuning controls V_g^s and choosing tentative values for the probe amplitude and frequency (both belonging to suitable *reference ranges/ search spaces, namely* $\mathcal{A}$= [A_{min}, A_{max}], $\mathcal{F}$=[f_{min}, f_{max}]; for more details see section 4.1). The probe frequency is initially considered *equal to the estimated oscillation frequency derived from linear analysis* while the probe amplitude is set to a few tenths of volts (i.e. A=0.3—0.7 V). Large-signal probe-driven HB simulations are then sequentially carried out; at the end of each HB run (inner tier) the probe admittance is evaluated. A built in optimization algorithm(outer tier) takes care in selecting the fittest values for the probe amplitude frequency according to the optimization goals Re(Y_p)=0; Im(Y_p)=0 *which states that net power flowing through the probe has to vanish*[16]*, when the oscillating steady state is reached* [14]. In the system (6.3) the vector **X** represents all the spectral components of the remaining circuit variables (other than A_o and f_o). As it is known, in practical implementation it is necessary to select a prescribed accuracy for the non-perturbation condition, which gets modified as in eq . (6.4).

SRA. Single Resonance Analysis

$$
\begin{array}{|l}
\mathcal{V}=[V_{\min}, V_{\max}] \,/\, \textit{voltage range} \\
\mathbf{V}=[V_g^1, V_g^2, V_g^3, V_g^4] \in \mathcal{V}^4 \;/\; \textit{four tuning controls} \\
V_g^i \leftarrow V_{0i} \in \,/\, \textit{tuning voltages are initialized} \\
/\, \textit{define the ranges for the unknowns}\,(A, f) \\
A \in [A_{\min}, A_{\max}] = \mathcal{A} \\
f \in [f_{\min}, f_{\max}] = \mathcal{F} \\
\text{introduce } \textit{the voltage probe at a measurement node } M \\
p(t) = A \sin 2\pi f t \;/\; * \text{ large signal probe } (\varphi = 0) \\
\text{introduce a } \textit{current meter at node } M \textit{ to evaluate } I_{p,\mathbf{V}}^{1,M}(A, f)
\end{array}
$$

$$
/ * \; \textit{inner} - \textit{tier}
$$

$$
\begin{array}{|l}
A \leftarrow A_0 (\equiv a V_{DD}, a \in]0.1, 1]) \,/\, * \text{tentative amplitude value} \\
f \leftarrow \hat{f}_{osc}^{\,i} \;\; /\, * \text{derived from lin. analysis} \\
\boxed{\mathbf{E}(\mathbf{X},\, A, f, \mathbf{V}) = \mathbf{0} \;\; /\; \text{solve } \textit{the harmonic balance equations}} \\
Y_{p,\mathbf{V}}^{(M)}(A, f) \leftarrow \dfrac{I_{p,\mathbf{V}}^{1(M)}(A, f)}{V_{p,\mathbf{V}}^{1(M)}} = \dfrac{I_{p,\mathbf{V}}^{1(M)}(A, f)}{A} \;/\; \textit{evaluate} \text{ the probe admittance}
\end{array}
\qquad (6.4)
$$

$$
\begin{array}{|l}
\textit{find } (A_o, f_o) \in \mathcal{A} \times \mathcal{F} \textit{ such that}: \\
/ * \; \textit{outer} - \textit{tier} \\
\boxed{\begin{array}{l} \left|\mathrm{Re}(Y_{p,\mathbf{V}}^{(M)}(A, f))\right| < \varepsilon \\ \left|\mathrm{Im}(Y_{p,\mathbf{V}}^{(M)}(A, f))\right| < \varepsilon \end{array}} \quad \begin{array}{l} /\, \textit{non} - \textit{perturbation conditions} \\ /\, \textit{as optimization goals} \\ (0 < \varepsilon << 1 \textit{ is the } \text{optimization tolerance}) \end{array}
\end{array}
$$

The simulation framework (6.4) is well suited for analyzing the discrete resonances in the DVCO Regarding the design, the amplitude[17] and the frequency of the probe signal are regarded as

[16] Since the removal of the triggering signal doesn't have to affect the large signal steady state solution, an oscillating voltage is present at the probe terminals, but no current has to flow through the probe, resulting in a zero probe admittance.

[17] The probe amplitude is set according to the required output power that the oscillator has to deliver at the fundamental. See appendix E.

design targets and kept fixed; instead a set of adjustable parameters $\boldsymbol{\eta}=[\eta_1, \eta_2,\ldots,\eta_p]$ is introduced in the system (6.4) which is modified as follows;

PSP. *Parametric* Synthesis Problem (single frequency)

$V_g^i \leftarrow V_{0i}$ / *tuning voltages are initialized*
$A \leftarrow A_o$ / *sets the desired osc. amplitude*
$f \leftarrow f_o$ / *sets the desired osc. frequency*
$\boldsymbol{\eta} = [\eta_1, \eta_2, ..., \eta_p]^T \in \quad \boldsymbol{\mathcal{P}} \subseteq \mathbb{R}^p$ / *parameter vector and search space*
$\eta_k \leftarrow \eta_{0k}, 1 \le k \le p$ / *parameters are initialized*
introduce *the* voltage *probe at a measurement node M*
$p(t) = A_0 \sin 2\pi f_0 t$ / * large signal probe (constant A_0, f_0)
introduce a *current meter at node M to evaluate* $I_{p,\mathbf{V}}^{1,M}(A_0, f_0, \boldsymbol{\eta})$

/ * *inner – tier*
$\mathbf{E}(\mathbf{X}, A_0, f_0, \boldsymbol{\eta}) = \mathbf{0}$ / solve the HB *parametric equations*
$Y_{p,\mathbf{V}}^{(M)}(A_0, f_0, \boldsymbol{\eta}) \leftarrow \dfrac{I_{p,\mathbf{V}}^{1,M}(A_0, f_0, \boldsymbol{\eta})}{V_{p,\mathbf{V}}^{1,M}} = \dfrac{I_{p,\mathbf{V}}^{1,M}(A_0, f_0, \boldsymbol{\eta})}{A_0}$ / *evaluate* the probe admittance

find $\boldsymbol{\eta} = [\eta_1, \eta_2, ..., \eta_p]^T \in \quad \boldsymbol{\mathcal{P}}$ *such that*:

/ * *outer – tier*
$\left|\mathrm{Re}(Y_{p,\mathbf{V}}^{(M)}(A_0, f_0, \boldsymbol{\eta}))\right| < \varepsilon$
$\left|\mathrm{Im}(Y_{p,\mathbf{V}}^{(M)}(A_0, f_0, \boldsymbol{\eta}))\right| < \varepsilon$
/ *non – perturbation conditions as optimization goals*
($0 < \varepsilon << 1$ is the tolerance)

(6.5)

In this section the nonlinear analysis of the DVCO circuit is carried out referring to the schemes (6.4) and (6.5). In particular, by employing the (6.4) the output power spectrum (up to the third harmonic) for the four discrete frequencies is found. Then, the algorithm (6.5) is used for optimizing the circuit, adjusting some controllable parameters. Specifically, four resistors are introduced in the schematic, whose resistance values are adjusted until the DVCO response is made close to the desired one.

Additionally, the discrete oscillation frequencies dependence on the values of constant-*k* sections series-inductances L_s and shunt-capacitances C_p is investigated, to the aim of selecting lumped components values which give a more uniform spacing among the four discrete resonances across the tuning bandwidth. As a consequence, the algorithm shown in (6.4) is iterated twice with respect the variables (L_s, C_p) *considered as parameters*[18], employing *two nested cycles spanning the domains* $L_{min} \le L_s \le L_{min}$; $C_{min} \le C_p \le C_{max}$.

[18] Parametric analysis refers to the *analysis of the solutions (discrete resonances) as certain parameters are varied*. Although parameters are involved as in (6.5) their role is *conceptually dual*. In eq (6.5), the unknown parameters have to be found (*they represent the outcome*) by means of an optimization process *in order to obtain a specific oscillation at a given frequency and amplitude* (synthesis problem), while in equation (6.6) it is considered *the sensitivity of the solutions* (A_o, f_o, *the outcomes)* with respect to two parameters *which are considered adjustable inputs of the problem* namely the *inductance* and the *capacitance* of the *constant-k* filter sections.

PAP.Parametric Analysis Problem.

/Parametric Analysis of the discrete resonances as C_p and L_s are varied

for $[i=1,...,4]$

/*initial* set-up

$\mathcal{V}=[V_{\min},V_{\max}]$ / *voltage range*

$\mathbf{V}=[V_g^1,V_g^2,V_g^3,V_g^4]\in\mathcal{V}^4$ / *four tuning controls*

for $[j=1,...4,j\neq i]\{$

$\begin{cases} V_g^i \leftarrow V_{on}(=-0.2V) \\ V_g^j \leftarrow V_{off}(=-1V)\ \} \end{cases}$ / *tuning voltages are initialized*

/*define the ranges for the unknowns* (A,f)

$A\in[A_{\min},A_{\max}]=\mathcal{A}$

$f\in[f_{\min},f_{\max}]=\mathcal{F}$

$A\leftarrow A_0$ /*tentative amplitude value

$f\leftarrow \hat{f}_{osc}^{\,i}$ /*derived from lin. analysis

introduce *the* voltage *probe at a measurement node M*

$p(t)=A\sin 2\pi ft$

introduce a *current meter at node M to evaluate* $I_{p,\mathbf{V}}^{1,M}(A,f)$

/* *nested cycles*

for $C_{min}\le C_p\le C_{max}\{$

for $L_{min}\le L_s\le L_{max}\ \{$

/* *inner – tier*

$\mathbf{E}(\mathbf{X},A,f,\mathbf{V},C_p,L_s)=\mathbf{0}$ /solve HB *equations* (*depending on* C_p *and* L_s)

$Y_{p,\mathbf{V}}^{(M)}(A(C_p,L_s),f(C_p,L_s))\leftarrow \dfrac{I_{p,\mathbf{V}}^{1(M)}}{V_{p,\mathbf{V}}^{1(M)}}(C_p,L_s)=\dfrac{I_{p,\mathbf{V}}^{1(M)}(A(C_p,L_s),f(C_p,L_s))}{A(C_p,L_s)}$

/* *outer – tier*

find $(A_o,f_o)\ \in\mathcal{A}\times\mathcal{F}$ *such that*:

$\left|\mathrm{Re}(Y_{p,\mathbf{V}}^{(M)}(A(C_p,L_s),f(C_p,L_s)))\right|<\varepsilon$

$\left|\mathrm{Im}(Y_{p,\mathbf{V}}^{(M)}(A(C_p,L_s),f(C_p,L_s)))\right|<\varepsilon$

update $\begin{cases} A_o\leftarrow A_o(C_p,L_s) \\ f_o\leftarrow f_o(C_p,L_s) \end{cases}$

$L_s\leftarrow L_s+\Delta L_s$ / increase the inductance

$\}$

$C_p\leftarrow C_p+\Delta C_p$ / increase the capacitance

$\}$ (6.6)

Subsequently, the DVCO tuning function, that is the neighboring sections' gate voltages variation with respect to the *frequency of the output oscillating signal, is studied*. It might be explored by assigning repeatedly different values to the gate voltages[19] $\{V_g^{(i+1)},\ V_g^{(i)}\}$, and determining the solutions accordingly with the technique (6.3). At the outset this approach gives a *coarse view* of the tuning algorithm, and may be used to understand the output power level and its variation throughout the tuning bandwidth. Nevertheless this methodology might lead to convergence failure, which occurs when heedlessly changing the tuning parameters, a *forbidden* combination of

[19] Assigning some values to $V_g^{(i+1)}$, $V_g^{(i)}$ which produce an oscillation in the range $[f_{i+1},\ f_i]$, as done empirically when testing the DVCO.

gate bias voltages $\{V_g^{(i+1)}, V_g^{(i)}\}$, being not able to provide any oscillation at the output[20] . Thus, without a *previous knowledge of* gates voltages' *admissible values* (those providing *an oscillating solution* to the Harmonic Balance simulations), it is more advisable to perform *frequency-swept, probe driven Harmonic Balance simulations* dealing with $\{V_g^{(i+1)}, V_g^{(i)}\}$ as two additional *optimization variables / synthesis parameters* to be sought in order to meet the *zero admittance* constraint at the probe port (i.e. $\mathrm{Re}(Y_p)=0$; $\mathrm{Im}(Y_p)=0$) and consequentially fulfill the *oscillating condition*[21].

The algorithm, sketched in its basic steps in (6.7), enable the *probe frequency* to be varied across the interval $[f_{i+1}, f_i]$, where f_{i+1} (or f_i) is the resonant frequency associated with the activation of $\boldsymbol{T}_{i+1}$ (or $\boldsymbol{T}_i$), with the purpose of investigating the DVCO tuning function in a *sub-interval of the whole tuning bandwidth*. For each value of probe frequency $f_{i+1} \le f \le f_i$ a *single frequency synthesis problem is solved, analogously to the case* (6.5), with the only difference that the probe amplitude, being not preset to a *constant value,* takes part in the optimization process. Referring to (6.5) the parametric vector $\boldsymbol{\eta} = [V_g^{(i+1)}, V_g^{(i)}, A]$ would thus include two neighboring sections bias voltages and the probe amplitude. In the algorithm depicted in (6.7) it is considered the possibility of a *forward* sweep, (from f_{i+1} to f_i) a *backward* sweep (from f_i to f_{i+1}) and *a two-way sweep* when the initial probe frequency *lies inside* the interval $[f_{i+1}, f_i]$. A frequency swept *solution consists in the triple* $\{A(f), V_g^{(i+1)}(f), V_g^{(i)}(f)\}$ where $A(f)$ accounts for the output power variation and $\{V_g^{(i+1)}(f), V_g^{(i)}(f)\}$ represent the oscillator tuning curves in the sub range $[f_{i+1}, f_i]$. As discussed in [15] however, the *solution to this problem is not unique*; herein it could be seen as a consequence of the *under-determinacy of the harmonic balance framework discussed earlier*. In fact, at each frequency in $[f_{i+1}, f_i]$ only *two equations* have to be simultaneously fulfilled for determining *three parameters:*

---

[20] According to the linear analysis carried out earlier (see section §6.3.3), it is seen that a *frequency shift in the output waveform occurs whenever two adjacent sections are biased in a complementary manner* in order to produce a *proper vector sum of the two reverse gains, fulfilling the closed loop oscillation condition*. Therefore, when the gate voltage of the i^{th} section is increasing and *simultaneously* the voltage of $(i+1)^{\text{th}}$ section is decreasing the output frequency is increasing from f_{i+1} to f_i . Just to clarifying things, for an *idealistic complementary* tuning rule the gate voltages $V_g^{(i+1)}, V_g^{(i)}$ (using *depletion-mode* FET with a gate *bias range* $[-V_{min}, 0]$) would be then constrained to *follow the linear relationship*;

$$\begin{cases} V_g^{(i)} = -V_{\min} + (u + V_{\min}) \\ V_g^{(i+1)} = -V_{\min} - u \end{cases} \qquad u \in [-V_{\min}, 0]$$

As a result, since the gate voltages are intertwined by the above relation *not every point of the region* $\mathcal{V} = \{ (V_g^{(i+1)}, V_g^{(i)}) \in [-V_{min}, 0] \times [-V_{min}, 0] \}$ *is admissible even when the voltages posses a perfectly symmetric trend.* For this reason, a *voltage-swept parametric analysis* $V_g^{(i+1)}, V_g^{(i)}$ might produce poor results at first, given that the *tuning algorithm is actually unknown*, and the nested cycle could get stuck in *forbidden regions of the parameters' space* $[-V_{min}, 0]$. Consequently, the more effective way to deal with the tuning function (in the first instance) is to scan a frequency range (*multi-frequency analysis*) and to include *the tuning voltages as optimization variables (that is, unknowns) along with the probe amplitude, that are suitably chosen by the optimization algorithm to meet the condition* $\mathrm{Re}(Y_p)=0$; $\mathrm{Im}(Y_p)=0$. Once the tuning function is known, then a more detailed voltage-swept parametric analysis follows.

[21] In simpler terms, as *the frequency of the probe* is varied, its *amplitude* and the *tuning controls* which *synthesize* an oscillating signal having *the same frequency of the probing signal* are selected by means of the same optimization process (5.3). This procedure may appear counterintuitive at first, since it reverses the logic sequence (cause → effect) that is observed experimentally. In the lab test, DVCO tuning voltages are selected first (*causes*) and the output oscillation at a certain frequency and with a given power is subsequently produced (*effect*). In the DVCO *tuning function HB simulation* however, an oscillation frequency is selected (*effect*) and the oscillation power level and the tuning controls (*causes*) are then *synthesized/optimized to provide* $\mathrm{Re}(Y_p)=0$; $\mathrm{Im}(Y_p)=0$.

$$
\begin{aligned}
&f \in [f_{i+1}, f_i] \,/\, \textit{frequency analysis range} \\
&\mathcal{V} = [V_{\min}, V_{\max}] \,/\, \textit{voltage range} \\
&\mathcal{A} = [A_{\min}, A_{\max}] \,/\, \textit{amplitude range} \\
&f \leftarrow f_0 \\
&\textit{find } (A_o, V_g^i, V_g^{i+1}) \in \mathcal{A} \times \mathcal{V}^2 \quad \textit{such that}: \\
&\begin{cases} \mathrm{Re}\left(Y_p\left(A(f_0), V_g^i(f_0), V_g^{i+1}(f_0)\right)\right) = 0 \\ \mathrm{Im}\left(Y_p\left(A(f_0), V_g^i(f_0), V_g^{i+1}(f_0)\right)\right) = 0 \end{cases}
\end{aligned}
$$

Assuming the two equation are solved by a certain pair $\{V_g^{(i+1)}(f_0),\ V_g^{(i)}(f_0)\}$ then probe amplitude is considered as *an unspecified parameter* (related to the *oscillator output power level*). Conversely, if *one of the voltage setting is left undetermined*, it exist more than *one voltage pair combination* at a fixed frequency, *corresponding to different probe amplitudes*, and consequently different voltage settings (*providing the same oscillation frequency*) are associated to different *output power levels,* a phenomenon referred to as *ambiguity in the DVCO tuning function* by the authors [6, 7],. Due to the non-uniqueness of the oscillating solutions, it is envisioned the possibility of selecting the ones that gives smoother output power variation throughout the tuning bandwidth [12] This could be achieved by placing an additional optimization goal in the outer tier of the algorithm (6.7), which forces the output power level at the fundamental to be constrained in the range $P_{min} \leq P_{out} \leq P_{max}$. However, due to the multi-objective optimization, the convergence might be difficult. For that reason, a third gate bias voltage (*which plays the role of an additional synthesis parameter*) can be selected *to relieve the computational burden* and speed up the optimization process. A pseudo-code description of the algorithm is provided in (6.8).

Finally, *after having achieved the knowledge of the tuning algorithm*, stability of the solutions is analyzed having recourse to *envelope transient simulations* [16] [17]. To that aim, tuning curves are first plotted in a parametric fashion, having families of curves indicating the oscillation frequency (ordinate axis) versus a gate bias voltage (abscissa axis) for certain values of the adjacent section bias control voltage (parameter). A simplified version of the algorithm for obtaining the parametric plots versus the gate bias voltages is depicted in (6.9), assuming the voltages are both swept in the same direction.

In what follows, a detailed description of the techniques that have been introduced in this section will be given.

FSA. Frequency-Swept Analysis

$for\{i = 1, 2, 3\}$

$/initial$ set-up

$\mathcal{V} = [V_{\min}, V_{\max}] / voltage\ range$

$\mathbf{V} = [V_g^1, V_g^2, V_g^3, V_g^4] \in \mathcal{V}^4 \ / \ four\ tuning\ controls$

$A \in [A_{\min}, A_{\max}] = \mathcal{A} \ / \ amplitude\ range$

$f \in [f_{i+1}, f_i] / \ frequency\ analysis\ range$

$for\{1 \le j \le 4,\ j \ne i,\ j \ne i+1\}$

$$\begin{cases} V_g^i \leftarrow V_{on}(=-0.2V) \\ V_g^{i+1} \leftarrow V_{on}(=-0.2V) \ / \ tuning\ voltages\ are\ initialized \\ V_g^j \leftarrow V_{off}(=-1V) \end{cases}$$

introduce *the probe at a measurement node M*

$p(t) = A \sin 2\pi ft$

introduce a *current meter at node M to evaluate* $I_{p,\mathbf{V}}^{1,M}(A, f)$

Tuning Curve Evaluation in the range $[f_{i+1}, f_i]$

$m \leftarrow 0$

$f^{(m)} \leftarrow f_0$ / *probe frequency*

$A^{(m)} \leftarrow A(f_0)$ / *initial amplitude at* $f_{i+1} \le f_0 \le f_i$

$$\begin{cases} V_g^{i(m)} \leftarrow V_g^i(f_0) \\ V_g^{i+1(m)} \leftarrow V_g^{i+1}(f_0) \end{cases} / \ initial\ voltages\ at\ f_{i+1} \le f_0 \le f_i$$

$\Delta f \leftarrow \dfrac{f_i - f_{i+1}}{n_p}$ / choose a step depending on the accuracy n_p

for $f_{i+1} \le f \le f_i$ {

$/* inner - tier$

$\mathbf{E}(\mathbf{X}, A, f, V_g^i, V_g^{i+1}) = \mathbf{0}$ //HB *equations*

$$Y_p^{(M)}(f) \leftarrow \frac{I_p^{1(M)}}{V_p^{1(M)}} = \frac{I_{p,\mathbf{V}}^{1(M)}(A(f), V_g^i(f), V_g^{i+1}(f))}{A(f)} / \ probe\ \text{admittance}$$

$/* outer - tier$

$find\ (A, V_g^i, V_g^{i+1}) \in \mathcal{A} \times \mathcal{V}^2 \ \ such\ \ that:$

$$\left|\mathrm{Re}\left(Y_p^{(M)}\left(A(f), V_g^i(f), V_g^{i+1}(f)\right)\right)\right| < \varepsilon$$

$$\left|\mathrm{Im}\left(Y_p^{(M)}\left(A(f), V_g^i(f), V_g^{i+1}(f)\right)\right)\right| < \varepsilon \qquad /non - perturbation\ conditions$$

$/as\ optimization\ goals$ (ε represents the accuracy)

$switch[f^{(m)}]$ {

$case(f^{(m)} = f_{i+1})$:

$f \leftarrow f + \Delta f$ / *march forward* (*from* f_{i+1} *to* f_i)

$case(f^{(m)} = f_i)$:

$f \leftarrow f - \Delta f$ / *sweep backward* (*from* f_i *down to* f_{i+1})

else:

$f^{(m)} \leftarrow f_k$

apply **FSA** *in* $[f_{i+1}, f_k[\cup]f_k, f_i]$ (6.7)

}

$$m \leftarrow m+1 \quad \Rightarrow \quad \text{update} \begin{cases} A_o(f^{(m)}) \leftarrow A_o(f^{(m+1)}) \\ V_g^i(f^{(m)}) \leftarrow V_g^i(f^{(m+1)}) \\ V_g^{i+1}(f^{(m)}) \leftarrow V_g^{i+1}(f^{(m+1)}) \end{cases}$$

O – FSA. Optimized-Frequency Swept Analysis.

for $i = 1,2,3$

$$
\begin{array}{|l}
\hline
/\,\textit{initial}\ \text{set-up} \\
\mathcal{V} = [V_{\min}, V_{\max}]\,/\,\textit{voltage range} \\
\mathbf{V} = [V_g^1, V_g^2, V_g^3, V_g^4] \in \mathcal{V}^4\ /\ \textit{four tuning controls} \\
A \in [A_{\min}, A_{\max}] = \mathcal{A}\ /\ \textit{amplitude range} \\
f \in [f_{i+1}, f_i]\,/\ \textit{frequency analysis range} \\
\textit{for}\{1 \le j \le 4, j \ne i, j \ne i+1\} \\
\begin{cases} V_g^i \leftarrow V_{on}(=-0.2V) \\ V_g^{i+1} \leftarrow V_{on}(=-0.2V)\ /\ \textit{tuning voltages are initialized} \\ V_g^j \leftarrow V_{off}(=-1V) \end{cases} \\
\text{introduce } \textit{the probe at a measurement node } M \\
p(t) = A\sin 2\pi ft \\
\text{introduce a } \textit{current meter at node } M \textit{ to evaluate } I_p^{1(M)}(A,f) \\
\hline
\end{array}
$$

Optimized Power Profile $[f_{i+1}, f_i]$

for $f_{i+1} \le f \le f_i$ {

$$
\begin{array}{|l}
\hline
m \leftarrow 0 \\
f^{(m)} \leftarrow f_0\ /\ \textit{probe frequency} \\
A^{(m)} \leftarrow A(f_0)\ /\ \textit{initial amplitude at } f_{i+1} \le f_0 \le f_i \\
\begin{cases} V_g^{i-1(m)} \leftarrow V_g^{i-1}(f_0) \\ V_g^{i(m)} \leftarrow V_g^{i}(f_0) \quad /\ \textit{initial voltages at } f_{i+1} \le f_0 \le f_i \\ V_g^{i+1(m)} \leftarrow V_g^{i+1}(f_0) \end{cases} \\
/^*\ \textit{inner} - \textit{tier} \\
\hline
\textit{solve}: \mathbf{E}(\mathbf{X}, A, f, V_g^{i-1}, V_g^i, V_g^{i+1}) = \mathbf{0}\ \ //\text{HB } \textit{synthesis equations on } V_g^{(i)}, V_g^{(i+1)}, V_g^{(i-1)} \\
\Pi_o^{(1)} = dBm(V_o^{(1)})\,/^*\textit{evaluate}\ \text{the output power level (fundamental freq)} \\
Y_p^{(M)}(f) \leftarrow \dfrac{I_p^{1(M)}}{V_p^{1(M)}} = \dfrac{I_{p,\mathbf{V}}^{1(M)}(A(f), V_g^{i-1}(f), V_g^i(f), V_g^{i+1}(f))}{A(f)}\ /\ \textit{probe}\ \text{admittance} \\
\hline
/^*\ \textit{outer} - \textit{tier} \\
\hline
\textit{find}\ (A, V_g^{i-1}, V_g^i, V_g^{i+1}) \in \mathcal{A} \times \mathcal{V}^3\ \textit{through optimization such that}: \\
\left|\mathrm{Re}\left(Y_p^{(M)}\left(A(f), V_g^{i-1}(f), V_g^i(f), V_g^{i+1}(f)\right)\right)\right| < \varepsilon \\
\left|\mathrm{Im}(Y_p^{(M)}(A_o, f_o, V_g^{(i-1)}, V_g^{(i)}, V_g^{(i+1)}))\right| < \varepsilon \qquad /\ \textit{non} - \textit{perturbation conditions} \\
\qquad\qquad\qquad\qquad\qquad\qquad\qquad\qquad\qquad\qquad (\varepsilon\ \text{represents the tolerance}) \\
P_{\min} \le \Pi_o^{(1)} \le P_{\max} \qquad /\ \text{constraint on output power at the fundamental} \\
\hline
\end{array}
$$

$$
\begin{array}{l}
\textit{switch}[f^{(m)}]\ \{ \\
\qquad \textit{case}\,(f^{(m)} = f_{i+1}): \\
\qquad\qquad f \leftarrow f + \Delta f\ /\ \textit{march forward}\,(\textit{from } f_{i+1} \textit{ to } f_i) \\
\qquad \textit{case}\,(f^{(m)} = f_i): \\
\qquad\qquad f \leftarrow f - \Delta f\ /\ \textit{sweep backward}\ (\textit{from } f_i \textit{ down to } f_{i+1}) \\
\qquad \textit{else}: \\
\qquad\qquad\qquad f^{(m)} \leftarrow f_k \\
\qquad\qquad\qquad \textit{apply}\ \ \mathbf{O} - \mathbf{FSA}\ \textit{in}\ [f_{i+1}, f_k[\cup]f_k, f_i] \\
\qquad\qquad\qquad \} \\
m \leftarrow m+1 \quad \Rightarrow \quad \text{update} \begin{cases} A_o(f^{(m)}) \leftarrow A_o(f^{(m+1)}) \\ V_g^i(f^{(m)}) \leftarrow V_g^i(f^{(m+1)}) \\ V_g^{i+1}(f^{(m)}) \leftarrow V_g^{i+1}(f^{(m+1)}) \end{cases} \\
\qquad\qquad\qquad \}
\end{array}
\qquad (6.8)
$$

V – SPA. Voltage- Swept Parametric Analysis

for $i = 1,2,3$

$/initial$ set-up

$\mathcal{V} = [V_{\min}, V_{\max}] / voltage\ range$

$\mathbf{V} = [V_g^1, V_g^2, V_g^3, V_g^4] \in \mathcal{V}^4$ / *four tuning controls*

$V_g^i \leftarrow U \in \mathcal{V}\ (U \geq V_{on})$;

$V_g^{i+1} \leftarrow W \in \mathcal{V}\ (W \geq V_{on})$ / active sections

if$(j \neq i, j \neq i+1)$

$V_g^j \leftarrow V_{off}\ (= -1V)$ / switched-off sections

$/define\ the\ ranges\ for\ the\ unknowns\ (A, f)$

$A \in [A_{\min}, A_{\max}] = \mathcal{A}$

$f \in [f_{\min}, f_{\max}] = \mathcal{F}$

introduce *the probe at a measurement node M*

$p(t) = A \sin 2\pi ft$ / * large signal probe $(\varphi = 0)$

introduce a *current meter at node M to evaluate* $I_{p,\mathbf{V}}^{1,M}(A, f)$

for $W = \{V_0, V_1, ..., V_k, V_{k+1}, ...V_r\} \subseteq \mathcal{V}\ (k = 0,1,...,r)\{$

$k \leftarrow 0$

$W^{(k)} \leftarrow V_0$

for $U = \{V_0, V_1, ..., V_m, V_{m+1}, ...V_s\} \subseteq \mathcal{V}\ (m = 0,1,...,s)$

{

$m \leftarrow 0$

$U^{(m)} \leftarrow V_0$

$/ * inner - tier$

$\mathbf{E}(\mathbf{X}, A, f, U^{(m)}, W^{(k)}) = \mathbf{0}$ //HB *equations* (*depending on* U, W)

$Y_{p,\mathbf{V}}^{(M)}(A, f) \leftarrow \dfrac{I_{p,\mathbf{V}}^{1(M)}(A, f)}{V_{p,\mathbf{V}}^{1(M)}} = \dfrac{I_{p,\mathbf{V}}^{1(M)}(A, f)}{A}$ / **evaluate* the probe admittance

find $A(U,W), f(U,W)\ \in \mathcal{A} \times \mathcal{F}$ *such that*:

$/ * outer - tier$

$\left|\mathrm{Re}(Y_{p,\mathbf{V}}^{(M)}(A, f))\right| < \varepsilon$

$\left|\mathrm{Im}(Y_{p,\mathbf{V}}^{(M)}(A, f))\right| < \varepsilon$ $/non - perturbation\ conditions$

$/as\ optimization\ goals$ (ε represents the accuracy)

update $\begin{cases} A_o \leftarrow A_o(U^{(m)}, W^{(k)}) \\ f_o \leftarrow f_o(U^{(m)}, W^{(k)}) \end{cases}$

$m \leftarrow m + 1$

$U^{(m)} \leftarrow V_{m+1}$

}

$k \leftarrow k + 1$

$W^{(k)} \leftarrow V_{k+1}$ }

(6.9)

6.2.1 NONLINEAR ANALYSIS OF THE DISCRETE RESONANCES. PARAMETRIC ANALYSIS OF THE OSCILLATION FREQUENCIES.

As outlined in the previous section, the DVCO nonlinear analysis begins with the *discrete oscillation frequencies* nonlinear evaluation, obtained by turning on each DVCO section at a time, and letting the remaining sections turned off. For each active section, biasing gate voltages are initialized with the same values used for the preliminary linear analysis. The active section is biased with $V_{g,act}$ = - 0.1 V, while the remaining sections are interdicted at ($V_{g,off}$ = -1V); the drain voltage is kept fixed at V_{DD}= +2V. The *i*-th *section* ($\mathbf{T}_i$) *oscillation frequency linear estimate* $f_{lin}^{(i)}$, found by *visual inspection of the probe admittance* (as described in § 6.5.1, corresponding to the resonance condition $\mathrm{Im}(Y_p(f_{lin}^{(i)}))=0$) is in the first instance set as a candidate value of the actual oscillation frequency, initializing the *large-signal probe frequency*. Therefore the scheme is the following:

$$\begin{cases} V_{g,act}^{(i)} = -0.1V, \ i = 1,...,4 \\ V_{g,off}^{(k)} = -1V, \ k = 1,...,4 \end{cases} (i \neq k) \Rightarrow \hat{f}_o^{(i)} = f_{lin}^{(i)} \tag{6.10}$$

Using the Auxiliary Generator technique presented in §4.1, and running a double tier optimization routine to fulfill the zero admittance probe condition, the four oscillating solutions are obtained.

Active Device $\mathbf{T}_i$	Oscillation Frequencies, f_i (GHz)	Output Power $P_{out}^{(1)}$ (dBm)
$\mathbf{T}_1$	1.791	3.04
$\mathbf{T}_2$	1.326	4.73
$\mathbf{T}_3$	1.963*	5.72
$\mathbf{T}_4$	1.696*	5.87

TABLE 6-3. Oscillation Frequencies and relative power level at the fundamental for the individual resonances.

Nevertheless, due to the very nature of the Harmonic Balance method, the existence of an oscillatory solution is no guarantee for its stability (*physical observability*) which should be checked with different methods, like *time domain* or properly initialized *envelope transient simulations* [16]. Moreover, it is not uncommon in the reverse DVCO, to possess multiple observable solutions which differ (in some cases greatly) for their power spectral profile. Therefore, it could happen that distinct probe amplitude candidate values *A'*, *A''*, *A'''*… *give rise* (as the output of the optimization process) *to distinct solutions having the same fundamental oscillation frequency*. This ambiguity [6, 7], could also be turned into an opportunity for selecting the output waveform which present some desirable features, such as an higher output power at the fundamental, lower phase noise, higher harmonic rejection. In the following discussion, it is assumed that the output waveforms have already been selected according to additional design goals, in order to deal with *unique* values of probe amplitudes associated to the distinct resonant frequencies.

The result of nonlinear analysis is shown in Fig. 6.5. It is seen that the activation of the two stages triggers oscillation having a frequency close to the one obtained by linear analysis with a very good rejection ratio of higher harmonics. However, in the case of the activation of the last two sections (T_3 and T_4) spurious resonances are excited, giving two contributions that fall within the highest end of the tuning bandwidth[22] The discrete resonances found are summarized in the Table III.6, with the spurious ones highlighted.

[22] Spurious oscillations might be triggered due to undesired feedback paths, to sub-optimal matching conditions, or to in-band spurious oscillation caused by active devices instabilities. In fact, recalling the distributed amplifier theory introduced in §2.4 (chapter II), in the output line two waves are travelling in opposite direction. The forward travelling wave superimpose with the backward travelling ones (responsible of the oscillation onset), creating an interfering pattern which could cause the appearance of spurious resonances. An empirical condition stated in [7] sets a minimum matching of 20 dB both in the drain and the gate line in order to avoid parasitic oscillations.

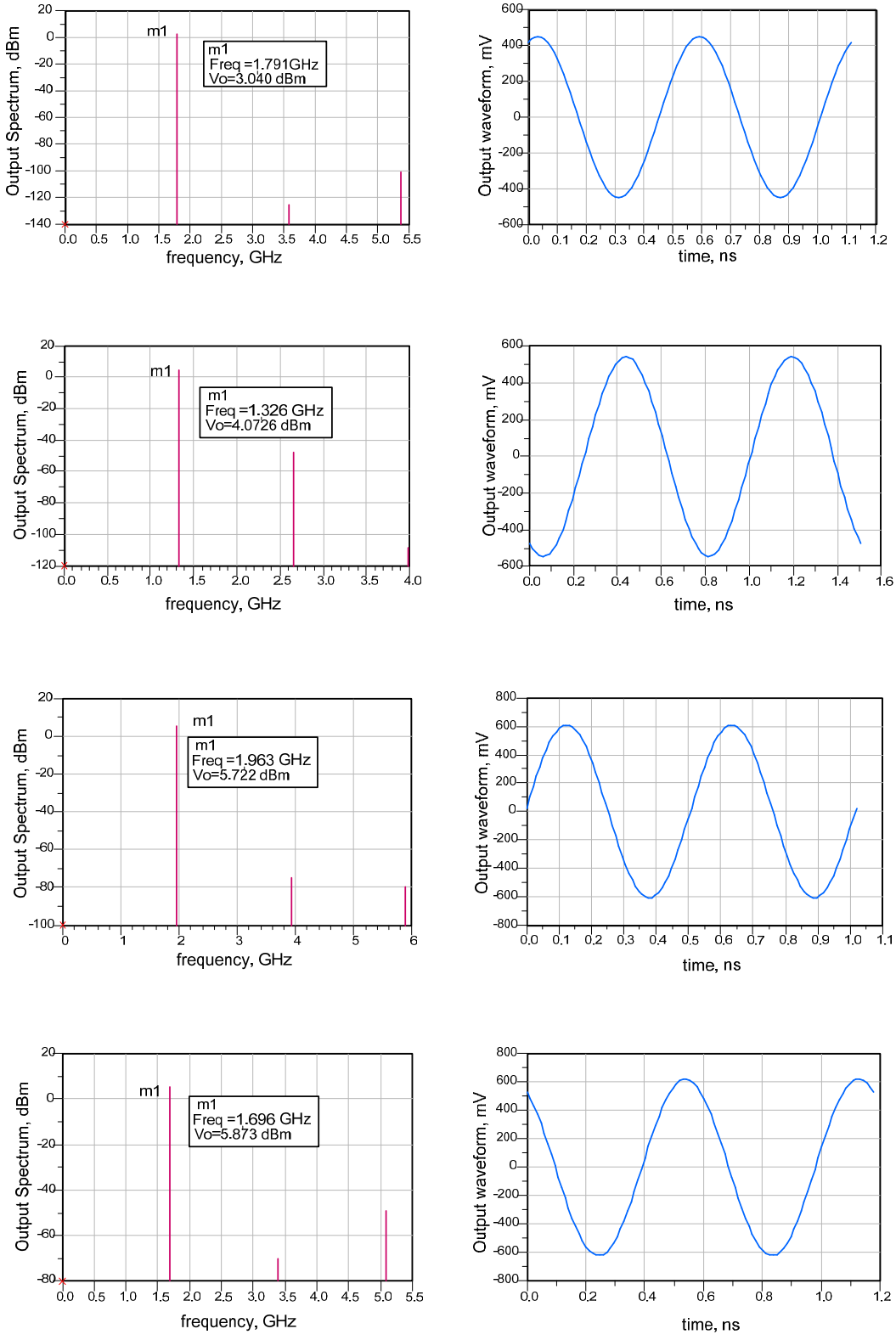

FIGURE 6-5. Output Power Spectra obtained using Auxiliary Generator drive Harmonic Balance simulations, at four different bias settings, relative to each section individual activation, with the remaining ones kept switched off. The representation is given both in the frequency domain (power spectrum) and in the time domain (waveforms). The last two oscillation frequencies have higher values than expected and should be quenched by introducing additional elements in the original schematic.

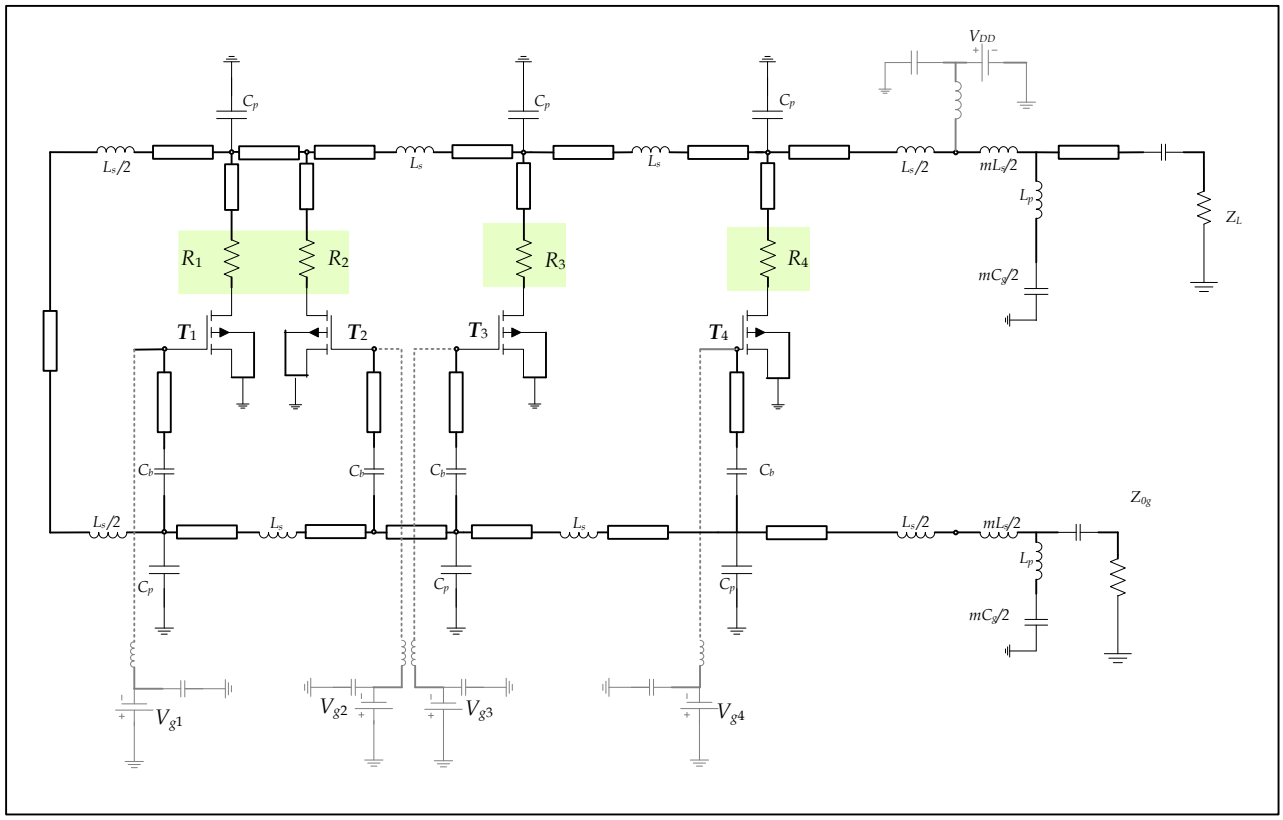

FIGURE 6-6. Introducing discrete resistors to avoid the onset of parasitic oscillations.

Therefore, the schematic needs to be modified in order to avoid the onset of parasitic oscillations. To that end, four series resistors are introduced in the DVCO schematic, connected between each active device drain and the drain line (Fig. 6.6). The resistors aim at dampen potential instabilities leading to in-band or out-of-band spurious oscillation, and at the same time to reduce the DC current consumption, without compromising too much the RF efficiency. These competing requirements can be fulfilled with a synthesis technique that makes use of the algorithm shown in (6.63), in which the four resistances R_1, R_2, R_3, R_4, play the role of the generic parameters η_1, η_2,…, η_p. In order to simplify the search process, all of the resistances were constrained to have the same value. After some simulations it was found that resistance values below 25 Ω didn't ensure parasitic oscillations onset. On the other hand, for values above 25 Ω the output power decreased sensibly. For that reason, a 25 Ω resistor was placed in the schematic. The discrete resonant frequencies obtained are shown in Fig. 6.7. The discrete oscillation frequencies match perfectly their linear estimates as shown in Table IV.6. It is noticed that a certain amount of distortion (lower harmonic rejection ratio) is present when activating the last two sections (T_3, T_4) due to the different loading conditions seen by each section.

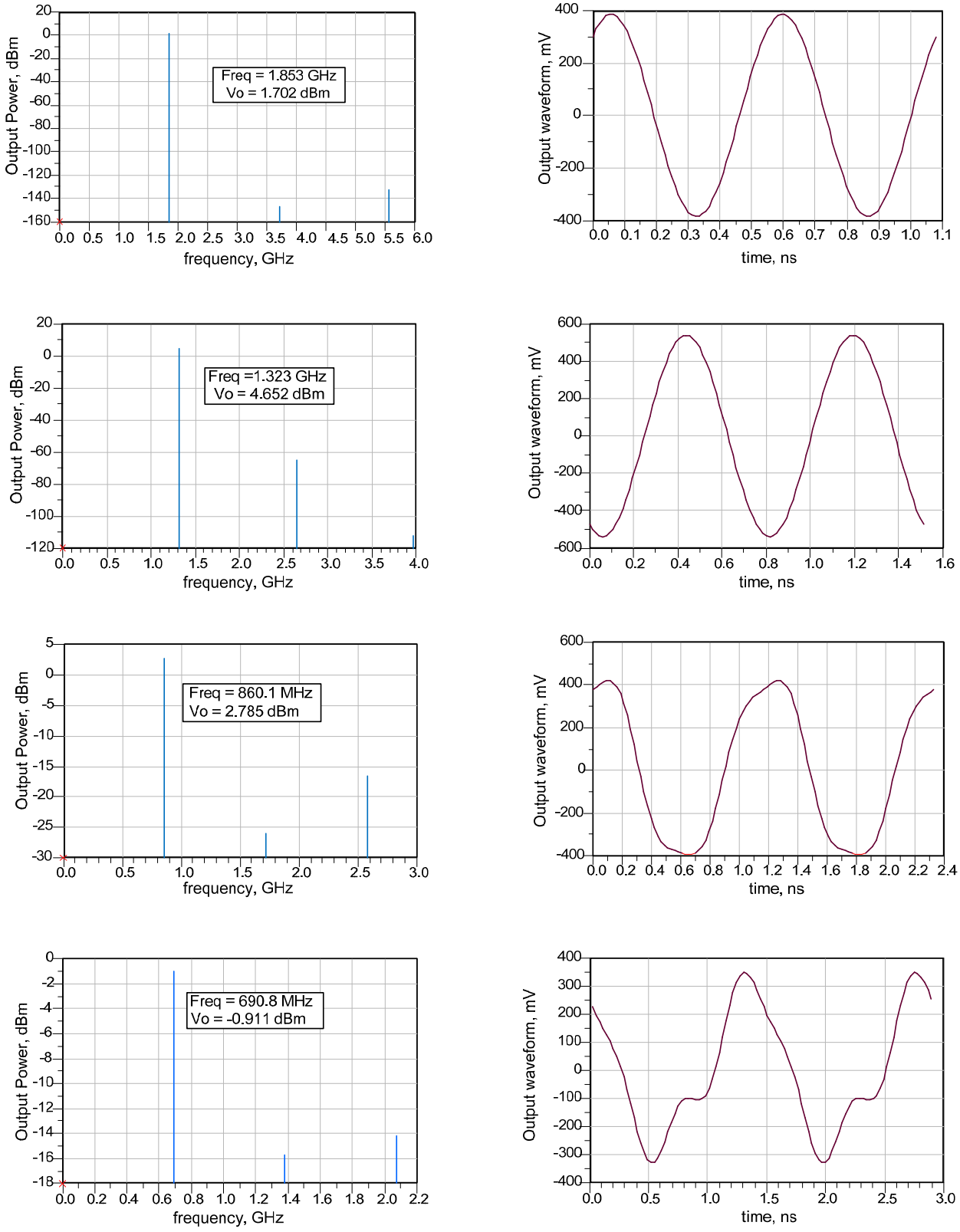

FIGURE 6-7. Modified DVCO Nonlinear analysis. The introduction of the resistors effectively removes unwanted oscillations, at the cost of worsening the harmonic rejection (increasing the waveform distortion).

Active Device $\mathbf{T}_i$	Oscillation Frequencies (linear estimates) $f_{i,\text{lin}}$ (GHz)	Oscillation Frequencies HB (R =25 Ω) f_i (GHz)	Output Power at the fundamental (R=25 Ω) P_{out} (dBm)
$\mathbf{T}_1$	1.8	1.853	1.7
$\mathbf{T}_2$	1.31	1.323	4.7
$\mathbf{T}_3$	0.860 (parasitic: 1.99 GHz)	0.86	2.8
$\mathbf{T}_4$	0.71 (parasitic:1.7 GHz)	0.69	-0.9

TABLE 6-4. Oscillation Frequencies and Power level comparison between the linear analysis result and the nonlinear simulation, when a 25 W resistor is connected in series to each drain.

After the individual resonances had been obtained, parametric analysis with respect to the basic constant-k filter cell inductance L_s and capacitance C_p was performed [18] to the aim of finding out an optimal distribution of the four discrete oscillations along the tuning bandwidth. Basically, the scheme used a double-iterated process with two nested cycles, in which for a given value of C_p (in the range [1 pF, 3 pF]) the inductance L_s is swept in the range [1 nH, 5 nH], according to the algorithm detailed in (6.6). The evolution of the oscillation frequencies for the individual resonances associated to the activation of the i-th device $\boldsymbol{T}_i$, are plotted as a function of inductance L_s for three different values of C_p (namely 1.2 pF, 2 pF, 3.3 pF) in Fig. 6.9. From the analysis carried out emerges what can be intuitively perceived, coherently with the theory of distributed amplifiers and oscillators implemented using constant-k filter sections. For a given capacitance C_p, the discrete resonant frequencies decrease as the series inductance L_s is increased. For a fixed value of inductance L_s, increasing the capacitance C_p corresponds to shifting all the four discrete resonances towards lower values[23]. Therefore, keeping the inductance L_s at its nominal value (L_s=3.3 nH) and choosing the value C_p=1.2 pF, the band between 1 and 2 GHz is covered, with resonances at f_1=2 GHz, f_2= 1.55 GHz, f_3= 1.15 GHz, f_4=980 MHz, as shown in Fig. 6.9, attaining the highest possible oscillation frequencies for a distributed oscillator with discrete inductors and capacitors[24].

[23] At a higher capacitance values (C_p= 3 pF) the variation of the four oscillation frequencies is more uniform than the one corresponding to lower frequency values. This might be ascribed at a lowpass filtering of the shunt capacitor

[24] The DVCO implemented with lumped inductors and capacitors (forming ladder networks or artificial transmission lines) suffers from intrinsic limitations due to lumped elements parasitics (a real capacitor present spurious inductance and additional resistance due to the losses, and similarly for an inductor) which are component dependent. Moreover, commercial lumped inductors and capacitors are produced and sold only at some specific (discrete) values. When the theoretical value of a capacitance or inductance doesn't match perfectly with the nominal capacitance/inductance of a real component , components whose nominal parameters (inductance/capacitance) are the closest available to the theoretical ones have been used. However, this approximation introduces an unavoidable mismatch.

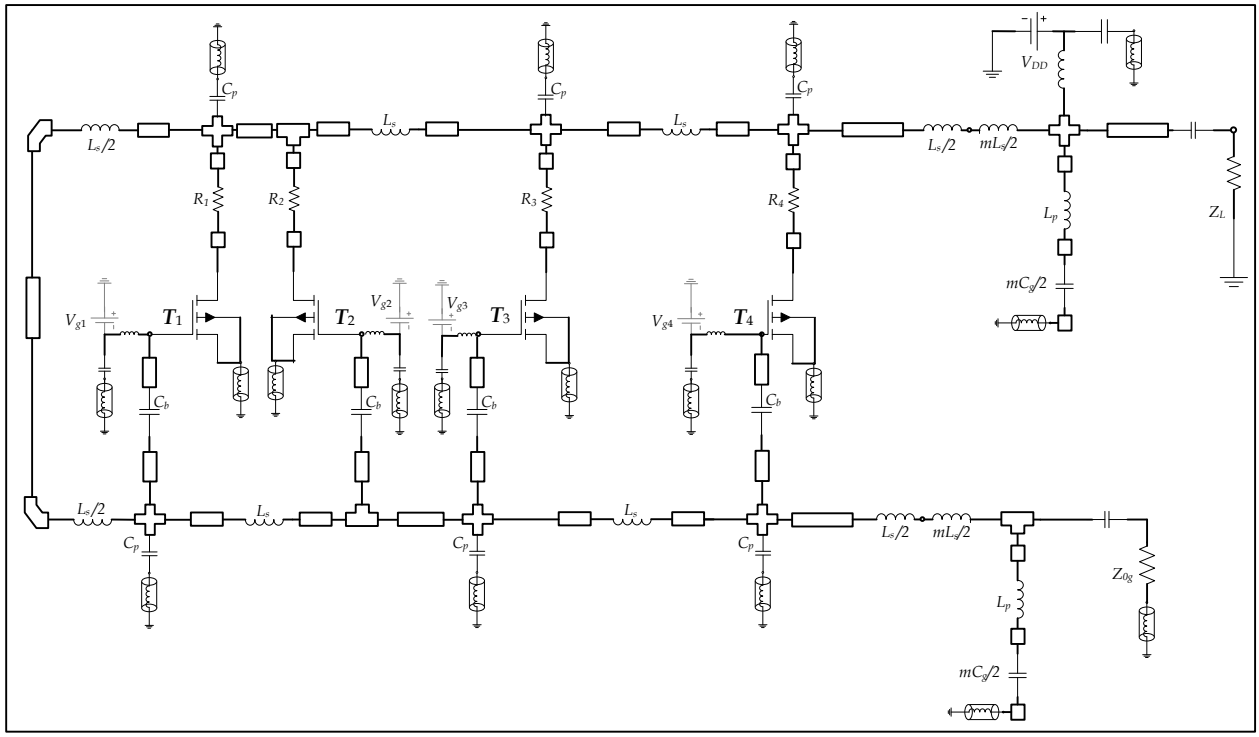

FIGURE 6-8. Detailed DVCO schematic.

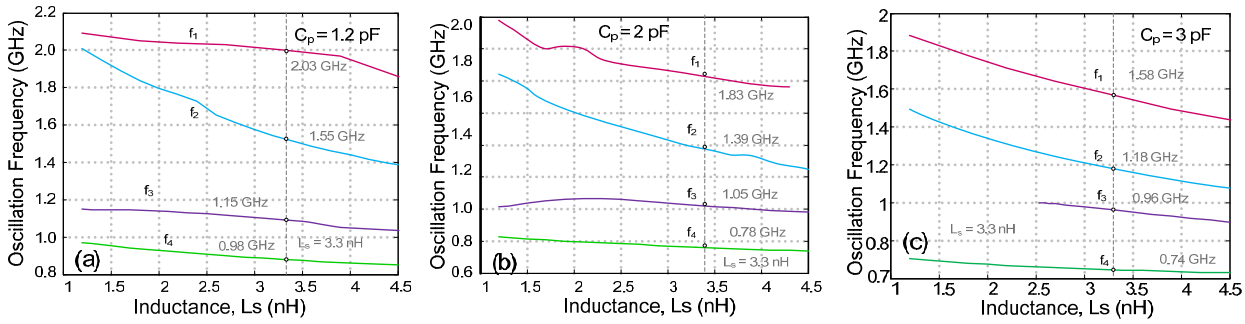

FIGURE 6-9. Parametric Solutions curves, illustrating the dependencies on the inductance (L_s) and capacitance (C_p) of the basic constant-*k* filter section for the four discrete resonances characterized by their frequencies f_1, f_2, f_3, f_4. Each graph shows the evolution of the four oscillating solutions when inductance is varied in the rage 1nH—4.5 nH, keeping the capacitance value constant [18]

6.3 Nonlinear Analysis of the Tuning Function. Stability Analysis of the Oscillation Frequencies

After having found the discrete resonances, it is possible to study the DVCO tuning function, expressing the dependence on the oscillation frequency on the tuning voltages. Recalling the DVCO basic tuning algorithm, the gate bias voltages of two adjacent sections (V_g^S; V_g^{S+1}) are varied in a complementary way (*e.g.* increasing V_g^S, and simultaneously decreasing V_g^{S+1}) to produce an oscillation whose frequency shifts continuously in the range [f_{S+1} , f_S] where f_{S+1} , f_S are the oscillation frequencies when the sections $\boldsymbol{T}_{s+1}$, $\boldsymbol{T}_s$ (s=1,…,*N*) are activated *separately* (see section §6.2

and [6—12] [15]). As a result, the whole tuning band for an N stage DVCO can be thought as the union of the N-1 sub-intervals, termed *frequency zones* according to the following scheme, which shows the three sub-bands in the case N= 4:

$$\begin{aligned} &B = \bigcup_{s=1,\ldots,N-1} B_s = \bigcup_{s=1,\ldots,N-1} [f_{s+1}, f_s] = [f_N, f_1] \Rightarrow \\ &B = B_1 \cup B_2 \cup B_3 = [f_4, f_1] \ \ (\textit{in case } N = 4) \\ &\textit{where}: \\ &B_1 = [f_2, f_1] \ \ (\textit{highest}) \\ &B_2 = [f_3, f_2] \ \ (\textit{central}) \\ &B_3 = [f_4, f_3] \ \ (\textit{lowest}) \end{aligned} \tag{6.11}$$

The DVCO tuning function can thus be iteratively analyzed in each sub-band B_s, in order to get (for the case N=4) three *functions defined implicitly*:

$$\begin{cases} \chi_1(V_g^1, V_g^2, f)_{f\in B_1} = 0 \\ \vdots \\ \chi_s(V_g^s, V_g^{s+1}, f)_{f\in B_s} = 0 \\ \vdots \\ \chi_{N-1}(V_g^{N-1}, V_g^N, f)_{f\in B_{N-1}} = 0 \end{cases} \Rightarrow (\text{in case } N = 4) \quad \begin{cases} \chi_1(V_g^1, V_g^2, f)_{f\in B_1} = 0 \\ \chi_2(V_g^2, V_g^3, f)_{f\in B_2} = 0 \\ \chi_3(V_g^3, V_g^4, f)_{f\in B_3} = 0 \end{cases} \tag{6.12}$$

such that when a pair of voltages (V_g^s; V_g^{s+1}) is altered to obtain a shift in the oscillation frequency across the s-th frequency zone B_s, the functions $\chi_s(V_g^s, V_g^{s+1}, f)=0$ *model the oscillator tuning locally.* Provided that (6.12) establish a relationship among three variables (V_g^s; V_g^{s+1}; f), there are multiple possibilities to get an *explicit representation* of the tuning curves from a single implicit function $\chi_s(V_g^s, V_g^{s+1}, f)=0$, s=1,…,N. In particular, two of them have been considered [6—12] [15,18]:

a) *frequency dependent curves* $V_g^s(f)$, $V_g^{s+1}(f)$ tracking separately the gate bias voltages as the oscillation frequency is varied in the range B_s = [f_{s+1}, f_s]

b) *voltage-dependent curves*, expressing the dependence of the oscillation frequency upon the gate bias voltage V_g^s, regarding as a parameter the subsequent section gate voltage V_g^{s+1}, and thus *obtaining a family of curves* in the plane *(f, V_g^s) labeled in* V_g^{s+1};

The two approaches are shown in (6.13). In particular, the representation in terms of voltage dependent curves provides precise information about the stability of the solutions at each frequency zone as reported in [15,18].

$$
\begin{aligned}
&f \in B_s = [f_{s+1}, f_s];\ V_g^s, V_g^{s+1} \in \boldsymbol{\mathcal{V}} = [V_{\min}, V_{\max}];\ s = 1, \ldots, N-1 \\
&a)\ \text{frequency-dependent curves} \\
&\chi_s\left(V_g^s, V_g^{s+1}, f\right) = 0 \Rightarrow \chi_s\left(V_g^s(f), V_g^{s+1}(f)\right) = 0 \Rightarrow \quad V_g^s = V_s(f)_{f \in B_s},\ V_g^{s+1} = V_{s+1}(f)_{f \in B_s} \\
&b)\ \text{voltage-dependent curves} \\
&\chi_s\left(V_g^s, V_g^{s+1}, f\right) = 0 \Rightarrow f = \Xi_s\left(V_g^s, V_g^{s+1}\right) = \xi_s\left(V_g^s\right)_{V_g^{s+1} \in \boldsymbol{\mathcal{V}}}
\end{aligned}
\tag{6.13}
$$

In both cases, the tuning curves have been found by means of parametric swept harmonic balance simulations [19] choosing just the auxiliary probe's frequency (case *a*) or the adjacent sections gate bias voltage (case *b*) respectively as parameters.

I. REPRESENTATION OF THE TUNING FUNCTION AS FREQUENCY DEPENDENT CURVES $V_g^s(f)$, $V_g^{s+1}(f)$.

Tracing the variation of the gate bias voltage with respect to frequency requires choosing one of the frequency zones B_s = [f_{s+1}, f_s] and setting the initial values for the gate voltages of the active sections T_s ,T_{s+1} at first. Essentially, considered that the frequency edges of the zone B_s are simply the *discrete resonances frequencies* (found when each section T_s , T_{s+1} are separately turned on) there are *three options to scan the frequency zone* B_s:

i. setting V_g^s=V_{off} ; V_g^{s+1}=V_{on} (V_q=V_{off} for $q \neq s,s+1$), initialize the auxiliary probe's amplitude and frequency values with the ones corresponding to the oscillatory solution at $f = f_{s+1}$, A=A_{s+1} *reusing the information obtained from the knowledge of the (s+1)-th resonance output spectrum*. Then the frequency of the auxiliary probe needs to be swept *forward* from f_{s+1} to f_s to cover the entire frequency zone B_s;

ii. setting V_g^s=V_{on} ; V_g^{s+1}=V_{off} (V_q=V_{off} for $q \neq s,s+1$), initialize the auxiliary probe's amplitude and frequency values with the ones corresponding to the oscillatory solution at $f = f_s$, A=A_s *reusing the information obtained from the knowledge of the s-th resonance output spectrum*. Then the frequency of the auxiliary probe needs to be swept *backward* from f_s to f_{s+1} to cover the entire frequency zone B_s;

iii. finding the solution at some intermediate frequency $f_{s+1} \leq f_p \leq f_s$ corresponding to a certain probe amplitude A_p and to V_g^s=V′; V_g^{s+1}=V′′ (with $V_{on} \leq V_g^s$, $V_g^{s+1} \leq V_{off}$, V_q=V_{off} for $q \neq s,s+1$) with the method exposed in section 6.4 (**SRA** algorithm). Then starting from the oscillatory solution at f_p the probe frequency needs to be swept *partly backward* from f_p down to f_{s+1} and *partly forward* from f_p to f_s.

The first two options are easier to implement, in that they are based on previous knowledge of the output spectra of the discrete resonances. However, given that a frequency zone could hundreds of MHz wide[25] and that the DVCO presents stiff nonlinearities it is usually problematic

[25] In the implemented example, the difference in frequency between the first two resonances it is 500 GHz approximately.

covering a frequency zone with a unique sweep with a fixed step-length[26] Δf. Therefore, it is often preferable to use the procedure (iii). After having obtained a solution for a specific value of frequency $f_{s+1} \le f_p \le f_s$, the probe frequency is swept from in each direction (backward down to f_{s+1}, and forward to f_s). When convergence isn't achieved or is problematic, the step-length is reduced (e.g. halved) and the simulation restarted. By doing so, let us suppose that a sub interval $[f', f'']\subset[f_{s+1}, f_s]$ is covered. Then the same procedure can be recursively applied to obtain the tuning plots in $[f_{s+1}, f']$ and in $[f'', f_s]$, making sure that the probe amplitude and the gate bias voltage values at the edges at the sub-intervals are properly initialized. By carefully using the *step-length adjustment* for Δf, and *bidirectional frequency sweeps across subzones* (subintervals of B_s) the tuning curves can be obtained with a high degree of accuracy[27] invoking the two tier HB procedure introduced in chapter IV and sketched in (6.14)—(6.16) as the probe frequency scans the desired range, considering the gate bias voltages V_g^s, V_g^{s+1} as synthesis parameters[28]. The complete algorithm is shown in the charts below.

FFS. **F***orward* **F***requency* **S***weep in* $B_s = [f_{s+1}, f_s]$
/ *initialization at* $f = f_{s+1}$

$V_g^{s+1} \leftarrow U(f_{s+1})$ / reusing the solution at $f = f_{s+1}$
$V_g^{s} \leftarrow W(f_{s+1})$
$A \leftarrow A(f_{s+1})$
choose n_f / number of frequency points to be analyzed
set step-lenght $\Delta f \leftarrow \dfrac{(f_s - f_{s+1})}{n_f}$

/ forward sweep in $[f_{s+1}, f_s]$

for $f = f_{s+1}$ *to* f_s {
solve **HBE.1**
$f \leftarrow f + \Delta f$
}

(6.14)

[26] Experience acquired from extensive HB tuning simulations seems to indicate that a major source of convergence failure is represented by the *sharp voltage transitions, when the voltage* V_g^s goes high (low) and simultaneously the voltage V_g^{s+1} goes low (high) while observing a frequency shift from f_{s+1} *to* f_s. *In that case a current on the branch of the* T_s *section must keep increasing up to tens of mA* (decreasing to a few μA) and simultaneously *a current on the branch of the* T_{s+1} *section must keep decreasing down a few μA* (increasing to tens of mA). In such circumstances, the difference in scale of the currents in two contiguous branch may hinder the convergence of the HB solution. Depending on the condition numbers of the matrices involved in the iterative computations of the HB system of equation, achieving the current balance **E(.)=0** might require many attempts, in which the step-length and the starting point needs to be carefully selected.

[27] The accuracy is measured by the distance between the achieved and desired goals, expressed by an error function. An intrinsic indicator could be represented by the residual current flowing through the harmonic probe (theoretically zero in the steady state oscillating regime) which should reach the lowest possible values. Good accuracy is then obtained with and error function norms better a tenth billionth (EF<$1*10^{-10}$) and with probe currents on the order of tens of microamperes.

[28] Although continuous solutions curves $V_g^s(f)$, $V_g^{s+1}(f)$ are found *that wouldn't necessarily imply that the output power vary in a continuous manner.* This fact is closely related to the existence of multiple solutions indexed with the same frequency which differ in terms of output power (discussion on 6.5.2).

BFS. **B***ackward* **F***requency* **S***weep in* $B_s = [f_{s+1}, f_s]$

$V_g^{s+1} \leftarrow U(f_s)$ / reusing the solution at $f = f_s$
$V_g^s \leftarrow W(f_s)$
$A \leftarrow A(f_s)$
choose $n_{\mathcal{F}}$ / number of frequency points to be analyzed
set step-lenght $\Delta f \leftarrow \dfrac{(f_s - f_{s+1})}{n_{\mathcal{F}}}$

/ backward sweep in $[f_{s+1}, f_s]$

for $f = f_s$ *down to* f_{s+1} {
solve **HBE.1**
$f \leftarrow f - \Delta f$
}

(6.15)

TFS. **T***wo – way* **F***requency* **S***weep in* $B_s = [f_{s+1}, f_s]$ (bidirectional sweep)
/ *initialization at an* intermediate frequency $f_{s+1} \le f_p \le f_s$
/ *find a solution at* $f = f_p \in [f_{s+1}, f_s]$ *applying* single frequency analysis

$V_g^s \leftarrow U(f_p)$
$V_g^{s+1} \leftarrow W(f_p)$
$A \leftarrow A(f_p)$

/ *split* $B_s = [f_{s+1}, f_s]$ *in two* subintervals
set $\mathcal{B}_p^s =]f_p, f_s]$
set $\mathcal{B}_{s+1}^p = [f_{s+1}, f_p[$ / $B_s = \mathcal{B}_{s+1}^p \cup \mathcal{B}_p^s \cup \{f_p\}$
/ bidirectional sweep *in* $[f_{s+1}, f_s]$
apply **FFS** *in* $\mathcal{B}_p^s$
apply **BFS** *in* $\mathcal{B}_{s+1}^p$
}

(6.16)

HBE.1

/ HB for gate voltages and probe amplitude optimization, fixed frequency

$f \in \mathcal{F} = [f_{\min}, f_{\max}]$ / *analysis range for the frequency*

$A \in \mathcal{A} = [A_{\min}, A_{\max}]$ / *search range for the amplitude*

$V_g^i \in \mathcal{V} = [V_{\min}, V_{\max}]$ / *search range for the voltages*

$\mathbf{V} = [V_g^1, V_g^2, V_g^3, V_g^4] \in \mathcal{V}^4$ / *tuning controls*

$[V_g^s, V_g^{s+1}] \leftarrow [u, w] = \mathbf{v} \in \mathcal{V}^2$ / voltages being analyzed

set max *iteration number* $N_{\max}$

set max *harmonic order* N_h

set tolerance ε

/ *find an oscillating solution described by* $\{A(f), \mathbf{v}(f)\} \in \mathcal{A} \times \mathcal{V}^2, f \in \mathcal{F}$

introduce the large signal harmonic probe *at a measurement node M*

$p(t) = A\sin(2\pi ft)$ / * large signal probe $(\varphi = 0)$

introduce a *current meter at node M to evaluate* $I_{p,\mathbf{V}}^{1,M}(A, f)$

$n \leftarrow 0$

initialize $(A^{(0)}, u^{(0)}, w^{(0)}) \leftarrow (A(f), V_g^s(f), V_g^{s+1}(f))_{f \in \mathcal{F}}$

set max *iteration number* $N_{\max}$

do{

/ * *inner – tier*

solve : $\mathbf{E}(\mathbf{X}(f), A(f), \mathbf{v}(f)) = \mathbf{0}$ / HB *analysis equations* $(f \in \mathcal{F})$

$$evaluate: Y_p^M(A(f), \mathbf{v}(f)) \leftarrow \frac{I_p^{1,M}(A(f), \mathbf{v}(f))}{V_p^{1,M}} = \frac{I_p^{1,M}(A(f), \mathbf{v}(f))}{A(f)} \ (f \in \mathcal{F})$$

/ * *outer – tier*

$$solve: \left|\mathbf{Y}(A(f), \mathbf{v}(f), f)\right| < \varepsilon \Rightarrow \begin{cases} \underset{\substack{A \in \mathcal{A} \\ (V_g^s, V_g^{s+1}) \in \mathcal{V}^2}}{\arg\min}\, \mathbf{Y}\left(A(f), V_g^s(f), V_g^{s+1}(f)\right)_{f \in \mathcal{F}} = -\varepsilon \\ \underset{\substack{A \in \mathcal{A} \\ (V_g^s, V_g^{s+1}) \in \mathcal{V}^2}}{\arg\max}\, \mathbf{Y}\left(A(f), V_g^s(f), V_g^{s+1}(f)\right)_{f \in \mathcal{F}} = \varepsilon \end{cases} \quad (\varepsilon = 1 \cdot 10^{-18})$$

with $\mathbf{Y}(\cdot) = \left[\operatorname{Re} Y_{p,\mathbf{u}}^M(\cdot), \operatorname{Im} Y_{p,\mathbf{u}}^M(\cdot)\right]^T$

$$if\left(\left\|\mathbf{E}(\mathbf{X}, A(f), V_g^s(f), V_g^{s+1}(f))\Big|_{\substack{V_g^s \in \mathcal{V} \\ V_g^{s+1} \in \mathcal{V}}}\right\| > K\right)\{ \ / \text{ in case of convergence failure}$$

$\Delta f \leftarrow \frac{\Delta f}{2}$ / *reduce step – lenght*;

$\varepsilon \leftarrow \varepsilon + \Delta\varepsilon$ / *reduce the tolerance* $(1 \cdot 10^{-18} \le \varepsilon \le 1 \cdot 10^{-12})$

$N_h --$ / *decrease the harmonic order*

$N_{\max} ++$ / *increase the iteration number*

apply bidirectional sweep **TFS**

starting from a different frequency $f_q \in \mathcal{F}$ }

$n \leftarrow n + 1$

update: $(A^{(n)}, u^{(n)}, w^{(n)}) \leftarrow (A^{(n+1)}, u^{(n+1)}, w^{(n+1)})$,

}

until $\left(\left(\left|\mathbf{Y}(A(f), \mathbf{u}(f), f)\right| > \varepsilon\right) \vee (n = N_{\max})\right)$ (6.17)

The results for both the tuning curves and the output power at the fundamental harmonic are shown in the two graphs below. The admissible range for the voltages has been chosen to be

the interval[29] $\mathcal{V}$=]-1V, 0V[while the frequency zones have been selected according to the four discrete frequencies[30]

Frequency Zones B_s	**Active Gate Voltages** (V_g^{s+1}, V_g^s)
B_3=[0.8 GHz, 1.15 GHz]	(V_g^4, V_g^3)
B_2=[1.15 GHz, 1.55 GHz]	(V_g^3, V_g^2)
B_1=[1.55 GHz, 2 GHz]	(V_g^2, V_g^1)

TABLE 6-5. Frequency zone definition and active voltage pairs

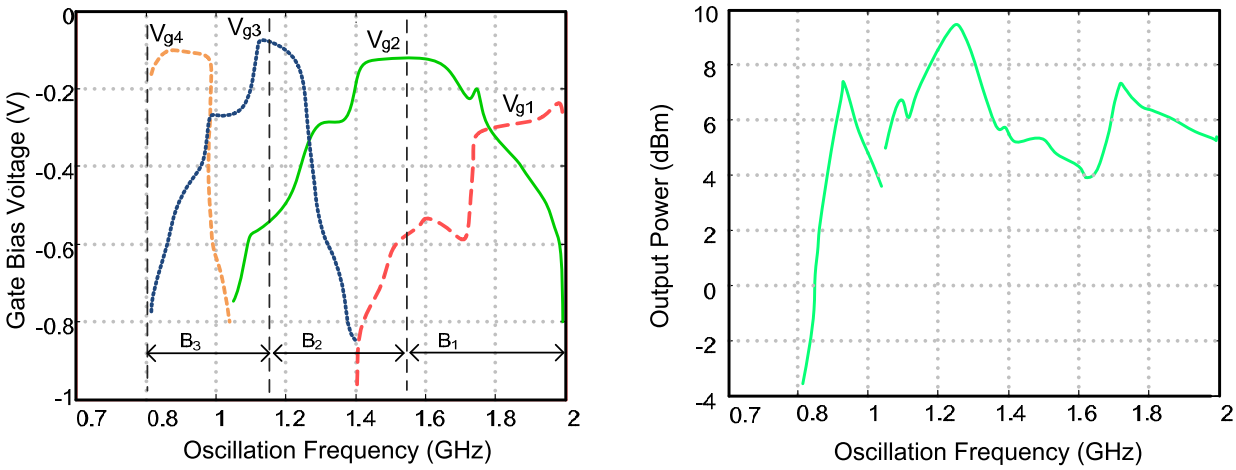

FIGURE 6-10. (left) Tuning graphs, [12, 15] illustrating the voltage settings needed to synthesize an oscillation whose frequency is comprised in the range 0.8 GHz—2 GHz. (right) Output power across the tuning range.

It is seen that the Harmonic Balance simulations confirms what had been found out by linear techniques described earlier and in [20]. In particular, it is noticed that the tuning voltages need to be varied in a *complementary manner* in order *to cover a given frequency zone* . However, contrarily to the description provided by the authors in [6—7], *the tuning voltages variation is quite nonlinear* and characterized by sharp and abrupt transition between the active/interdiction bias. Moreover the tuning function *is hardly symmetrical* and *gives rise to discontinuities in the output power profile* (as highlighted in Fig. 6.10) *as a consequence of multiple coexisting solutions* obtained for different bias

[29] For a RESENAS (formerly NEC) NE3509M04 the range of gate voltages for which the device is *typically on,* is the interval]-0.5 V, 0V[

[30] The frequency sweeps have been performed across wider ranges containing each frequency zone as subintervals; they are represented in the table.

voltages settings delivering the same oscillation frequency. The output power at the fundamental frequency starts to increase above 0.8 GHz, and then ranges between 4 dBm and 9 dBm across the tuning range [1 GHz, 2 GHz].

II. REPRESENTATION OF THE TUNING FUNCTION AS VOLTAGE DEPENDENT CURVES $f = \xi_s\,(V_g^s)_{\,V_g^{s+1} \in \mathcal{V}}$

An alternative representation for the tuning curves contemplates the gate voltages (V_g^{s+1}, V_g^s), s=1, 2, 3 as independent *analysis parameters;* as their values span the admissible range $\mathcal{V}$ = [V_{min}, V_{max}] *the parametric oscillating solution* is found when both the admittance of the probe and the harmonic balance system of equations becomes null:

$$\begin{aligned} &\mathbf{Y}\left(A\left(V_g^{s+1}, V_g^s\right), f\left(V_g^{s+1}, V_g^s\right)\right) = \mathbf{0} \\ &\mathbf{H}\left(\mathbf{X}\left(V_g^{s+1}, V_g^s\right), p\left(A\left(V_g^{s+1}, V_g^s\right), f\left(V_g^{s+1}, V_g^s\right)\right)\right) = \mathbf{0} \end{aligned} \tag{6.18}$$

as the large signal probe $p(t)= A \sin(2\pi ft)$ values of amplitude and frequency as well as the other circuit variables depend now on the gate voltages relative to the s-th frequency zone. Parametric solution plots could then be drawn tracking the variation of the output oscillation frequency as one control voltage (V_g^s) is swept across $\mathcal{V}$=[V_{min}, V_{max}]= [-1V, 0V] while the other (V_g^{s+1}) takes iteratively the values $\{V_1, V_2, \ldots, V_r\} \subset \mathcal{V}$ according to the scheme introduced in (6.19) which makes use of two nested voltage sweeps. All the considerations regarding the forward sweep, backward sweep, and bidirectional sweep exposed earlier apply in this case as well, provided that the frequency variable f is substituted with one of the gate controls V_g^s. The complete algorithm is shown in (6.19) — (6.22).

$$\begin{array}{l} \textit{Voltage} - \textit{Swept Tuning Curves } f = \xi\left(V_g^s, V_g^{s+1}\right) \\ /\,\textit{obtain the osc. frequency as function of two tuning controls} \\ V_g^s \in \boldsymbol{\mathcal{V}},\ V_g^{s+1} \in \boldsymbol{\mathcal{W}} = \left\{V_1, V_2, \ldots, V_r\right\} \subset \boldsymbol{\mathcal{V}} \\ \textit{for} \quad V_g^{s+1} = V_1, V_2, \ldots, V_r \\ \qquad\qquad \textit{apply } \mathbf{FVS} \quad / \text{ forward } \textit{voltage} \text{ sweep} \\ \qquad\qquad \text{or } \mathbf{BVS} \ / \text{ backward } \textit{voltage} \text{ sweep} \\ \qquad\qquad \textit{or } \mathbf{TVS} \ / \text{ two-way voltage sweep} \end{array} \tag{6.19}$$

FVS. **F***orward* **V***oltage* **S***weep*

/ *Parametric Analysis of the solutions* (increasing V_g^s, constant V_g^{s+1})

/*initializing with a* single point solution for $V_g^{s+1} \leftarrow V_k \in \boldsymbol{\mathcal{W}}$, $V_g^s \leftarrow V_{\min}$

$$\begin{aligned} &V_g^{s+1} \leftarrow V_k \in \boldsymbol{\mathcal{W}} \\ &V_g^s \leftarrow V_{\min} \\ &A \leftarrow A_0 \in \boldsymbol{\mathcal{A}} \\ &f \leftarrow f_0 \in \boldsymbol{\mathcal{F}} \end{aligned}$$

/forward sweep for $V_g^s \in \boldsymbol{\mathcal{V}}$

for $V = V_{\min}$ *to* $V_{\max}$ {

choose $n_{\mathcal{V}}$ /number of voltage points to be analyzed

set step-lenght $\Delta V \leftarrow \dfrac{(V_{\max} - V_{\min})}{n_{\mathcal{F}}}$

solve **HBE.2**

$V \leftarrow V + \Delta V$

}

(6.20)

BVS. **B***ackward* **V***oltage* **S***weep*

/*Parametric Analysis of the solutions* (decreasing V_g^s, constant V_g^{s+1})

/*initializing with a* single point solution for $V_g^{s+1} \leftarrow V_k \in \boldsymbol{\mathcal{W}}$, $V_g^s \leftarrow V_{\max}$

$$\begin{aligned} &V_g^{s+1} \leftarrow V_k \in \boldsymbol{\mathcal{W}} \\ &V_g^s \leftarrow V_{\max} \\ &A \leftarrow A_0 \in \boldsymbol{\mathcal{A}} \\ &f \leftarrow f_0 \in \boldsymbol{\mathcal{F}} \end{aligned}$$

/backward sweep for $V_g^s \in \boldsymbol{\mathcal{V}}$

for $V = V_{\max}$ *downto* $V_{\min}$ {

choose $n_{\mathcal{V}}$ /number of voltage points to be analyzed

set step-lenght $\Delta V \leftarrow \dfrac{(V_{\max} - V_{\min})}{n_{\mathcal{F}}}$

solve **HBE.2**

$V \leftarrow V - \Delta V$

}

(6.21)

TVS. **T***wo – way* (*bidirectional*) **V***oltage* **S***weep*

/*Parametric Analysis of the solution with bidirectional sweep*

(V_g^s spans $\boldsymbol{\mathcal{V}}$ either decreasing or increasing from V_p , V_g^{s+1} is constant) {

/*initializing with a* single point solution for $V_g^{s+1} \leftarrow V_k \in \boldsymbol{\mathcal{V}}$, $V_g^s \leftarrow V_p \in$ Int($\boldsymbol{\mathcal{V}}$)

$$\begin{aligned} &V_g^{s+1} \leftarrow V_k \in \boldsymbol{\mathcal{V}} \\ &V_g^s \leftarrow V_p \in \text{Int}(\boldsymbol{\mathcal{V}}) \\ &A \leftarrow A_0 \in \boldsymbol{\mathcal{A}} \\ &f \leftarrow f_0 \in \boldsymbol{\mathcal{F}} \end{aligned}$$

/*perform* forward sweep in $[V_p, V_{\max}]$, backward sweep in $[V_{\min}, V_p]$

set $\boldsymbol{\mathcal{V}}' = [V_p, V_{\max}]$;

set $\boldsymbol{\mathcal{V}}'' = [V_{\min}, V_p]$

execute **FVS**{$\boldsymbol{\mathcal{V}}'$};

execute **BVS**{$\boldsymbol{\mathcal{V}}''$}

}

(6.22)

HBE.2

/HB Equations, at constant gate controls, optimized for probe amplitude and frequency

$V_g^{s+1} \in \boldsymbol{\mathcal{W}} = \{V_1, V_2, ..., V_r\} \subset \boldsymbol{\mathcal{V}}$ / *analysis values for the voltage* V_g^{s+1}

$V_g^s \in \boldsymbol{\mathcal{V}} = [V_{\min}, V_{\max}]$ / *analysis range for the voltage* V_g^s

$A \in \boldsymbol{\mathcal{A}} = [A_{\min}, A_{\max}]$ / *search range for the amplitude*

$f \in \boldsymbol{\mathcal{F}} = [f_{\min}, f_{\max}]$ / *search range for the frequency*

$p(t) = A\sin(2\pi ft)$ / introduce large signal harmonic probe at node M

introduce a *current meter at node M to evaluate* $I_{p,\mathbf{v}}^{1,M}(A, f)$

set max *iteration number* $N_{\max}$

set max *harmonic order* N_h

set tolerance ε

/ *find an oscillating solution described by* $A\left(V_g^s, V_g^{s+1}\right), f\left(V_g^s, V_g^{s+1}\right)$

initialize $(A_o, f_o) \leftarrow \left(A\left(V_g^s, V_g^{s+1}\right), f\left(V_g^s, V_g^{s+1}\right)\right)$

do{

/ * *inner – tier*

solve: $\mathbf{E}\left(\mathbf{X}\left(V_g^{s+1}, V_g^s\right), \left(A\left(V_g^{s+1}, V_g^s\right), f\left(V_g^{s+1}, V_g^s\right)\right)\right) = \mathbf{0}$ / HB *parametric equations on* $V_g^{(s)}, V_g^{(s+1)}$

evaluate: $\mathbf{Y}\left(A(V_g^s, V_g^{s+1}), f(V_g^s, V_g^{s+1})\right) \leftarrow \dfrac{I_{p,\mathbf{v}}^{1,M}(A(V_g^s, V_g^{s+1}), f(V_g^s, V_g^{s+1}))}{V_{p,\mathbf{v}}^{1,M}(A(V_g^s, V_g^{s+1}), f(V_g^s, V_g^{s+1}))} = \dfrac{I_{p,\mathbf{v}}^{1,M}(A(V_g^s, V_g^{s+1}), f(V_g^s, V_g^{s+1}))}{A(V_g^s, V_g^{s+1})}$

/ * *outer – tier*

$$\textit{solve}: \left|\mathbf{Y}(A(V_g^s, V_g^{s+1}), f(V_g^s, V_g^{s+1}))\right| < \varepsilon \Rightarrow \begin{cases} \underset{\substack{A\in\boldsymbol{\mathcal{A}} \\ f\in\boldsymbol{\mathcal{F}}}}{\arg\min}\, \mathbf{Y}(A(V_g^s, V_g^{s+1}), f(V_g^s, V_g^{s+1})) = -\varepsilon \\ \underset{\substack{A\in\boldsymbol{\mathcal{A}} \\ f\in\boldsymbol{\mathcal{F}}}}{\arg\max}\, \mathbf{Y}(A(V_g^s, V_g^{s+1}), f(V_g^s, V_g^{s+1})) = \varepsilon \end{cases} \qquad (\varepsilon = 1\cdot 10^{-18})$$

$$\textit{with}: \mathbf{Y}(\cdot) = \left[\operatorname{Re} Y_{p,\mathbf{v}}^M(\cdot), \operatorname{Im} Y_{p,\mathbf{v}}^M(\cdot)\right]^T$$

/ in case of convergence failure

if $\left(\left\|\mathbf{E}\left(\mathbf{X}\left(V_g^{s+1}, V_g^s\right), p\left(A\left(V_g^{s+1}, V_g^s\right), f\left(V_g^{s+1}, V_g^s\right)\right)\right)\right\| > K\right)$ {

$\Delta V \leftarrow \dfrac{\Delta V}{2}$ / *reduce step – lenght*

$\varepsilon \leftarrow \varepsilon + \Delta\varepsilon$ / *increase the tolerance* $(1\cdot 10^{-18} \le \varepsilon \le 1\cdot 10^{-12})$

$N_h --$ / *decrease the harmonic order*

$N_{\max} ++$ / *increase the iteration count*

apply bidirectional sweep **TVS**

starting from a different voltage $V_g^s = V_q \in \boldsymbol{\mathcal{V}}$ }

update $(A^{(n-1)}, f^{(n-1)}) \leftarrow (A^{(n)}, f^{(n)}),\ n \le N_{\max}$

}

until $\left(\left(\left|\mathbf{Y}(A(V_g^s, V_g^{s+1}), f(V_g^s, V_g^{s+1}))\right| > \varepsilon\right) \vee (n = N_{\max})\right)$

plot $f_o\left(V_g^s\right)_{V_g^{s+1}\in\boldsymbol{\mathcal{W}}}$, $V_g^s \in \boldsymbol{\mathcal{V}}$

(6.23)

The three voltage parametric plots are shown in Fig. 6.11 [18], illustrating the evolution of the oscillation frequency when the gate voltage V_g^s spans the interval [-1V, 0V], for discrete values of the neighboring section gate voltage V_g^{s+1} = {-0.8V, -0.6V,-0.5V, -0.4V, -0.3V,

-0.2V, -0.1V} at each frequency zone. To a discerning eye it appears clear that for different combination of (V_g^{s+1}, V_g^s) *the same oscillation frequency could be obtained;* e.g in the first zone, corresponding to the graph (a) for -0.6V$\leq V_g^1 \leq$-0.3V, V_g^2 ={-0.3V,-0.2V, -0.1V} the oscillation frequency takes identical values in the range [1.7 GHz, 1.8 GHz]. Moreover, in some subintervals of the analysis range $\mathcal{V}$ =[-1V, 0V] the oscillation frequency presents *turning points* connecting different sections (*branches*) of the curve characterized by different stability properties of the parametric solution which have been investigated by means of a properly initialized envelope transient simulation [16,17] and discussion on chapter IV).. By analyzing the solutions with the method described earlier it is found that each time a turning point occurred, the stability of the solutions switched from stable to unstable and vice versa.

The practical implication of the stability analysis comes from the consideration that the stable solutions are the only ones observable in reality [3]. Therefore inspecting the graphs () it is possible to acquire information regarding *the gates control voltages forbidden values* (or ranges) *which produce no oscillation* (generate an unstable solution). For example, in the graph which keeps track of the frequency variation in the first zone (Fig. 6.11a), for V_g^2 =-0.1V and -0.6 V $\leq V_g^1 \leq$ -0.5 V it is observed a *frequency jump along the solution path of the stable solution* from 1.6 GHz to 1.7 GHz (approx.) and similarly for other values of V_g^1, V_g^2. This phenomenon is compatible with the tuning algorithm described in [6, 7] for the control voltages V_g^{s+1}, V_g^s should be varied in complementary manner to obtain the tuning in the zone B_s, but only a stability analysis *proves it right in nonlinear terms.* In fact, the convergence of the Harmonic Balance system of equation from (HBE.1, HBE.2) it is not a sufficient condition to infer about the stability of its solutions.

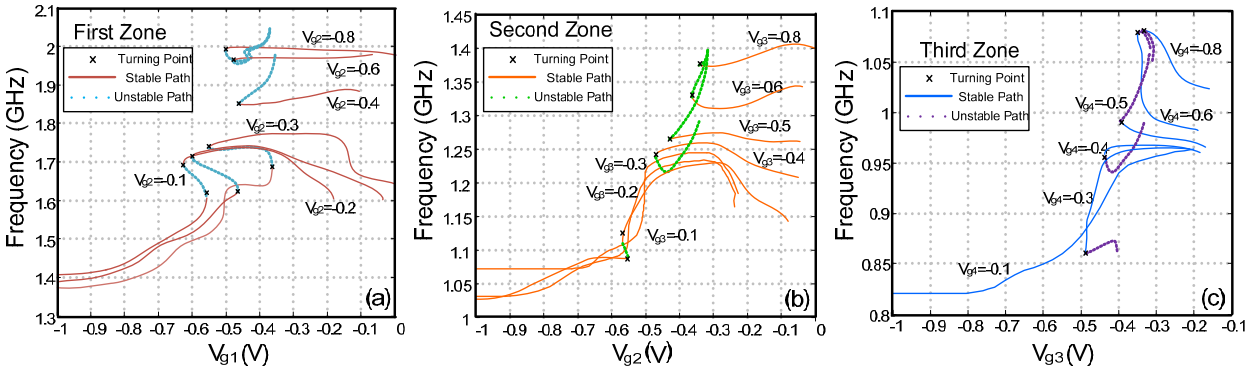

FIGURE 6-11. Family of curves [18] expressing the evolution of the oscillatory solutions across each frequency zone, as a function of one gate bias voltage, with the neighboring gate voltage taken as parameter; (a) first zone, (b) second zone, (c) third zone. The graphs indicate the existence of multi-valued solutions and turning points. The stability of the oscillating solutions has been assessed with properly initialized envelope transient simulations.

6.4 Optimized Power Profile over the DVCO Tuning Range.

In the Harmonic Balance oscillator analysis essentially a nonlinear *extended system* of algebraic equations is solved in a two tier procedure; the outer tier, starting from reasonable estimates, iteratively looks for the most fitting values for the amplitude and frequency of the oscillating signal (in order to satisfy the null admittance condition at the probe port) which are then passed to

the inner tier to simulate all the relevant circuit variables with standard HB routines. This procedure as shown in [12, 15] can be easily generalized to include additional design specifications and thus be cast into a *multi-objective optimization routine*. A noteworthy application consists in finding a smooth output power profile for the DVCO using a third gate bias voltage as an additional optimization variable as illustrated in [12]. The new design specification consists in minimizing the variations of the output power level at the fundamental frequency of the oscillating signal across the tuning bandwidth [1- 2 GHz]. To that aim the output power level is evaluated[31]:

$$W = P_{out}\left(A, f, V_g^{(s-1)}, V_g^{(s)}, V_g^{(s+1)}\right)\Big|_{\substack{A\in\mathcal{A}\\ f\in\mathcal{F}\\ V_g^k\in\mathcal{V}}} \tag{6.24}$$

which quite naturally depends upon all the optimization variables (the *endogenous ones* being the amplitude and frequency of oscillation, the *exogenous ones* being the gate control voltages). The new variable E is constrained to have a tighter range than the original power profile[32]. A gradient or quasi-Newton optimization program is then invoked to fulfill the constraints (outer-tier equations):

$$\begin{aligned} &P_{out}\left(A_o, f_o, V_g^{(s-1)}, V_g^{(s)}, V_g^{(s+1)}\right)\Big|_{\substack{A_o\in\mathcal{A}\\ f_o\in\mathcal{F}\\ V_g^k\in\mathcal{V}}} \geq W_{\min}; \qquad \mathrm{Re}\left[Y\left(A_o, f_o, V_g^{(s-1)}, V_g^{(s)}, V_g^{(s+1)}\right)\Big|_{\substack{A_o\in\mathcal{A}\\ f_o\in\mathcal{F}\\ V_g^k\in\mathcal{V}}}\right] = 0 \\ &P_{out}\left(A_o, f_o, V_g^{(s-1)}, V_g^{(s)}, V_g^{(s+1)}\right)\Big|_{\substack{A_o\in\mathcal{A}\\ f_o\in\mathcal{F}\\ V_g^k\in\mathcal{V}}} \leq W_{\max}; \qquad \mathrm{Im}\left[Y\left(A_o, f_o, V_g^{(s-1)}, V_g^{(s)}, V_g^{(s+1)}\right)\Big|_{\substack{A_o\in\mathcal{A}\\ f_o\in\mathcal{F}\\ V_g^k\in\mathcal{V}}}\right] = 0 \end{aligned} \tag{6.25}$$

and the best choice for the five variables (A_o, f_o, V_g^{s+1}, V_g^s, V_g^{s+1}) is iteratively evaluated and updated once the inner-tier Harmonic Balance equations are solved as for the algorithm FSA.

[31] A measurement equation in the simulator engine allows knowing all the node voltages at each harmonic, as well as its power content. In Agilent ADS 2008® for example the command "dBm(Vout[1])" delivers the output power at the fundamental frequency, at the node having the label "Vout".

[32] The optimal range, has to be found after some preliminary assessment of the DVCO output power, either obtained numerically or empirically (building a prototype). A heuristic procedure can however be used if no prior information is available, based on a dicotomic approach. The optimal power range initially agrees with a typical one i.e. [-5 dBm, +10 dBm]. Then it is halved in steps, as the power optimization is carried out, until convergence issues arise due to the infeasibility of solutions. In case the nonlinear output power profile had been already determined, the optimal range for E would be kept centered around the average value of the output power level curves throughout the tuning range as done in [12] in which [3 dBm, 7 dBm] has been chosen (centered around 5 dBm).

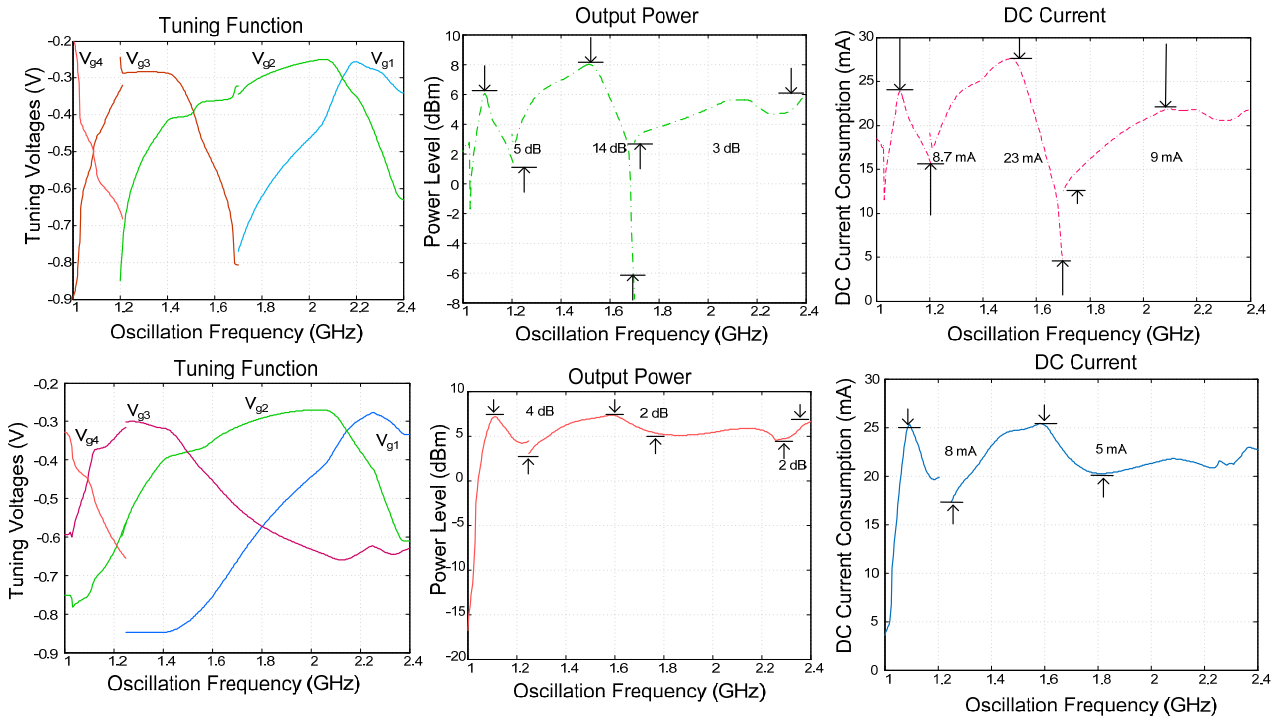

FIGURE 6-12. A different optimization scheme leads to reduced variations in the output power and DC supply current throughout the tuning range: (above) tuning function, output power and DC current before the optimization; (below) optimized output power and DC current consumption.

Incidentally, it was discovered that setting the aforementioned multiobjective optimization framework for finding the smooth output power profile, increased the Harmonic Balance simulations' convergence speed, and avoided high jumps (discontinuities) in the output power curves due to a inadequate initialization *at the edges* of each frequency zone $B_s = [f_{s+1}, f_s]$. An intuitive explanation could be given based on the fact the use of an extra-condition *setting the power range,* forces the HB simulator to seek on a *tighter range of admissible voltage probe amplitudes* leveraging on the flexibility provided by an additional parameter (third gate voltage).

The sought after curves are reported in Fig. 6.12. By comparison, it is noticed how adding a third gate voltage as an optimization variable does not qualitatively alter the tuning function (though small numerical differences may exist) but at the same time, brings important benefits in terms of output power variation reduction.

Using nonlinear analysis /optimization tools it is therefore shown that a DVCO with a smoother (or maximally flat) power profile can be designed, exploiting a third gate voltage control. In order to apply the tuning function that provides minimum output power variation, the DVCO tuning algorithm should be digitally stored in a look up table to reduce the possibility of catching unintended oscillation modes.

6.5 Transient Analysis. DVCO Settling Time.

The analysis carried out so far has provided insights and quantitative assessment of the DVCO operation in terms of its spectral characteristic and tuning behavior. Compared to time domain analysis, the benefits of having an oscillator circuits solved in the frequency domain (as discussed in chapter IV are remarkable, in that the algorithms converge *naturally* to the steady state

solution, avoiding the direct integration of the integro-differential equations governing the oscillator circuit evolution. Detailed as it might be, a nonlinear description with Harmonic Balance gives no guarantee about the stability of the oscillating solutions. Moreover, there are some performance indicators, related to the *oscillator responsiveness*[33] (i.e. oscillations *settling-time*), which necessarily require a *transient analysis*. Thus to complete the nonlinear analysis/synthesis of the DVCO, time domain transient simulations have been performed, using a commercial EDA for microwave circuits suite (Agilent ADS® 2008).

The transient analysis requires no external probe[34] to be connected to the DVCO, and once the gate bias voltages are specified, the simulation is run[35]. The resistance values have been altered to facilitate and speed up the convergence of time domain algorithm[36]. In order to reduce the complexity, all the discrete components (inductance and capacitance) have been substituted by their ideal models, the via-holes have been modeled as a constant lumped inductance of L_h=0.2 nH. As the drain resistance is chosen greater than 50 Ω, the simulation deliver the *DVCO output voltage time domain plot*, shown in Fig. 6.13, which have been obtained setting R_i= 55 Ω and biasing individually each section with $V_{g,on}$= -0.1 V (spectral plots are obtained by a straightforward Fourier transform). Evidently, having altered the schematic and introduced idealized model for the discrete components, the *individual resonances frequency distribution* (as well as their output power level) is affected.

[33] In case of *free running oscillators* important parameters related to its transient behavior are the oscillation *settling-time*, measuring the *latency or time lapse* to obtain stable oscillations, after the circuit has been correctly biased and powered. In case the oscillator is *injection-locked* to an RF-source, it is interesting also to consider the *oscillator locking-time*, measuring the maximum delay at which the driven oscillator synchronizes itself with the external source.

[34] Sometimes, it could be necessary to insert a *small* voltage/current *pulse generator,* or alternatively a *small noise* current/voltage *generator*, (available as standalone component in many EDA software libraries) in order *to trigger the oscillations.*

[35] A transient simulation palette requires the specification of the *integration method* (in this work, it has been used *Gear's second order finite difference method*) of the *time-sweep* (start/stop time), and the *maximum time-step* (which has to be chosen to accurately to track high-frequency signals). In order to evaluate the output signal emerging from a distributed parameter element, its *impulse response* has to be obtained via an *Inverse Fourier Transform* of the corresponding *frequency domain transfer function*, and subsequently needs to be *convolved with the input signal.*. Some parameters control the *maximum number of frequency points* at which the impulse response needs to be evaluated, the *maximum frequency* (at which the impulse response should be computed), the difference between samples in the frequency domain (at which the transfer function is analyzed). In general, owing to the DVCO complexity, whenever possible convolution models were approximated with simpler (proprietary) ones.

[36] In fact, it is noticed that for R_i < 50 Ω *convergence in the time domain* is very troublesome, *possibly due to the stiff nonlinearities present in the active device model* [1]

Active Section	Settling Time (ns)	Frequency (GHz)	Output Power (dBm)
T_1	7	2.340	-1.026
T_2	15	1.640	0.163
T_3	30	1.160	-1.880
T_4	50	0.980	-7.353

TABLE 6-6. DVCO settling time for selected oscillations.

From the time domain waveform it clearly appears that the settling time [21] *increases as the section are subsequently being activated*, which indirectly confirms the basic mechanism for oscillations onset in a reverse mode DVCO detailed in the introductory sections. In fact, since when activating *farther sections* the four resonances are associated with *increasingly longer loopback paths*, so the corresponding signal *transit-time* varies accordingly, determining ever greater *latencies/settling times* (lowest for the first section, highest for the fourth).

The DVCO tuning algorithm might also be explored resorting to time domain simulations, by simply assigning the values (V_g^{s+1}, V_g^s) and observing if a resonance is achieved. Long sequences of transient simulations would be needed to figure out the variation of the *tuning voltages/output power* with respect to the oscillation frequency, assigning the (V_g^{s+1}, V_g^s) values based on a trial and error scheme, owing to the ever-present convergence failure risk determined by a wrong choice of the biasing voltages. Hence, it appears more effective to analyze the circuit steady state in the frequency domain (as discussed in the last sections), and use the time domain simulations merely to confirm the results.

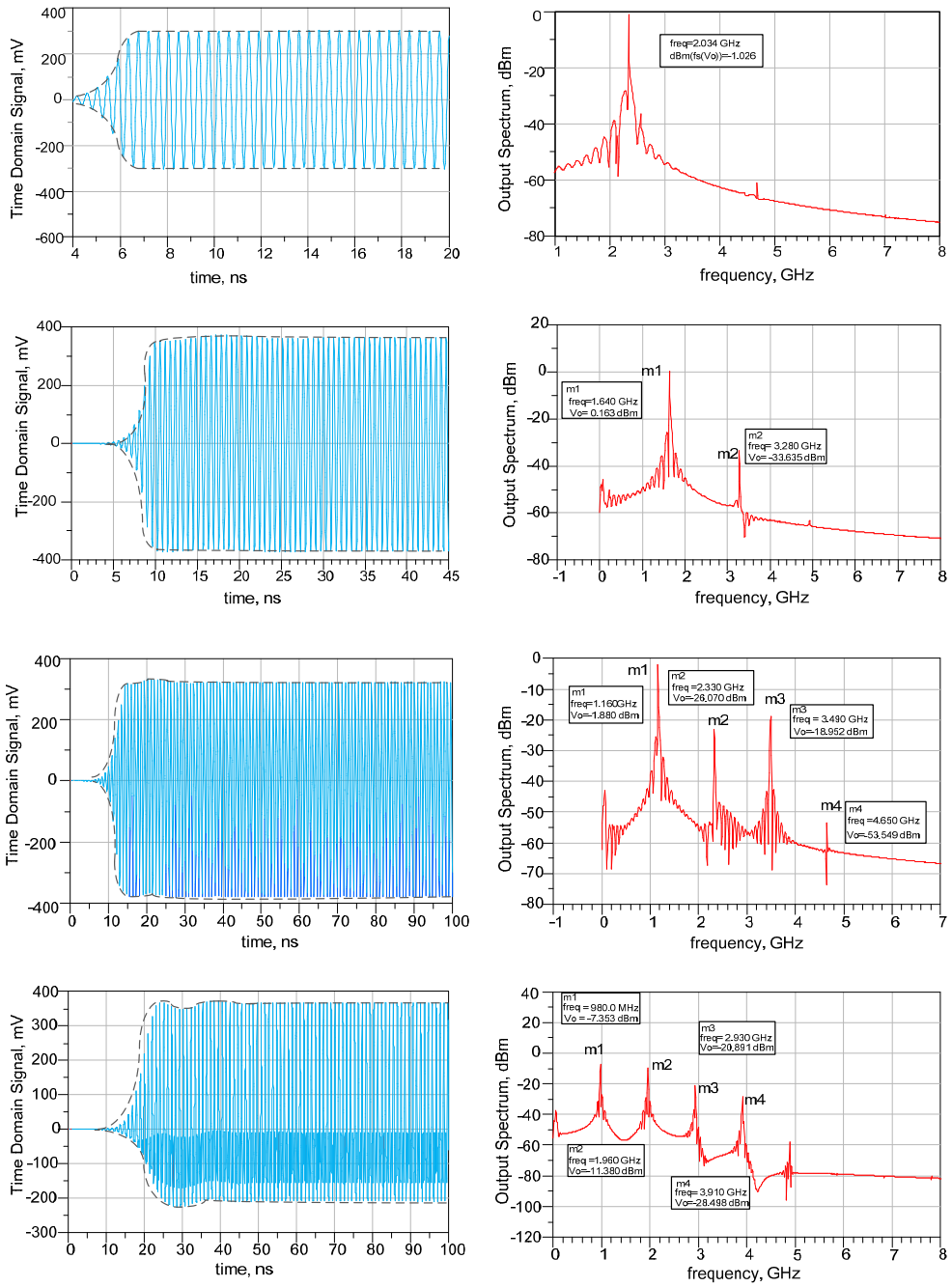

FIGURE 6-13. (left) Transient Analysis of the four DVCO individual resonances, whose frequencies decrease from top to bottom suitable for assessing the DVCO settling time from time domain waveforms inspection; (right) output power spectra.

6.6 PHASE NOISE NONLINEAR SIMULATION.

A very important figure of merit of *a free running oscillator* relies in its *spectral purity*, i.e. the ability to concentrate the RF power (at the various higher order harmonics) in a very narrow bandwidth located close to the nominal oscillation frequency (or its higher order harmonics), thus resembling an *ideal frequency pulse (spectral line)*. Noise disturbances[37] in the circuit, are transferred

[37] Major contributions comes from active device baseband noise, and resistive paths thermal noise, among others [22—28].

to the phase of the oscillating signal- which varies randomly- and reflected in the oscillator flawed timing, due to irregularly spaced zero crossing of the generated sine wave [22-25] . In turn, random phase fluctuations in the time domain determine a FM modulation process near the up-converted carrier, which spread out the RF energy around the nominal oscillation frequency. The RF power distribution around the nominal oscillation frequency can thus be measured by the *phase noise,* which can be *operatively defined* as the *phase spectral density* (per-unit bandwidth) of the oscillating signal *at a frequency offset from the nominal carrier frequency*, relative to the signal power at the nominal oscillation frequency. Phase noise may critically affect the circuit performance, especially when employed in RF front end receivers. Therefore, an adequate assessment of the DVCO phase noise is deemed essential [26-28].

Many commercial simulators allow a quick estimation of the *phase noise spectral density* curves, taking advantage of their nonlinear Harmonic Balance numerical routines introducing noise generators at specific ports [29]. Oscillator phase noise is evaluated taking advantage of the built-in single ended oscillator port which operates analogously to the harmonic probe introduced earlier[38] and noise controller simulation engines which specify the range of offset frequencies around the large signal carrier and the nodes used for noise computation, as well as the physical quantities to be displayed (e.g phase noise spectrum, absolute noise voltage spectrum, relative noise voltage spectrum at the selected nodes). In particular, the algorithms introduced in (internal references) are performed automatically. The determination of the oscillating solution starts *with a linear search*, (after having provided an initial guess for the oscillating frequency) in which the triggering conditions are evaluated, much like the technique described in section 6.4.1. Afterwards, automatic amplitude tracking procedure starts, to the aim of determining the large signal oscillation frequency and output power. The determination of the phase noise spectrum around the large signal carrier frequency begins with a refinement of the oscillatory solution; subsequently the phase noise spectrum is computed using a conversion matrix approach to account for the effect of nonlinear mixing of small signal noise with large signal carrier [30] [31] for a definite offset range of frequencies from the carrier. Simulation results reported on Fig. 6.14 show the voltage noise level (on the left) and the phase noise (on the right) for the four discrete resonances (computed in the offset-frequency range [1 KHz, 10 MHz] from each carrier). At a constant offset frequency of 1 MHz from the carrier, the phase noise ranges from -106.5 dBc/Hz at the 1.813 GHz carrier frequency to a maximum of -128 dBc/Hz at the 677 MHz carrier.

[38] The oscillator port can be utilized as voltage or current harmonic probes, whether they are inserted in a series configuration (breaking DVCO the feedback loop) or in a shunt configuration (between the output node and the ground). Best results are obtained by inserting the oscillator port in series, just before the first section, *breaking the oscillator loop.*

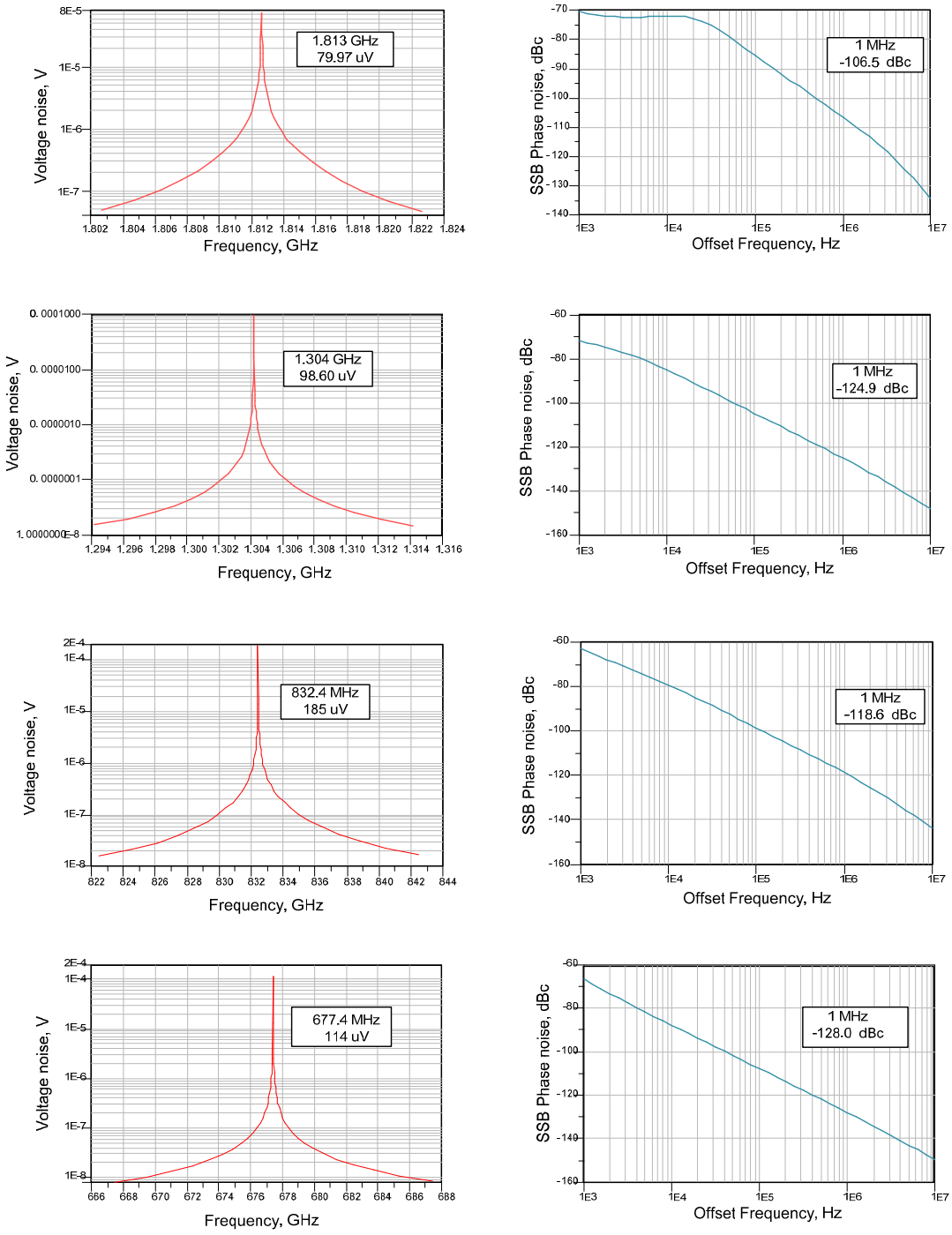

FIGURE 6-14. Simulated DVCO Voltage Noise and Phase Noise, near the four discrete resonances.

6.7 Reverse Mode DVCO Implementation and Measurements

6.7.1 DVCO Layout preparation and Physical Design

Distributed voltage controlled oscillator layout was undoubtedly inspired by the considerations made on [20] opting for an implementation which included cascaded *LC sections* constituting *artificial transmission lines. Physical connectivity among lumped components* is provided by 50 Ω *microstrip lines* printed on a Arlon A25-N® substrate (woven fiberglass-reinforced, ceramic filled

laminate substrate with H=0.502 mm, ε=3.38 @10 GHz, tanδ= 0.0025) whose typical lengths which are a fraction of the wavelengths of the oscillating signal[39]. The *compactness of the circuit* is essential for benefitting of *high-frequency* operations; however *prototype scalability* becomes a hard task using several lumped components. In fact, *a minimum spacing is required* for adequately placing the components/devices, yet guaranteeing enough room *to prevent spurious coupling* (as dictated by EMI/EMC prescriptions) and for being able to perform manual soldering.

The DVCO feedback path is realized by connecting both the drain and gate line, which required the use of to optimally chamfered 90° microstrip bends, placing an additional inductor whose nominal[40] value is $L_g/2 + L_d/2 = L_f$ = 3.3 nH. Unlike the Skvor design the DC feed network (basically a *high pass* LC filter) was placed *inside* the oscillator area, close to each DC-block gate capacitor C_b. The transistor pads' and via holes pad layout were designed taking into account the geometrical constraints discussed earlier. In addition to that, via holes were placed in the immediate vicinity of each FET source node[41]. The via holes pad and the transistor pad were designed with the help of an integrated CAD environment in Agilent ADS® 2008, and analyzed via *Method of Moments* (2.5 D electromagnetic simulation) to understand the field distribution, so to derive *multiport S parameters*, which were in turn employed (after they have been exported as a Dataset file) to obtain a more precise assessment of the DVCO tuning characteristics in the Harmonic Balance simulations.

6.7.2 DVCO PROTOTYPE IMPLEMENTATION DETAILS

After the DVCO layout is prepared, the circuit is simulated using the most accurate description available. Substituting built-in microstrip components in the originally simulated schematic with *abstract multi-port blocks,* containing the EM simulations frequency domain data (*multi-port S-parameters),* detailed HB simulations on the *updated schematic* follow, aimed at finding possible discrepancies. Being the last step before the *physical implementation*, it is mandatory that the circuit behaves as closely to what has been previously expected; otherwise *design changes* need to be made. The frequencies associated to the four individual resonances and the tuning curves were verified, observing a *shift of towards lower values* by no more than 10%.

The board engraving was performed using LPKF ProtoMat® C100/HF Circuit Board Plotter/ milling machine. via holes to the ground plane were drilled using the same equipment which was digitally controlled by means of proprietary CAM software. *Via holes metallization* was executed using the LPKF ProConduct® *vacuum table* which enable plating through (previously drilled) holes without using expensive electrochemical processes, making use of a *conductive polymer* which is

[39] The wavelength corresponding to maximum operating frequency. S-parameter optimization showed that this approximation was adequate.

[40] The actual value of the feedback inductor L_f should take into account the inductive effect of the comparatively longer length of the feedback line section; thus it could be less than 3.3 nH.

[41] It was explored the possibility of connecting various ground pads with lots of via holes (typically six per pad, forming ground islands) together and with each FET source node in order to improve the grounding but the results was an increase in spurious oscillations. From the lesson learned, it was decided to have separate grounds for each FET device.

applied all over the board with the help of a squeegee[42]. The metalizing paste diffuses through the via holes, a process which is facilitated by the use of a vacuum pump. After this step is completed, the board is baked at controlled temperature for about thirty minutes, in order for the metallic coating to be hardened. Electrical checking the via holes ground connection (with the help of a digital multimeter indicating a zero resistance path across all the via holes) is an essential task to be performed before soldering the components.

DVCO prototype soldering was *manually* carried out within in-house lab-facilities (CTTC Engineering Labs) with acceptable results. Up to five boards were built and tested, before obtaining a good prototype. All electrical connections were visually (with the aid of a microscope) and electrically inspected (by means of a multimeter). Chip inductors (from Toko® LL-FSL 1608 series, 1.6×0.8 (l×w) mm) capacitors (from Murata® GRM18, 1.6×0.8 (l×w) mm) resistors (from Neohm®, thick film resistors CRG series 1.6×0.8 (l×w) mm), were used, having previously accounted for spurious behavior (e.g. Electrical Series Resonances for the inductors/capacitors which hinder the performance, etc.). As already discussed, four HJ-FET from (formerly NEC) Renesas® NE3509 M04 (L to S band low noise amplifier) which guarantee an adequate transconductance ($g_m \geq 80\ mS$) level up to 6 GHz. *The components* (resistors /inductors/capacitors) electrical parameters were occasionally changed, to improve the oscillator's stability across the operational range. It occurred more often with FET's *drain series stabilizing resistors*[43] R_d (range 10—30 Ohm) and with *the matching resistor* R_g (range 45—55 Ohm). The series inductors forming part of the constant-k sections were left at their nominal value of L_s= 3.3 nH (TOKO inductors LL-FSL 1608 series) while the DC blocking gate capacitors (MURATA capacitors GRM 18 series) were altered to equalize[44] the output power level. DC blocking capacitors were chosen to have the following sequence C_{b1}= 3 pF, C_{b2}= 9 pF, C_{b3}= 18 pF, C_{b4}= 27 pF in the final prototype. The DC filtering capacitors of the end section were chosen to be of C_f =100 pF. The shunt capacitors of the LC sections were set at the nominal value C_p = 2.1 pF.

6.7.3 DVCO MEASUREMENTS. TUNING, POWER, DC CURRENT, PHASE NOISE.

The negative voltages for the gate bias controls are provided by a four outputs digitally adjustable DC power supply (Agilent N6700® series), which can be adjusted to a tenth of mV accuracy. The positive (common) drain voltage is provided by another independent power supply. Great care was put on *ensuring adequate grounding* in order *to avoid floating ground, or ground loops* issues. To that aim, it was chosen to ground separately the negative (gate) and the positive (drain) DC power supplies, adding big (1 uF) filtering capacitors between each grounded terminal and the negative (positive) terminal. The drain voltage was (constantly) set to V_D = + 2V, the negative gate bias voltages V_{Gi} ranged in the in the interval [-1V, 0V].

---

[42] The board is placed on the table which is connected to an electrical vacuum pump, and the air is drawn from the bottom board plane; an adhesive film prevent the conductive paste to seep underneath where not intended.

[43] After carefully checking parasitic oscillation onset the most appropriate resistor was introduced. Some iterations were needed to select it –trading off stability vs decrease in output power.

[44] As farther sections are getting activated, their associated oscillation frequency moves towards the lower end of the tuning bandwidth. In order to deliver a nearly constant *input (gate) impedance* to the oscillating signal, the DC blocking capacitors should have lower capacitance for the first stages and higher for the last, as gathered from the definition of a capacitive impedance $Z_c = (1/2\pi fC)$.

The oscillator output port is connected to an Agilent Spectrum Analyzer, to investigate the power content in the frequency domain. Moreover, the drain DC current is limited to $I_{D,max}$ = 60 mA for safety reason[45]. The DC gate current was bounded[46] too ($I_{G,max}$ =0.001 mA)

As a precautionary measure the circuit is initially biased with V_D= 0V (that is, drain power supply is turned off[47]); and all the four transistors are interdicted choosing V_{Gi} = -1V. Only after having ensured that *no transistor is activated* (gate bias voltage at -1V, well below the activation threshold) the drain power supply is set to V_{DD} = 2V. In case the circuit is working well, this configuration corresponds to the DVCO *rest state*, with *no oscillations* and *zero current DC consumption* at the drain node[48]. The circuit is initially checked by its ability to produce four different resonances when each transistor is *individually* biased in the active zone. Experimentally, is seen that the onset of discrete oscillations is obtained when the gate voltages are greater than $V_{Gi,\ on} \approx$ -0.45V approx. The expected oscillations frequencies should be decreasing as each stage gets turned on, from the first to the last. When the experimental results showed a discrepancy with respect to the expected behavior, it was usually necessary to check the soldering. Occasionally, it was necessary to use different resistance values for the drain series resistors R_d or to modify the values of the shunt capacitance C_p, in order to achieve better performance.

Tuning curve are inspected by directly varying gate bias voltage in pairs, following the suggestion in [7] and the results obtained from nonlinear simulations. The tuning algorithm is thus analyzed separately in each frequency zone $B_s = [f_{s+1}, f_s]$ *(s=1,2,3)*; the gate voltages V_G^{s+1}; V_G^s are altered in a *complementary manner* (as discussed earlier). When the voltage V_G^{s+1} = *-1V* (T_{s+1} is off) and V_G^s *is at (near) zero Volts* (T_s *is on) an oscillation is produced at the output whose frequency is* f_s. Subsequently, while the T_{s+1} *is kept constantly off (setting* V_G^{s+1} = *-1V,)* V_G^s is decreased[49] (i.e. "*continuously*" taking negative values, leading towards the complete interdiction of the s-th section), and the frequency variation is tracked by looking at the spectral line movements in the spectral analyzer ($f \rightarrow f_{s+1}$), up to the point that oscillation is quenched (due to the fact that the *s*-th section is interdicted whenever gets lower than $V_{G,on}^s \approx$ -0.45V). The same procedure is repeated for different values of V_G^{s+1} *throughout the voltage range [-1V, 0V]; discrete values with a 100 mV separation could be initially chosen (-1V, -0.9V,….-0.2V, -0.1V, 0V) in order to have a coarse estimate of the tuning*

[45] That means that the drain power supply automatically switches from a *voltage controlled mode* to a *current controlled mode* whenever the current limit is exceeded, making the power supply voltage *drop to lower values* in order to fulfill the maximum ratings.

[46] Although the gate current is usually much lower in HJ-FET devices due to high *gate port* impedance, this action often avoided the transistors to get unknowingly damaged by improper settings (e.g erroneously *reversing the polarity,* selecting a positive voltage, *higher than the breakdown junction voltage*).

[47] In fact, accidentally supplying a nonzero common drain voltage prior to the gate biasing *(i.e. with* V_{Gi} *=0* V) *would mean the simultaneous activation (saturation) of all the transistors* (*since the HJ-FETs are depletion mode*) leading to an excess DC current that might easily damage the active components.

[48] indicating no faults on the connections, no missing capacitors, no damaged active device, no spurious resistive path to the ground

[49] The voltage-step *needs not to be constant*. Due to the nonlinear tuning algorithm, the same increment Δv *causes different frequency jumps* Δf *in the oscillating signal.*

range, annotating for each combination of the gate voltages V_G^{s+1} *and* V_G^s the values of *oscillation frequency* (f), *the output power at the fundamental* (P_{out}) the output DC current consumption (I_D). To get a more detailed view, (in case frequency jumps are observed on the output spectrum, i.e. subintervals of each B_s for which no oscillation is detected) the role of V_G^{s+1} *and* V_G^s *are exchanged, so that* V_G^s *is kept fixed at a value belonging to the discrete set (-1V, -0.9V,….-0.2V, -0.1V, 0V), while* V_G^{s+1} *is continuosly increased from -1V to complete saturation of the* T_{s+1} transistor. Collecting all the data for the three different frequency zones B_s , the experimental tuning curves have been traced, along with the DC current supply and output power at the first harmonic throughout the tuning range, and are represented in Fig. 6.15.

The task was complicated by the presence of anomalies[50] *in the DVCO experimental behavior*. In some cases, a change in bias voltages caused asymmetrical variations in oscillation frequency and in the output power depending on whether *one section was led towards activation* (when one of the two control voltages *was increased above* $V_{G,on}^s \approx$ -0.45V while maintaining the other off) *or interdiction* (when one of the two control voltages *was dropped below* $V_{G,on}^s \approx$ -0.45V, while maintaining the other off); the circuit manifested *hysteresis with respect to the control voltages*[51]. It also occurred that small variation in one of the two control voltages had no effect in frequency shifting, but only on output power, showing the eventuality of having *many possible (degenerate) oscillating solutions characterized by having the same value of fundamental frequency, but possessing diverse spectral characteristics* (different spectral purity, different power at the fundamental, different rejection ratio).

Phase noise measurements *over the band of interest*, have been carried out making use of the proprietary companion software of the E 440A Agilent Spectrum Analyzer, which enabled a careful assessment of the SSB noise by using the internal E440A phase detector, and averaging methods (ensemble averages out of many realizations) to refine the final results which are shown in the fig 6.15. Phase noise at 1 MHZ offset from the carrier was assessed by selecting some representative frequencies across the tuning range (fig. 6.15). the phase is also traced for a variable offset (100 kHz, 10 MHz) for some of them. Heuristically, one could argue that larger phase noise values are expected when two devices are simultaneously operating in the active zone, which in turn causes a sudden increase in DC current consumption. This argument is confirmed by looking at the graphs. It is noticed that lowering the drain bias voltage, and use blocking capacitor in parallel (10pF//10nF//10uF) at the DC feed network to the individual gates (to improve the filtering of the power supply) the DVCO figure of merit improves.

[50] Often times macroscopic frequency drifting, instabilities, spurious oscillation, self-oscillating mixer regime, chaotic spectrum (not achieving perfect synchronization) were observed, that partly was attributed to implementation errors (not achieving perfect phase matching in the gate/drain line) and partly to spurious coupling or EMI issues.

[51] The implication is that the turn-on and turn-off gate voltages values for the DVCO are different; generally it was observed $V_{G,off}^{s(hys)}$ =-0.65 V

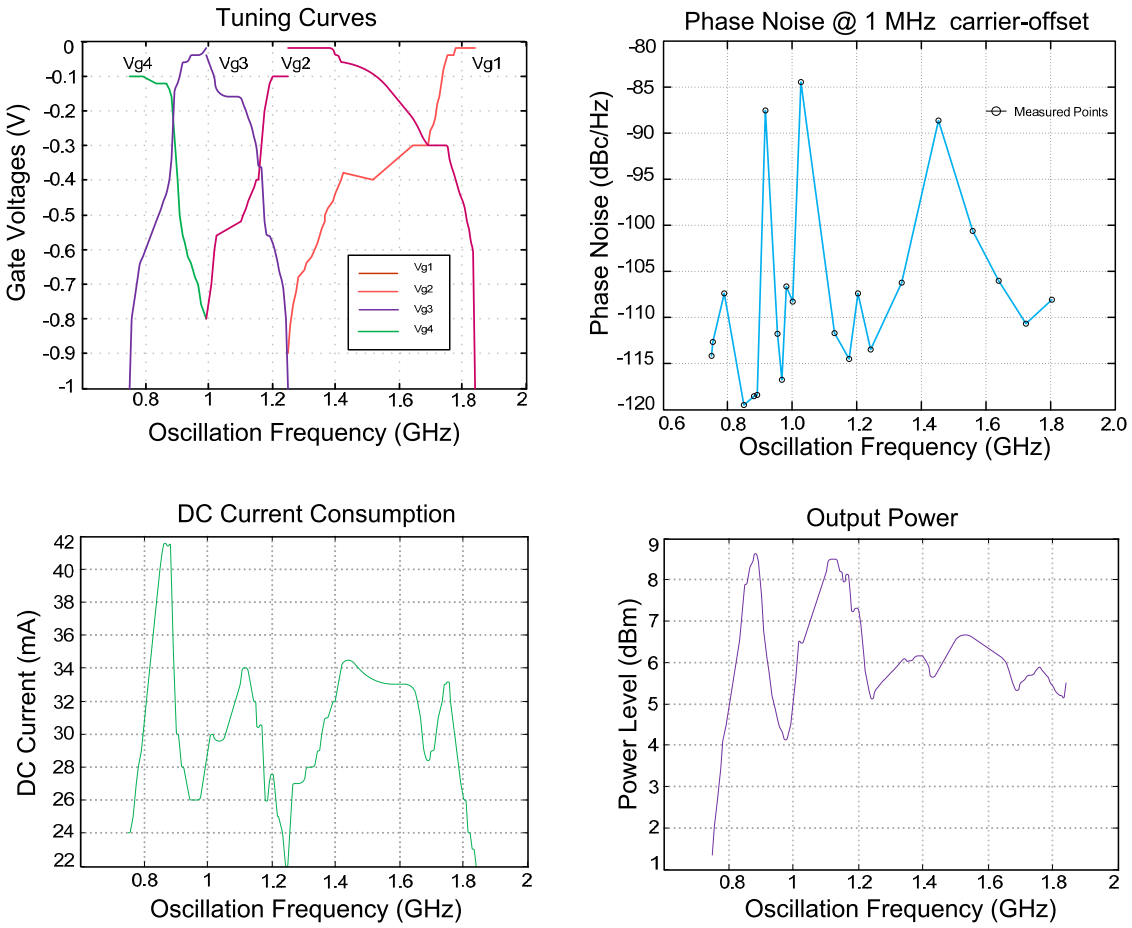

FIGURE 6-15. Measurement results for the implemented DVCO.

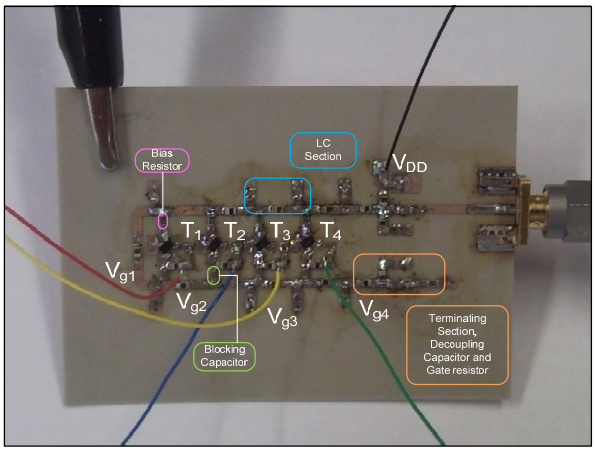

FIGURE 6-16. DVCO prototype built using conventional PCB techniques, employing microstrip lines patterned on a dielectric substrate and discrete components.

6.8 Alternative DVCO Design.

The reverse mode DVCO is seen to possess many attractive features making it suitable to be employed in wideband radio receivers. A monolithic implementation (MMIC) would certainly be preferred to be used in next generation user terminals for mobile communication. To this end, a

design employing the fewest components possible should be envisioned. In fact, constant-*k* section could be designed having recourse only to basic transmission (*microstrip*) line sections. In particular as shown in [4, 5, 11] a sequence of Stepped Impedance short[52] microstrip sections can be used to realize low pass ladder networks having an inductive series arm and a capacitive shunt arm; high impedance (Hi-Z) short sections emulate the inductive behavior while low impedance (Low-Z) the capacitive one[53]. Furthermore, padding capacitors (shunting drain/gate line to the ground) could be easily obtained by connecting parallel open stubs [11] with an adequate aspect ratio (length/width). By converting each lumped *LC* element to its distributed counterpart, the DVCO layout becomes susceptible to be integrated, along with the standard processes /technologies for fabricating monolithic microwave transistors.

Needless to say, the MMIC realization [32—35] calls for a higher level of accuracy and confidence in the simulations, since once the circuit has been fabricated there is no room for performance optimization by manual substitution of its electrical components. In view of the fact that the experimental verification of the previously designed oscillator required a substantial amount of time for empirically troubleshooting various issues (i.e. eliminating spurious oscillations) and since there was no possibility of implementing the DVCO in monolithic form having recourse only to the on-site facilities, it has been deemed more convenient still rely on some modifiable components, by having the *LC* constant–*k* sections filters redesigned according to the considerations exhibited in [7]. Hence, *only the inductive series* part of the constant-*k* (or *m*- derived) section is implemented by means of *high-impedance, (electrically) short microwave sections,* maintaining the *discrete (chip) capacitors for the shunt arm,* and possibly for the padding capacitors [12].

In particular, the DVCO was laid out on the same dielectric substrate (Arlon A 25 N, with H=0.5 mm ε=3.8 @ 10 GHz) used for the previous circuit and employed four NE 3509 M04 as active devices. The major differences reside in:

- *Choice of tinier components*, 1005 series (1.0×0.5 ($l \times w$) mm);
- *DC feeding /RF blocking networks* providing the four gate voltages V_{gi} which are kept out of the DVCO functional area. The *DC gate bias voltage networks* and the *active device gates* are connected by a short wire which is manually bent to cross the *microstrip track* (in [7], bond-wires had been used used in its place). In order to reduce the effect of the *wire inductance*, an RC network, with a resistance 5.1 kΩ and a 10 nF capacitance has been employed (like in [7]). Drain common bias voltage has been supplied using a high pass filter network *L*=100 nH, *C*=10 nF directly connected to the drain line.

[52] Length is relative to the wavelength λ corresponding at the maximum frequency of the signal in the circuit. A section is considered (electrically) short when its length corresponds to a fraction of λ, for example: $l=\lambda/10$

[53] In general for a microstrip line of length l , an inverse relationship among the line impedance Z_0 and its width w is observed, assuming the substrate parameters are kept fixed through the frequency range of interest. Therefore, the higher the impedance the thinner the line ($Z_0 \uparrow$, $w \downarrow$) and vice versa, the lower the impedance the ticker the line. Inductors are then realized making use of short thin (Hi-Z) sections; capacitors, are implemented using short thick (Lo-Z) sections.

- *Inductors aren't used across the signal path*, therefore the number of components to be soldered is dramatically reduced (essentially remaining the four HJ-FETs, the capacitors, and the element for the Bias networks). *Obviously the terminating sections are made up of adequately sized (and matched) microstrip line open stubs. Hi-Z inductive lines constant-k and m-derived sections,* are realized by looking at the frequency response of their ideal lumped counterpart. Starting from reasonably close values for their *aspect ratio (l/w)* the lines are designed by imposing the similarity in their input/output match and transfer ratio between the lumped ideal circuit and the one using distributed components;

- *No series - drain resistor is used for stabilizing the active device;*

Despite it appeared simpler to be implemented, it required much more effort than the previous design based on artificial transmission lines. In particular the harmonic balance program[54] suffered often from convergence issues, due to the stiff nonlinear problem associated with a complex distributed structure.

The oscillator was designed to possess a wider tuning range (1—4 GHz). Microstrip line impedance was chosen to be in the range[55] of 80 Ω -100 Ω, giving values of their width which span from 0.50 mm to 0.25 mm (20 mil to 10 mil). The length of each section was dictated by the minimum admissible separation and was set to 10mm approx (400mil). After having laid out the circuit, the linear and nonlinear analysis followed, in order to derive the four oscillations frequencies and the tuning curve as explained before (insert reference to pictures).

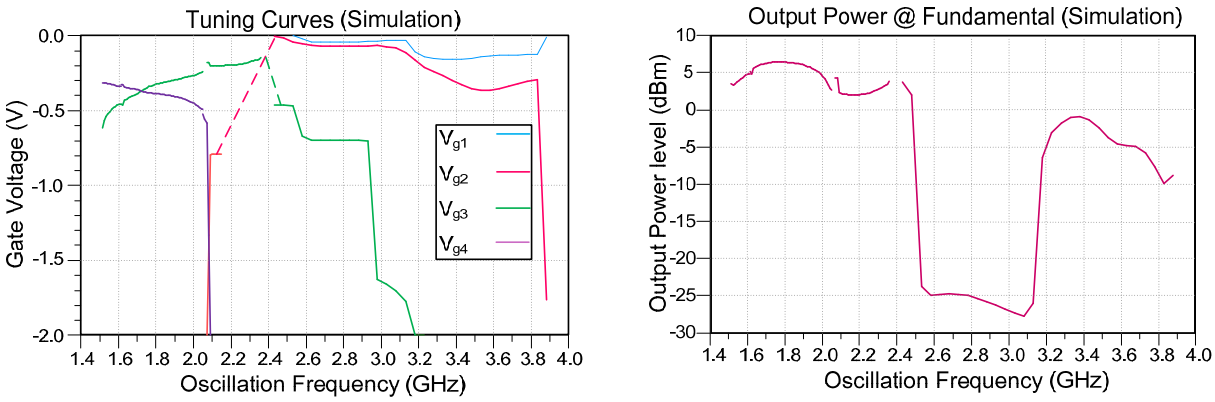

FIGURE 6-17. Simulated tuning curves and output power for the alternative implementation

[54] The harmonic probe method showed its limitations. An intensely debated topic is in fact whether this method could be easily applied to any oscillator topology, or it *is topology dependent* (discrete, single stage/cascaded-multi stage /distributed /ring oscillators) and even *waveform dependent* (*harmonic oscillators vs recalcitrant oscillators*). The work [] delineates a theoretical framework which extends the analysis method introduced in earlier sections.

[55] Due to feasibility constraints, the width of the microstrip lines couldn't reach too small values. The lines were synthesized with a numerical tool, integrated in the EDA commercial software environment used for the DVCO design

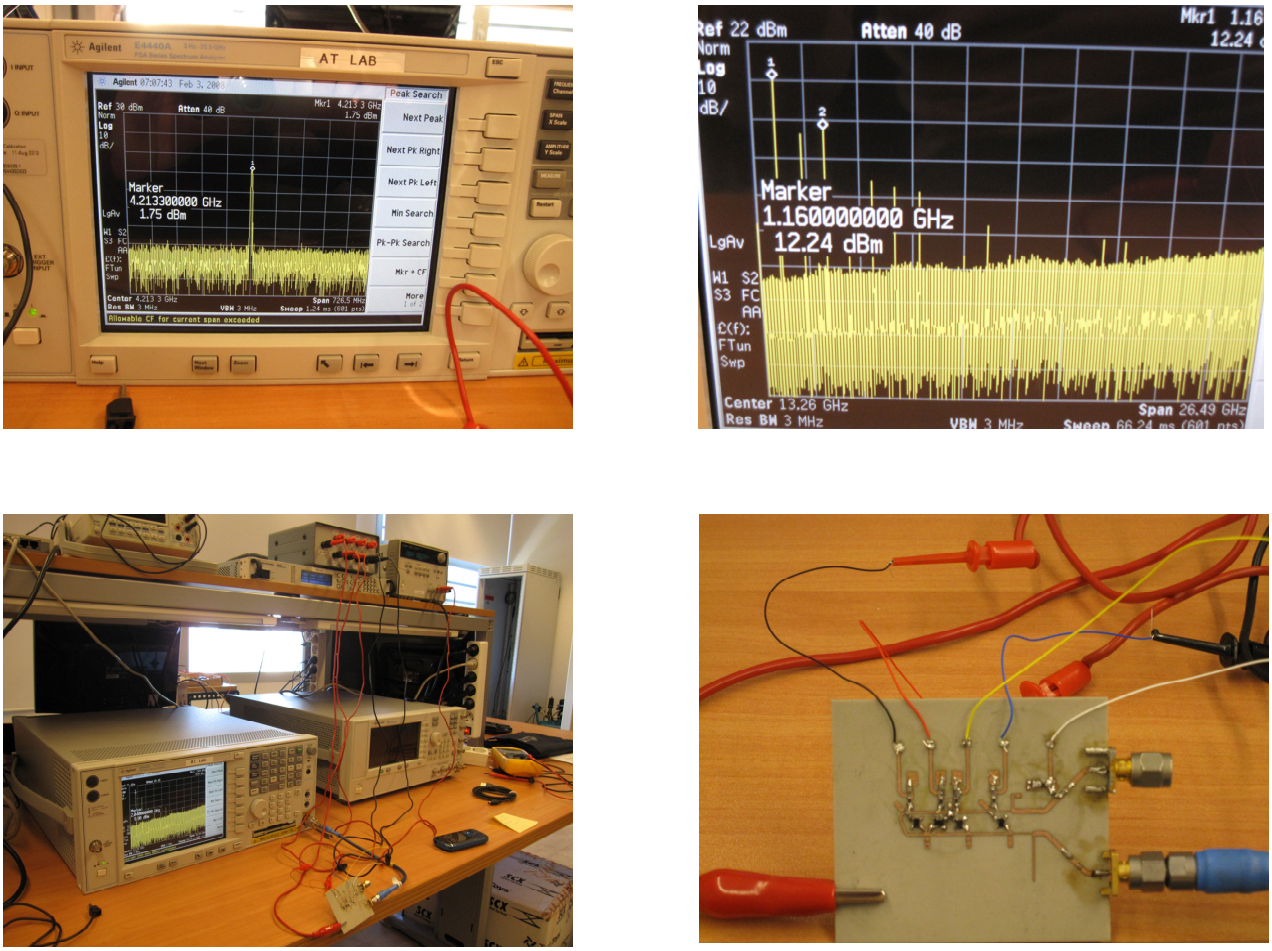

FIGURE 6-18. Alternative DVCO implementation & measurements benchmark.

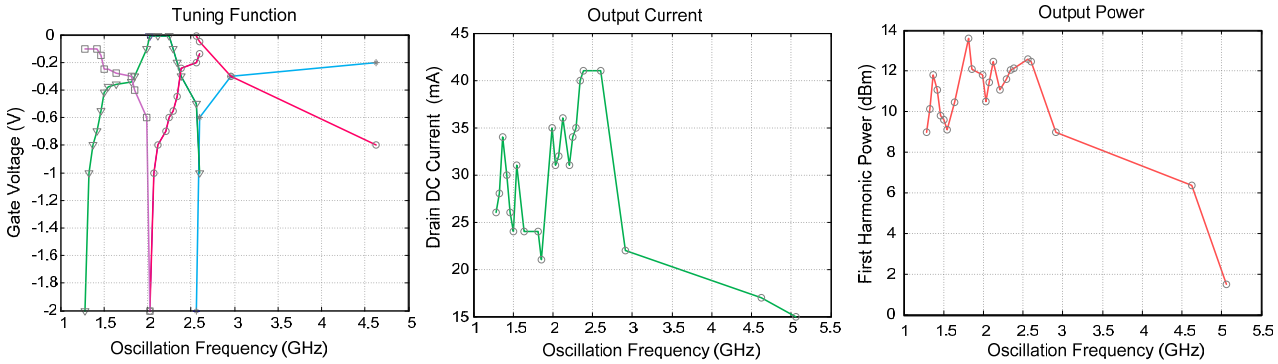

FIGURE 6-19. Measured tuning algorithm, DC current, and Output Power at the fundamental for the alternative DVCO.

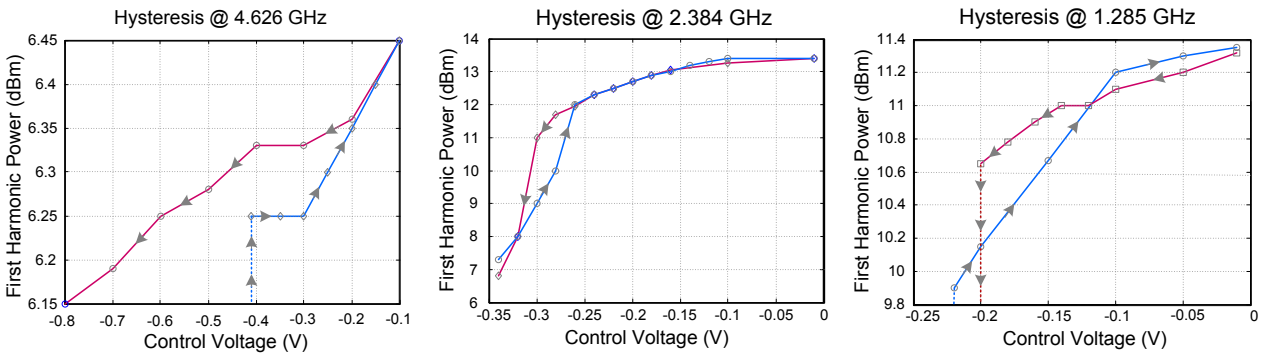

FIGURE 6-20. Hysteresis phenomenon occurring in the alternative DVCO implementation.

The measurement results showed greater mean power, greater bandwidth but reduced tuning capabilities in comparison with the previous prototype. In order to address these issues, possible solutions to be further investigated are the following (*reference to the formula* (6.50) *in which phase shift is linked to individual resonances*):

- *DVCO parametric analysis with different separation across the sections.* HB simulations have been carried out by introducing a parametric length, characterizing the separation among sections. The minimum separation is obviously dictated by practical constraints (the feasibility of the prototype), the maximum one depends on the amount of "tuning range shrinking" (referring to (6.50))

- *the impact of introducing a phase shifter in the feedback loop as a mean for compensating tuning difficulties.* A variable phase-shifter could be introduced to obtain a more regular spacing of the individual oscillation frequencies. In preliminary simulation a parametric phase variable has been swept and the effect on the tuning curves has been assessed.

6.9 Injection Locking in Reverse Mode DVCO.

The DVCO could also serve as a distributed frequency divider when the injection signal has a frequency of $\omega_{inj} = 2\omega_o$ *or* $3\omega_o$. The confirmation of the superharmonic injection locking at *twice* (or *thrice*) the autonomous oscillation frequency was obtained experimentally, based on the last built prototype, which was designed according to the considerations exposed in section (insert section number). The circuit featured two ports; one for analyzing the output spectrum (on the drain line) the other used for signal injection (on the gate line). The signal generator used was from Agilent (E4428C ESG Analog Signal Generator) guaranteeing exceptional performance in terms of near carrier phase noise and accuracy in power/frequency settings. The superharmonic and subharmonic locking range was then measured at the four different discrete resonances, with different injection strengths varying from -20 dBm to 0 dbm. The following table summarizes the results. In some circumstances it was not possible to achieve synchronization at the second harmonic of the autonomous resonance. In fact the DVCO transmission networks exert a lowpass filtering by design; thus some injected signals get quenched, especially those whose frequencies

fall in the transmission coefficient high attenuation range[56]. In that case, it was chosen to inject a subharmonic frequency (at one half of the free running oscillation frequency) or a triple frequency. In particular, this occurred when the second stage was turned on as illustrated on the Table 6.7.

Oscillation Frequency (GHz), Active $\mathbf{T}_i$	Injected Power (dBm)	Sub-harmonic (½) Locking Frequency (GHz)	Super Harmonic (2) Locking Frequency (GHz)	Super Harmonic (3) Locking Frequency (GHz)	Locking Range(MHz)
1st, T_1 ON 4.83857	-20	x	9.67682	x	0.78
	-10	x	9.67540	x	1.92
	0	x	9.67772	x	5.64
Second, T_2 ON 2.91513	-20	x	x	8.74180	1.16
	-10	x	x	8.73550	11.5
	0	x	x	8.71430	16.4
Second(*),T_2 ON 2.91513	-20	1.4575	x	x	No locking(***)
	-10	1.4574	x	x	1.2
	0	1.4578	x	x	19.3
Third, T_3 ON 1.67117	-20	x	3.35530	x	12
	-10	x	3.32520	x	65
	0	x	3.39040	x	No locking(***)
Third(**), T_3 ON 1.673581	-20	5.02502	x	x	2.5
	-10	5.01001	x	x	15
	0	4.95730	x	x	23
Fourth. T_4 ON 1.1462	-20	x	2.2933	x	4.3
	-10	x	2.3023	x	7
	0	x	2.3398	x	50

TABLE 6-7. Injection locking DVCO measurements.

Moreover, the injected signal had power a dramatic influence on the autonomous oscillation. Too small injection strengths simply give no noticeable locking effect; e.g. this happens when a subharmonic ½ frequency is injected at -20 dBm, when the second section is turned on. On the

56. The *transmission coefficient* is measured by ratio of *load voltage* (at the end of the drain line) to the *input voltage* (at the beginning of the gate line). It presents, a high attenuation range, which starts right after the low-pass cutoff frequency, which is determined by a *transmission zero introduced by* the last *m-derived section*.

contrary, a too high injection power can turn the autonomous oscillation off, as occurs when a double frequency is provided at 0 dBm, when the third section is activated.

6.10 CONCLUSIONS

The reverse gain Distributed voltage controlled oscillator is seen to represent a promising candidate to be implemented in future generation radio equipment, due to its very wideband multi GHz tuning range, and deserves further scrutiny. Although two decades have passed since this topology was devised, very basic analysis/design approaches, relying mainly on linear analysis, have been used to assess its performance but this methodology lacked in predictive power. In fact, many questions regarding the oscillator tuning algorithm, its power variation throughout the tuning band, its harmonic rejection, its phase noise, its injection locking synchronization profile, were answered by looking at data obtained by measurements. In this chapter, it has been shown how to get all the relevant oscillator figures of merit by adequately employing nonlinear simulation tools.

In particular, harmonic probe driven, frequency domain steady state simulations were carried out to get a detailed picture of the oscillator tuning function and power variation, in a simpler and more effective manner than the commonly used time domain transient simulations. Moreover, the harmonic balance simulation framework delivered increased flexibility, allowing one to quickly evaluate the DVCO parametric solution curves, for the purpose of analyzing/synthesizing/optimizing the circuit performance. Linear analysis is not entirely dismissed as it serves for estimating the discrete individual frequency, to gain insight in their distribution across the tuning bandwidth, in the initial DVCO design. Time domain simulations as well address more specific issues, like the oscillator settling time determination.

In the context of the probe driven HB simulations, the probe frequency regarded as a parameter is swept to determine the associated tuning voltages and output power in a sub-range of the overall tuning bandwidth, with a two-tier optimization routine. At each frequency point, the probe amplitude (determining the oscillator output power) and two neighboring sections gate voltages are adjusted to meet the nonlinear oscillation condition at the probe port. This process is slightly modified, and in another set of simulations, two voltages are independently swept and the probe amplitude and frequency evaluated. The results showed clearly the voltage values for which resonances could not occur due to unstable solutions, which were detected by taking advantage of properly initialized envelope transient simulations.

Two different reverse mode DVCOs were implemented, following the examples available in the literature. One made use of Artificial Transmission lines, as a signal distribution network. A second implemented prototype used periodically loaded uniform line sections. Both of them were laid out on a microstrip board, using PCB printing techniques on microwave dielectric substrates. The prototype implemented with artificial transmission line sections gave the best measurement results, achieving satisfactory agreement with simulations. The second prototype was mainly used for analyzing the DVCO superharmonic (subharmonic) injection locking behavior, in order to realize effective frequency dividers (multipliers).

6.11 REFERENCES

[1] F. Giannini and G.Leuzzi. *Nonlinear Microwave Circuit Design*, Wiley, June 28, 2004.

[2] C.-R.,Chang, M.B Steer, S. Martin,and E.Jr. Reese, "Computer-aided analysis of free-running microwave oscillators," *IEEE Transactions on Microwave Theory and Techniques*, vol. 39, no. 10, pp.1735-1745, Oct. 1991.

[3] A. Suarez and R. Quéré. *Stability Analysis of Nonlinear Microwave Circuits*. Artech House publishers, Jan 2003.

[4] T.T.Y. Wong. *Fundamentals of Distributed Amplification*. London: Artech House, 1993.

[5] B.S. Virdee, A.S. Virdee and B.Y. Banyamin. *Broadband Distributed Amplifiers*. Artech House, 2004.

[6] L. Divina and Z. Škvor, "Experimental verification of a distributed amplifier oscillator", *Proceedings of the 25th European Microwave Conference (EuMC) 1995,* vol.2, pp. 1163–1167, Sept. 1995.

[7] L. Divina and Z. Škvor, " The Distributed Oscillator at 4 GHz," *IEEE Transactions On Microwave Theory And Techniques,* vol. 46, no. 12, pp 2240-2243, Dec. 1998.

[8] ARLON MED® "A25-N, data sheet".[On-line] retrieved from http://www.arlon-med.com/25N25FR.pdf [Mar. 21, 2013].

[9] RENESAS® (formerly NEC) "NE3509-M04 GaAs HJ-FET data sheet," [On-line] Available: http://documentation.renesas.com/doc/YOUSYS/document/PG10608EJ02V0DS.pdf [Mar. 21, 2013].

[10] K. Bowers, and R. Patrick, "Broadband Distributed Amplifiers", [On-line] Available: http://www.inst.eecs.berkeley.edu/~ee217/sp03/projectsSP99/Dist_Amp_b+r.pdf [Mar 21, 2013].

[11] D. Pozar. *Microwave Engineering*. New York: Wiley, February 5, 2004.

[12] A. Acampora, A. Collado, and A. Georgiadis, "Nonlinear analysis and optimization of a Distributed Voltage Controlled Oscillator for Cognitive Radio," *Proceedings of the 2010 IEEE International Microwave Workshop Series (IMWS) on RF Front-ends for Software Defined and Cognitive Radio Solutions*, pp.1-4, Feb. 2010.

[13] Agilent Technologies®, "Advanced Design System (ADS®) 2008, documentation,"available: http://cp.literature.agilent.com/litweb/pdf/ads2008/ads2008.html [Mar. 21, 2013]

[14] K. Kurokawa, "Some Basic Characteristic of Broadband Negative Resistance Oscillators", *Bell Systems Technical Journal* [On-line], vol.48, pp. 1937-1955, June 1969. Available: http://www.alcatel-lucent.com/bstj/vol48-1969/articles/bstj48-6-1937.pdf [Mar.20, 2103].

[15] A Acampora, and A. Georgiadis, "Wideband Voltage Controlled Oscillators for Cognitive Radio Systems," *Advances in Cognitive Radio Systems*,[On-line] Cheng-Xiang Wang and Joseph Mitola III, Ed. InTech, pp. 1-24, July 2012. Available: http://www.intechopen.com/books/advances-in-cognitive-radio-systems/wideband-voltage-controlled-oscillators-for-cognitive-radio-systems [Mar. 21, 2013].

[16] E. Ngoya, and R. Larcheveque, "Envelope transient analysis: A new method for the transient and steady state analysis of microwave communication circuits and systems", *Proceedings of the IEEE MTT-S International Microwave Symposium Digest, 1996*, vol.3, June 1996, pp.1365-1368

[17] H.G. Brachtendorf, G. Welsch, and R. Laur, "A time-frequency algorithm for the simulation of the initial transient response of oscillators", *Proceedings of the 1998 IEEE International Symposium on Circuits and Systems, (ISCAS '98)* vol.6, 31 May-3 Jun 1998, pp.236-239

[18] A. Collado, A. Acampora, and A. Georgiadis, "Nonlinear analysis and synthesis of distributed voltage controlled oscillators,"*Cambridge International Journal of Microwave and Wireless Technologies*, vol.2, no.2, pp.159-163, April 2010.

[19] K.S. Kundert, K.S. White, and A. Sangiovanni-Vincentelli. *Steady-state methods for simulating analog and microwave circuit*. Kluwer Academic Publishers, March 1990 (Springer reprint of hardcover 1st edition, December 2010).

[20] Z.Škvor, S.R. Saunders, and C.S. Aitchison, "Novel decade electronically tunable microwave oscillator based on the distributed amplifier," *IEEE Electronics Letters* , vol.28, no.17, pp.1647-1648, Aug. 1992.

[21] W. Egan. *Phase-Lock Basics*. New York: Wiley, 1998

[22] D. B. Leeson, "A simple model of feedback oscillator noise spectrum," *Proceedings of the IEEE* , vol.54, no.2, pp. 329- 330, Feb. 1966

[23] J.-C. Nallatamby, M. Prigent, M. Camiade, and J. Obregon, "Phase noise in oscillators - Leeson formula revisited," *Microwave Theory and Techniques, IEEE Transactions on* , vol.51, no.4, pp. 1386- 1394, Apr 2003

[24] A. Hajimiri, and T.H. Lee, "A general theory of phase noise in electrical oscillators," *IEEE Journal of Solid-State Circuits*, vol.33, no.2, pp.179-194, Feb 1998.

[25] Jing Zhang, Haitao Mei, and T. Kwasniewski, "Prediction of phase noise in CMOS distributed oscillators," *Proceedings of the 2003 SBMO/IEEE MTT-S International Microwave and Optoelectronics Conference, 2003 (IMOC 2003),* vol.1, pp. 157- 162 vol.1, 20-23 Sept. 2003.

[26] Jing Zhang, T. Kwasniewski, and Mei, Haitao "Analysis and Simulation of Phase Noise in Distributed Oscillators," *Proceedings of the 49th IEEE International Mid-West Symposium on Circuits and Systems, 2006. (MWSCAS '06)*, vol.1, pp.312-316, 6-9 Aug. 2006

[27] C.J. White, and A. Hajimiri, "Phase noise in distributed oscillators," *Electronics Letters*, vol.38, no.23, pp. 1453- 1454, 7 Nov 2002.

[28] Xiaofeng Li, O.O. Yildirim, Wenjiang Zhu; and Donhee Ham, "Phase Noise of Distributed Oscillators," *IEEE Transactions on Microwave Theory and Techniques,* vol.58, no.8, pp.2105-2117, Aug. 2010

[29] Zhang, Jing; Kwasniewski, Tad; Mei, Haitao, "Analysis and Simulation of Phase Noise in Distributed Oscillators," *Proceedings of the 49th IEEE International Midwest Symposium on Circuits and Systems, 2006 (MWSCAS '06)*, vol.1, pp.312-316, 6-9 Aug. 2006.

[30] S.Ver Hoeye, A. Suarez,and J. Portilla, "Techniques for oscillator nonlinear optimization and phase-noise analysis using commercial harmonic-balance software," *IEEE MTT-S International Microwave Symposium Digest 2000*, vol.1, pp.95-98 vol.1, June 2000.

[31] V.Rizzoli, A. Costanzo, F. Mastri, C. Cecchetti, "Harmonic-balance optimization of microwave oscillators for electrical performance, steady-state stability, and near-carrier phase noise," *IEEE MTT-S International Microwave Symposium Digest, 1994,* pp.1401-1404 vol.3, 23-27, May 1994.

[32] K. Bhattacharyya, "23.97GHz CMOS Distributed Voltage Controlled Oscillators with Inverter Gain Cells and Frequency Tuning by Body Bias and MOS Varactors Concurrently," *Proceedings of the 23rd International Conference on VLSI Design, 2010. (VLSID '10),* pp.182-187, Jan. 2010.

[33] K. Bhattacharyya and T.H. Szymanski, "Performance of a 12GHz monolithic microwave distributed oscillator in 1.2V 0.18μm CMOS with a new simple design technique for frequency changing," *Proceedings of the 2005 IEEE Annual Conference on Wireless and Microwave Technology, (WAMICON 2005),* pp. 33, April 2005.

[34] Z. A. Shaik, and P.N. Shastry, "A novel distributed voltage-controlled oscillator for wireless systems,"*Proceedings of the 2006 IEEE Radio and Wireless Symposium (RWS '06),* pp. 423- 426, Jan. 2006.

[35] N. Seller,*et al.*, "A 10GHz Distributed Voltage Controlled Oscillator for WLAN Application in a VLSI 65nm CMOS Process,"*Proceedings of the 2007 IEEE Radio Frequency Integrated Circuits Symposium (RFIC 2007),* pp.115-118, June 2007.

CHAPTER VII. CONCLUSIVE REMARKS

7.1 MAIN RESULTS

The benefits of using nonlinear simulation techniques for assessing nonlinear microwave oscillators' operation have been explored in this work, specifically in the cases of Triple-Push Oscillators (coupled oscillators) and Distributed Oscillators. As previously discussed, conventional linear analysis/simulation techniques possess limited predictive power and can be used just as a first approximation to indicate whether a possible oscillation will occur and what will its estimated frequency be. In order to obtain a detailed view of the circuit operation, it is therefore necessary to undertake a more sophisticated approach, based on nonlinear methods (chapter III and IV) which include time domain (Transient/Convolution), frequency domain (Harmonic Balance) and mixed domain methods (Envelope Transient simulations).

A significant part of the discussion has regarded the description of Harmonic Balance simulation techniques for autonomous circuits, run on a commercially available microwave circuit simulator and based on customizable auxiliary generators/voltage harmonic probes (chapters IV), and applied subsequently to concrete designs (chapters V and VI). The advantages over the time domain methods have been shown to reside in much faster simulation times, due to the direct convergence to steady state solutions (avoiding the transient computation, as discussed in chapter III) and the possibility to easily integrate a parametric analysis (chapter IV, V, and VI) in order to appreciate quantitatively the effect some critical circuit variables have on the overall performance. It is important to notice that, although similar methods are nowadays integrated in most commercial EDA software for microwave circuit analysis, they do not offer the same flexibility.

It has been illustrated how Harmonic Balance simulations jointly with auxiliary generator technique permitted to keep track of three different oscillating modes in a Triple Push Oscillator at 6 GHz(chapter V), in which three different voltage-type auxiliary generators specified the diverse amplitude-phase relationships among the oscillating nodes. Moreover, the effect of a variable coupling strength and phase has been considered, by investigating the effect of a variable coupling line length and attenuation at the coupling node of each elemental oscillator to derive hints, which ensured the onset of the third-harmonic generating mode. Analogously (chapter VI), auxiliary generators driven HB simulations permitted the derivation of the voltage tuning curves for a distributed voltage controlled oscillator in the band [0.8 GHz, 2 GHz], the parametric study of its four discrete resonances, an optimization of its power profile and the determination of its stability properties (when used jointly with Envelope Transient simulations).

7.1.1 EMPIRICAL VALIDITY

The validity of the results obtained in simulation was established by measurements on prototypes that were built using on site facilities. In some cases, a small to moderate discrepancy between the simulated output power/oscillation frequency and the corresponding measured values was observed. Since supportable simulation results depend on the availability of accurate nonlinear models for the active devices, lumped elements parasitics and real-world electromagnetic EMI/EMC effects on distributed circuits, a relative error of ±10% could be expected when the previous modeling conditions aren't entirely fulfilled. For example, in the case of the DVCO tuning curves (chapter VI) the measurement results has indicated a 200 MHz shift with respect to the simulated values, which can be partially ascribed to implementation errors, but also to modeling mismatches and imperfect accounting of the electromagnetics/propagation phenomena arising in the distributed structure, leading to multiple revisions in the final implementation; many times the final values for certain components (like the series drain resistors) were adjusted to deliver optimal performance, guaranteeing a close match with the simulated results. In fact, the qualitative variation, as evident from a visual comparison of the tuning plots, DC current supply, and output power at the fundamental (throughout the tuning range) is preserved.

In the alternative implementation exposed in section 6.8, however the tuning algorithm was more difficult to derive, due to hysteresis phenomena, and to high frequency spurious oscillations which severely limited DVCO operation. Possible causes include:

- inadequate isolation of RF signal from DC sources and from environmental noise;
- losses and interference due to the DC feed network which due to unavailability of bond-wires connection, was fabricated resorting to a short metallic wire in series with a high impedance;
- choice of the substrate which has H=0.502 mm, ε_r =3.38 (at 10 GHz) and doesn't allow to build microstrip tracks possessing impedance higher than 100 Ω, without excessively reducing their width. In fact, in a DVCO designed with transmission lines only, in order to force the backward propagating wave to reenter the feedback loop, the impedance should be increasing from the first section to the last (creating a sort of tapered line), which entails decreasing the width of the microstrip track from section to section.

Possible remedies have been investigated. In particular it has been considered:

- *DVCO parametric analysis with different separation across the sections*. HB simulations have been carried out by introducing a parametric length, characterizing the separation among sections. The minimum separation is obviously dictated by practical constraints (the feasibility of the prototype), the maximum one depends on the amount of "tuning range shrinking"
- *the impact of introducing a phase shifter in the feedback loop as a mean for compensating tuning difficulties.* A variable phase-shifter could be introduced to obtain a more regular spacing of the individual oscillation frequencies. In preliminary simulation a parametric phase variable has been swept and the effect on the tuning curves has been assessed.

A very limited discrepancy is also perceptible in the measurement results related to the Triple Push oscillators (exposed in chapter V). In fact, looking carefully at the measurement spectra, one would note that two oscillating modes are established at the same oscillation frequency (M_2, M_4 at 1.9 GHz approx.) while the other occurs at a slightly higher frequency (M_1 at 2.1 GHz, approx) therefore they aren't strictly simultaneously stable. Nevertheless, it should be remarked that this circuit was optimized to avoid the onset of other modes than the rotating wave solutions (M_2), so the appearance of the spurious modes (M_1, M_4) was possible thanks to a detuning of the bias voltages of the core oscillators, which caused in turn an inevitable frequency shift in the output oscillations.

7.1.2 A REMARK ON AUXILIARY GENERATORS DRIVEN HARMONIC BALANCE SIMULATIONS

The simulation approach employed extensively throughout this work relies on the Harmonic Balance method in conjunction with suitable probes to trigger the oscillating solution, as it has been explained in chapter IV. This scheme is based on a optimization problem, which finds the fittest value of probe amplitude and frequency that fulfill the non perturbation conditions at the probe port, making the admittance at the probe port close to zero. The usually chosen optimizer is the Gradient Descent (or steepest descent) method; therefore the convergence to local minima of the admittance function is possible, characterized persistently high values of the cost function (i.e. higher than 10^{-4}). In this case the optimization algorithm should be restarted, with different (although close) candidate values for the auxiliary generator frequency and amplitude. The same reasoning applies when studying injection locked / synchronized regime, to the amplitude and the phase of the probe, being the frequency determined by the external source.

Often the results, expressed in terms of the oscillator spectral characteristics at the output node, seem to vary slightly depending on the probe insertion point. Even though the explanation of this issue goes beyond the scope of our research (see references on chapter IV), it nevertheless had an obvious impact on it, since it poses the issue of the uniqueness of solutions, which is crucial when comparing simulated results with measured ones. In the case of DVCO design, this concern added to the ambiguity shown in the tuning function as illustrated in chapter VI, even though the final measurement agreed significantly with the simulations.

7.2 PROSPECTS: FORTHCOMING RESEARCH TASKS

Based on the achieved results, both the triple push oscillator and the distributed oscillator topologies appear to be valid solutions with respect to a possible implementation as subsystems in next generation wireless terminals transceivers. Their main features however, remain different. In fact, the triple push oscillator topology, is mainly used for high (fixed) frequency signal generation, while the distributed voltage controlled oscillator delivers mainly a wideband tuning range, but at lower frequencies. A possible extension of this work consist in conceiving a single device, which would operate at a higher frequency range (ideally in the 60 GHz) bandwidth and still preserving great tuning capabilities. All the design issues that have been detailed in earlier sections should be addressed. The injection locking behavior of the oscillators presented in this work needs to be further investigated.

7.2.1 POSSIBLE RESEARCH TASKS REGARDING TRIPLE-PUSH OSCILLATORS

- *Tunable triple push oscillator; topologies analysis and design.* A triple-push VCO would benefit from a wide tuning range for the third harmonic signal, that is three times as much as the tuning range associated with the core oscillators (see chapter II and references therein). It should be detailed the topology/layout used; as well as the method for altering the oscillation frequency. In fact the layout topology could be minimally transformed, introducing only three varactor diodes, or considering each core oscillator as a standalone VCO. The impact of misaligned oscillation frequencies at each core oscillator output would need to be studied in a detailed way by means of nonlinear analysis technique to prevent a worsening in the performance, and the appearance of spurious oscillation modes.
- *Injection locked triple push oscillator.* As frequently an oscillator circuit is synchronized to an external driving signal, it could be interesting to perform a nonlinear analysis of injection locking in the triple push oscillator, deriving quantitative relationships between the locking phase and one critical circuit parameter (i.e. a bias voltage). Then different scenarios could be contemplated. A triple push oscillator could be driven by different injection sources (one as a minimum, three as a maximum); their effect could be compared considering also different metrics and tradeoffs like DC power consumption vs. Spectral purity. The injection locking signal could be any integer ratio *p:q* of each core oscillator's nominal oscillation frequency; therefore, super-harmonic and sub-harmonic synchronization can be studied as special cases.
- *Integrated triple push oscillator.* The triple push oscillator was prototyped with discrete components and printed microstrip lines on a dielectric substrate to quickly provide an empirical validation of the nonlinear simulation results. Though conceptually valid, this design still occupies a comparatively large size. Thanks to recent advances in the silicon technology at RF frequencies, the triple push oscillator could be made tiny enough to be employed in any commercial communication equipments (handheld devices). A feasibility study of an integrated triple push oscillator might be devised.

7.2.2 POSSIBLE RESEARCH TASKS REGARDING DISTRIBUTED OSCILLATORS

- *New DVCO topologies in order to guarantee a multi band operation*. The DVCO topology studied in this thesis, ensures a continuous tuning range, which agrees with the passband of the embedded transmission structure. In this work, it has been chosen to use cascaded, low-pass, (*m*-derived) constant-*k (equivalent)* sections as recommended in the literature (chapter I, II, VI). A possible extension involve choosing a distribution network which possess a different transfer function*, such as a cascade of band-pass and/or band-stop components*, in order to have a *multi-band* operation. According to preliminary simulation results, a parametrical (nonlinear) analysis indicate that this goal might also be accomplished by varying the separation among the sections in a DVCO, by considering an asymmetrical spacing in the gate line/drain line. Subsequently, the simulations results would need to be confirmed by measurements on a real prototype.
- *Injection locked DVCO.* Injection Locking has been practically assessed on the alternative implementation as shown in section 6.8, but there was lacking an in-depth study of the DVCO synchronization behavior when forced by an external oscillator, considering its injection power and frequency as parameters.

- *Low voltage supply, Low phase noise DVCO*. A low power, low phase noise distributed voltage controlled oscillator could be designed. In fact, based on preliminary measurement results, a positive correlation among DC current consumption and DVCO phase noise was found throughout the tuning range; since the DC current consumption is an increasing function of the voltage drain bias, by reducing the voltage supply a noticeable decrease in phase noise might be expected. Nevertheless, the output RF power is seen to decrease as well. A nonlinear analysis of this competing figures should deliver a more energy-efficient and spectral pure device.
- *Integrated DVCO with digitally reconfigurable transmission lines*. Finally, the possibility of having an integrated version of the distributed voltage controlled oscillator might be explored. Instead of using the conventional components, digitally controlled transmission lines [1] can be included, providing tuning capabilities. Therefore, *forward gain mode distributed oscillators*, which have been already presented in integrated form, might be endowed with a precisely controllable tuning mechanism overcoming their main limitation

7.3 REFERENCES

[1] T. LaRocca, *et al*. "Millimeter-Wave CMOS Digital Controlled Artificial Dielectric Differential Mode Transmission Lines for Reconfigurable ICs," *Proceedings of the IEEE International Microwave Symposium 2008 (IMS 2008)*, pp.181- 184, June 2008.

APPENDIX A. DYNAMICS OF COUPLED NONLINEAR OSCILLATORS RINGS.

A system of nonlinear oscillators can be described by a system of ordinary differential equations (distributed coupling is neglected), depending on a control parameter:

$$\dot{\mathbf{x}} = \mathbf{f}(\mathbf{x}, \mu), \quad \mathbf{x} \in \mathbb{R}^n, \mathbf{f}(\mathbf{x}) \in \mathbb{R}^n, \ \mu \in \mathbb{R} \tag{a.1}$$

Maintaining the analogy with the electrical oscillators, μ can be regarded as any circuital parameter, e.g a bias voltage across an active device whose variation is the main cause of self sustained oscillations; increasing it gradually, the DC operating point defined by the equilibrium solution of (a.1)

$$\dot{\mathbf{x}} = 0 \Rightarrow \mathbf{f}(\mathbf{x}_0, \mu) = 0 \tag{a.2}$$

becomes unstable due to an increase of the active devices gain and oscillations are triggered. By looking at the poles of the closed loop transfer function, one could notice that, as the bias voltage is changed, a pair of complex conjugate poles will shift from the left half plane ($\mathrm{Re}(p(\mu))<0$, stable) to the right half plane ($\mathrm{Re}(p(\mu))>0$, unstable), assuming the (purely imaginary) value $p(\mu_0) = \pm j\omega_0$ at $\mu = \mu_0$.

In order to have the onset of an oscillation, the *classical Hopf Bifurcation theorem* suggests [] inspecting the linear version of the system (a.1) in the neighborhood of ($\mathbf{x}_0$, μ_0) described by the Jacobian $\mathbf{J}=[\mathrm{d}\mathbf{f}/\mathrm{d}\mathbf{x}](\mathbf{x}_0, \mu)$. Specifically, to obtain a limit cycle in the system described by (a.1) the eigenvalues of $\mathbf{J}$ should be lying on the imaginary axis for some value μ_0 of μ, and crossing the real axis with non-zero speed. In formulas:

$$\begin{aligned} &\mathbf{L} = \left[\frac{\partial f_i}{\partial x_j}\right](\mathbf{x}_0, \mu_0) \Rightarrow \underbrace{\dim\ker(\mathbf{L} - \lambda(\mu_0)I) = 1}_{\text{simple eigenvalue for } \mu=\mu_0} \\ &\underbrace{\lambda(\mu_0) = \pm j\omega_0}_{\text{imaginary eigenvalue at } \mu_0} \quad (\omega_0 \neq 0), \qquad \underbrace{\left.\frac{d\,\mathrm{Re}(\lambda(\mu))}{d\mu}\right|_{\mu=\mu_0} \neq 0}_{\substack{\text{eigenvalue crossing the imaginary axis} \\ \text{with non-zero speed}}} \end{aligned} \tag{a.3}$$

For the Hopf bifurcation theorem to be applied, the eigenvalue which fulfils (a.3) needs to be *simple*. When modeling rings of coupled oscillators, the (a.2) presents in general eigenvalues with algebraic multiplicity greater than one due to symmetrical coupling terms in system (a.1), and the Hopf bifurcation theorem cannot be any longer employed.

A generalization that holds for *any symmetrical network of coupled oscillators* has been provided by Golubitsky et al., which makes use of group theoretical results and manages to predict the appearance of certain arrangements of spatial and temporal symmetries (corresponding to the oscillation modes introduced in chapter II and IV) when a system of coupled oscillators experiences an Hopf Bifurcation. In order to figure out the concepts of symmetries one can consider a simple system of two symmetrically coupled oscillators. The oscillators can behave synchronically (being in phase) or anti-synchronically (one being half-period out of phase with respect to the other). Synchronic behavior allows us to swap the oscillators, having the system of equation unaltered; technically the system of equation is said to be equivariant with respect to the permutation of two elements. Anti-synchronic behavior apparently breaks the symmetry; however defining a composite transformation as a permutation followed by half period time shift, the equations remain unchanged also in the case of anti-synchronic solution. It is possible to express in abstract notation the action of these two different group of transformation (swapping elements, or simultaneously swapping and time shifting) considering, for example, rings of four coupled oscillators. The state of the system is determined by the vector $\mathbf{v}(t)=[v_1(t), v_2(t), v_3(t), v_4(t)]$. Assuming that, for instance the first two oscillators behave identically (perfectly synchronized) then the state $\mathbf{v}(t)$ won't change when swapping $v_1(t)$ with $v_2(t)$.

Defining the permutation π consistently with the operation described above, it results $\mathbf{v}(t)= \pi\ (\mathbf{v}(t))$; this is an example of spatial symmetry. Temporal symmetries involve the phase locking mechanism among oscillating elements. Consider the case in which $v_1(t)$ is half period out of phase with $v_2(t)$, and same occurs among $v_3(t)$ and $v_4(t)$. The state $\mathbf{v}(t)$ of the system remains unchanged if the oscillators pairs (1,2) and (3, 4) are interchanged (by means of the operator ρ) and simultaneously the time is shifted by half a period, which implies a mixed spatio-temporal symmetry:

$$\begin{array}{ll} \text{If :} & \text{Then:} \\ v_2(t) = v_1(t+T/2) & \mathbf{v}(t)=[v_1(t), v_2(t), v_3(t), v_4(t)] = \\ v_4(t) = v_3(t+T/2) & \left[v_2(t+T/2), v_1(t), v_4(t+T/2), v_3(t)\right] = \rho \cdot \mathbf{v}(t+T/2) \end{array} \tag{a.4}$$

The theory of dynamical systems in presence of symmetry is mostly inspired by the previous considerations. At a glance and omitting the technical details, the *equivariant Hopf bifurcation theorem* (by Golubitsky et al.) states that *more branches of periodic solutions (oscillation modes) are possible in symmetrically coupled oscillators.* Each of the branches is characterized a *spatiotemporal symmetry group* Σ which is a subgroup of $\Gamma \times S^1$ where elements of Γ can be thought as *spatial symmetries*, and are represented by a compact Lie Group, (concretely by linear operators over *n*-dimensional vector spaces) and elements of S^1 as *temporal symmetries* or *phase shifts* (S^1 can be identified with $\mathbb{R}/\mathbb{Z}$, the circle group). Moreover, the amount of symmetry of each oscillating mode is accounted in each *isotropy subgroup*, defined as the set of transformations which leave a specific periodic solution of (a.1) unaltered.

Summarizing all the previous considerations it is possible to state the "*Equivariant Hopf Bifurcation Theorem*". In particular suppose (considering again the system (a.1) and its equilibrium point (a.2)) that *the action of the group* Γ *commutes with the function* $\mathbf{f}(\mathbf{x},\mu)$, due to the symmetries governing the equations:

$$\begin{array}{l} \gamma \in \Gamma \subset \mathbf{GL}_n \ \Rightarrow\ \mathbf{f}(\boldsymbol{\gamma} \cdot \mathbf{x}, \mu) = \boldsymbol{\gamma} \cdot \mathbf{f}(\mathbf{x}, \mu) \\ \mathbf{GL}_n = \left\{ \mathcal{L} : V \to \mathbb{R}^n \ \text{s.t.}\ \mathcal{L}(\alpha\mathbf{v} + \beta\mathbf{w}) = \alpha\mathcal{L}(\mathbf{v}) + \beta\mathcal{L}(\mathbf{w}),\ \alpha, \beta \in \mathbb{C}\ \mathbf{v}, \mathbf{w} \in V \subset \mathbb{R}^n \right\} \end{array} \tag{a.5}$$

where to fix our ideas, $\mathbf{GL}_n$ can be identified with the set of real n^2-dimensional matrices, acting on n-dimensional vectors via the usual matrix-vector product:

$$\boldsymbol{\gamma} \cdot \mathbf{x} = \begin{pmatrix} \gamma_{11} & \cdots & \gamma_{1n} \\ \vdots & \ddots & \vdots \\ \gamma_{n1} & \cdots & \gamma_{nn} \end{pmatrix} \begin{pmatrix} x_1 \\ \vdots \\ x_n \end{pmatrix} = \left(\sum_{k=1}^{n} \gamma_{ik} x_k \right)_{i=1,\ldots,n} \tag{a.6}$$

A periodic solution x(*t*) of (a.1) *presents a spatial symmetry* if for a certain γ in Γ, γx(*t*) = x(*t*). Now suppose the eigenspace corresponding to the imaginary eigenvalues $\pm j\omega_0$ has dimension *n*, due to the appearance of multiple eigenvalues (it could be justified via the centre manifold theorem [needed]):

$$\ker\left(\mathbf{L} \pm j\omega_0 \mathbf{I}\right) = \mathbb{R}^n \ \text{ where } \mathbf{L} = \left[\frac{\partial \mathbf{f}}{\partial \mathbf{x}}\right](\mathbf{x}_0, \mu_0) \tag{a.7}$$

The methodology to follow in this case is to have a decomposition of the group representation in a certain vector space into the direct sum of simpler representations which are irreducible []. The eigenspace of the Jacobian evaluated at the equilibrium point turns out to be a Γ *simple representation, taking the form* $W \oplus W$ (*absolutely irreducible for* Γ) or Y *(irreducible, but not absolutely irreducible for* Γ).

Along with these facts, a suitable group action for time shifts remains to be defined in the *n-dimensional* real vector space. It is possible to show that the circle group $S^1 = \mathbb{R}/\mathbb{Z}$ acts on $\mathbb{R}^n$ via the exponential matrix of the Jacobian evaluated at ($\mathbf{x}$, μ_0):

$$\forall \mathbf{x} \in V,\ \mathbf{L}(\mathbf{x}) = \left(\partial f_i \,/\, \partial x_j\right)\Big|_{(\mathbf{x},\mu_0)},\ \ \theta \in S^1$$
$$\theta \cdot \mathbf{x} = e^{-2\pi\theta \mathbf{L}(\mathbf{x})} \cdot \mathbf{x} \tag{a.8}$$

Now, is possible to define a *joint spatiotemporal action on T-periodic solutions of the system* (a.1):

$$(\boldsymbol{\gamma}, \theta) \in \Gamma \times S^1 : (\boldsymbol{\gamma}, \theta) \cdot \mathbf{x}(t) = \boldsymbol{\gamma} \cdot \mathbf{x}\left(t + \theta T / 2\pi\right) \tag{a.9}$$

in which Γ acts as a matrix multiplication and θ represents phase shifts. The spatiotemporal symmetry group is then a subset of $\Gamma \times S^1$ representing all possible spatiotemporal transformations which leave T periodic solutions unaltered

$$\Sigma \subset \Gamma \times S^1 = \left\{(\boldsymbol{\gamma}, \theta) \in \Gamma \times S^1 : \boldsymbol{\gamma} \cdot \mathbf{x}(t + \theta T \,/\, 2\pi) = \mathbf{x}(t)\right\} \tag{a.10}$$

Defining the *isotropy subgroup*

$$\Sigma_{\mathbf{x}} \subset \Gamma \times S^1 = \left\{\boldsymbol{\gamma} \in \Gamma : \boldsymbol{\gamma} \cdot \mathbf{x}(t) = \mathbf{x}(t)\right\} \tag{a.11}$$

and the *fixed point subspace of the spatiotemporal symmetry group*:

$$\mathrm{Fix}(\Sigma) = \left\{\mathbf{x} \in \mathbb{R}^n \,/\, \boldsymbol{\sigma} \cdot \mathbf{x} = \mathbf{x},\ \boldsymbol{\sigma} \in \Sigma \subset \Gamma \times S^1\right\} \tag{a.12}$$

the equivariant Hopf bifurcation theorem then can be stated as follows. Given Σ_ξ an isotropy subgroup of $\Gamma \times S^1$ and assuming dim(Fix(Σ))=2, and considering the system of ODEs (a.1), the equilibrium point (a.2) subject to the assumption in (a.3) with dim(ker($\mathbf{L} \pm j\omega_0$))>1. Then there is a unique branch of small amplitude periodic solutions of with period near $2\pi/\omega_0$, having Σ as their spatiotemporal symmetry group, with S^1 acting on periodic solutions as phase shifts

The interesting point is that, regardless of the complex dynamics described by the system (a.1), solutions can always be found by applying exclusively group theoretical considerations which lect the implicit symmetry in the system. As a consequence, in the literature many models of symmetrically coupled oscillators' networks have been investigated (for example those presenting the symmetries of n-sided polygon called dihedral symmetry and indicated with $\mathbf{D}_n$), with different order (up to six elements coupled oscillator) and different kind of coupling (unidirectional vs. two-way coupling). In our case, the star coupling network is by no means different than the ring coupling with three elements. So the results for isotropy groups applied to a three–members coupled oscillator rings are also valid for the triple push oscillator topology.

APPENDIX B. DISTRIBUTED AMPLIFIER GAIN WITH LOSSY ARTIFICIAL TRANSMISSION LINES. DERIVATION OF THE EQ. (2.40) .

Recalling that for the *k-th* device:

$$i_k = -g_m v_{gk} = -\frac{g_m V_{in}}{\sqrt{\left(1-\omega^2/\omega_c^2\right)\left(1+\omega^2/\omega_g^2\right)}} e^{-(k-1/2)\gamma_g - j\theta_g} \tag{b.1}$$

and each of this current contribution get summed up to constitute half of the drain current (forward propagating)

$$I_{out} = \frac{1}{2}\sqrt{\frac{Z_{o\pi}^d}{Z_{oT}^d}} \cdot \sum_{k=1}^{N} i_k e^{-(N-k+1/2)\gamma_d} \tag{b.2}$$

ing the (b.1) into the expression for I_{out}

$$\begin{aligned} I_{out} &= -\frac{1}{2}\frac{g_m V_{in}}{\sqrt{\left(1-\omega^2/\omega_c^2\right)\left(1+\omega^2/\omega_g^2\right)}}\sqrt{\frac{Z_{o\pi}^d}{Z_{oT}^d}}\sum_{k=1}^{N} e^{-(k-1/2)\gamma_g - j\theta_g} e^{-(N-k+1/2)\gamma_d} = \\ &= -\frac{1}{2}\frac{g_m V_{in}}{\sqrt{\left(1-\omega^2/\omega_c^2\right)\left(1+\omega^2/\omega_g^2\right)}}\sqrt{\frac{Z_{o\pi}^d}{Z_{oT}^d}} e^{-(\gamma_g+\gamma_d)/2} e^{-N\gamma_d} e^{-j\theta_g} \sum_{k=1}^{N} e^{k(\gamma_d-\gamma_g)} \end{aligned} \tag{b.3}$$

thus setting $u = \gamma_d - \gamma_g$, the output current is found evaluating the last sum in (b.3).
Recalling the sum of the first N terms of a geometric progression, we have that:

$$\begin{aligned} \sum_{k=1}^{N} e^{ku} &= \frac{e^u\left(e^{uN}-1\right)}{e^u-1} = \frac{e^{u/2}e^{u/2}\left(e^{uN}-1\right)}{e^u-1} = \frac{e^{u/2}\left(e^{uN}-1\right)}{e^{u/2}-e^{-u/2}} \\ &= \frac{2e^{u/2}}{\sinh(u/2)}\left(e^{(uN/2)}e^{(uN/2)}-1\right) = \frac{2e^{u/2}e^{(uN/2)}}{\sinh(u/2)}\left(e^{(uN/2)}-e^{-(uN/2)}\right) \\ &= e^{u(N+1)/2}\frac{\sinh(Nu/2)}{\sinh(u/2)} \end{aligned} \tag{b.4}$$

theore:

$$\sum_{k=1}^{N} e^{k(\gamma_d-\gamma_g)} = e^{(\gamma_d-\gamma_g)(N+1)/2}\frac{\sinh\left[N(\gamma_d-\gamma_g)/2\right]}{\sinh\left[(\gamma_d-\gamma_g)/2\right]} = e^{(\alpha_d-\alpha_g)(N+1)/2}\frac{\sinh\left[N(\alpha_d-\alpha_g)/2\right]}{\sinh\left[(\alpha_d-\alpha_g)/2\right]} \tag{b.5}$$

provided that the phase match between drain and gate line is fulfilled ($\beta_g=\beta_d$). Substituing the expression (b.5) into the (b.3) the output current is found which is the (2.39). To obtain the gain function (2.40) from the definition:

$$G = \frac{P_{out}}{P_{in}} = \frac{1/2\left|I_{out}\right|^2 \mathrm{Re}(Z_L^d)}{1/2\left|\frac{V_{in}}{Z_{oT}^g}\right|^2 \mathrm{Re}(Z_{oT}^g)} \tag{b.6}$$

and substituting (b.6) into (2.39) the (2.40) is obtained.

APPENDIX C. REVERSE GAIN OF A DISTRIBUTED OSCILLATOR WITH TWO ACTIVE SECTIONS (2.74)

To evaluate the reverse gain of the distributed oscillator when two sections are simultaneously active, is required to compute of two complex numbers expressed in exponential form, representing the individual reverse gains for the p-th and q-th sections. Given two complex numbers $z=Ae^{j\xi}$, $w=Be^{j\eta}$ we have:

$$\begin{aligned} & z = Ae^{j\xi}, \qquad w = Be^{j\eta}, \qquad z+w = Ce^{j\zeta} \\ & C = |z+w| = \left|Ae^{j\xi}+Be^{j\eta}\right| = \sqrt{\left(Ae^{j\xi}+Be^{j\eta}\right)\left(Ae^{j\xi}+Be^{j\eta}\right)^{*}} \\ & \quad = \sqrt{A^2+2AB\cos(\xi-\eta)+B^2} \\ & \zeta = \tan^{-1}\left(\frac{\mathrm{Im}(z+w)}{\mathrm{Re}(z+w)}\right) = \tan^{-1}\left(\frac{A\sin\xi+B\sin\eta}{A\cos\xi+B\cos\eta}\right) \end{aligned} \tag{c.1}$$

A simplified expression for the phase ζ can be found for $\xi, \eta \approx 2\pi$ and Re(z+w) >> Im(z+w) (which in turn implies $\zeta \approx 2\pi$ so that the trigonometric functions could be suitably approximated up to the first order as:

$$\begin{aligned} & \tan^{-1}(s)\big|_{s\ll 1} \approx s \\ & \sin(\psi)\big|_{\psi\ll 2\pi} \approx \psi \\ & \cos(\psi)\big|_{\psi\ll 2\pi} \approx 1 \end{aligned} \tag{c.2}$$

where s, ψ represent two generic arguments of the trigonometric functions. Using the (c.2) for the expression of the phase ζ in (c.1):

$$\zeta \approx \frac{A\sin\xi+B\sin\eta}{A\cos\xi+B\cos\eta} \approx \frac{A\xi+B\eta}{A+B} \tag{c.3}$$

Therefore eq. (2.74) is obtained substituting the generic complex numbers z, w with the reverse gain functions for the p-th and q-th sections, setting:

$$\begin{aligned} & A = \frac{Z_{om}^{\pi}(\omega)g_{mp}}{2}, \qquad B = \frac{Z_{om}^{\pi}(\omega)g_{mq}}{2} \\ & \xi = (2p-1)\beta(\omega)+\pi, \qquad \eta = (2q-1)\beta(\omega)+\pi \end{aligned} \tag{c.4}$$

APPENDIX D. MINIMAL REVERSE GAIN TO ACHIEVE OSCILLATIONS. CRITICAL PHASE DIFFERENCE AMONG ACTIVE SECTIONS.

In section (§6.3.4) it was mentioned that the distributed reverse gain oscillator needs an additional transistor placed crosswise among the first two sections, in order to guarantee a continuous tuning range. Intuitively, it could be argued that if the difference among the phases of two reverse gain functions of two different stages $G_p^{(rev)}$, $G_q^{(rev)}$ *approaches* π*, then the magnitude of the sum* $G_p^{(rev)} + G_q^{(rev)}$ *gets closer to zero, thus the condition for triggering oscillations cannot be fulfilled. (illustrative examples in pictures).* A way to prove it analytically consists in starting from the definition of the oscillation condition expressed in terms of real and imaginary part of the total loop gain:

$$\begin{cases} \left| G_p^{(rev)} + G_q^{(rev)} \right| \geq 1 \\ \Theta_{(p,q)}^{(rev)} = 2c\pi, \quad (c \in \mathbb{Z}) \end{cases} \Leftrightarrow \begin{cases} \mathrm{Re}\left(G_p^{(rev)} + G_q^{(rev)} \right) \geq 1 \\ \mathrm{Im}\left(G_p^{(rev)} + G_q^{(rev)} \right) = 0 \end{cases} \tag{d.1}$$

Working out the second of the (d.1) (omitting the superscript for convenience) choosing the equality for the minimum total loop gain:

$$\begin{cases} \left| G_p \right|_{\min} \cos\Theta_p + \left| G_q \right|_{\min} \cos\Theta_q = 1 \\ \left| G_p \right|_{\min} \sin\Theta_p + \left| G_q \right|_{\min} \sin\Theta_q = 0 \end{cases} \tag{d.2}$$

and finding the minimum value for the magnitude of G_p *in terms of* G_q, Θ_p, Θ_q from the second equation:

$$\left| G_p \right|_{\min} = -\left| G_q \right|_{\min} \frac{\sin\Theta_q}{\sin\Theta_p} \tag{d.3}$$

substituting it in the first equation:

$$\begin{aligned} &-\left| G_q \right|_{\min} \frac{\sin\Theta_q}{\tan\Theta_p} + \left| G_q \right|_{\min} \cos\Theta_q = 1 \Rightarrow \\ &\left| G_q \right|_{\min} \left(\tan\Theta_p \cos\Theta_q - \sin\Theta_q \right) = \tan\Theta_p \Rightarrow \\ &\left| G_q \right|_{\min} = \frac{\tan\Theta_p}{\left(\tan\Theta_p \cos\Theta_q - \sin\Theta_q \right)} = \frac{\sin\Theta_p}{\cos\Theta_p \left(\tan\Theta_p \cos\Theta_q - \sin\Theta_q \right)} \\ &= \frac{\sin\Theta_p}{\left(\sin\Theta_p \cos\Theta_q - \sin\Theta_q \cos\Theta_p \right)} = \frac{\sin\Theta_p}{\sin\left(\Theta_p - \Theta_q \right)} \end{aligned} \tag{d.4}$$

entering (d.4) in (d.3):

$$\begin{aligned} \left| G_p \right|_{\min} &= -\left| G_q \right|_{\min} \frac{\sin\Theta_q}{\sin\Theta_p} = -\frac{\sin\Theta_q}{\sin\left(\Theta_p - \Theta_q \right)} \\ \left| G_q \right|_{\min} &= \frac{\sin\Theta_p}{\sin\left(\Theta_p - \Theta_q \right)} \end{aligned} \tag{d.5}$$

From the previous equations, it immediately follows that when the phase difference (Θ_p -Θ_q) is close to π the minimum gain required for triggering an oscillation grows to infinity. As a result, there won't be any tuning capability for all the frequencies for which the phase difference of the individual loop gains $G_p^{(rev)}$, $G_q^{(rev)}$ gets close to π. It could be shown that in the original schematic (derived directly from the distributed amplifier) Θ_1, Θ_2 are π out of phase, which prevents reaching the oscillation condition (d.1). By placing an additional transistor between the first and the second sections

(placed crosswise, such that its drain is connected to the drain of T_1 and its gate is connected to the gate of T_2) extra transconductance and appropriate phase rotation are provided, in order to ensure a total loop gain phase shift of 2π[skvor]. Moreover, it could be also proven that only one additional transistor suffices for having a continuous tuning across the band [ω_1, ω_N], since for (Θ_p -Θ_q)<< π for p, q>2. In fact, from the formulas for the phases of the reverse loop gains of the p-th and q-th sections:

$$\begin{cases}\Theta_p = \pi + (2p-1)\beta(\omega) \\ \Theta_q = \pi + (2q-1)\beta(\omega)\end{cases} \Rightarrow \Delta\Theta_{(p,q)} = \Theta_p - \Theta_q = 2(p-q)\beta(\omega)$$
$$\Rightarrow \beta(\omega) = \frac{\Delta\Theta_{(p,q)}}{2(p-q)} \tag{d.6}$$

where β(ω) represent the phase contribution of the a constant k section (T or Π form). Then, assuming an upper bound for the difference $\Delta\Theta_{(p,q)}$ of π, the maximum phase shift of a filter section in order to achieve oscillations when both the transistor $\mathbf{T}_p$, $\mathbf{T}_q$ are active will be:

$$\beta_{MAX} = \frac{\pi}{2(p-q)} \tag{d.7}$$

and its value is shown in the table below (Table D.1) in the case of a nine stage oscillator [ ] N=1,…,9 for increasing values of (p-q).

(p-q)	1	2	3	4	5	6	7	8
β_{MAX}	π/2	π/4	π/6	π/8	π/10	π/12	π/14	π/16

Table D1

Moreover, when a single section (p) is active and the oscillator resonates at the frequency ω_p the phase of the reverse loop gain Θ_p=2π, theore

$$\Theta_p = \pi + (2p-1)\beta(\omega) = 2\pi \Rightarrow$$
$$\Rightarrow \beta_p = \frac{\pi}{(2p-1)} \tag{d.8}$$

which represents the phase associated to the cascaded filter sections up to the p-th section β_p.

p	1	2	3	4	5	6	7	8	9
β_p	π	π/3	π/5	π/7	π/9	π/11	π/13	π/15	π/17

Table D2

The previous table shows the variation of the phase shift across the different sections p=1,…,N. It is evident that major phase rotations occur in the first five sections. For example when turning on the first and the second stage, the phase contribution of the cascaded filter sections is between π and π/3, between the first and the second is between π/3 and π/5 and so on. Since for N>5 the phase differences (β_p -β_q) are well below the critical phase shift β_{max} these devices can be omitted. The phase associated with the $\mathbf{T}_5$, is below the corresponding critical phase (π/8) so this can be retained and form a pair with $\mathbf{T}_4$; for the same reason transistors $\mathbf{T_1}$, $\mathbf{T}_3$ are kept since when tuning adjacent stages (p-q=1, first column of table D.1) the critical phase difference for the constant k filter section (i.e. π/2) will never be reached, as can be immediately seen. However, when turning on the first section ($\mathbf{T}_1$), a phase rotation of π is needed, which clearly exceeds β_{max} .

Theore comparing table (#) with table (#), when both the transistors $\mathbf{T}_1$ and $\mathbf{T}_2$ are active there exists a range of phase values for the which loop gain $\pi/2 < \beta < \pi$ in which is not possible to achieve continuous tuning in the frequency band [f_2, f_1]. This issue is solved by connecting an additional transistor between the first two sections (T_{12}) , in order to provide the adequate phase rotation to fulfill the oscillation condition across all the tuning range []. The transistor has to be placed crosswise, with its drain connected with T_1's drain and its gate connected with T_2's gate. By doing so, a minimum step of (p-q)= 1/2 is allowed when tuning adjacent stages, theore the table D1 gets transformed in the following

(*p-q*)	½	1	2	3	4	5	6	7	8
β_{MAX}	π	π/2	π/4	π/6	π/8	π/10	π/12	π/14	π/16

Table D.3

in which a maximum phase rotation (relative to the propagation constant of the k filter sections) of π is tolerated when tuning among the neighboring sections T_1, T_{12}, T_2, and a maximum shift of π/2 is permitted when tuning the last two stages T_3 ,T_4, which enables the oscillation condition across all the tuning range.

APPENDIX E. RELATION AMONG PROBE AMPLITUDE (PEAK VOLTAGE) AND PROBE POWER (DELIVERED AT Z_0 = 50 Ω)

Often times it is required to specify the probe amplitude value *A* (expressed in volts) for obtaining oscillations whose output power level at the fundamental should be *P* (expressed in dBm). This occurs:

- when initializing the probe amplitude, in a single frequency HB simulation (*analysis*);
- when designing an oscillator whose output power needs to be specified (*synthesis*);
- when using the probe as a driving generator for *studying the injection-locking*

In this case a simple conversion formula exists between the probe amplitude *A* and its power *P*. Assuming the probe impedance is Z_0, by definition of power *P* in dBm:

$$P(\text{dBm}) = 10\log\left(\frac{A_{rms}^2(\text{V})}{Z_0 P_0}\right)_{P_0=1\text{mW}} \quad \text{where:}\ A_{rms} = \frac{A}{\sqrt{2}} \tag{e.1}$$

as the power relative to P_0= 1mW. The inverse relationship reads:

$$A_{rms}(\text{V}) = \sqrt{Z_0 P_0 \cdot 10^{\frac{P(\text{dBm})}{10}}} \tag{e.2}$$

which rewritten in terms of the peak voltage *A*:

$$A(\text{V}) = \sqrt{2 Z_0 P_0 \cdot 10^{\frac{P(\text{dBm})}{10}}}$$

Now if we assume Z_0=50 Ω and P_0= 1mW, (2 Z_0 P_0) = 0.1 (V^2) leading to the simple formula

$$A(\text{V}) = \sqrt{0.1 \cdot 10^{\frac{P(\text{dBm})}{10}}} = 10^{\left(\frac{P(\text{dBm})}{10}-1\right)\cdot\frac{1}{2}} \tag{e.3}$$

which relates the probe amplitude value to the power delivered at its port across a fifty-ohm load.

© ALESSANDRO ACAMPORA, 2013. All rights reserved.

This Page Intentionally Left Blank